Nanoparticle Dynamics in Polymer Solutions and Gels: A Simulation Approach

Valerio Sorichetti

THÈSE POUR OBTENIR LE GRADE DE DOCTEUR DE L'UNIVERSITÉ DE MONTPELLIER

En Physique

École doctorale: Information Structures Systèmes (I2S)

Unité de recherche: Laboratoire Charles Coulomb

Nanoparticle Dynamics in Polymer Solutions and Gels: A Simulation Approach

Présentée par Valerio SORICHETTI

Le 28 Novembre 2019

Sous la direction de Walter KOB et Virginie HUGOUVIEUX

Devant le jury composé de

Walter KOB, Professeur, Université de Montpellier	Directeur de thèse
Virginie HUGOUVIEUX, Chargée de recherche, INRA	Co-encadrante
Jörg BASCHNAGEL, Professeur, Université de Strasbourg	Rapporteur
Angel MORENO SEGURADO, Tenured Scientist, CSIC	Rapporteur
Antoine BOUCHOUX, Chargé de recherche, INRA	Examinateur
Ralf EVERAERS, Professeur, ENS Lyon	Examinateur
Julian OBERDISSE, Directeur de recherche, CNRS	Président du jury

UNIVERSITÉ DE MONTPELLIER

NANOPARTICLE DYNAMICS IN POLYMER SOLUTIONS AND GELS: A SIMULATION APPROACH

VALERIO SORICHETTI

Thesis submitted for the degree
of Doctor of Philosophy
in Physics
at the University of Montpellier

2019

Abstract

Polymer nanocomposites, systems of polymers containing nanoparticles (NPs), are fascinating systems that have many applications in material science, biology and medicine, but also pose challenges to theoretical physics. One of the fundamental problems in the physics of nanocomposites is to understand how the structure and dynamics of the system depends on key parameters, such as NP size and volume fraction and the typical size of the polymeric mesh. In this thesis we use molecular dynamics simulations to study the structural and dynamic properties of NPs embedded in liquid and solid polymer-nanocomposites. We observe that when weakly attractive, well dispersed NPs are added to a dense polymer solution, both the polymers and the NPs experience a dynamical slowing down. We find that, in qualitative agreement with experiments, this dynamical slowing down is captured by a confinement parameter in the form h/λ, where h is the average distance between the surfaces of neighboring NPs (*interparticle distance*). We are able to show that for the NPs, λ can be interpreted as the hydrodynamic radius of the NP, whereas for the polymers it behaves as a cooperativity length scale. Simulating disordered, polydisperse polymer networks containing purely repulsive NPs, we find that small NPs can freely diffuse through the entanglement mesh, while large NPs are transiently trapped and can only move through a sequence of "jumps" (hopping motion). We find that the parameter controlling NP localization is the ratio between the NP diameter and the localization length of the crosslinks. Finally, we propose a new method to characterize the geometrical mesh size in polymer liquids, a quantity that is important to describe the diffusion of NP in a disordered medium.

Résumé

Les nanocomposites de polymères, systèmes de polymères contenant des nanoparticules (NP), sont des systèmes fascinants qui ont de nombreuses applications en science des matériaux, en biologie et en médecine, mais qui posent également des défis en physique théorique. L'un des problèmes fondamentaux de la physique des nanocomposites est de comprendre comment la structure et la dynamique du système dépendent de paramètres clés, tels que la taille et la fraction volumique des NP et la taille typique du maillage polymère. Dans cette thèse, nous utilisons des simulations de dynamique moléculaire pour étudier les propriétés structurelles et dynamiques des NP incorporées dans des nanocomposites de polymères liquides et solides. Nous observons que lorsque des NP faiblement attractives et bien dispersées sont ajoutées à une solution de polymères dense, les polymères et les NP subissent un ralentissement dynamique. Nous trouvons que, en accord qualitatif avec les expériences, ce ralentissement dynamique est capturé par un paramètre de confinement sous la forme h/λ, où h est la distance moyenne entre les surfaces des NP voisines (*interparticle distance*). Nous pouvons montrer que pour les NP, λ peut être interprété comme le rayon hydrodynamique des NP, alors que pour les polymères il se comporte comme une échelle de longueur de coopérativité. En simulant des réseaux de polymères polydispersés désordonnés contenant des NP purement répulsives, nous constatons que les petites NP peuvent diffuser librement à travers le maillage d'enchevêtrement, tandis que les grosses NP sont piégées de façon transitoire et ne peuvent se déplacer que par une séquence de "sauts" (mouvement de *hopping*). Nous constatons que le paramètre contrôlant la localisation des NP est le rapport entre le diamètre des NP et la longueur de localisation des crosslinks. Enfin, nous proposons une nouvelle méthode pour caractériser le maillage géométrique dans les liquides de polymères, une quantité importante pour décrire la diffusion des NP dans un milieu désordonné.

ACKNOWLEDGEMENTS

A doctoral thesis marks the end of a journey, but also the beginning of another.

Thanks to Jörg Baschnagel and Angel Moreno, who kindly agreed to be the referees for this thesis, and also to the other members of my thesis committee: Ralf Everaers, Julian Oberdisse and Antoine Bouchoux. I thank all of them for their thorough evaluation of my work, for the stimulating questions and for the very interesting discussion. I am especially grateful to Jörg Baschnagel, with whom I had the opportunity to discuss in Mainz and also the day after the defense: I feel that I have learned a lot from these short discussions. Julian was also a member of my annual thesis committee, and for this I have to thank him twice. Thanks also to the other members of the committee, Xavier Frank and Christian Ligoure.

I would not have chosen to undertake this journey if it were not for all the people who have passed on to me their curiosity and passion for science. I would therefore like to thank my professors at La Sapienza University and especially Francesco Sciortino, who passed on to me the passion for soft matter and who supervised the dissertations of both my *laurea* and my *laurea magistrale*. Even after the end of my university career, Francesco was always there to answer my questions and help me clarify my many doubts, always teaching me something deep and new.

The realization of this thesis would not have been possible without the guidance and constant support of my coordinators, Walter Kob and Virginie Hugouvieux. Walter has been a real teacher for me during these three years, accompanying me with his wisdom and patience and passing on to me a small part of his vast knowledge of statistical physics and disordered systems. Characteristics of Walter that I have appreciated the most are his frankness, his stubbornness, and his honesty. He is the kind of scientist who won't be satisfied until he understood everything about a problem, a rare characteristic in a time which favors quick and sensational publications. The door to his office was literally always open for me, and I think that few other supervisors would have allowed me to grown up as much as a researcher in these three years. Virginie played an equally important role, even in the period immediately after my arrival in Montpellier, when she helped me navigate the treacherous sea of the French administration. Always willing to engage in lengthy discussions on physics and to help me solve problems of all kinds with her characteristic rigor and thoroughness, Virginie's presence has been fundamental in completing this journey. I should also mention that without her unrivaled mastery in finding errors and inconsistencies, our papers and preprints wouldn't have been half as good!

My stay at Charles Coulomb Laboratory during these three years has also been made more enjoyable by the presence of exceptional colleagues: Misaki, Andrea, Marouane, Yoshihiko, Anshul, Joris, Chris, Daniel, Murari, Camille, Benjamin, Zhen, Athina, Qinyi and Ramon. Most of all I have to thank Misaki, Marouane and Yoshihiko for sharing the office with me and stoically putting up with me. Thanks also to Daniele, for having helped me many times, with patience, to solve scientific and non-scientific conundrums, and to all the other permanent members of the statistical physics group, who have always treated me with kindness. To conclude this long list, thanks also to the members of the soft matter and theoretical physics groups, in particular Domenico Truzzolillo, Luca Cipelletti, Julian Oberdisse,

Andrea Parmeggiani and John Palmeri, for the many interesting discussions and for their precious advice. A special thanks to Domenico for all the coffees and the chats. Last but not least, thanks to Doris for her kindness and efficiency.

Regarding research, a large part of which is still ongoing, I have to sincerely thank my friends and collaborators Andrea, Lorenzo and José, who agreed to embark with me on a long project (although if they had known it would have been so long, they probably would have kindly declined!). I would like to thank in particular Lorenzo, for his willingness to discuss even on weekends and at late times despite the many work commitments (but without giving up *calcetto*!) and Andrea, who did half the hard work of simulation and data analysis. Thanks also to Emanuela, who believes in us, and Cristian, without whom we would be much further behind.

There's more to life than PhD theses and reasearch: thanks then to my friends in Montpellier, who have made these three years unforgettable: Sergio, Laura, Eleonora, Lorenzo, Marta, Irene, Ivano, Mathieu, Corentin, Yohann, Pierre, Romain, Lolo, Angela, Giorgio, Marina, Antoine, Ana, Omar, Caroline, Pedro ... The list goes on, and I would surely forget to write down someone's name! However, I will never forget Montpellier thanks to them. Finally, thanks to my parents and my grandparents, since without their unconditioned support I would not be where I am today, and to Debora, who after three years still puts up with me.

This thesis has been financed by LabEx NUMEV, funded by the Investissements d'Avenir French Government program, and by INRA.

LIST OF ACRONYMS

ANM	Affine network model
BC	Boundary conditions
BWdG	Brochard-Wyart–de Gennes
CPR	Cai-Panyukov-Rubinstein
FENE	Finite extensible nonlinear elastic
FJC	Freely jointed chain
FS	Flory-Stockmayer
HI	Hydrodynamic interactions
HS	Hard spheres
LJ	Lennard-Jones
MC	Monte Carlo
MCT	Mode-coupling theory
MD	Molecular dynamics
MSD	Mean-squared displacement
NP	Nanoparticle
OC	Overlapping chains
OS	Overlapping spheres
OZ	Ornstein-Zernike
PDF	Probability density function
PNC	Polymer nanocomposite
PNM	Phantom network model
PSD	Pore size distribution
RCP	Random close packing
RDF	Radial distribution function
RMS	Root-mean squared
SAW	Self-avoiding (random) walk
SCGLE	Self-consistent generalized Langevin equation
SD	Squared displacement
SE	Stokes-Einstein
WCA	Weeks-Chandler-Andersen

INDICE

1

INTRODUCTION

This thesis is about polymers. It is customary for books and research papers on *X* to begin by informing the reader that *X* is ubiquitous, and can be found everywhere in everyday life. There are few subjects, however, for which this really holds true: Polymers are one of these subjects. A polyester shirt, a plastic bottle, nylon stockings, rubber car tires, a beef steak, a paper airplane, leather gloves, a silk dress: Most of the matter that we touch, see and even eat everyday is made of or contains polymers. Our own body contains an enormous variety of polymers, from the DNA which stores our genetic information, to proteins like actin, which is essential for muscle contraction and is one of the main components of the cytoskeleton, or hemoglobin, which is responsible for oxygen transport in blood cells. It is therefore clear why the study of polymers is such an active area of research in many different fields, such as engineering, material science, chemistry and biology.

Figura 1 – Entangled polymers

Polymers (long molecules made of covalently bonded elementary units called *monomers*) are an extremely interesting subject, however, also for a theoretical physicist. In (non-charged) atomic or molecular liquids, spatial correlations are usually short-ranged and the dynamical behavior of an atom/molecule is mainly dictated (at length scales where hydrodynamics can be neglected) by that of its close neighbors[1]. Polymer liquids, however, have built-in long-range interactions originating from the connectivity of the chains[2,3]. The dynamics of a monomer in a polymer chain does not only depend on nearby molecules, but also on each of the monomers which are part of the same chain: If one extremity of the chain moves, the whole chain has to follow. This can lead to very complex long-range correlations in polymer liquids with long chains, as it is clear from the schematic representation in Fig. 1. If we imagine to pull out a chain from such a system, we will quickly realize that this is by no means easy: To pull out chain 1, we have first to pull out chains 2 and 3, but to pull out chains 2 and 3 we have first to pull out chains 4, 5, 6, and 7, and so on. The task is almost impossible, as those who have tried to remove tangled hair from a hair brush will know very well. In polymer physics, this effect is known as *entanglement* (not to be confused with the quantum effect!), and it is at the origin of many of the peculiar behaviors of polymeric liquids, some of which are still not understood today.

Entanglements are one of the reasons why the "spherical molecule" approximation, which is so dear to theoretical physicists, and can be quite successful in obtaining the main qualitative features of some molecular liquids, is bound to fail miserably if used to describe a dense polymer liquid[4]. When the chains are shorter and/or the density lower, entanglements disappear and a theoretical description of the system becomes somewhat easier[2]. Even

in this case, however, the situation is complicated by the presence of several different length and time scales: From the length scale of a single bond/monomer ($\simeq$ 1 Å) to the scale of the persistence length[5] ($\simeq$ 10 Å) and the scale of the whole chain ($\simeq$ 100 Å). In many-chain systems, even larger length scales can intervene: Close to the critical point of demixing of a polymer blend, density fluctuations with typical length scales of $\simeq$ 1000 Å are predicted and observed[6]. Whereas in an atomic liquid the only relevant length scale is in most cases the atomic radius, in a polymeric liquid all these length scales are relevant and associated to qualitatively different types of motion, which happens on very different time scales. Even for an isolated polymer, the long-range interactions induced by the chain's connectivity make an exact theoretical treatment extremely challenging, to the point that even predicting the chain conformation in 3D space is a very non-trivial task[7]. A detailed mathematical description of even a simple polymeric system is thus almost impossible: This is when computer simulations come into play.

Computer simulations allow to study polymeric systems with all the essential details, but without the approximations which are usually introduced in analytical models in order to make the calculation manageable. However, a full atomistic simulation of a polymer liquid, employing chemically realistic force fields, is only feasible for very small systems[6]: This is apparently very troublesome, since, as discussed above, the relevant length scales in such systems can be much larger than the size of a monomer. Luckily, however, it turns out that polymers have some *universal* properties which depend on the existence of very few essential ingredients, such as chain connectivity and excluded volume. These characteristics are easily incorporated in simulations by adopting a *coarse-grained* model[6], i.e., a simplified description of the polymer itself. Many of the essential *universal* properties of polymer liquids are present in simulations which model the polymer simply as a chain of hard spheres connected by rigid bonds ("pearl necklace" model[6]). Even a simple random walk on a lattice with the condition that the walk cannot visit the same lattice site twice (self-avoiding random walk; see Fig. 2) correctly predicts many properties of polymers with astonishing precision[6]. This is because, as we mentioned above, some properties of polymeric systems are universal and do not depend at all on the particular chemical structure of the polymer.

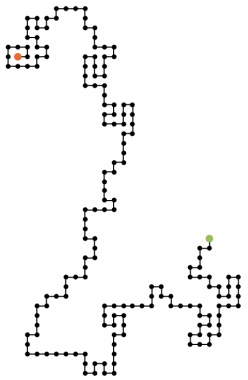

Figura 2 – A self-avoiding random walk in 2D.

In recent years, the simulation approach has been fruitfully applied to all kinds of polymer systems: melts, blends, polyelectrolytes, gels, films, *et cetera*. One class of polymeric material which received a lot of attention, mainly because of technological applications, is that of *polymer nanocomposites* (PNC): Polymer solutions, melts or gels (but most commonly melts) containing nanoparticles (NP), i.e., particles of size between $\simeq$ 1 and $\simeq$ 100 nm. From a theoretical point of view, these systems are even more challenging than purely polymeric ones, since the presence of the NPs brings into the system other relevant length, time and energy scales: NP size, size of NP aggregates, NP-polymer interaction energy, typical time scale of NP diffusion etc. The situation can become even more complex when considering more peculiar NP types, such as polymer-grafted NPs. The behavior of PNCs is extremely rich, and far from being completely understood[8].

In this thesis, we will use a simulation approach to study the properties of dense polymer solutions and disordered gels containing spherical NPs. In particular, we will focus on the dy-

namics of the polymer chains (in the case of solutions) and of the NPs, trying to understand what are the relevant parameters controlling their diffusion, and what is the microscopic mechanism behind the observed behaviors. The thesis is organized as follows. In Chapter 2 we give a brief historical overview of the main events of theoretical polymer science from its beginnings to the present day, focusing in particular on the figures of three scientists who revolutionized this field. In Chapter 3, we summarize the main concepts of polymer science. In Chapter 4, we discuss some of the salient characteristics of PNCs, concentrating on PNCs containing spherical NPs, which are the theme of this work. We also give a short outline of the main theories dealing with the dynamics of NPs and polymers in PNCs. In Chapter 5, we report and discuss the results of molecular dynamics simulations of a dense polymer solution containing spherical NPs. We show that the diffusion of both polymers and NPs is captured by a confinement parameter in the form h/λ, where h is the mean interparticle distance and λ is a parameter. We also show that for the NPs, this parameter can be interpreted as the hydrodynamic radius of the NPs. In Chapter 6, we study the structural and dynamic properties of disordered, polydisperse, defect-free polymer networks. In Chapter 7, we simulate the same networks studied in Chapter 6, but this time with embedded NPs. We show that the dynamics of the NPs is controlled by the ratio C_r between NP size and crosslink localization length: NPs of size $C_r \lesssim 1$ can freely diffuse in the system, whereas NPs of size $C_r \gtrsim 1$ are transiently trapped by the crosslink/entanglement mesh and can only diffuse through a series of sudden "jumps" separated by long intervals of localization. We conclude in Chapter 9 with a summary of this work and a discussion of the results obtained and of possible directions for future research. Finally, in Chapter 8, we propose a new method to precisely characterize the mesh size in polymer solutions using the concept of pore size distribution.

2

A BRIEF HISTORY OF POLYMER SCIENCE

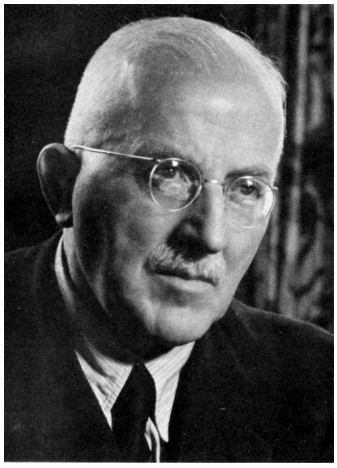

Figura 3 – Hermann Staudinger (1881–1965)

The term "polymer" was coined in 1833 by Jöns Jacob Berzelius, one of the founding fathers of modern chemistry, to describe compounds of the same chemical composition that exhibited very different properties[9]. Eleven years later, polymers gained immense technological relevance with the discovery of the vulcanization process by the American chemist and engineer Charles Goodyear, which gave birth to the rubber industry. It was not until 1922, however, that the German physicist Hermann Staudinger understood the true nature of polymers as long chains of identical repeating units[10a]. This represented a revolutionary concept for Staudinger's contemporaries, who where extremely reluctant to accept the existence of molecules with molecular mass exceeding 4000 g mol^{-1} and considered micellar-type aggregates to be responsible for the unusual properties of such materials[9,11]. The existence of polymers was finally acknowledge by the majority of the scientific community during the late 20s, also thanks to the brilliant work of J. Meyer, H. F. Mark and W. H. Carothers, the inventor of nylon[11]. In 1953, the pioneering work of Staudinger was rewarded with the Nobel Prize for Chemistry "for his discoveries in the field of macromolecular chemistry".

The concept of long molecules of repeating units bound by covalent bonds had scarcely found root when in 1930 W. Kuhn published the first paper in which the methods of statistical physics were applied to a polymeric system, deriving formulas expressing the molecular weight distribution in degraded cellulose. This work was followed in the successive years by those of P. J. W. Debye, H. M. James, E. Guth, L. R. G. Treloar, M. L. Huggins and others. However, the person who almost single-handedly laid the theoretical foundations of polymer science was a young researcher who in 1934 joined Carothers team at Dupont: Paul John Flory.

Working at Dupont, the young Flory was able to solve the problem of molecular size distribution in condensation polymerization, showing that the molecular weights are distributed exponentially[12]. In the following years, Flory revolutionized the theoretical understanding of polymers: He developed the first quantitative theory of gelation (later generalized by W. Stockmayer), one of the first theories of rubber elasticity, the Flory-Huggins formula for the entropy of mixing of polymer solutions[b]and a theoretical explanation for the fact that the effective radius of real chains is larger than what predicted by the simple random walk model.

[a] Staudinger was also the one who coined the term "macromolecule".
[b] This result was obtained essentially simultaneously by M. L. Huggins by A. J. Staverman[12].

Flory predicted that the exponent ν, which is currently called "Flory exponent", relating the molecular radius to the molecular weight, would have a value of $3/5$, which is very close to the actual value of $\simeq 0.588$ yielded by modern theories[c]. Flory also showed, however, that there exist a special temperature, which he referred to as the θ (*theta*) temperature, at which a real chain adopts an ideal, random-walk configuration.

He also predicted that a polymer would also assume an ideal configuration in a dense melt (*Flory's ideality hypothesis*), since "Although a chain molecule in the bulk state interferes with itself, it has nothing to gain by expanding, for the decrease in interaction with itself would be compensated by increased interference with its neighbors"[11]. This hypothesis proved to be extremely accurate and was confirmed in numerous experiments. In 1953, he published his *Principles of Polymer Chemistry*[11], which after more than half a century remains still today a massively relevant text in the field. In 1974, Flory was awarded the Nobel Prize for Chemistry "for his fundamental achievements, both theoretical and experimental, in the physical chemistry of the macromolecules". The work of Flory laid the foundations for the work of many theoretical physicists in the years that followed his seminal works. Among this multitude of scientist, however, two stand out as giants to almost rival Flory's own legacy.

Figura 4 – Paul John Flory (1910–1985)

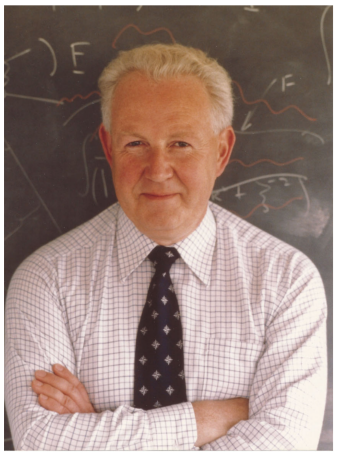

Figura 5 – Sir Samuel Frederick Edwards (1928–2015). From Ref. 13.

Samuel Frederick Edwards begun his career at Harvard as a student of Nobel Prize winner Julian Schwinger, working on quantum electrodynamics and high energy physics[13]. In the mid 1960s, as professor of Theoretical Physics at the University of Manchester, Edwards met with Geoffrey Gee, head of chemistry, to discuss the outstanding problems in his area in the hope of finding new interesting problems that could provide him a challenge. It happened like this that Edwards became interested in polymers. In his own words, the problems of polymer physics

> *...had all been tackled in the Fifties by Flory, Huggins, Zimm, Stockmayer, Rouse, Wall and Gee himself. The outline of the subject was all there and I was coming into it ten years late. But all these authors, impressive as their work was, did not know the advances made in field theories and I realized the long random chains of polymers were a physical manifestation of field theories. A polymer was a Feynman path, the density of a polymer suspension was a field variable*[13].

In 1965, Edwards published a paper[7] on the statistical mechanics of a single polymer chain in solution which "in one stroke founded the modern quantitative understanding of polymer matter"[14]. One of the central problems in polymer physics was to determine, given

[c] It later turned out that this result was due to a fortuitous cancellation of errors. In particular, both the elastic energy and the repulsion energy were largely overestimated[2].

the number N of monomers in a chain, its configuration in 3D space, and in particular its radius R. This is a complicated problem because real chains have excluded volume, which prevents different chain sections from overlapping and disrupts chain conformation in a highly nontrivial way. As mentioned above, Flory was able to provide a heuristic solution, arriving at the conclusion that R is proportional to $N^{3/5}$, instead of the $N^{1/2}$ predicted by the random walk model, which neglects the excluded volume altogether. Edwards was able to solve the problem to excellent approximation by formulating it as a self-consistent field problem where the chain interacts with a mean field generated by its own density of monomers, using the same technique as that used by Hartree to solve the problem of electron motion in an atom. With this approach, he was also able to give the dependence of Flory's exponent on the dimensionality of space d, obtaining $\nu = 3/(d+2)$. This relation, which in 3D gives Flory's exponent $\nu = 3/5$, turns out to be exact in 1, 2 and 4 spatial dimensions[13] [d].

Following his work on chain conformation, Edwards tackled the problems of single and multi-chain dynamics and chain constraint by crosslinks or topological entanglements. While dealing with the latter, he invented the replica method[13] (or "replica trick") , which he would later put to use in his work with P. W. Anderson on spin glasses[15]. In a 1967 paper[16] he addressed the problem of the effect of topological entanglements on the elastic properties of rubber, setting the stage for the work of de Gennes. In 1973, in collaboration with J. W. V. Grant, he predicted that the viscosity η in an entangled melt would scale as N^3, which is very close to the experimental result of $N^{3.4}$. In Cambridge, working with M. Doi and following upon de Gennes's ideas, he laid out a comprehensive theory of polymer dynamics and rheology, which culminated in 1985 with the publication of the monograph *The Theory of Polymer Dynamics*[3], which is still today one of the most influential textbooks on polymer physics.

The one who, alongside Edwards and Doi, more contributed to the theoretical understanding of polymer dynamics was the French Pierre-Gilles de Gennes. After graduating in 1955 from the École Normale Supérieure of Paris[17], de Gennes worked first under A. Herpin in Saclay and then under C. Kittel in Berkeley, conducting studies on magnetism. de Gennes was deeply influenced by Kittel, who thought that physical reasoning should always accompany abstract mathematical calculations[17]. These ideas drove him during his career to try his hardest to make his ideas accessible also to the non-specialists. In 1961 he moved to Orsay, where he worked until 1971, giving fundamental contributions to the fields of superconductivity and liquid crystals, which resulted in the publications of two books, *Superconductivity of Metals and Alloys* (1966) and *The Physics of Liquid Crystals* (1974).

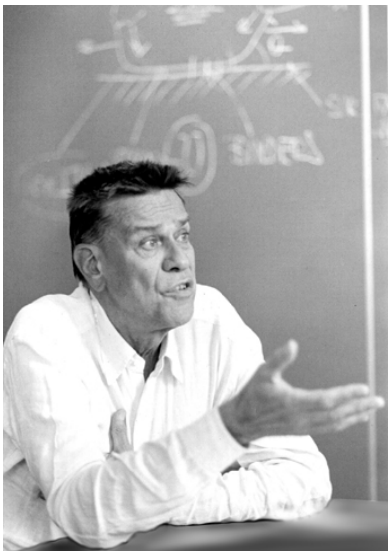

Figura 6 – Pierre-Gilles de Gennes (1932–2007) Photo by Marc Fermigier/ESPCI Paris.

In 1971, de Gennes published his seminal paper[18] on the dynamics of crosslinked polymers, introducing the concept of *reptation*, according to which a chain in a crosslinked network (or in an entangled solution/melt) is con-

[d] In more than 4 spatial dimensions, $\nu = 1/2$ and the polymer is ideal.

fined to a tube-like region and can only slide along the tube [e] in a snake-like fashion. As discussed above, this paper, which was based on previous ideas of Edwards[16], paved the way for the work of Edwards and Doi, who developed the full implications of it. One year later, de Gennes made another contribution which shook the world of polymer science, showing in a one-page article that the behavior of a polymer chain is governed by the same equations of a magnetic system with an n-dependent order parameter in the limit $n \to 0$[20]. Using this analogy, de Gennes obtained the value $\nu = 0.597$ for Flory's exponent, which is a (small) improvement on the $\nu = 3/5$ result of Flory and Edwards (the real value being, as mentioned above, $\nu \simeq 0.588$). It was now possible to use K. Wilson's renormalization group techniques to study polymers. Quoting Joann and Cates:

> *To many theorists, this was a revelation: dirty-looking polymeric systems could now be addressed using the elegant formal tools of statistical physics*[17].

This breakthrough got de Gennes the Nobel Prize for Physics in 1991, "for discovering that methods developed for studying order phenomena in simple systems can be generalized to more complex forms of matter, in particular to liquid crystals and polymers". de Gennes's contributions to the field of polymer physics culminated in 1979 with the publication of *Scaling Concepts in Polymer Physics*[2]. In this book, widely appreciated still today, deep concepts of polymer physics are presented in a simple, elegant way, with the least possible use of sophisticated mathematics. In this and many other ways, de Gennes's book stands as complementary to the work of Doi and Edwards. The scaling approach adopted by de Gennes aimed at isolating the fundamental physics of a problem, without worrying for the exact solutions (which he was, however, fully capable of working out). A striking example is the prediction of the scaling behavior of density in a semidilute polymer solution, which can be obtained from Flory's ideality argument by considering the solution as a melt of "blobs"[2].

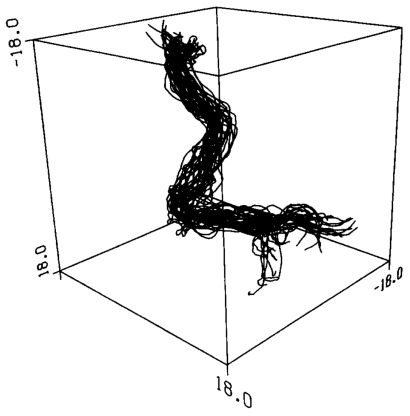

Figura 7 – Configurations of the primitive path of a chain in a dense melt (from Ref. 21).

Starting from the 80s, a new tool started to become predominant in polymer science: computer simulations. Computational methods had been used in polymer science since the early 50s by pioneers such as F. T. Wall[22]. The Monte Carlo was born in 1946 by an idea of Stanislaw Ulam, who at the time was working on nuclear weapons projects at the Los Alamos National Laboratory[23,24]. Apparently, the idea for the Monte Carlo method came to Ulam as he "was convalescing from an illness and playing solitaires"[23]. Ulam discussed his ideas with J. von Neumann, who wrote the first Monte Carlo codes for ENIAC, the first electronic general-purpose computer. The Monte Carlo method is perfectly suited for the study of the conformational properties of polymers, since, as discussed above, a polymer is essentially a self-avoiding random walk, i.e., a random walk that doesn't intersect with itself. Already in 1959, Wall and Erpenbeck used Monte Carlo methods to calculate Flory's exponent ν with excellent accuracy, obtaining $\nu = 0.59$ in 3D and $\nu = 0.75$ in 2D[25]

[e] In a 1977 paper[19], Edwards will coin for the "axis " of the tube along which the chain slides the term *primitive path*.

[f]. In the following years, many different algorithms were developed, such as the pivot algorithm, the slithering snake algorithm and the bond fluctuation model, which made Monte Carlo simulations of polymers increasingly more efficient[27]. In the 80s and 90s, thanks to the work of scientists such as K. Binder, K. Kremer, A. Sokal, W. Paul, D. Y. Yoon, J. Baschnagel, D. W. Heermann, A. Milchev and D. P. Landau, Monte Carlo techniques became one of the predominant tools of theoretical polymer science[6].

In 1979, Bishop *et al.* performed the first molecular dynamics simulation of a polymer system[28], which was followed by the works of K. Kremer, G. Grest, J. H. R. Clarke, B. Dünweg, M. J. Stevens, R. Everaers and many others[6]. Whereas Monte Carlo methods can mainly probe the structural properties of a physical system, but are unable (except for some particular cases) to study its dynamics, molecular dynamics simulations allow to do both. In 1988, Kremer, Grest and Carmesin were the first to prove in molecular dynamics simulations the existence, in entangled polymer melts, of a dynamic regime in which the mean-squared displacement $\langle r^2(t)\rangle$ of the monomers scales as $t^{1/4}$, which had been been predicted by de Gennes in his 1972 paper on reptation[29]. Moreover, simulations made it possible for the first time to visualize the chain's reptating motion directly[21], as shown in Fig. 7. Today, Monte Carlo and molecular dynamics simulations are an indispensable tool for theoretical polymer science, and are responsible every year for many new and exciting discoveries.

[f] In 2010 a fast implementation of the pivot algorithm was used to obtain the astonishingly accurate estimate $\nu = 0.587597(7)$ for the Flory exponent by simulating self-avoiding walks of length $N = 10^6$ [26].

3

BASIC CONCEPTS OF POLYMER PHYSICS

In this Chapter, we review some basic concepts of polymer physics. In particular, we will discuss the conformations of ideal and real chains (Sec. 3.1), the structural properties of many-chains systems (Sec. 3.2), how structural properties can be obtained from scattering experiments (Sec. 3.3), the dynamics of isolated chains and of polymer liquids (Sec. 3.4), the physics of networks and gels (Sec. 3.5). We conclude this Chapter with a short overview of simulations of polymer systems in Sec. 3.6. Most of what is discussed in this Chapter can be found in standard textbooks[2,3,5,11,30], but we feel that it is useful to report it here, in order to give a self-contained and coherent presentation and also to introduce the notation that will be used throughout this work.

A polymer is a large molecule (a *macromolecule*) composed of many covalently bonded elementary units, called *monomers*[5]. The monomers can be either all identical (*homopolymer*) or different from each other (*heteropolymer*). The process of polymer formation, in which bonds between the monomers are formed, is called *polymerization*, and therefore the number of monomers N in a polymer is called its *degree of polymerization*. The value of N is in principle infinite, and polymers containing an enormous number of monomers can be found in nature: The largest human chromosome, for example, contains approximately 220 million base pairs[31]. Polymer can also have many different structures and topologies, as shown in Fig. 8. In this Chapter, however, we will mainly focus on the simplest of all structures, i.e., the linear polymer (Fig. 8a).

From a physical point of view, many of the interesting and unique properties of polymers come from the fact that they are *fractal* objects. To understand this concept, let us consider a solid sphere in three dimensions: Its mass m is related to the radius R by the relation $m = 4\pi R^3\rho/3$, where ρ is the mass density. For a two-dimensional disk, we have $m = \rho\pi R^2$. For a one-dimensional rod of length R, we have $m = \rho R$. For a generic object which "lives" in d spatial dimensions, we expect therefore that

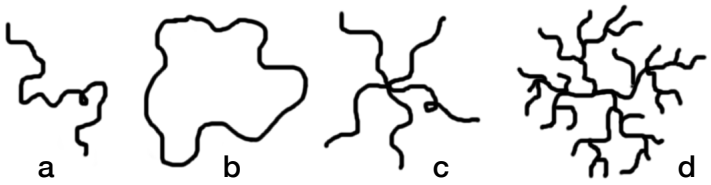

Figura 8 – Example of polymers with different structures: linear (a), ring (b), star (c), randomly branched (d).

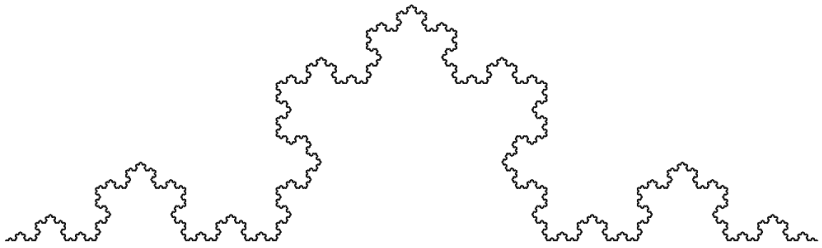

Figura 9 – The Koch curve, a fractal with dimension $\ln(4)/\ln(3) \simeq 1.26$.

$$m \propto R^d. \tag{1}$$

A polymer "lives" in three dimensions; however, the relation between its mass m and its linear size R is not, in general, $m \propto R^3$, but rather $m \propto R^{\mathcal{D}}$, where $\mathcal{D}$ changes continuously from 1 in a stretched state, to $\simeq 1.7$ for a polymer in solution[a], to 2 for a polymer in a dense melt, to 3 in a completely collapsed state[5]. Loosely speaking, an object that satisfies the relation $m \propto R^{\mathcal{D}}$, with $\mathcal{D}$ smaller than the dimension d of the space where the object "lives", is called a fractal[32], and the exponent $\mathcal{D}$ is known as the *fractal dimension* of the object. The fractal dimension of a polymer can therefore vary from 1 to 3. Moreover, since the mass of a polymer is also proportional to its degree of polymerization, $m \propto N$, a polymer satisfies the relation

$$N \propto R^{\mathcal{D}} \quad \mathcal{D} \in [1,3]. \tag{2}$$

Another characteristic of fractals is that they are *self-similar*: the parts they are made of resemble the whole. This property is apparent, for example, when considering the Koch curve (Fig. 9). Polymers display self-similarity, although of course only on length scales which are sufficiently larger than the monomer size. As we will see in Sec. 3.2, this property is extremely important in polymer physics, since it implies that in many situations the conformation of a large enough portion of a polymer chain is identical to the conformation of the whole chain.

3.1 CONFORMATIONS OF POLYMER CHAINS

3.1.1 *Ideal chains*

Consider a flexible linear homopolymer of N monomers. If $\mathbf{r}_i$ is the position vector of (the center of mass of) the ith monomer, we can define a *bond vector* $\mathbf{b}_i = \mathbf{r}_{i+1} - \mathbf{r}_i$, and an *end-to-end vector* as

$$\mathbf{r}_e \equiv \sum_{i=1}^{N-1} \mathbf{b}_i = \mathbf{r}_N - \mathbf{r}_1 \tag{3}$$

[a] Under good solvent conditions[5].

The thermodynamic (statistical) average of $\mathbf{r}_e$ is clearly zero: $\langle \mathbf{r}_e \rangle = 0$. We can consider, however, the mean-squared end-to-end distance,

$$\langle r_e^2 \rangle \equiv \langle \mathbf{r}_e \cdot \mathbf{r}_e \rangle = \sum_{i=1}^{N-1} \sum_{j=1}^{N-1} \langle \mathbf{b}_i \cdot \mathbf{b}_j \rangle \tag{4}$$

If all the bond vectors have the same length, $|\mathbf{b}_i| = \ell \ \forall i$, we can rewrite the above relation as

$$\langle r_e^2 \rangle = \ell^2 \sum_{i=1}^{N-1} \sum_{j=1}^{N-1} \langle \cos \theta_{i,j} \rangle \tag{5}$$

where $\cos \theta_{i,j} \equiv \mathbf{b}_i \cdot \mathbf{b}_j / (|\mathbf{b}_i| \ |\mathbf{b}_j|)$ is the cosine of the angle between the i-th and j-th bond vectors.

We can rewrite Eq. (5) as

$$\langle r_e^2 \rangle = C_N (N-1) \ell^2 \tag{6}$$

where

$$C_N \equiv \frac{1}{N-1} \sum_{i=1}^{N-1} \sum_{j=1}^{N-1} \langle \cos \theta_{i,j} \rangle \tag{7}$$

The simplest polymer model is the *freely jointed chain* (FJC), for which there is no orientational correlation between different bonds and thus $\langle \cos \theta_{i,j} \rangle = \delta_{ij}$ (here δ_{ij} is the Kronecker delta). For a FJC we have therefore

$$\langle r_e^2 \rangle = (N-1) \ell^2 \quad \text{(FJC)} \tag{8}$$

We note that Eq. (8) is formally identical to the expression for the mean-squared displacement of a random walk, with $N-1$ playing the role of the number of steps taken by the walker and ℓ of the step length[33].

If $\langle \cos \theta_{i,i+k} \rangle$ decays more rapidly than k^{-1} for large k (short-range orientational correlation), then $\lim_{N \to \infty} C_N = C_\infty$ is a finite number[34], called *Flory's characteristic ratio*. For large enough N, we have therefore

$$\langle r_e^2 \rangle = C_\infty (N-1) \ell^2 \simeq C_\infty N \ell^2 \quad (N \text{ large}) \tag{9}$$

We obtain therefore a relation which is identical to Eq. (8), with the only difference that the bond length ℓ has been renormalized to an *effective bond length* $b = \sqrt{C_\infty} \ell$. A chain that satisfies the relation $\langle r_e^2 \rangle \propto N$ is called an *ideal chain*. That the orientational correlation $\langle \cos \theta_{i,i+k} \rangle$ must decay more rapidly than k^{-1} is a necessary condition for a chain to be ideal.

Let us now introduce the *contour length* $\mathcal{L} \equiv (N-1) \ell$, so that we can rewrite Eq. (9) as

$$\langle r_e^2 \rangle \simeq C_\infty \ell \mathcal{L} = \ell_K \mathcal{L} \quad (\mathcal{L} \text{ large}) \tag{10}$$

The constant $\ell_K \equiv C_\infty \ell = b^2/\ell$ is called the *Kuhn length*. For a FJC, $\langle r_e^2 \rangle \simeq \ell \mathcal{L}$ for large enough N. We see therefore that the Kuhn length can be interpreted as the bond length of an *equivalent freely-jointed chain*, i.e., a FJC with bond length ℓ_K containing $N_K \equiv \mathcal{L}/\ell_K$ *Kuhn monomers*: $\langle r_e^2 \rangle \simeq \ell_K^2 N_K$.

The root-mean-squared (RMS) end-to-end vector of an ideal chain, $R_e \equiv \sqrt{\langle r_e^2 \rangle}$, satisfies, for large enough N,

$$R_e = b N^{1/2} \quad \text{(ideal chain)} \tag{11}$$

where b is an effective bond length. Since R_e is a measure of the chain's linear size, by comparing Eq. (11) and Eq. (2) that an ideal chain has fractal dimension $\mathcal{D} = 2$.

Another important quantity is the RMS *radius of gyration* (often called simply "radius of gyration"), $R_g \equiv \sqrt{\langle r_g^2 \rangle}$, where

$$\begin{aligned} r_g^2 &\equiv \frac{1}{N} \sum_{i=1}^{N} (\mathbf{r}_i - \mathbf{r}_{\text{cm}})^2 \\ &= \frac{1}{2N^2} \sum_{i,j=1}^{N} (\mathbf{r}_i - \mathbf{r}_j)^2 \end{aligned} \tag{12}$$

with $\mathbf{r}_{\text{cm}} = \frac{1}{N} \sum_{i=1}^{N} \mathbf{r}_i$ is the position vector of the chain's center of mass. It can be shown that for an ideal chain

$$\langle r_g^2 \rangle = \frac{b^2 N}{6} \tag{13}$$

and therefore $\langle r_e^2 \rangle / \langle r_g^2 \rangle = 6$.

3.1.2 *Real chains*

We have seen in Sec. 3.1.1 that a necessary condition for a chain to be ideal is that the orientational correlation $\langle \cos \theta_{i,i+k} \rangle$ must decay faster than k^{-1}. If $\langle \cos \theta_{i,i+k} \rangle \equiv \langle \cos \theta(k) \rangle$ decays as k^{-1} or more slowly, i.e., as $k^{-\alpha}$, with $0 < \alpha < 1$, we have, for large N[34],

$$R_e^2 \simeq N \ell^2 \int_0^N \langle \cos \theta(k) \rangle \mathrm{d}k \propto \begin{cases} N^{2-\alpha} & 0 < \alpha < 1 \\ N \ln N & \alpha = 1 \end{cases} \tag{14}$$

Since $1 < 2 - \alpha < 2$, we see that these long-range correlations lead to a *swelling* of the chain, i.e.,

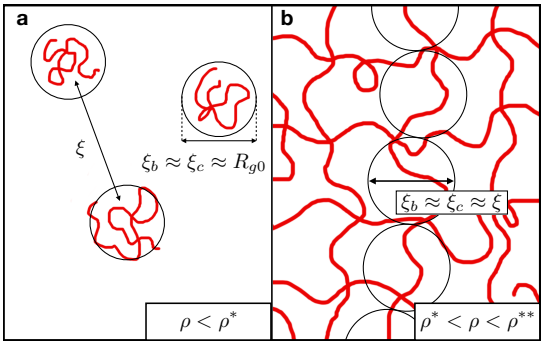

Figura 10 – Schematic representation of a polymer solution in the dilute (a) and semidilute (b) regimes. Circles denotes the blobs, of size ξ_b. The other relevant length scales are the geometrical mesh size, ξ, and the polymer correlation length, ξ_c. In the semidilute regime, these three length scales are very similar. In the dilute regime, however, ξ is very different from the other two.

$$R_e \propto \begin{cases} N^{\nu} & 0 < \alpha < 1 \\ (N \ln N)^{1/2} & \alpha = 1 \end{cases} \tag{15}$$

where $\nu \equiv (2 - \alpha)/2 \in (\frac{1}{2}, 1)$ is called the *Flory exponent*.

In real chains, long-range correlations are present because the monomers have an associated *excluded volume*, i.e., one monomer cannot occupy the space which is already taken by another. Because of this simple fact, it is incorrect to assume that the interaction between monomers which are separated by a large *chemical distance* k is negligible. If we consider an ideal chain with linear dimension $R \propto N^{1/2}$, the mean number of monomer-monomer contacts inside the chain's *pervaded volume* R^3 will be proportional to $N \cdot (N/R^3) \propto N^{1/2}$: For long chains, this number will therefore be quite large.

Solvents in which polymers assume swollen configurations are called *good solvents*, whereas solvents in which chains assume a collapsed configuration are called *poor solvents*. In good solvents, repulsion dominates the monomer-monomer interaction, while in poor solvents attraction is more relevant. It has been shown both theoretically and experimentally that a polymer in good solvent assumes a configuration corresponding to a self-avoiding random walk (SAW)[3,5], and that its RMS end-to-end distance (and every other measure of its linear size) satisfies

$$R_e \propto N^{\nu} \tag{16}$$

where $\nu \simeq 0.588$ is a universal constant[5,26]. The fractal dimension of a swollen chain is therefore $\mathcal{D} = 1/\nu \simeq 1.70$.

3.2 MANY-CHAINS SYSTEMS

3.2.1 *Solutions, melts and the concept of blob*

In Sec 3.1 we have discussed the statistics of isolated chains. We will now briefly summarize the properties of polymer solutions, in which many chains are immersed in a solvent. For simplicity, we will consider the case of an "ideally good", or *athermal* solvent[5] of monodisperse chains ($N = \text{const.}$). In an athermal solvent, the size R of an isolated chain, measured either as the end-to-end distance R_e or the radius of gyration R_g, satisfies the relation

$$R_0 \equiv \lim_{\rho \to 0} R \approx b N^{\nu}. \tag{17}$$

In the previous relation, and also in what follows, we use the symbol $\approx$ to indicate that two quantities are proportional through a dimensionless factor of order 1, while we will use the symbol $\simeq$ when two quantities can be considered approximately equal.

In a dilute solution, the chains are far away from each other and their conformation remains unperturbed; this condition is schematically represented in Fig. 10a. As the monomer density ρ is increased, the chains will eventually start to overlap and the solution will enter the *semidilute regime* (Fig. 10b). By considering the chains as spheres of radius R_0, we can estimate the density ρ^* at which the chains start to interpenetrate (*overlap density*) by equating ρ to the density of monomers inside the sphere:

$$\rho^*(N) \simeq \frac{N}{\frac{4}{3}\pi R_0^3} \approx \frac{N}{R_0^3} \approx b^{-3} N^{1-3\nu}. \tag{18}$$

We note that

$$\lim_{N \to \infty} \rho^*(N) = 0, \tag{19}$$

i.e., infinitely long chains are never in the dilute regime. For $\rho > \rho^*$, the chains overlap. The understanding of this apparently complicated regime can be made easier *via* the concept of *blob*, first introduced by de Gennes[2]. A blob is defined as a region of space of linear size ξ_b which mostly contains monomers from a single chain and solvent (Fig. 10a-b). Inside the blob, the monomers are unperturbed by the presence of other chains, and the chain conformation is the same as in a dilute solution. It is evident from the definition that blobs are *space-filling*: if N_b is the number of monomers inside a blob, we have

$$\rho \approx \frac{N_b}{\xi_b^3}. \tag{20}$$

Moreover, since the chain conformation inside a blob is that of a swollen chain, we have

$$\xi_b \approx b N_b^{\nu} \tag{21}$$

From Eqs. (20) and (21), we can derive the density dependence of the blob size ξ_b:

$$\begin{aligned} \xi_b &\approx b(b^3\rho)^{-\nu/(3\nu-1)} \\ &\approx R_0 \left(\frac{\rho}{\rho^*}\right)^{-\nu/(3\nu-1)}, \end{aligned} \tag{22}$$

where the definitions of R_0 and ρ^* were used to obtain the second equation. We note that, since $\nu \simeq 0.588$, $-\nu/(3\nu-1) \simeq -0.770$.

To understand what happens at length scales $r > \xi_b$, we will first turn our attention to the case of a *melt* of chains, i.e., a system with no solvent, in which the monomers are closely packed (monomer volume fraction $\phi \approx b^3\rho \approx 1$). A chain in a melt is subject to two external potentials: one, U_s, generated by monomers on the same chain, and another, U_d, generated by the other chains. The potential U_s is proportional to the local monomer density, $U_s \propto \rho(\mathbf{r})$, and has a peak around the chain's center of mass: for an isolated chain, this potential is responsible for the swelling of the chain and the decrease of the fractal dimension from $\mathcal{D} = 2$ to $\mathcal{D} \simeq 1.70$. The potential U_d is also proportional to the local density; however, in a dense melt the local density fluctuations are very small and $\rho(\mathbf{r}) \simeq$ const. As a consequence, $U_{\text{tot}} = U_s + U_d \simeq$ const.: the potential U_d has a *well* around the center of mass of the chain, which perfectly cancels the effect of U_s. As a result, chains in a melt have an ideal conformation. This surprising result was first presented by Flory[11], and it is therefore known as the *Flory ideality hypothesis* or Flory theorem[2b]

In a semidilute solution, the blobs are space-filling: Therefore, a semidilute solution can be considered as a closely packed system of blobs, since the blob volume fraction ϕ_b satisfies (cfr. Eq. (20))

$$\phi_b \approx \frac{\rho}{N_b}\xi_b^3 \approx 1. \tag{23}$$

Therefore, on length scales $r > \xi_b$ we can consider the solution as a *melt of blobs*, and the chain conformation is that of an ideal chain with the blob as fundamental unit:

$$\begin{aligned} R &\approx \xi_b \left(\frac{N}{N_b}\right)^{1/2} \\ &\approx bN^{1/2}(b^3\rho)^{-(\nu-1/2)/(3\nu-1)} \\ &\approx R_0 \left(\frac{\rho}{\rho^*}\right)^{-(\nu-1/2)/(3\nu-1)}, \end{aligned} \tag{24}$$

where Eqs. (20) and (22) and the definitions of ρ^* and R_0 were used. Using the numerical value $\nu \simeq 0.588$, we find $R \propto \rho^{-0.115}$: The chain size decreases weakly with increasing density in a semidilute solution.

If density is further increased, the solution will eventually become a melt. The transition to the melt state takes place when the monomer volume fraction $\phi \approx b^3\rho$ becomes of order 1, or equivalently when $\rho \approx b^{-3}$. The density at which the melt state is reached is sometimes

[b] The validity of Flory hypothesis has been verified in numerous experiments[35]; however, we mention that it is nowadays known that noticeable deviations from ideal behavior are actually observable in melts[36].

denoted ρ^{**}. As discussed above, in a melt $\xi_b \approx b$ and chains are ideal on all length scales. In the opposite limit we have a dilute solution, where chains do not overlap and therefore $\xi_b \approx R_0$, (Fig. 10a). Between these two regimes, we find the semidilute behavior, given by Eq. (22). We can thus summarize the scaling behavior of ξ_b as follows:

$$\xi_b \approx \begin{cases} R_0 & \rho < \rho^* \\ b(b^3\rho)^{-\nu/(3\nu-1)} & \rho^* < \rho < \rho^{**} \\ b & \rho > \rho^{**}, \end{cases} \tag{25}$$

We note that imposing continuity between the three relations in Eq. (25), and recalling that $R_0 \approx bN^\nu$ we obtain $\rho^* \approx b^{-3}N^{1-3\nu}$ and $\rho^{**} \approx b^{-3}$, as expected. For the chain size, we have from Eq. (24)

$$\frac{R}{R_0} \approx \begin{cases} 1 & \rho < \rho^* \\ (\rho/\rho^*)^{-\frac{\nu-1/2}{3\nu-1}} & \rho^* < \rho < \rho^{**} \\ N^{1/2-\nu} & \rho > \rho^{**}, \end{cases} \tag{26}$$

where we have used the fact that for $\rho > \rho^{**}$ the chains are ideal, and therefore $R \approx bN^{1/2}$. Exploiting the relation $R_0 \approx bN^\nu$ and introducing the dimensionless scaling variable χ, defined as[37,38c]

$$\chi \equiv N(b^3\rho)^{1/(3\nu-1)} \approx \left(\frac{\rho}{\rho^*}\right)^{1/(3\nu-1)}, \tag{27}$$

we can rewrite Eq. (25) in the following dimensionless form:

$$\frac{\xi_b}{R_0} \approx \begin{cases} 1 & \chi < \chi^* \\ \chi^{-\nu} & \chi^* < \chi < \chi^{**} \\ N^{-\nu} & \chi > \chi^{**}. \end{cases} \tag{28}$$

It is easy to verify from the scaling relations for ρ^* and ρ^{**}, that $\chi^* \equiv \chi(\rho^*) = 1$ and $\chi^{**} \equiv \chi(\rho^{**}) = N$. We note that χ^* is independent of N, whereas χ^{**} depends on N. Conversely, ρ^* depends on N, whereas ρ^{**} is independent of N.

The main drawback of the blob concept is that there is no quantity which can be measured in experiments or simulations which unambiguously correspond to the blob size ξ_b. We will see below that it is possible to introduce two different quantities, the density fluctuation correlation length and the geometrical mesh size, which have the same scaling behavior as ξ_b in the semidilute regime and are accessible from simulations or experimental data.

[c] We choose to use χ and not ρ/ρ^* as a scaling variable since ρ^* is not a sharply defined quantity.

3.2.2 *The geometrical mesh size*

If we take a snapshot of a semidilute polymer solution, its structure will be very similar to that of a network with a certain average geometrical *mesh size* (Fig. 10). This intuitive concept can be made more precise by defining the *geometrical mesh size* ξ as the average linear size of the pores (i.e., volumes containing only solvent) in the system. Based on this definition, it is clear that in the semidilute regime the geometrical mesh size will be equivalent to the blob size apart from a multiplicative factor:

$$\xi \approx \xi_b \quad (\rho^* < \rho < \rho^{**}) \tag{29}$$

However, if we want to maintain our definition of ξ as the average size of the pores, then it is clear that the relation (29) cannot be extended outside of the semidilute regime. This can be understood by considering that in the dilute regime $\rho < \rho^*$ the mesh size is nothing else than the average distance between neighboring chains, i.e., $\xi \approx (\rho/N)^{-1/3}$, and becomes infinite in the limit $\rho \to 0$, whereas $\xi_b \approx R_0$. Moreover, in the concentrated regime $\rho > \rho^{**}$ the size of the pores becomes vanishingly small, $\xi \to 0$, while $\xi_b \approx b$. To summarize, we expect the following behavior for the geometrical mesh size ξ as a function of ρ:

$$\xi \approx \begin{cases} (\rho/N)^{-1/3} & \rho < \rho^* \\ b(b^3\rho)^{-\nu/(3\nu-1)} & \rho^* < \rho < \rho^{**} \\ f(\rho) & \rho > \rho^{**}, \end{cases} \tag{30}$$

where $f(\rho)$ is a decreasing function of ρ for $\rho > \rho^{**}$. In terms of the scaling variable χ,

$$\frac{\xi}{R_0} \approx \begin{cases} \chi^{-\nu+1/3} & \chi < \chi^* \\ \chi^{-\nu} & \chi^* < \chi < \chi^{**} \\ f[\rho(\chi)] & \chi > \chi^{**}. \end{cases} \tag{31}$$

3.3 MEASUREMENT OF STRUCTURAL PROPERTIES FROM SCATTERING EXPERIMENTS

There are several ways to study the structural and dynamical properties of a polymer liquid experimentally, but the most common are probably those based on static and dynamic scattering techniques[5,30]. In this Section, we briefly review some theoretical results related to scattering measurements of structural properties.

3.3.1 *Single chain structure*

When an electromagnetic wave of wave is incident on a system of M point particles with position vectors $\mathbf{r}_1, \ldots, \mathbf{r}_M$, the intensity of the coherent scattered radiation for a given wavevector $\mathbf{q}$ is proportional to a function $S(\mathbf{q})$, called *structure factor* (or, sometimes, *scattering function*)[1,5,30]:

$$S(\mathbf{q}) \equiv \frac{1}{M} \sum_{k,j=1}^{M} \langle \exp[-i\mathbf{q} \cdot (\mathbf{r}_k - \mathbf{r}_j)] \rangle. \tag{32}$$

When studying isotropic systems, the spherically average structure factor, $S(q)$ (with $q \equiv |q|$) is often considered:

$$S(q) \equiv \frac{1}{4\pi} \int_0^{2\pi} \mathrm{d}\phi \int_0^{\pi} \sin\theta \mathrm{d}\theta \; S(\mathbf{q}) \tag{33}$$

The real space counterpart of $S(q)$ is the *radial distribution function* $g(r)$, defined as[1]

$$g(r) \equiv \frac{1}{4\pi M \rho r^2} \sum_{\substack{k=1 \\ j \neq k}}^{M} \langle \delta(|\mathbf{r} + \mathbf{r}_k - \mathbf{r}_j|) \rangle, \tag{34}$$

where $\rho = M/V$ is the particle number density. Indeed, it can be shown that the two quantities are related by a Fourier transform[1]:

$$S(q) = 1 + 4\pi\rho \int_0^{\infty} [g(r) - 1] \frac{\sin(qr)}{qr} r^2 \mathrm{d}r \tag{35a}$$

$$g(r) = \frac{1}{2\pi^2 \rho} \int_0^{\infty} [S(q) - 1] \frac{\sin(qr)}{qr} q^2 \mathrm{d}q \tag{35b}$$

The radial distribution function offers a more direct interpretation than the structure factor, since $4\pi\rho r^2 g(r)\mathrm{d}r$ represents the probability to find a monomer at distance $r < x < r + \mathrm{d}r$ from a randomly chosen particle. However, measuring $g(r)$ experimentally is more challenging than measuring $S(q)$, and therefore we will focus our discussion on the latter.
The structure factor of a polymer solution/melt containing N_c chains of length N is[30]

$$\begin{aligned} S(\mathbf{q}) &= \frac{1}{NN_c} \sum_{\alpha,\beta=1}^{N_c} \sum_{k,j=1}^{N} \langle \exp[-i\mathbf{q} \cdot (\mathbf{r}_{\alpha,k} - \mathbf{r}_{\beta,j})] \rangle \\ &= S_1(\mathbf{q}) + \frac{N_c - 1}{N} \sum_{k,j=1}^{N} \langle \exp[-i\mathbf{q} \cdot (\mathbf{r}_{1,k} - \mathbf{r}_{2,j})] \rangle \\ &= NP(\mathbf{q}) + (N_c - 1) S_2(\mathbf{q}) \end{aligned} \tag{36}$$

where we have introduced the *single-chain structure factor*,

$$S_1(\mathbf{q}) \equiv \frac{1}{N} \sum_{k,j=1}^{N} \langle \exp[-i\mathbf{q} \cdot (\mathbf{r}_{1,k} - \mathbf{r}_{1,j})] \rangle, \tag{37}$$

and the *chain form factor* $P(\mathbf{q}) \equiv S_1(\mathbf{q})/N$. Therefore, $S(\mathbf{q})$ can be expressed as a single-chain component, $S_1(\mathbf{q})$ plus a contribution from scattering between different chains, $(N_c - 1)S_2(\mathbf{q})$.

The exponential term appearing in $S_2(\mathbf{q})$,

$$\exp[-i\mathbf{q}\cdot(\mathbf{r}_{1,k}-\mathbf{r}_{2,j})] = \exp(-iq|\mathbf{r}_{1,k}-\mathbf{r}_{2,j}|\cos\theta), \tag{38}$$

vanishes for $q|\mathbf{r}_{1,k}-\mathbf{r}_{2,j}| \gg 1$, i.e., when the distance between the chains is much larger than the wavelength λ of the incident radiation ($\lambda = 2\pi/q$). For a dilute solution, we can therefore write

$$S(\mathbf{q}) \simeq S_1(\mathbf{q}) \quad \text{(dilute solution)} \tag{39}$$

For $q|\mathbf{r}_k - \mathbf{r}_j| \ll 1$ (i.e. small *scattering angle*), the exponential term in the single chain structure factor can be expanded:

$$\exp[-i\mathbf{q}\cdot(\mathbf{r}_k-\mathbf{r}_j)] = 1 + \mathbf{q}\cdot(\mathbf{r}_k-\mathbf{r}_j) - \frac{1}{2}[\mathbf{q}\cdot(\mathbf{r}_k-\mathbf{r}_j)]^2 + \dots \tag{40}$$

By keeping terms up to the second order and using the fact that $\langle \mathbf{r}_k - \mathbf{r}_j\rangle = 0$, in addition to the isotropy of the chains, we obtain[5,30]

$$\begin{aligned} S_1(\mathbf{q}) &\simeq N - \frac{1}{2N}\sum_{k,j=1}^{N}\langle[\mathbf{q}\cdot(\mathbf{r}_k-\mathbf{r}_j)]^2\rangle \\ &= N - \frac{q^2}{6N}\sum_{k,j=1}^{N}\langle(\mathbf{r}_k-\mathbf{r}_j)^2\rangle \\ &= N - \frac{1}{3}(qR_g)^2 \\ &\simeq \frac{N}{1+(qR_g/\sqrt{3})^2} \end{aligned} \tag{41}$$

where the definitions of radius of gyration r_g (Eq. (12)) and of RMS radius of gyration, $R_g \equiv \sqrt{\langle r_g^2\rangle}$, were used. Incidentally, we note that Eq. (41) implies that the isothermal compressibility of a dilute polymer solution is $\kappa_T = N/\rho k_B T$, since $\kappa_T = S(0)/\rho k_B T$, where $S(0) \equiv \lim_{q\to 0} S(q)$ [1d]. The expansion performed in Eq. (41) is accurate if $qR_g \ll 1$, or equivalently if $R_g \ll \lambda$: if this condition is satisfied, it is possible to measure the chain radius of gyration by performing a scattering experiment on a dilute solution. Most of times light scattering is used, since the wavelength of visible light, which goes from $\simeq 380$ to $\simeq 740$ nm, is usually much larger than the chain size ($\simeq 10$ nm).

For an ideal chain, $S_1(q)$ can be calculated explicitly. The result is $S_1(q) = NP_D(qR_g)$, where[5,30]

$$P_D(x) = \frac{2}{x^4}\left(e^{-x^2} + x^2 - 1\right) \tag{42}$$

[d] This result can also be obtained from the ideal gas equation. For a dilute polymer solution, we can write $P = \rho_c k_B T = \rho k_B T/N$, were $\rho_c = N_c/V$ is the density of chains and $\rho = N_c N/V$ the density of monomers. Since $\kappa_T = \frac{1}{\rho}\left(\frac{\partial\rho}{\partial p}\right)_{T,N_c}$, we obtain $\kappa_T = N/\rho k_B T$.

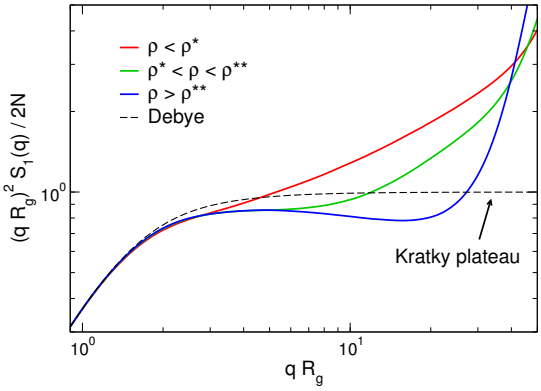

Figura 11 – Kratky plot from molecular dynamics simulations of Kremer-Grest bead-spring chains of length $N = 200$. The overlap density for this system is $\rho^* \simeq 0.03$, while $\rho^{**} \simeq 0.3$. The densities shown are $\rho = 10^{-3}$ (red curve), 0.20 (green curve) and 0.85 (blue curve). The latter corresponds to a dense melt. The dashed line is the Debye prediction, Eq. (42).

is called the *Debye function*. For $qR_g \gg 1$, we have therefore for an ideal chain

$$S_1(q) \simeq \frac{2N}{(qR_g)^2} \propto q^{-2} = q^{-\mathcal{D}} \quad (qR_g \gg 1) \tag{43}$$

where $\mathcal{D} = 2$ is the fractal dimension of the chain. It can be shown that the result $S_1(q) \propto q^{-\mathcal{D}}$ for $qR \gg 1$ is true for any value of the fractal dimension $\mathcal{D} = 1/\nu$ [30].

Often, it is useful to consider the so-called *Kratky plot*, in which $(qR_g)^2 S_1(q)/2N$ is plotted as a function of qR_g. The regime (43) results in this case in a *Kratky plateau*, since $(qR_g)^2 S_1(q)/2N \simeq 1$. In Fig. 11, we show the Kratky plot of flexible chains of length $N = 200$ at different monomer densities ρ, obtained from molecular dynamics simulations of the Kremer-Grest model (see Sec. 3.6). We can see that the Debye function, Eq. (42), gives a good approximation of the data at low qR_g for all values of ρ. In the concentrated regime ($\rho > \rho^{**}$) the chains assume more ideal conformations than for $\rho < \rho^{**}$, as predicted by the Flory ideality theorem, and a feature similar to the Kratky plateau is developed. However, relevant qualitative differences are still present even at such high densities. This, however, should not come as a surprise, since a $N = 200$ chain is still rather short. Moreover, it is known that chains in a melt actually show deviations from ideality, which are observable in the Kratky plot even for very long $N = \mathcal{O}(10^4)$ chains [36].

3.3.2 *Solutions and melts: The correlation length*

Let's now consider scattering from single chains in solution, which can be studied in neutron scattering experiments by introducing a small concentration of deuterated chains in a solution of non-deuterated chains. We have seen in Chapter 3.2 that chains in solution have swollen conformations on length scales $r < \xi_b$ and ideal conformations on length scales $r > \xi_b$, where ξ_b is the blob size.

For the discussion above about the q dependence of S_1 at large values of q, we expect therefore for a polymer in a semidilute solution [2,5,37]:

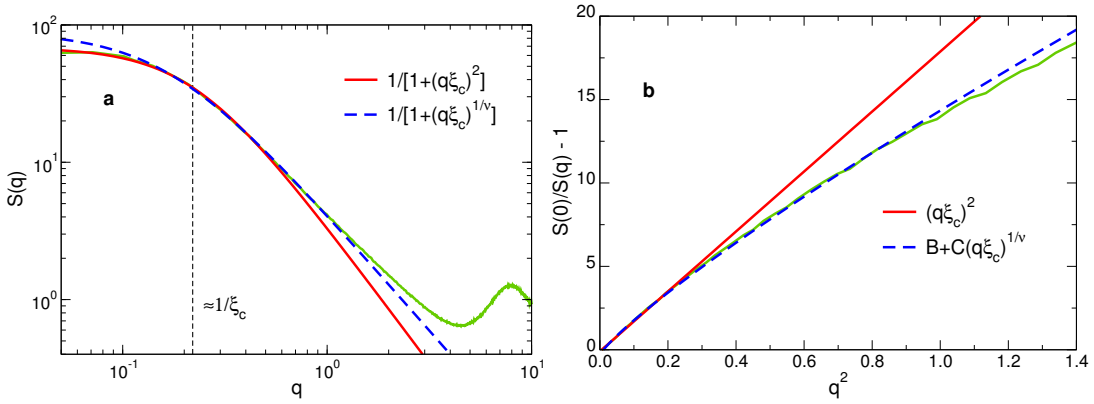

Figura 12 – (a) Total structure factor from molecular dynamics simulations of Kremer-Grest bead-spring chains of length $N = 1000$ in the semidilute regime ($\rho/\rho^* \simeq 2$). The regimes $S(q) \propto [1 + (q\xi_c)^2]^{-1}$ (continuous red curve) and $S(q) \propto [1 + (q\xi_c)^{1/\nu}]^{-1}$ (dashed blue curve) are shown. The approximate value of the inverse correlation length, ξ_c^{-1}, is also shown. (b) Ornstein-Zernike plot of the same quantity. With reference to Eq. (45), we have $B = S(0)/A - 1$ and $C = S(0)/A$.

$$S_1(q) \simeq \begin{cases} N/[1 + (qR_g)^2/3] & q < R_g^{-1} \\ Aq^{-2} & R_g^{-1} \ll q \ll \xi_b^{-1} \\ Bq^{-1/\nu} & \xi_b^{-1} \ll q \ll b^{-1} \\ \mathcal{O}(1) & q \gg b^{-1}, \end{cases} \tag{44}$$

where $A, B > 0$ are constants. We note that in concentrated solutions/melts $\xi_b \approx b$, and therefore the $q^{-1/\nu}$ regime disappears, in agreement with Flory's theorem (Sec. 3.2.1): The chains are ideal at all length scales. In the dilute regime, on the other hand, $\xi_b \approx R_g$, and therefore it is the q^{-2} regime that disappears: The chains are swollen on all length scales.

The quantity which is most often measured in scattering experiments is the total structure factor $S(q)$, since it requires no special preparation of the sample. We have seen that in the dilute regime $S(q) \simeq S_1(q)$; in the semidilute regime, we have[2,5]

$$S(q) \simeq \begin{cases} S(0)/[1 + (q\xi_c)^2] & q \ll \xi_c^{-1} \\ A/[1 + (q\xi_c)^{1/\nu}] & \xi_c^{-1} \ll q \ll b^{-1} \\ \mathcal{O}(1) & q \gg b^{-1}, \end{cases} \tag{45}$$

where $A > 0$ is a constant. In Fig. 12a, we show $S(q)$ for a semidilute solution of polymers of length $N = 1000$. The data are obtained from molecular dynamics simulations of the Kremer-Grest model (see Sec. 3.6). The two regimes $S(q) \propto [1 + (q\xi_c)^2]^{-1}$ and $S(q) \propto [1 + (q\xi_c)^{1/\nu}]^{-1}$ are highlighted. The peak at $q \simeq 8$ is due to correlations on the monomer scale, and it is typical of all liquids[39].

We will now discuss the interpretation of the quantity ξ_c appearing in Eq. (45). From Eq. (45), we see that at low q the structure factor is described by the function

$$S(q) = \frac{S(0)}{1 + (q\xi_c)^2} \quad (q \ll \xi_b^{-1}), \tag{46}$$

called the *Ornstein-Zernike* function[2,5,30,40] (for a derivation of this expression, see Appendix A). In Fig. 12b, we show an "Ornstein-Zernike" plot of the same structure factor shown in Fig. 12a: here, $S(0)/S(q) - 1$ is plotted as a function of q^2, resulting in a straight line with slope ξ_c^2.

From Eq. (46), we can obtain the large r behavior of the radial distribution function $g(r)$, using Eq. (35b)[2,3,30,40e]:

$$g(r) = 1 + \frac{S(0)}{4\pi\xi_c^2\rho}\left(\frac{e^{-r/\xi_c}}{r}\right) \quad (r \gg \xi_b) \tag{47}$$

Since, as mentioned above, $4\pi\rho r^2 g(r)$ represents the probability to find a monomer at distance $r < x < r + \mathrm{d}r$ from a randomly chosen monomer, it is apparent from Eq. (47) that ξ_b must be interpreted as the correlation length of the density fluctuations, i.e., it represents a *density fluctuation correlation length* (or simply "correlation length"). We have seen in Sec. 3.2 that in a semidilute solution, the only relevant length scale is the blob size ξ_b. It is therefore natural to assume that $\xi_b \approx \xi_c$ in the semidilute regime[5,30]. Moreover, it is clear that in the dilute regime we must have $\xi_c \approx R$, with R the chain size. Indeed, since $S(q) \simeq S_1(q)$ in the dilute regime, by comparing Eq. (41) and Eq. (46) we immediately get

$$\xi_c = R_{g0}/\sqrt{3} \quad (\rho < \rho^*) \tag{48}$$

We are therefore lead to the conclusion that, for densities smaller than ρ^{**} (the onset of the concentrated/melt regime), the correlation length corresponds to the blob size

$$\xi_b \approx \xi_c \quad (\rho < \rho^{**}) \tag{49}$$

This is a very relevant result, since it relates the blob size to a physically measurable quantity. However, the relation $\xi_b \approx \xi_c$ loses its validity in the concentrated/melt regime. Indeed, we have seen that for $\rho > \rho^{**}$ the blob size coincides with the monomer size: $\xi_b \approx b$. The structure of a polymer liquid at such high density is virtually the same as that of a dense liquid[41], and its correlation length can be evaluated from a modified version of Eq. (47)[39,42,43]:

$$g(r) = 1 + \frac{B}{r}e^{-r/\xi_c}\sin\left(\frac{2\pi r}{\lambda} + \theta\right), \tag{50}$$

where $B, \lambda > 0$ and θ are constants. In dense liquids, the correlation length *increases* with increasing density due to local packing constraints[41]. Therefore, for $\rho > \rho^{**}$ the correlation

[e] To be more precise, Eq. (46) follows formally from Eq. (35b) if $g(\mathbf{r}) = 1 + Ae^{-r/\xi_c}/r - \delta(\mathbf{r})/\rho$. The presence of the delta distribution is however only an artifact stemming from the fact that we are connecting the large r behavior of $g(r)$ with the small q behavior of $S(q)$. In any case, since we are interested in the large r behavior, this factor can be disregarded. For more details, see Appendix A.

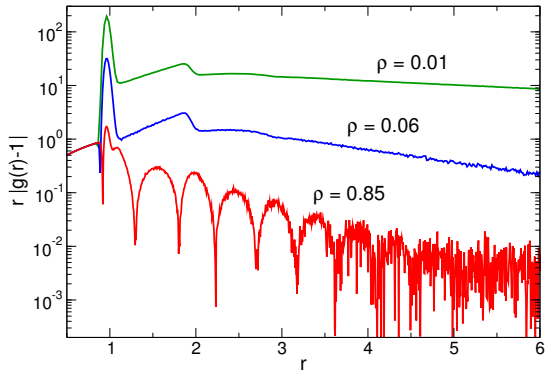

Figura 13 – The quantity $r|g(r) - 1|$ from molecular dynamics simulations of Kremer-Grest bead-spring chains of length $N = 200$ at different densities. For this system, $\rho^* \simeq 0.03$, whereas $\rho^{**} \simeq 0.3$. The $\rho = 0.85$ state corresponds to a dense melt.

length of a polymer liquid is an increasing function of ρ and the relation $\xi_b \approx \xi_c$ loses its meaning. To summarize, the behavior of ξ_c as a function of ρ is as follows:

$$\xi_c \approx \begin{cases} R_0 & \rho < \rho^* \\ b(b^3\rho)^{-\nu/(3\nu-1)} & \rho^* < \rho < \rho^{**} \\ h(\rho) & \rho > \rho^{**}, \end{cases} \tag{51}$$

where $h(\rho)$ is an increasing function of ρ for $\rho > \rho^{**}$.

In Fig. 13, we compare the RDFs of polymers of length $N = 200$ at different densities by showing the quantity $r|g(r) - 1|$. Data are from molecular dynamics simulations of the Kremer-Grest model; for this system, $\rho^* \simeq 0.03$. One sees that at low density $r|g(r) - 1|$ decays exponentially, as per Eq. (47), whereas at high density it shows an oscillatory decay with an exponential envelope, as per Eq. (50).

3.4 DYNAMICS

3.4.1 *Unentangled polymer dynamics: The Rouse model*

One of the simplest models of polymer dynamics is the Rouse model: In this model, the chain is represented as a collection of N beads (monomers) connected by springs, immersed in a heat bath; each bead-spring unit is meant to represent a chain segment. The hydrodynamic interactions between different beads are completely neglected, so that the total friction acting on the chain is simply $\zeta_R = N\zeta$, where ζ is the friction that a single monomer feels by action of the solvent[5]. From ζ_R it is possible to obtain the chain's diffusion coefficient, D_R, through the Einstein relation[44]:

$$D_R = \frac{k_B T}{\zeta_R} = \frac{k_B T}{N\zeta} \tag{52}$$

In order to connect D_R to the relaxation time of the chain, we consider the mean-squared displacement (MSD) of the chain's center of mass, defined as

$$\langle r_{\mathrm{cm}}^2(t)\rangle \equiv \langle |\mathbf{r}_{\mathrm{cm},\alpha}(t) - \mathbf{r}_{\mathrm{cm},\alpha}(0)|^2\rangle = g_3(t) \tag{53}$$

where $\mathbf{r}_{\mathrm{cm},\alpha}$ is the center of mass of the α-th chain. This quantity is related to D_R by another relation due to Einstein[44]:

$$D_R = \lim_{t\to\infty} \frac{\langle r_{\mathrm{cm}}^2(t)\rangle}{6t} \tag{54}$$

From Eq. (52), we can derive a scaling estimate of the chain's relaxation time τ_R, which is the time needed for the chain to diffuse over a distance of the order of its size R (Rouse time):

$$\tau_R \approx \frac{R^2}{D_R} \approx \frac{\zeta N R^2}{k_B T} \approx \frac{\zeta b^2}{k_B T} N^{2\nu+1} \approx \tau_0 N^{2\nu+1}, \tag{55}$$

where $\tau_0 \approx \zeta b^2/k_B T$ is the monomer relaxation time, i.e, the time a monomer would need to diffuse a distance b if it were detached from the chain. Therefore, for an ideal chain ($\nu = 1/2$), $\tau_R \propto N^2$.

In the Rouse model, the MSD of the chain's center of mass is always linear in time[3] [f]:

$$\langle r_{\mathrm{cm}}^2(t)\rangle \propto t. \tag{56}$$

A motion of this type is usually called *diffusive*.

The situation is more complicated, however, if we consider the MSD of the monomers, defined as

$$\langle r^2(t)\rangle \equiv \langle |\mathbf{r}_k(t) - \mathbf{r}_k(0)|^2\rangle = g_1(t) \tag{57}$$

with $\mathbf{r}$ the position vector of a monomer. Indeed, it is found that[3]

$$\langle r^2(t)\rangle \propto \begin{cases} t & t < \tau_0 \\ t^{1/2} & \tau_0 < t < \tau_R \\ t & t > \tau_R. \end{cases} \tag{58}$$

For $\tau_0 < t < \tau_R$, the MSD of the monomers satisfies the relation $\langle r^2(t)\rangle \propto t^\beta$, with $\beta = 1/2$. Whenever a relation of this type, with $0 < \beta < 1$, is obeyed, the motion is said to be *subdiffusive*. To understand the origin of this subdiffusive regime, it is sufficient to consider the following: since polymers are self-similar fractals, a section of an ideal chain containing n monomers will have a (Rouse) relaxation time

[f] In reality, the dynamics of polymers in the absence of hydrodynamics interactions is not perfectly diffusive, since a subdiffusive regime $g_3(t) \propto t^\beta$ is present at intermediate times[21,45,45–47,47–49]. Such a transient is most likely due to non-Gaussian dynamics caused by intermolecular correlations[47]; in simulations of polymer melts ($\rho = 0.85$), the value of β was found to be $\simeq 0.8$[21,45,47–49].

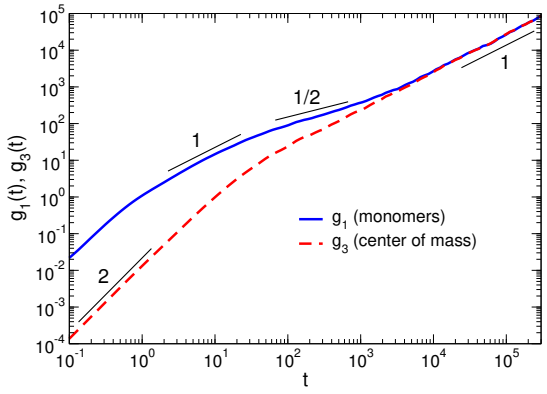

Figura 14 – MSD of the monomers (g_1) and of the chain's center of mass (g_3) from molecular dynamics simulations without hydrodynamic interactions of chains of length $N = 200$ in the dilute regime ($\rho/\rho^* \simeq 0.3$). When computing g_1, only the $N/2+1$ monomers in the middle portion of the chains have been considered, in order to mitigate chain end effects.

$$\tau_n \approx \tau_0 n^2 \tag{59}$$

During the time τ_n, such a chain section will move a distance of the order of its own size, which is $\approx bn^{1/2}$. The MSD of the monomers in the section can thus be estimated as

$$\langle r^2(\tau_n)\rangle \approx b^2 n \approx b^2 \left(\frac{\tau_n}{\tau_0}\right)^{1/2} \tag{60}$$

In Fig. 14, we show the MSD of the monomers (g_1) and of the chain's center of mass (g_3) from molecular dynamics simulations of polymer chains of length $N = 200$. The MSD of the center of mass goes from ballistic, $\langle r^2(t)\rangle \propto t^2$, to diffusive, whereas $g_1(t)$ clearly shows the dynamical regimes of Eq. (58), despite the presence of finite chain length effects.

The Rouse model was developed to describe the motion of an isolated chain in solution. Unfortunately, it turns out that neglecting the hydrodynamic interaction is too strong an approximation, and the Rouse model gives a very poor description of the motion of chains in dilute solutions. However, it is found experimentally that this model gives a very good description of the motion of short chains in a melt[5]. The reason is that in a melt hydrodynamic interactions are screened by the presence of the neighboring chains, in the same way as excluded volume interaction[5]. In a melt, the viscous friction experienced by a chain arises from the presence of the other chains, and the friction coefficient ζ_R can be related to the melt viscosity η:

$$\eta_R \propto \zeta_R = N\zeta \tag{61}$$

To sum up, the Rouse model predicts for a polymer melt (taking into account the fact that the chains have ideal conformation, see Sec. 3.2) $\tau_R \propto N^2$, $D_R \propto N^{-1}$ and $\eta_R \propto N$.

3.4.2 *The Zimm model*

We have mentioned how the Rouse model gives the wrong results when hydrodynamic interactions cannot be neglected, as in the case of dilute solutions. A theory which takes into account hydrodynamic interactions was developed by Zimm[3,5]. In the Zimm theory, it is assumed that any chain section drags with it the solvent in its pervaded volume. The friction coefficient of the whole chain can therefore be estimated by using Stokes's law[1]:

$$\zeta_Z \approx \eta_s R, \tag{62}$$

where η_s is the viscosity of the solvent. As we have done for the Rouse model, from ζ_Z we can estimate the diffusion coefficient D_Z using the Einstein relation:

$$D_Z \approx \frac{k_B T}{\zeta_Z} \approx \frac{k_B T}{\eta_s R}, \tag{63}$$

and from D_Z we can estimate the relaxation time (Zimm time):

$$\tau_Z \approx \frac{R^2}{D_Z} \approx \frac{\eta_s R^3}{k_B T} \approx \tau_0 N^{3\nu}. \tag{64}$$

Since $\nu \simeq 0.588$, the Zimm time has a weaker N dependence than the Rouse time. With arguments analogous to those used in the case of the Rouse model, it is possible to estimate the time dependence of the monomer MSD $\langle r^2(t) \rangle$[3]:

$$\langle r^2(t) \rangle \propto \begin{cases} t & t < \tau_0 \\ t^{2/3} & \tau_0 < t < \tau_Z \\ t & t > \tau_Z. \end{cases} \tag{65}$$

Also in the Zimm model the monomer moves subdiffusively at intermediate times, but with a subdiffusive exponent $(2/3)$ which is larger than the one obtained from the Rouse model $(1/2)$. In semidilute solutions, the Zimm model applies for length scales up to $\approx \xi_b$ (blob size); this is a consequence of the fact than hydrodynamic interactions and excluded volume interactions are screened on similar length scales[5]. On larger length scales, the Rouse model applies.

3.4.3 *Entangled polymer dynamics*

Despite the success in describing the dynamics of melts of short chains, the simple Rouse model fails when the chains become longer than some critical value N_e. Indeed, for long chains it is found that $\tau \propto N^{3.4}$, $D \propto N^{-2.4}$ and $\eta \propto N^{3.4}$. A striking qualitative difference is also observed in the stress relaxation modulus $G(t)$, which describes the response of the system to an imposed strain[3,5] and is related to the viscosity by the relation[5]

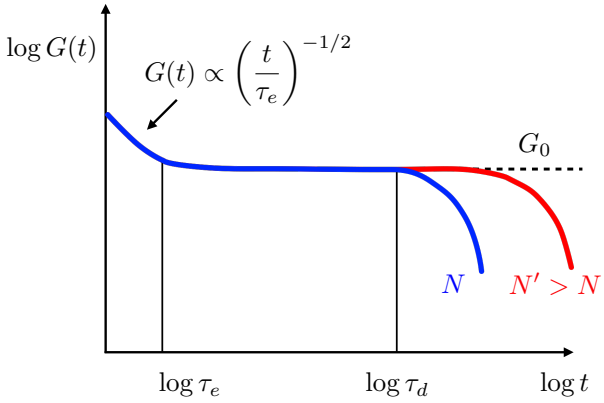

Figura 15 – Qualitative behavior of the stress relaxation modulus $G(t)$ of two polymer melts with different chain lengths N, N', with $N' > N$. At $t < \tau_e$, $G(t) \propto (t/\tau_e)^{-1/2}$[3]. For $t > \tau_e$ (entanglement time), $G(t)$ displays a flat region called the *rubbery plateau*. The value of $G(t)$ in the rubbery plateau, G_0, is called the *plateau modulus*. At $t \approx \tau_d$ (disengagement time), $G(t)$ decays to zero, i.e., the system starts to flow.

$$\eta = \int_0^\infty G(t)dt. \tag{66}$$

In the Rouse model, $G(t)$ is given by the sum of exponentially decaying terms[3,5],

$$G(t) = \frac{\rho k_B T}{N} \sum_{p=1}^{N} \exp(-t/\tau_p), \tag{67}$$

where τ_p is the Rouse relaxation time of a (ideal) chain section containing N/p monomers (see Eq. (59)):

$$\tau_p \approx \frac{\zeta b^2}{k_B T} \left(\frac{N}{p}\right)^2 \approx \tau_0 \left(\frac{N}{p}\right)^2. \tag{68}$$

The longest relaxation time is of course the relaxation time of the whole chain, which corresponds to the Rouse time, $\tau_R \approx \tau_0 N^2$. For $t > \tau_R$, $G(t)$ will have almost completely decayed to zero. However, when a strain is applied to a melt of long chains, it is found that $G(t)$ exhibits a plateau at intermediate times before decaying completely, similarly to elastic solids such as rubber[3,5] (Fig. 15).

The first to shed some light on these peculiar behavior were Edwards[16,19] and de Gennes[18]. In his work on crosslinked polymers, Edwards realized that the fact that chains cannot cross would lead to the confinement of every chain in a tube-like region, the *Edwards tube*. Later, de Gennes realized that the same mechanism would govern the motion of long chains in a melt, since most of the monomers are far from the chain ends and therefore at intermediate time scales they don't "realize" that the ends are free and not fixed. In de Gennes's model, the chain diffuses along its confining tube in a way analogous to the motion of a worm; this

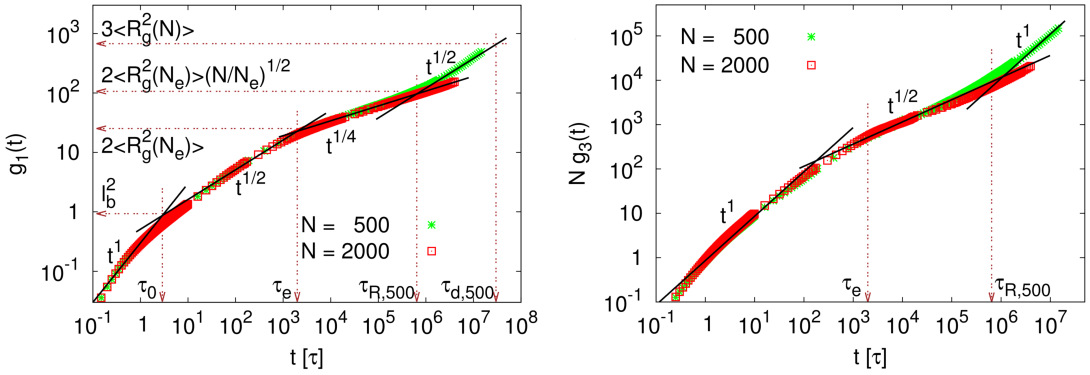

Figura 16 – MSD of the monomers (g_1) and of the chain's center of mass (g_3) from molecular dynamics simulations of systems of chains of length $N = 500$ (red symbols) and $N = 2000$ (green symbols) in a dense melt ($\rho = 0.85$). The dynamical regimes in Eqs. (72) and (73) are clearly visible. Adapted from Ref. 52.

motion was called by de Gennes *reptation*, from the latin *reptare*, "to creep".

The tube diameter, d_T, can be connected to an *entanglement length* N_e by using ideal chain statistics[3]:

$$d_T \approx b N_e^{1/2} \tag{69}$$

The average number of entanglements per chain is therefore given by N/N_e: if $N < N_e$, the system is unentangled and the Rouse model applies, whereas for $N > N_e$ de Gennes's reptation model applies. The value of the entanglement length N_e can be estimated by measuring the value of the stress relaxation modulus $G(t)$ in the rubbery plateau, G_0, which is called the *plateau modulus* (Fig. 15). Indeed, the reptation model predicts[3]

$$G_0 = \frac{4\rho k_B T}{5 N_e} \tag{70}$$

At intermediate times, the chain performs Rouse motion along the tube, with diffusion coefficient $D_e = k_B T / N\zeta$. The tube itself, however, has a random walk conformation, with contour length $\mathcal{L}_T \approx d_T(N/N_e)$. Therefore, the relaxation time τ_d, i.e., the time needed for the chain to reptate out of the tube and start diffusing (*disengagement time*), will satisfy

$$\tau_d \approx \frac{\mathcal{L}_T^2}{D_e} \approx \frac{\zeta d_T N^3}{k_B T N_e^2} \approx \tau_0 \frac{N^3}{N_e} \propto N^3, \tag{71}$$

which is close to the experimental behavior $\tau_d \propto N^{3.4}$. The reptation model also predicts $D \propto N^{-2}$ and $\eta \propto \tau_d \propto N^3$, which are also in disagreement with experiments. This discrepancy is partly due, as first recognized by Doi[3,50,51], to the phenomenon of *contour length fluctuations*: the contour length of the tube is not constant, but rather fluctuates in time, leading to a stronger dependence of τ_d, D and η on N.

The reptation model prediction for $\langle r^2(t) \rangle$ and $\langle r_{\mathrm{cm}}^2(t) \rangle$ is more complicated that the one predicted by the Rouse model[3]:

$$\langle r^2(t)\rangle \propto \begin{cases} t & t < \tau_0 \\ t^{1/2} & \tau_0 < t < \tau_e \\ t^{1/4} & \tau_e < t < \tau_R \\ t^{1/2} & \tau_R < t < \tau_d \\ t & t > \tau_d \end{cases} \tag{72}$$

$$\langle r^2_{\rm cm}(t)\rangle \propto \begin{cases} t & t < \tau_e \\ t^{1/2} & \tau_e < t < \tau_R \\ t & \tau > \tau_R, \end{cases} \tag{73}$$

where $\tau_e \approx \tau_0 N_e^2$ is the Rouse relaxation time of a portion of chain containing N_e monomers. The $\langle r^2(t)\rangle \propto t^{1/4}$ and $\langle r^2_{\rm cm}(t)\rangle \propto t^{1/2}$ regimes for $\tau_e < t < \tau_R$ are due to the fact that the chain performs an essentially one dimensional Rouse relaxation along the random-walk-like tube region (a "random walk on a random walk"). We note that both in the Rouse and in the reptation model, we expect $\langle r^2(t)\rangle$ and $\langle r^2_{\rm cm}(t)\rangle$ to coincide for t longer than the longest relaxation time of the system, since the whole chain moves coherently.

3.4.4 *Experimental measurement of dynamic properties*

Dynamic quantities such as $\langle r^2_{\rm cm}(t)\rangle$ and the diffusion coefficient can be measured experimentally via *dynamic light scattering* (DLS)[3,5,30,53]. The time autocorrelation function of the scattered intensity is related to the *intermediate scattering function*[g] $F(\mathbf{q},t)$[1,53], which is a generalization of the (static) structure factor $S(\mathbf{q})$, Eq. (32):

$$F(\mathbf{q},t) \equiv \frac{1}{M}\sum_{k,j=1}^{M} \langle \exp[-i\mathbf{q}\cdot(\mathbf{r}_k(t) - \mathbf{r}_j(0))]\rangle, \tag{74}$$

Analogously to what we have done in Sec. 3.3 for $S_1(\mathbf{q})$, for small scattering angles $qR_g \ll 1$ we can expand the single-particle intermediate scattering function, $F_1(\mathbf{q},t)$[3,30]:

$$F_1(\mathbf{q}) \simeq N - \frac{q^2}{6N}\sum_{k,j=1}^{N} \langle (\mathbf{r}_k(t) - \mathbf{r}_j(0))^2\rangle \tag{75}$$

For $t > \tau_{\rm rel}$, with $\tau_{\rm rel}$ the relaxation time of the chain, it can be shown that[30]

$$\langle (\mathbf{r}_k(t) - \mathbf{r}_j(0))^2\rangle \simeq \langle [\mathbf{r}_{\rm cm}(t) - \mathbf{r}_{\rm cm}(0)]^2\rangle = \langle r^2_{\rm cm}(t)\rangle \tag{76}$$

and therefore

[g] Some textbooks, such as Doi-Edwards[3] and Rubinstein-Colby[5] refer to $F(\mathbf{q},t)$ as the *dynamic structure factor*. Here, we adopt the terminology of Hansen-McDonald, where the term "dynamic structure factor" is used to denote the temporal Fourier transform of the intermediate scattering function, $S(\mathbf{q},\omega) = \frac{1}{2\pi}\int F(\mathbf{q},t)e^{i\omega t}dt$

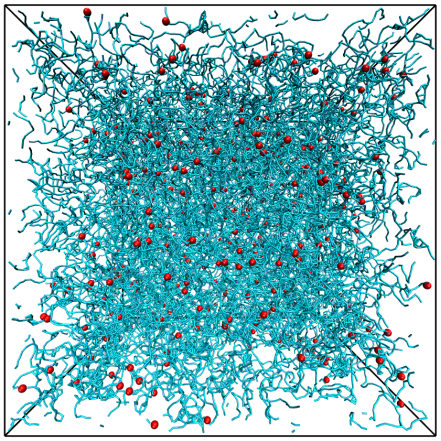

Figura 17 – A network of $N_2 = 46465$ bifunctional particles (blue cylinders representing their bonds) and $N_3 = 486$ trifunctional particles (red spheres). Total number density $(N_2 + N_3)/V = 0.047$, fraction of reacted sites $p_b = 0.9986$. The network was generated by simulating patchy particles (see Ch. 6). Data courtesy of L. Rovigatti.

$$F_1(\mathbf{q}, t) \simeq N\left(1 - \frac{q^2}{6}\langle r^2_{\rm cm}(t)\rangle\right) \quad (qR \ll 1, t > \tau_{\rm rel}) \tag{77}$$

In the limit $t \to \infty$, we obtain from Einstein's relation (54)

$$F_1(q, t) \simeq N(1 - q^2 Dt) \simeq N \exp\left(-q^2 Dt\right) \quad (qR \ll 1, t \to \infty) \tag{78}$$

3.5 NETWORKS AND GELS

In polymeric system, bonds can be present between different polymer chains (Fig. 17). These bonds, called *crosslinks*, can either be *physical*, when they can be broken *via* thermal fluctuations, or *chemical*, when they cannot (the typical case being that of covalent bond)[5]. When inter-chain bonds are introduced in a polymeric system, a variety of different structures can be formed, such as rings, dendrimers, combs, and randomly branched structures[5] (see Fig. 8). Also bond formation itself can proceed through different physical processes: for example, a branched structure can be created by taking a mixture of bifunctional and f-functional particles (the crosslinkers) with $f > 2$, and initiating polymerization reaction. Another method consists in taking a system containing already formed chains and initiating the crosslinking *via* some chemical agent, electromagnetic radiation (photo-crosslinking) or electron irradiation[54].

After a certain extent of reaction, a percolating network, i.e., a molecule spanning the whole system, will appear. This "giant molecule" is called a *gel*, while the polydisperse mixture of branched polymers which is not part of the giant molecule is called the *sol*[h]. We encounter many polymeric gels in everyday life, which can be either physical, like gelatin, or chemical, like Epoxy glue and rubber.

[h] Sometimes, a distinction is made between (dry) polymer networks and gels, in which a gel is a network which is swollen in a solvent[5].

In the present Section, we will present a brief overview of the Flory-Stockmayer theory of gel formation and of the main models to describe the elastic properties of gels.

3.5.1 *Flory-Stockmayer theory of gelation*

In the 1940s, Flory presented the first quantitative theory of gelation[11,55–57], obtaining explicit expressions for trifunctional –and partly also for tetrafunctional– branching units. This theory was later generalized by Stockmayer[58,59], who was able to obtain general formulas for systems containing branching units of any given functionality.

The key assumptions of the Flory-Stockmayer (FS) theory are the following[58]:

1. Cyclic structures (loops) are assumed not to occur ("no-loops" assumption).
2. At any stage during the reaction, all unreacted functional groups are considered to be equally reactive.

We will here consider the case of a system containing N_2 bifunctional monomers and N_f f-functional monomers, with valence $f > 2$. The total number of monomers is $N_{\text{tot}} = N_2 + N_f$. The total number of binding sites (also called *functional groups*) in the system is therefore $fN_f + 2N_2$. For this case, the FS theory predicts that the number of molecules composed of n f-functional monomers and k bifunctional monomers is

$$m_{nk} = fN_f p_f^{n-1}(1-p_f)^k p_b^{n+k-1}(1-p_b)^{fn-2n+2}\left(\frac{(fn-n+k)!}{n!k!(fn-2n+2)!}\right), \tag{79}$$

where we have introduced the fraction of binding sites belonging to the f-functional monomers,

$$p_f \equiv \frac{fN_f}{fN_f + 2N_2}, \tag{80}$$

and the bond probability or *extent of reaction* (fraction of reacted sites),

$$p_b \equiv \frac{2(N_{\text{tot}} - M)}{fN_f + 2N_2} = \frac{N_b}{N_b^{\max}}, \tag{81}$$

with M the total number of molecules:

$$M \equiv \sum_{k,n\geq 0} m_{nk}. \tag{82}$$

In Eq. (81) we have also introduced the number of bonds, $N_b = N_{\text{tot}} - M$, and the maximum number of bonds, $N_b^{\max} = (fN_f + 2N_2)/2$.

The critical bond probability at which percolation occurs (*gel point*) is found to be[58]

$$p_b^c = \frac{1}{1 + (f-2)p_f} \tag{83}$$

Above the gel point, the giant molecule –the gel– appears. In the thermodynamic limit $N_{\text{tot}} \to \infty$, this molecule has infinite size[i].

In the case of N_f identical f-functional monomers, with $f \geq 2$, the above expressions are greatly simplified. The number of molecules of size n can be obtained simply by taking $k = 0$ and $p_f = 1$ in Eq. (79); the result is

$$m_n = f N_f p_b^{n-1} (1 - p_b)^{fn-2n+2} \left(\frac{(fn-n)!}{n!(fn-2n+2)!} \right) \tag{84}$$

and the critical bond probability becomes $p_b^c = (f-1)^{-1}$.
In the special case $f = 2$ (linear polymers), one obtains

$$m_n = N_2 (1 - p_b)^2 p_b^{n-1} \quad (f = 2) \tag{85}$$

Eq. (85) can also be used to derive an expression for the strand length distribution in a polymer gel containing both bifunctional and f-functional particles. Indeed, this is equivalent to remove all f-functional particles and analyze the size distribution of the resulting ensemble of linear chains[61], which formally amounts to replacing p_b with $p_2 p_b$ in Eq. (85), where

$$p_2 \equiv \frac{2N_2}{fN_f + 2N_2} = 1 - p_f \tag{86}$$

The result is therefore simply

$$m_n = N_2 (1 - p_b p_2)^2 (p_b p_2)^{n-1} = N_2 (1 - p_b p_2)^2 e^{-(n-1)|\ln(p_b p_2)|}. \tag{87}$$

From Eq. (87) it is possible to calculate the average strand length $\langle m_n \rangle$:

$$\langle m_n \rangle = \frac{\sum_{n=1}^{\infty} n m_n}{\sum_{n=1}^{\infty} m_n} = \frac{1}{1 - p_2 p_b}, \tag{88}$$

Regarding the behavior of the system past the gel point, i.e., for $p_b > p_b^c$, the prediction of Stockmayer is different from that of Flory. Flory assumes that the sol phase continues to interact with the gel phase also past the gel point, whereas Stockmayer assumes that the gel and the sol do not interact[62]. It turns out, as Stockmayer himself suspected[58], that Flory's assumption (sometimes called Flory's "post-gel" assumption) is the correct one, and that Eq. (79) can be applied to the sol also past the gel point, as long as loops are not formed in sol clusters (but the formation of loops is allowed in the gel)[63,64]. This implies that Eq. (87) remains valid also for $p_b > p_b^c$, and in particular also in the fully-bonded ground state ($p_b = 1$) of the system[63,64]. In this case, we simply have

[i] We note that above the gel point the number of bonds cannot be calculated as $N_b = N_{\text{tot}} - M$ anymore. Indeed, this would imply that the number of molecules becomes zero ($M = 0$) for $p_b = N_{\text{tot}}/N_b^{\max}$, which is clearly absurd. The solution to this apparent contradiction is that for $p_b > p_b^c$ the formation of loops is allowed in the gel (but only there), and therefore forming a new bond doesn't imply that M is reduced by 1 anymore[60,61].

$$\langle m_n \rangle = \frac{1}{1-p_2} = \frac{1}{p_f} = 1 + \frac{2N_2}{fN_f} \tag{89}$$

3.5.2 *Models of rubber elasticity*

In this section, we will briefly review the main results of classical models of rubber elasticity. These models aim to predict how a polymer network responds to a deformation. The fundamental quantity when studying how a solid responds to deformation is the *elastic modulus E*, which is defined as the ratio between the applied stress σ (force per unit area) to the applied strain γ (displacement per unit length)[65]:

$$E \equiv \frac{\sigma}{\gamma} \tag{90}$$

There are different kinds of moduli, depending on the type of deformation which is applied:

- The *shear modulus G* describes an object's tendency to shear (the deformation of shape at constant volume) when acted upon by opposing forces.
- The *Young modulus Y* describes tensile elasticity, or the tendency of an object to deform along an axis when opposing forces are applied along that axis.
- The *bulk modulus K* describes volumetric elasticity, or the tendency of an object to deform in all directions when uniformly loaded in all directions. It is related to the isothermal compressibility $\kappa_T \equiv -\frac{1}{V}\left(\frac{\partial V}{\partial P}\right)_{T,N}$, since $\kappa_T = K^{-1}$[1].

The three moduli are connected by the following relation[65]:

$$Y(G + 3K) = 9KG \tag{91}$$

The simplest model of rubber elasticity is the *affine network* model (ANM), which was by Treloar starting from ideas of Kuhn[66–68]. The ANM assumes that[69]: (1) The network strands are freely-jointed chains, (2) the end-to-end distance of the chains is the same as that of chains in the un-crosslinked state, (3) there is no change in volume on deformation and (4) the crosslinks displace affinely with macroscopic deformation. These assumptions lead to the following prediction for the shear modulus[5]:

$$G_{\text{affine}} = \rho_s k_B T = \frac{\rho k_B T}{N_s} \tag{92}$$

where ρ_s is the number density of strands, ρ is the monomer density and $N_s = \rho/\rho_s$ is the effective strand length. In the affine network model, it is assumed that the ends of the strands are fixed in space and displaced affinely with the whole network. In real networks, the strand ends are attached to other strands *via* crosslinks, which can move around their average positions. The simplest model to incorporate the crosslinks fluctuations is the *phantom network* model (PNM) of James and Guth[68,70–73]. The PNM model assumes that[69]: (1) The chains are

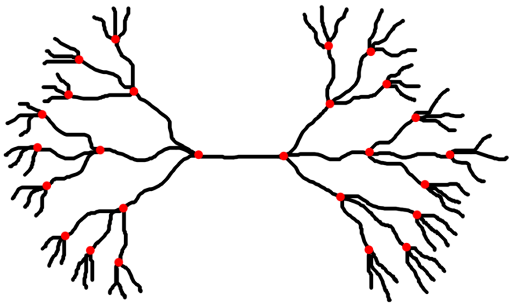

Figura 18 – Network with tetravalent crosslinks (red dots) and a Bethe lattice structure.

Gaussian, (2) there are no excluded volume interactions, so that the chains can freely pass through one another (from this assumption comes the name “phantom network") and (3) all crosslinks at the surface of the network are fixed and deform affinely with macroscopic strain, while all crosslinks and chains inside the bulk of the network fluctuate around their mean positions. In addition to these assumption, it is usually assumed in order to simplify the calculations that (4) all the strands have the same length, and (5) the network has the topology of a Bethe lattice[5,69,74], as that shown in Fig. 18. The PNM predicts a smaller shear modulus than the one predicted by the affine network model[5]:

$$G_{\text{phantom}} = \rho_s k_B T \left(1 - \frac{2}{\langle f \rangle}\right) = G_{\text{affine}} \left(1 - \frac{2}{\langle f \rangle}\right) \tag{93}$$

where $\langle f \rangle$ is the average crosslink functionality. Eq. (93) can also be expressed as

$$G_{\text{phantom}} = k_B T(\rho_s - \rho_{cl}) \tag{94}$$

where ρ_{cl} is the crosslink density, which is equal to $2\rho_s/\langle f \rangle$, since there are on average $\langle f \rangle/2$ strands per crosslink.

Both the ANM and the PNM assume that the network has no defects, i.e., no dangling ends or similar structure, such as dangling loops, which are attached to the network by only one end. These structures do not contribute to the modulus, since they do not respond to deformations (they are *elastically inactive*). If the number density of elastically active strands ρ_a is known, we can still use Eq. (94) and calculate the shear modulus as $G = k_B T(\rho_a - \rho_{cl})$.

We note that in both models, we can express the shear modulus as

$$G_x = \rho_x k_B T = \frac{\rho k_B T}{N_x} \tag{95}$$

where ρ_x is the effective strand density and N_x is the effective strand length. In the ANM, $N_x = N_s$, whereas in the PNM $N_x = N_s\langle f \rangle/(\langle f \rangle - 2)$.

Both the ANM and the PNM, however, share a fundamental flaw: In both models, the strands are aware of the presence of other strands only through the presence of the crosslinks. In reality, however, as discussed in Sec. 3.4.3, the presence of other chains introduces topological constraints called *entanglements* on any given strand. Since chains cannot move

through each other, these entanglements act basically as additional crosslinks. We have seen (Eq. (70)) that for an entangled melt the plateau modulus is $G_e \approx \rho k_B T / N_e$. The modulus of an entangled polymer network can be approximated as the sum of the contribution coming from the crosslinks and that coming from the entanglements[5]:

$$G \simeq G_x + G_e = k_B T(\rho_x + \rho_e) \approx \rho k_B T \left(\frac{1}{N_x} + \frac{1}{N_e} \right). \tag{96}$$

The term $\rho_x + \rho_e$ appearing in Eq. (96) can be interpreted as an effective strand density ρ^{eff} and can be used, for example, to evaluate the size of the tube diameter in a system with both crosslinks and entanglements. In an entangled, non-crosslinked system, $d \approx b N_e^{1/2} = b(\rho/\rho_e)^{1/2}$. It follows that if both crosslinks and entanglements are present, we can evaluate the effective tube diameter as

$$d^{\text{eff}} \approx b \left(\frac{\rho}{\rho^{\text{eff}}} \right)^{1/2} = b \sqrt{\frac{N_x N_e}{N_x + N_e}}. \tag{97}$$

We note that Eqs. (96) and (97) can be rewritten as

$$G \approx \frac{\rho k_b T}{N^{\text{eff}}} \tag{98a}$$

$$d \approx b (N^{\text{eff}})^{1/2}, \tag{98b}$$

where $N^{\text{eff}} = N_x N_e / (N_x + N_e)$ is an effective strand length which takes into account both the crosslinks and the entanglements. We note that if $N_e \ll N_x$, $N_{\text{eff}} \simeq N_e$ and if $N_x \ll N_e$, $N_{\text{eff}} \simeq N_x$, as expected.

3.6 COMPUTER SIMULATIONS

Computer simulations provide an invaluable tool for the study of polymer liquids for many reasons. First, they allow to get rid of undesired effects which are unavoidable in experiments, like chain length polydispersity, and to fully control the properties of the system. Second, they allow to measure directly quantities which are extremely challenging to measure in experiments, like the dynamics of single chain segments, while also allowing the measurement of observables which are routinely studied in experiments. Simulations allow to submit the system to unphysical transformations in order to study specific aspects: for example, chains can be made to contract to measure the entanglement length[75], or they can be made able to cross each other in order to "turn off" the effect of topological entanglements[76,77]. The drawback is that simulations are usually able to access system sizes and time scales which are much smaller than those accessible in experiments. However, regarding time scales this is not always true, as in the study of some specific properties simulations can access *wider* time windows than those accessible in experiments[78].

3.6.1 *Molecular Dynamics (MD)*

The two main techniques used in simulations are Monte Carlo (MC) and molecular dynamics (MD).

In MD simulations, the particles are assumed to interact through some (usually continuous) potential $\mathcal{U}$, which depends on the particles' positions $\{\mathbf{r}\} \equiv \mathbf{r}_1, \ldots, \mathbf{r}_N$. The potential is usually taken to be two- or three-body. Newton's equation, $m_i \ddot{\mathbf{r}}_i = -\nabla_i \mathcal{U}(\{\mathbf{r}\})$, is then solved for every particle in the system using some integration scheme[79–81]. A good time integrator should be numerically stable, time reversible and symplectic[80,81]: an example of widely used integrator which possesses all these characteristics is the velocity Verlet integrator[82]. A MD scheme which simply integrates Newton's equations will sample the microcanonical (NVE) ensemble. Since most experiments are performed at constant temperature and pressure (isothermal-isobaric or NPT ensemble) or at constant temperature and volume (isothermal-isochoric or NVT ensemble), several schemes have been developed in order to perform MD simulations which samples other ensembles[79–81]. Several techniques have also been developed to perform MD simulations of molecules in a solvent without having to simulate explicitly an enormous number of solvent molecules. The simplest approach is Langevin dynamics[83], where instead of Newton's equation, Langevin's equation is integrated:

$$m_i \ddot{\mathbf{r}}_i = -\nabla_i \mathcal{U}(\{\mathbf{r}\}) - m_i \Gamma \dot{\mathbf{r}}_i + \sqrt{2 m_i \Gamma k_B T}\, \boldsymbol{\zeta}(t). \tag{99}$$

The second term on the right-hand side of Eq. (99) represents viscous friction, with Γ the friction coefficient, and the third term is a stochastic[j] force which represents collisions with solvent molecules (T is temperature). The $\boldsymbol{\zeta}(t)$ vector satisfies

$$\langle \boldsymbol{\zeta}(t) \rangle = 0 \tag{100a}$$

$$\langle \boldsymbol{\zeta}(t) \cdot \boldsymbol{\zeta}(t') \rangle = \delta(t - t'). \tag{100b}$$

Eq. (100b) tells us that the correlation time is infinitely short. We note that the prefactor $\sqrt{2 m_i \Gamma k_B T}$ is derived from the fluctuation-dissipation theorem[85]. Langevin dynamics can mimic the viscous friction exerted by the solvent on the molecules, but it doesn't implement solvent-mediated hydrodynamic interactions (HI) between molecules. When HI cannot be neglected, more sophisticated schemes are needed, such as multi-particle collision dynamics[86]. For a review of simulation methods which include HI, we refer to Ref. 87.

When the friction Γ is very large, the inertial term $m_i \ddot{\mathbf{r}}_i$ can be neglected compared to the "viscous" term $m_i \Gamma \dot{\mathbf{r}}_i$[79] and Eq. (99) becomes

$$\gamma_i \dot{\mathbf{r}}_i = -\nabla_i \mathcal{U}(\{\mathbf{r}\}) + \sqrt{2 \gamma_i k_B T}\, \boldsymbol{\zeta}(t). \tag{101}$$

where $\gamma_i \equiv m_i \Gamma$. This approximation corresponds to a very viscous solvent, in which inertia is basically negligible[88]; the resulting dynamics is called Brownian dynamics or overdamped Langevin dynamics.

[j] Usually a Gaussian distribution is chosen, but other choices are possible[84].

The main limit of MD simulations when applied to polymer systems is that the relaxation time of a polymer liquid grows very quickly with chain length N. Indeed, as discussed in Sec. 3.4, the relaxation time of an unentangled polymer grows as N^2, while for an entangled polymer it grows as $N^{3.4}$. For crosslinked polymers and star polymers the situation is even worse, since the relaxation time increases *exponentially* respectively with chain length[76,89] and with the (square root of the) number of arms[90]. Therefore, even with modern computers, equilibrating systems of very long chains can be prohibitive. This constitutes a problem, since very long chains are often needed in order to observe theoretically predicted behaviors[52].

3.6.2 *Monte Carlo (MC)*

In MC simulations, the phase space of the system is randomly sampled following a rule that reproduces the desired probability distribution[79–81]. The advantage of MC with respect to MD is that unphysical moves can be performed, which can significantly speed up the equilibration of the system. The obvious drawback is that in most situations only static properties can be studied, since MC "dynamics" is usually too different from the actual dynamics of the system – even though this is not always the case[91]. MC simulations can be performed either on a lattice or in the continuum. MC-based lattice models, such as the bond fluctuation model[6,27,92] have been very successful in studying the static (and dynamic!) properties of dense many chain systems in the pioneering times of polymer simulations[37,38,93–95]. For a detailed discussion of the many MC techniques used in polymer science, several excellent reviews are available: In particular, we refer to 27, 6 and 34.

3.6.3 *Coarse-grained models*

One possible approach to simulating a polymer liquid would be to perform an all-atom simulation in which the atoms interact with each other through empirical potentials, whose form can be inferred from quantum *ab inito* simulations[96] (we note that a full *ab initio* simulation of even a single, relatively short polymer would be very challenging even for modern computers). This approach is valid, using modern computers, for relatively small systems of short chains, but it quickly becomes unmanageable when the number of degrees of freedom grows. A possible solution is to introduce a *coarse-grained model*, in which groups of atoms are replaced by "super atoms" which interact through effective potentials[6,34,97]. In a typical coarse-grained model of a polymer, the "super atom" is meant to represent a polymer segment of size comparable to the Kuhn length, containing several monomers.

In order for a coarse-grained model to reproduce successfully the behavior of real systems, it is important for it to be able to mimic the main qualitative aspects of the interactions between the different molecules present in the system. The most widely used coarse-grained models for polymer systems fall into the category of the so-called *bead-spring* model: in such models, every polymer segment (or monomer) is represented as a sphere, connected to neighboring monomers along the chains with springs. The general form of a bead-spring potential (neglecting torsion contributions) is

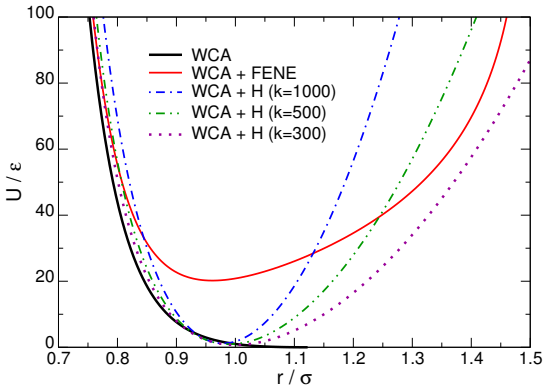

Figura 19 – Comparison between the WCA potential (Eq. (104)), a combination of WCA and harmonic potential (Eq. (105)) and a combination of WCA and FENE potential (Eq. (106)). For the FENE potential, the values $r_{\max} = 1.5$, $k = 30$ were used. For the harmonic potential, $r_0 = 0.961$ and $k = 1000$ (dash-dotted line), 500 (dash-double dotted line) and 300 (dotted line).

$$\mathcal{U}(\{\mathbf{r}\}) = \sum_{\text{all pairs}} \mathcal{U}_{\text{all}}(r_{ij}) + \sum_{\substack{\text{bonded}\\ \text{pairs}}} \mathcal{U}_{\text{bond}}(r_{ij}) + \sum_{\substack{\text{bonded}\\ \text{triplets}}} \mathcal{U}_{\text{bend}}(\mathbf{r}_i, \mathbf{r}_j, \mathbf{r}_k), \tag{102}$$

where $r_{ij} \equiv |\mathbf{r}_i - \mathbf{r}_j|$.

The term $\mathcal{U}_{\text{all}}$ acts between all pairs of polymer segments. A commonly used expression for this interaction is the truncated and shifted Lennard-Jones (LJ) potential[98],

$$\mathcal{U}_{\text{LJ}}(r) = \begin{cases} 4\epsilon\left[\left(\frac{\sigma}{r}\right)^{12} - \left(\frac{\sigma}{r}\right)^{6}\right] + E(r_c) & r \le r_c \\ 0 & \text{otherwise,} \end{cases} \tag{103}$$

where r_c is the cutoff radius and $E(r_c)$ ensures that $U_{\text{LJ}}(r_c) = 0$. Commonly used values are $r_c = 2.4\sigma - 2.5\sigma$[77,99] and $r_c = 2 \cdot 2^{1/6}\sigma$[100]. These choices are a compromise between the wish to include the major part of the attractive interaction and the need to keep the potential short-ranged, in order to reduce the number of interactions to evaluate. When the cutoff radius coincides with the minimum of the potential, $r_c = 2^{1/6}\sigma$, the potential becomes purely repulsive, and it is called Weeks-Chandler-Andersen (WCA) potential[101] (Fig. 19):

$$\mathcal{U}_{\text{WCA}}(r) = \begin{cases} 4\epsilon\left[\left(\frac{\sigma}{r}\right)^{12} - \left(\frac{\sigma}{r}\right)^{6}\right] + 1 & r \le 2^{1/6} \\ 0 & \text{otherwise,} \end{cases} \tag{104}$$

A purely repulsive potential allows to reproduce good/athermal solvent conditions, whereas an attractive potential allows to simulate poor or theta solvent conditions[34].

The term $\mathcal{U}_{\text{bond}}$ acts only between bonded segments and it represents stiff chemical bonds. One of the simplest form is the harmonic bond with cutoffs[38],

$$\mathcal{U}_{\mathrm{H}}(r) = \begin{cases} \frac{1}{2}k(r - r_0)^2 & r_{\min} \leq r \leq r_{\max} \\ \infty & \text{otherwise,} \end{cases} \tag{105}$$

where k is the spring constant. The cutoff radii $r_{\min}$ and $r_{\max}$ can be finite or respectively 0 and ∞[102]. More widely used is the so-called "finite extensible nonlinear elastic" (FENE) potential[28,103,104]

$$\mathcal{U}_{\mathrm{FENE}}(r) = \begin{cases} -\frac{1}{2}kr_{\max}^2 \ln\left[1 - (r/r_{\max})^2\right] & r \leq r_{\max} \\ \infty & \text{otherwise.} \end{cases} \tag{106}$$

For small $r/r_{\max}$, the FENE potential is harmonic: $\mathcal{U}_{\mathrm{FENE}}(r) \simeq kr^2/2$. The FENE potential has two main advantages with respect to the harmonic potential: The first is that the FENE is by definition finitely extensible, since it diverges for $r \to r_{\max}$, and therefore no cutoff is needed[104]. Moreover, when using the FENE potential, chain crossing can be prevented with a much smaller value of k compared to the harmonic potential (Fig. 19), meaning that the forces generated are smaller and therefore a larger integration time step can be used.

Kremer and Grest[21,105] proposed to use a combination of the WCA and FENE potential, with $k = 30\epsilon/\sigma^2$ and $r_{\max} = 1.5\sigma$, to study dense polymer melts[k] (monomer density $\rho \simeq 0.85\sigma^{-3}$). With this choice of parameters, the equilibrium bond length at zero temperature is $r_e = 0.961$. Nowadays, the Kremer-Grest model is by a large margin the most widely used bead-spring model, having been employed in more than 800 simulation studies as of today[1].

The last term in Eq. (102), $\mathcal{U}_{\mathrm{bend}}$, represents a bond bending potential. In the original Kremer-Grest model, the chains were taken to be fully flexible. However, in certain situations systems of fully flexible chains can show rather strong deviations from the theoretically predicted behavior[52], and it is therefore sometimes necessary to reduce the flexibility of the chain by introducing an energy penalty associated with bond bending. The bond bending potential is a function of the bond angle θ, which is defined for three consecutive monomers $i-1, i$ and $i+1$ along the chain as

$$\theta \equiv \arccos\left(-\frac{\mathbf{r}_{i-1,i} \cdot \mathbf{r}_{i,i+1}}{|\mathbf{r}_{i-1,i}|\ |\mathbf{r}_{i,i+1}|}\right), \tag{107}$$

where $\mathbf{r}_{i,j} \equiv \mathbf{r}_i - \mathbf{r}_j$.

Several choices are possible for this potential, such as[6,106–108]:

$$\mathcal{U}_{b1}(\theta) = k_\theta[1 + \cos(\theta)] \tag{108a}$$

$$\mathcal{U}_{b2}(\theta) = \frac{1}{2}k_\theta[\cos(\theta) - \cos(\theta_0)]^2 \tag{108b}$$

[k] We note that the same model had been already used by Bishop *et al.* in the very first MD simulation of a polymer[28], although the value of $r_{\max}$ and k were different ($r_{\max} = 1.95\sigma$, $k = 20\epsilon/\sigma^2$).

[1] Source: Google Scholar.

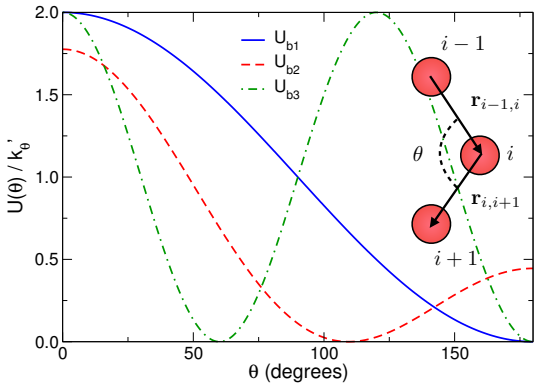

Figura 20 – Comparison between the bending potentials of Eqs. (108). Continuous line: Eq. (108a), with $k_\theta = k'_\theta = 1$. Dashed line: Eq. (108b), with $k_\theta = 2k'_\theta$ and $\theta_0 = 109.5°$ (tetrahedral angle). Dash-dotted line: Eq. (109) with $k_\theta = 2k'_\theta$ and $\theta_c = 120°$. The curve has been shifted up by 2 for clarity. Cartoon: schematic representation of the angle θ (Eq. (107)).

It has been recently pointed out by Kremer and Hsu [109] that the bending potential (108a) can lead to rather artificial stretched chain conformations upon cooling, as it is evident from the fact that $\theta = \pi$ (rod-like chain) in the ground state. To prevent these unphysical effects on chain conformation in simulations at low temperature, they proposed the potential

$$U_{b3}(\theta) = \begin{cases} -k_\theta \sin^2(\pi\theta/\theta_c) & 0 < \theta < \theta_c \\ 0 & \text{otherwise.} \end{cases} \tag{109}$$

This potential prevents chain deformation upon cooling and also gives rise to conformations which are in perfect agreement with the freely rotating chain model [109]. The potentials $\mathcal{U}_{bk}(\theta)$, $k = 1, 2, 3$ are shown in Fig. 20. We note that the potential $\mathcal{U}_{b3}(\theta)$ has been shifted up by 2 in order to make the comparison with the other two easier.

In conclusion, care should be taken when choosing the form of $\mathcal{U}_{\text{bend}}(\theta)$, in that the potential should be adapted to the simulated system.

4

POLYMER NANOCOMPOSITES

In the early 1990s, Toyota researcher showed that the adding $\simeq 2-4$ vol% of mica-type nanoclay to nylon was sufficient to increase the yield and tensile strength of the material by a factor of five, and its heat distortion temperature by almost 90 degrees[110,111]. Following these pioneering studies, it became soon clear that the addition of nanoparticles (NP), i.e., particles of any shape with size between 1 and 100 nm[112], to a polymeric system could be used to obtain a drastic improvement not only of the mechanical, but also of the optical, thermal, electrical, magnetic and transport properties of the material[113–122]. The possibility for such numerous technological application, together with the growing availability of NPs of specific size and shape (nanotubes, nanocubes, platelets, fullerenes, dendrimers, grafted particles, etc.) sparked a great interest in these *polymer nanocomposites* (PNC), making them the center of a very active field of research. From a physical point of view, nanocomposites are interesting systems because of the extremely rich behaviors of their structural, dynamical, mechanical and thermodynamic properties. Such a variety of different behaviors originates from the interplay between many factors: NP size and shape, polymer length and rigidity, polymer and NP volume fractions, polymer-NP interaction are all elements which strongly influence the properties of the PNC, and changing a single parameter can lead to striking qualitative changes[122].

Despite the vastness of the literature on PNC currently available, we are still far from a complete understanding of these fascinating systems, as many fundamental questions remain unanswered[8]. One of the fundamental aspects that remains to be fully understood is how the dynamics of the polymers and the NPs (e.g. their diffusion and its effect on the PNC viscosity) depends on the microscopic details of the system. The importance of this problem is by no means limited to technological applications: In biophysics, the dynamics of proteins in the crowded cytoplasmatic environment can strongly influence cellular functions[123,124], while in medicine recent years have seen a growing interest in the development of new and more efficient forms of NP-mediated drug delivery[125–128]. The dynamics of PNCs represents a tough challenge for theoretical physics mainly because of the large number of length and time scales introduced by the presence of the polymers. In a binary mixture of particles (molecules or colloids), the only relevant length scales are the sizes of the two types of particles. In a PNC, on the other hand, the length scales in play are many more, since apart from the NP size σ_N we have to consider the monomer size σ, the Kuhn length ℓ_K, the mesh size ξ, the tube diameter d and the chain size R. To each of these length scales, a different time scale is associated: as a consequence, the behavior of the system will strongly depend on the length and time scales at which it is probed.

In what follows, we will give a brief description of the structural and dynamic properties of PNCs, discussing some of the numerous experimental and theoretical works on the subject.

Since this is the topic of the present work, we will mainly discuss studies involving spherical, non-grafted NPs. The aim is not to give an exhaustive review of the field of PNCs, but rather to give a minimum amount of context to the following Chapters.

4.1 STRUCTURE AND PHASE BEHAVIOR

The phase behavior of PNCs is extremely complex, so much so that even for model PNCs no full phase diagram has been enunciated[8]. This is due to the fact that in conventional PNCs, the NP size is smaller or comparable to the size of the polymer, i.e., $R_N \lesssim R_g$, with R_N the NP radius and R_g the polymer radius of gyration. When $R_N \lesssim R_g$, it is said that a system is in the "nanoparticle" or "protein" limit[129]. The opposite regime, $R_N \gg R_g$, called the "colloid" limit, is relatively easy to handle, since the NP-NP interaction can be reduced to an effective depletion pair potential mediated by the polymers[130–133]. The nanoparticle limit, however, is much trickier, since an accurate description in terms of effective pair potentials is not possible[134–136]. In the present section, we will briefly discuss some of the most relevant structural and thermodynamical properties of PNCs. For simplicity, we will limit our discussion to systems of linear chains containing spherical NPs.

4.1.1 *NP dispersion*

Although NP aggregation is desirable for some applications[121,138,139], it greatly increases the difficulty of understanding the general mechanisms governing the physical properties of PNCs; therefore, in most experimental studies on model PNCs aimed at understanding their general properties it is desirable to achieve good (uniform) NP dispersion[140,141] (Fig. 21). This is because aggregation introduces size polydispersity and dynamical heterogeneity in the system. In athermal[a] PNCs, it has been established by theoretical[142–145], experimental[140,146] and simulation[99,147–152] studies that the polymer-induced depletion interaction acting on the NPs causes NP aggregation, and eventually a macroscopic phase separation. This entropic phase separation can be avoided either by introducing an attractive interaction between the polymers and the NPs (for example by introducing functional groups on NP surface[122,141]), or by grafting on the NP surface polymer chains with the same chemical composition as the matrix polymers, which can sterically shield the attractive depletion interaction[8,99,122,153–158]. It has also been shown the thermodynamic stability of a NP dispersion is enhanced when the NP radius is smaller than the polymer's radius of gyration ($R_N < R_g$), i.e., in the nanoparticle limit[140].

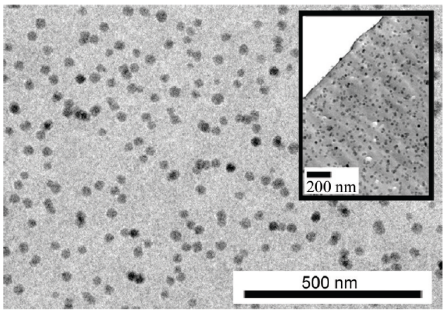

Figura 21 – Cross-sectional TEM image showing silica NPs (2 vol%) in a polystyrene-silica PNC. *Inset*: cross-sectional TEM image of the near surface. Adapted from Ref. 137.

[a] The term "athermal" is used here to denote a system where all the interactions are purely repulsive, but not necessarily hard-sphere like.

4.1.2 *Chain conformation*

Even today, it is still highly debated how the conformation of polymer chains in a PNC is affected by the presence of the NPs[122,158]. It is clear that NP concentration, quality of NP dispersion, NP-polymer size ratio, NP shape and polymer-NP interaction all play a role in determining chain conformation. However, at present, no theoretical model has been able to explain in a satisfactory way the results of all the experiment and simulations which have probed this aspect of PNCs.

Nakatani *et al.*[159] studied blends of silica NPs in PDMS[b] through neutron scattering, observing chain expansion for $R_g > R_N$ and chain contraction for $R_g \simeq R_N$[159].

Sen *et al.*[160] studied PNCs of silica NPs in polystyrene, finding that chain dimensions remain unperturbed for NP volume fractions up to $\simeq 30\%$ and $0.57 \lesssim R_g/R_N \lesssim 1.57$. However, it has been pointed out that TEM images seem to reveal that the NPs were not well dispersed in the studied PNCs[161]. Later experimental studies, however, found analogous results in PNCs with well-dispersed NPs[162,163].

Mackay *et al.*[140] and Tuteja *et al.*[161] found up to $10-20\%$ chain expansion in polystyrene PNCs containing well-dispersed polystyrene NPs at volume fractions $\phi_N \lesssim 10\%$. This effect was only observed for $R_g > R_N$, in agreement with the results of Ref. 159.

Using the SC/PRISM theory, Frischknecht *et al.*[164] found that attractive NPs smaller than the polymers cause chain expansion. Also from the point of view of computer simulations there are contrasting results regarding the effect of NPs on chain conformation[158].

Karatrantos *et al.*[152] performed MD simulations of PNCs containing spherical NPs at volume fractions ranging from 10% to 40%, finding that polymer-NP interactions play a crucial role both in NP dispersion and in the effect of NPs on chain conformations: Repulsive NPs of size larger than some threshold value tend to aggregate and leave polymer dimensions unperturbed, while attractive NPs are well dispersed and cause the polymer chains to be stretched and flattened when $R_g > R_N$. Large NPs ($R_g < R_N$) leave polymer dimensions unchanged irrespectively of the character of the polymer-NP interactions.

In conclusion, further theoretical and experimental studies are needed in order to gain a satisfactory understanding of what are the fundamental parameters in controlling chain conformation in PNCs, and what is the general mechanism behind the different observed behaviors.

4.2 NANOPARTICLE DYNAMICS

Several approaches have been used to gain a theoretical understanding of the dynamics of NPs in PNCs. Because of the complexity of these systems, most theories focused on the problem of a single NP diffusing in a polymer solution or melt, a situation which corresponds to the case of very low NP concentration in experiments and simulations. Moreover, most theories consider the case of spherical NPs, which can be characterized by a single length scale (the NP diameter σ_N), and are therefore easier to handle than more complex shapes such as rods. We will briefly review the theories that have been most successful in interpreting the experimental and simulation data. Among the models not described here, we mention the geometric obstruction models[165–167] and the hydrodynamic models[168–173]. For a review of some of these models, we refer the reader to Ref. 174. All the theories described in this section

[b] polydimethylsiloxane

only deal with the problem of a single NP in a polymer liquid. To the best of our knowledge, no theoretical attempt has yet been carried out to tackle the much more challenging problem of the diffusion of several interacting NPs in a polymer liquid.

4.2.1 *Brochard-Wyart–de Gennes (BWdG) scaling theory*

One of the earliest theoretical approach to the problem of NP diffusion in a polymer liquid was carried out by Brochard-Wyart and de Gennes using scaling arguments[175]. Brochard-Wyart and de Gennes, who considered entangled polymer melts, argued that, while particles larger than the tube diameter d experience the macroscopic viscosity of the melt, particles of diameter $\sigma_N < d$ would experience a much smaller viscosity $\eta \propto \sigma_N^2$. This is because such a small particle does not have to disentangle any chain in order to move, but rather it must displace chain portions of size $\approx \sigma_N$ *inside* the tube. From ideal chain statistics, these chain portions will contain $n(\sigma_N) \approx (\sigma_N/b)^2$ monomers, where b is the effective bond length. The NP will therefore experience a σ_N-dependent viscosity which can be estimated using the Rouse model (see Sec. 3.4.1):

$$\eta(\sigma_N) \approx \eta(b) \left(\frac{\sigma_N}{b}\right)^2, \tag{110}$$

where $\eta(b)$ is the viscosity of a monomer liquid with the same density as the melt.

From the viscosity, we can obtain the viscous friction coefficient ζ using the Stokes relation,

$$\zeta(\sigma_N) = f\pi\eta(\sigma_N)\sigma_N, \tag{111}$$

where f is a numerical factor between 2 and 3 which depends on the hydrodynamic boundary conditions, with $f = 2$ for pure slip and $f = 3$ for pure stick boundary conditions[176]. Finally, from ζ we can obtain the diffusion coefficient D using the Einstein relation:

$$D = \frac{k_B T}{\zeta(\sigma_N)} = \frac{k_B T b^2}{f\pi\eta(b)\sigma_N^3} \propto \sigma_N^{-3} \tag{112}$$

The conventional Stokes-Einstein equation,

$$D = \frac{k_B T}{f\pi\eta\sigma_N} \propto \sigma_N^{-1}, \tag{113}$$

valid for a spherical particle diffusing in a continuum solvent with viscosity η, is therefore not valid for a small particle ($\sigma_N < d$) in an entangled melt. The violation of the Stokes-Einstein relation has been observed in numerous experiments and simulations of polymer solutions and melts[77,177–183].

4.2.2 *Cai-Panyukov-Rubinstein (CPR) scaling theory*

The BWdG scaling theory was extended by Cai, Panyukov and Rubinstein[184], who included in their discussion polymer solutions and also treated the intermediate time dynamics of the NPs. Cai *et al.* distinguished between three dynamic regimes, depending on the ratio between the NPs size and two relevant length scales of the solution/melt: the mesh size ξ[c] and the tube diameter d.

For $\sigma_N < \xi$ (small size regime), the particle can slip through the mesh and it is therefore barely affected by the presence of the polymers. Its motion will therefore be diffusive, with diffusion coefficient

$$D_s \approx \frac{k_B T}{\eta_s \sigma_N} \tag{114}$$

where η_s is the solvent viscosity. In a melt, $\xi < b < \sigma_N$ and this regime disappears.

For $\xi < \sigma_N < d$ (intermediate size regime), the dynamics of the NP is not affected by the entanglements, but it is coupled to the fluctuation modes of the chains. The motion of the NP is diffusive up to a time

$$\tau_\xi \approx \frac{\eta_s \xi_b^3}{k_B T} \approx \tau_0 \left(\frac{\xi}{b}\right)^3, \tag{115}$$

which corresponds to the Zimm relaxation time of a polymer strand of size ξ_b (see Sec. 3.4.2). For times $t > \tau_\xi$, NP motion is coupled to that of the a polymer segment containing $(t/\tau_\xi)^{1/2}$ blobs (see Eq. (59)), and therefore the NP experiences a time-dependent effective viscosity (cf. Eq. (110))

$$\eta_{\text{eff}}(t) \approx \eta_s \left(\frac{t}{\tau_\xi}\right)^{1/2} \tag{116}$$

leading to an effective diffusion coefficient

$$D_{\text{eff}}(t) \approx \frac{k_B T}{\eta_{\text{eff}} \sigma_N} \approx D_s \left(\frac{t}{\tau_\xi}\right)^{-1/2}, \tag{117}$$

which in turn will lead to the following MSD for the NPs:

$$\langle r_N^2(t) \rangle \approx D_{\text{eff}}(t) t \approx D_s (\tau_\xi t)^{1/2}. \tag{118}$$

Therefore, the theory predicts that for $t > \tau_\xi$ the NPs will move subdiffusively, with an exponent $1/2$. The motion becomes diffusive only when the size of the chain sections control-

[c] The authors consider ξ as equivalent (in a scaling sense) to the blob size ξ_b, i.e. $\xi \approx \xi_b$. However, as discussed in Ch. 3.2.2, this is only strictly true in the semidilute regime. We will however follow the presentation of the authors and consider $\xi \approx \xi_b$ in the present section.

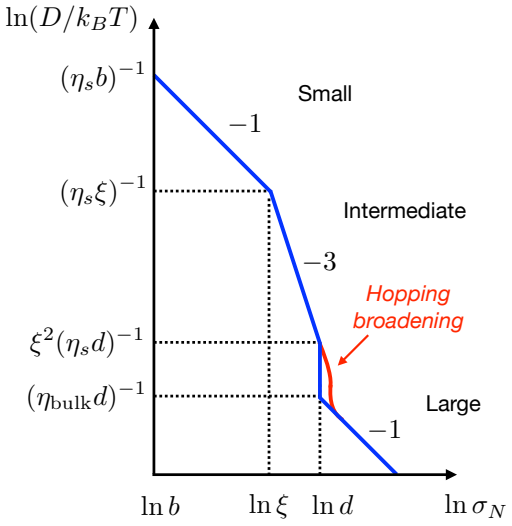

Figura 22 – Scaling behavior of the NP diffusion coefficient D in CPR theory, Eq. (125). The theory predicts that the sudden jump at $\sigma_N \approx d$ is broadened by the hopping process[184,185].

ling viscosity becomes comparable with the NP diameter; since these chain sections contain $(t/\tau_\xi)^{1/2}$ blobs, this condition translates to

$$\xi \left(\frac{t}{\tau_\xi}\right)^{1/4} \approx \sigma_N \tag{119}$$

and therefore the motion of the NPs will become diffusive for t larger than τ_{σ_N}, where

$$\tau_{\sigma_N} \approx \tau_\xi \left(\frac{\sigma_N}{\xi}\right)^4 \approx \tau_0 \frac{\sigma_N^4}{b^3 \xi} \tag{120}$$

The NP terminal diffusion coefficient can then be estimated from Eq. (118):

$$D_{\rm eff}(\tau_{\sigma_N}) \approx D_s \left(\frac{\tau_{\sigma_N}}{\tau_\xi}\right)^{-1/2} \approx D_s \left(\frac{\xi}{\sigma_N}\right)^2 \approx \frac{k_B T \xi^2}{\eta_s \sigma_N^3} \tag{121}$$

In the case of a melt $\xi \approx b$[d] and therefore we obtain the BWdG result, Eq. (112).

For $\sigma_N > d$ (large size regime), the NPs are trapped by the entanglements, and they follow the same subdiffusive regime as the intermediate size particles up to the relaxation time of an entanglement strand,

$$\tau_e \approx \tau_\xi \left(\frac{d}{\xi}\right)^4 \approx \tau_0 \frac{d^4}{b^3 \xi}. \tag{122}$$

For $t > \tau_e$, large particles are trapped by the entanglements and their MSD reaches a plateau

[d] This is only strictly true for densities not too much larger than ρ^{**}, for which $\xi \approx \xi_b \approx b$. However, for $\rho > \rho^{**}$ the mesh size ξ decreases monotonically with increasing ρ.

$$\langle r_N^2(\tau_e)\rangle \approx D_{\text{eff}}\tau_e \approx D_s(\tau_\xi\tau_e)^{1/2} \approx \frac{d^2\xi}{\sigma_N} \tag{123}$$

According to Cai *et al.*, the motion of large particles can then proceed by two mechanisms. The first one is *constraint release*, i.e., the reptation of the surrounding polymers leading to the release of the entanglements. The second one is *hopping*, i.e., local fluctuations of the entanglement mesh which can allow the NPs to "jump" from one entanglement cage to another[185]. The release of the entanglements by reptation of the chains will happen at the time $t \approx \tau_d \approx \tau_e(N/N_e)^{3.4}$ (disengagement time – see Chapter 3.4.3). For $t > \tau_d$, the dynamics of the NPs is predicted to be diffusive, with diffusion coefficient given by the Stokes-Einstein relation,

$$D \approx \frac{k_B T}{\eta_{\text{bulk}}\sigma_N}, \tag{124}$$

where η_{bulk} is the bulk viscosity of the solution, which has value $\eta_{\text{bulk}} \approx G_0\tau_d$[5].

To summarize, the CPR prediction for the diffusion coefficient D of a NP of diameter σ_N in an entangled polymer solution/melt is:

$$\frac{D}{k_B T} \approx \begin{cases} \eta_s^{-1}\sigma_N^{-1} & \sigma_N < \xi \\ \eta_s^{-1}\xi^2\sigma_N^{-3} & \xi < \sigma_N < d \\ \eta_{\text{bulk}}^{-1}\sigma_N^{-1} & d < \sigma_N \end{cases} \tag{125}$$

These three regimes are also represented in Fig. 22. For unentangled systems, Eq. (125) must be modified by replacing the tube diameter d with R_g, where R_g is the polymer's radius of gyration[184].

4.2.3 *SCGLE theory*

The CPR scaling theory represents a significative improvement with respect to the BWdG. However, being a scaling theory, it is unable to predict numerical coefficients and does not give a microscopic foundation to its predictions. One of the first attempts to develop a microscopic theory of NP motion in polymer liquids was carried out by Egorov[186] using mode-coupling theory (MCT)[1]. Egorov, who limited his analysis to unentangled polymers, stated that the diffusion coefficient of NPs of diameter $\sigma_N < 2R_g$ scaled approximately as $D \propto \sigma_N^{-2}$, in contrast with the BWdG theory, which predicts $D \propto \sigma_N^{-3}$, although this is probably due to the fact that the σ_N value he considered in his calculations were not small enough to properly observe the $D \propto \sigma_N^{-3}$ regime. In the same year, Yamamoto and Schweizer[187] proposed a theoretical approach based on a combination of MCT ideas, Langevin dynamics and PRISM theory[188]; in many respects, the theory of Yamamoto and Schweizer can be regarded as an improved version of the theory of Egorov. In order to better address the motion of small NPs in entangled melts, Yamamoto and Schweizer later proposed a more general theory, which contained the previous one as a particular result[189]. The new theory combined the self-consistent Langevin equation (SCLGE) theory[1] with MCT ideas. One of

the assumptions of SCLGE theory is that the NP diffusion coefficient can be approximated as the sum of a non-hydrodynamic (D_{nhd}) plus a hydrodynamic (D_{hd}) contribution[187,189]:

$$D = D_{\text{nhd}} + D_{\text{hd}}. \tag{126}$$

The term D_{nhd} comes from binary collisions between the NP and solvent molecules and from the coupling of NP motion with the structural relaxation modes of the solvent, whereas the D_{hd} term comes from coupling of the NP motion with the transverse current mode of the solvent[186,190] and can be approximated using the Stokes-Einstein (SE) relation[187]:

$$D_{\text{hd}} = D_{SE} = \frac{k_B T}{f \pi \eta_{\text{bulk}} \sigma_N} \tag{127}$$

where η_{bulk} is the bulk viscosity of the polymer liquid, which can be approximated as

$$\eta_{\text{bulk}} = \eta_R \left[1 + \left(\frac{N}{N_e} \right)^2 \right], \tag{128}$$

where $\eta_R = \eta(b)N$ is the Rouse viscosity. Eq. (128) is a "minimalist" analytic expression that properly captures both the unentangled Rouse limit ($N \ll N_e$) and the entangled limit ($N \gg N_e$)[187]. The main predictions of the theory are the following; in *unentangled melts*, D_{nhd} is given for $\sigma_N < 2R_g$ by

$$D_{\text{nhd}} = \frac{3 k_B T {R_g}^2}{\pi \eta_R \sigma_N^3} \propto \sigma_N^{-3}. \tag{129}$$

This is in agreement with the BWdG scaling prediction. The SE behavior is recovered when $D_{SE} \geq D_{\text{nhd}}$, i.e., for $\sigma_N \geq 3R_g$.

In *entangled melts*, the diffusion constant scales as σ_N^{-3} for $\sigma_N < d$. For $\sigma_N \gtrsim 2d$ there is a continuous crossover towards SE behavior. The crossover from non-hydrodynamic to SE behavior becomes sharper with increasing degree of entanglement N/N_e, and for heavily entangled melts SE behavior is only recovered for rather large NP sizes, $\sigma_N \approx 10d$. This is in contrast with the BWdG and CPR scaling theories, which both predict a sharp crossover at $\sigma_N \approx d$[e]. The above described behaviors are shown in Fig. 23.

When the effect of the entanglements is negligible, SCLGE theory also predict subdiffusive NP motion at intermediate times, with subdiffusive exponent $\alpha = 1/2$: $\langle r_N^2(t) \rangle \propto t^{1/2}$. It has also been verified via numerical SCLGE calculations that this trend is followed by large particles in an almost universal way[189]. However, comparison with simulations reveals severe limitations of the theory in correctly predicting MSD slopes and crossover times (more details can be found in Ref. 189).

[e] Cai-Panyukov-Rubinstein actually predict that this crossover is broadened by hopping processes, but even so it remains fairly sharp (cf. Fig. 22).

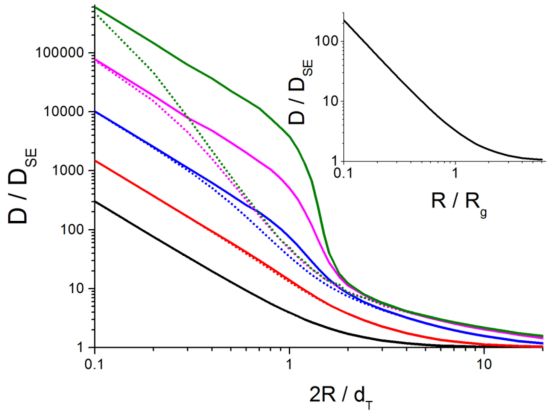

Figura 23 – Ratio between the NP diffusion coefficient and the SE prediction as a function of the confinement ratio σ_N/d (here $d_T = d$ and $R = \sigma_N/2$), as predicted from SCLGE theory for different values of N/N_e. From bottom to top, the solid lines correspond to $N/N_e = 1, 2, 4, 8$ and 16. Dashed lines are prediction from the theory of Ref. 187, where it was assumed that NP transport is solely mediated by polymer relaxation also for small NPs ($\sigma_N < d$). *Inset*: same quantity for unentangled melt; in this case, the confinement parameter is $\sigma_N/2R_g$. We note that in both plots, the power-law decay at small confinement parameter values has slope -2, i.e. $D \propto \sigma_N^{-3}$. From Ref. 189.

4.2.4 *Activated hopping*

In entangled polymer liquids, the motion of particles of size larger than the tube diameter d can proceed through the release of the entanglements (*constraint release*), which happens on time scales of the order of the disengagement time, $\tau_d \propto N^{3.4}$. For very long chains, τ_d can become larger than the experimental time, so that the NPs become permanently trapped (on the experimental time scale). In polymer solids containing irreversible crosslinks, like dry networks (e.g. rubbers) and gels, the situation becomes even more extreme, since the constraint release mechanism is completely turned off. However, even in this case of extreme confinement, the motion of NPs can still happen through the mechanism of *hopping*, i.e., activated motion triggered by local fluctuations of the entanglement/crosslink mesh.

Dell and Schweizer[191] developed a theory of hopping based on the nonlinear Langevin equation (NLE) theory[192]. In their work, they considered a general system containing both crosslinks and entanglements, and defined a mean entanglement length N_x, which results from both crosslinks and entanglements, from the plateau modulus, $N_x \approx \rho k_B T/G_0$. The tube diameter can then be estimated as $d \approx bN_x^{1/2}$. The starting point of the theory is a dynamic free energy $F(r)$ (r = displacement of the particle from its initial position), which is a rather complicated function of the system's parameter and of the monomer-monomer and monomer-NP pair correlation functions. This free energy assumes a simpler form in the so-called "random structure model", which assumes (1) that the monomers pack randomly around the NPs, and (2) that the polymer structure factor $S(q)$ can be approximated by its long wavelength limit, i.e., $S(q) \simeq \lim_{q\to 0} S(q) \equiv S_0$. In addition, (3) the NPs are treated as hard spheres.

Under these approximations, $F(r)$ can be evaluated analytically, and an expression which depends only on $d, R_N = \sigma_N/2, S_0, b$ and ρ is obtained. From $F(r)$, we can define a localization length r_L (position of the first minimum of F), a barrier position r_B (position of the first

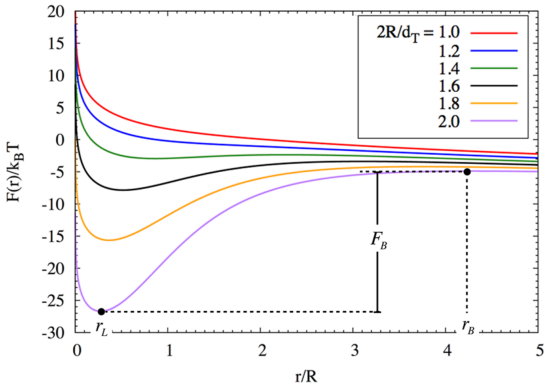

Figura 24 – Dynamic free energy $F(r)$, in units of k_BT, for various values of the confinement parameter $C = \sigma_N/d$ (here $d_T = d$ and $R = \sigma_N/2$) based on the random structure model with $\rho = 18b^{-2}d^{-1}$ and $S_0 = 0.25$. The onset of localization (appearance of the minimum in F) happens at $2R/d \simeq 1.32$. Localization length r_L, barrier position r_B and barrier height F_B are shown. From Ref. 191.

maximum of F) and a barrier height $F_B \equiv F(r_B) - F(r_L)$. A graphical representation of $F(r)$ and of these quantities is given in Fig. 24, which also gives us an intuitive interpretation of $F(r)$: In order to move through the mesh, a particle has to "jump" out of the free energy well. We can therefore define a mean jump length $\Delta r_h \equiv r_B - r_L$ and a mean hopping time

$$\tau_h = 2\beta\zeta \int_{r_L}^{r_B} e^{-F(r)/k_BT} \mathrm{d}r \int_0^r e^{-F(r')/k_BT} \mathrm{d}r', \tag{130}$$

where ζ is the short time friction constant. For polymer melts, the approximated theory predicts the onset of localization (appearance of a minimum in F) to happen for NP diameters $\sigma_N \approx d$, as intuition would suggest. It is useful to introduce a confinement parameter $C \equiv \sigma_N/d$; we can then say that localization starts at a critical value $C_c \approx 1$. Immediately after the start of localization, the mean jump length Δr_h, the free energy barrier F_B and the mean hopping time, can be approximated, for $\rho = 18b^{-2}d^{-1}$ (a typical value for melts), by

$$\Delta r_h \approx \sigma_N (C - C_c)^{\alpha} \tag{131a}$$

$$\frac{F_B}{k_BT} \approx (C - C_c)^{\beta} \tag{131b}$$

$$\tau_h \approx \tau_N \exp[\gamma(C - C_c)] \tag{131c}$$

where $\tau_N \approx \zeta\sigma_N^2/k_BT$ is the NP short time scale. Eq. (131)a is approximately valid for $0 < C - C_c \lesssim 1$, Eq. (131)b for $0 < C - C_c \lesssim 0.4$ and Eq. (131)c for $0 < C - C_c \lesssim 0.3$[191]. In these ranges of validity, the exponents have value $\alpha \simeq 0.48$, $\beta \simeq 1.7$ and $\gamma \simeq 16$. For stronger confinement $C \gg 1$, $\Delta r_h \propto C^2$, $F_B/k_BT \propto C^3$ and the increase of τ_h is stronger than exponential in $C - C_c$. The hopping diffusion constant can be estimated as $D_h \approx \Delta r_h^2/6\tau_h$; for $0 < C - C_c \lesssim 0.3$, therefore, we can write the approximate expression

$$D_h \approx \frac{\Delta r_h^2}{6\tau_h} \approx \frac{k_B T}{\zeta}(C - C_c)^{2\alpha} \exp[-\gamma(C - C_c)] \quad (0 < C - C_c \lesssim 0.3) \tag{132}$$

The authors also estimated that in entangled liquids, considering experimentally accessible values of the degree of entanglement, $N/N_x \lesssim 200$, hopping will only be observable in a small range of confinement parameters, $1.5 \lesssim C \lesssim 1.8$.

The problem of hopping diffusion was also considered by Cai, Panyukov and Rubinstein using scaling arguments[185]. The authors considered both polymer solids (dry networks and gels) and liquids; for the solids, they considered considered two different regimes, depending on the relative magnitude of the entanglement length resulting from topological entanglements, N_e, and that resulting from crosslinks, N_x[f]: the entangled regime ($N_x > N_e$) and the unentangled regime ($N_x < N_e$). In the entangled regime, the density of crosslinks, $\rho_x \approx \rho/N_x$, is larger than the density of entanglements, $\rho_e \approx \rho/N_e$ (here ρ is the total monomer density). In the unentangled regime, the opposite is true.

For NPs of size $\sigma_N > d_x \approx bN_x^{1/2}$ (large NPs) in unentangled dry networks, the theory predicts that jump length Δr_h, barrier height F_B and hopping time τ_h are given respectively by

$$\Delta r_{h,x} \approx b \tag{133a}$$

$$\frac{F_{B,x}}{k_B T} \approx C_x^2 \tag{133b}$$

$$\tau_{h,x} \approx \tau_0 N_x^2 C_x \exp\left(C_x^2\right) \tag{133c}$$

where τ_0 is the monomer relaxation time and $C_x \equiv \sigma_N/d_x$ is the confinement parameter. Hopping diffusion is predicted to become experimentally observable at the time $\tau_{h,x}^{\text{net}} = \tau_{h,x} d_x/(bC_x)$, and the hopping diffusion coefficient is given by

$$D_{h,x} \approx \frac{b^2}{\tau_{h,x}} \approx \frac{b^2}{\tau_0 N_x^2 C_x} \exp\left(-C_x^2\right). \tag{134}$$

For particles of size $\sigma_N > d_e \approx bN_e^{1/2}$ in entangled dry networks ($N_e < N_x$, or equivalently $d_e < d_x$), the CPR hopping theory predicts

$$\Delta r_{h,e} \approx b \tag{135a}$$

$$\frac{F_{B,e}}{k_B T} \approx C_e \tag{135b}$$

$$\tau_{h,e} \approx \tau_0 N_e^2 \exp(C_e) \tag{135c}$$

where $C_e \equiv \sigma_N/d_e$. Hopping becomes observable at time $\tau_{h,e}^{\text{net}} \approx \tau_{h,e} d_e/(bC_e)$, and the hopping diffusion coefficient is given by

[f] We note that here N_x doesn't have the same meaning as in Dell and Schweizer (Ref. 191). However, we use the same notation in order to be more consistent with the notation of Cai, Panyukov and Rubinstein (Ref. 185).

$$D_{h,e} \approx \frac{b^2}{\tau_{h,e}} \approx \frac{b^2}{\tau_0 N_e^2} \exp(-C_e) \tag{136}$$

By comparing Eqs. (133b) and (135b), we see that entanglement cages are "softer", in the sense that the free energy barrier depends less strongly on the confinement parameter. Qualitatively, this due to the fact that entanglements, unlike crosslinks, can move through the sliding motion of a chain upon another, thereby loosening the local mesh.

The mobility of NPs of diameter $d_x < \sigma_N < d_x^2/d_e$ is affected by both entanglements and crosslinks, but dominated by the entanglements, since for these values of σ_N we have $F_{B,x} < F_{B,e}$. However, at the diameter $\sigma_{N,e} \approx d_x^2/d_e$ the two barriers become of comparable size ($F_{B,x} \approx F_{B,e}$), and for $\sigma_N > \sigma_{N,e}$ NP mobility is dominated by the crosslinks. In conclusion, we note that the above scaling analysis can be easily extended to entangled and unentangled polymer gels by replacing the effective bond length b with the blob size ξ_b.

4.2.5 *Experimental results*

The breakdown of the Stokes-Einstein (SE) relation for particles with radius $R_N < R_g$ (in unentangled solutions/melts) or $R_N < d$ (in entangled solutions/melts) predicted by the BWdG, CPR and SCGLE theories has been observed in several experiments. Tuteja and Mackay[178] measured the diffusion coefficient D_N of cadmium selenide NPs in an entangled polystyrene (PS) melt where $R_N < d$, finding $D/D_{SE} \simeq 200$, with $D_{SE} = k_B T/(6\pi R_N \eta_{\text{bulk}})$ the Stokes-Einstein prediction.

A similar result was obtained by Grabowski *et al.*[180], who measured D_N for gold NPs two different PBMA[g] melts, one unentangled ($N/N_e = 0.1$) and one entangled ($N/N_e = 7.2$). They found that in the entangled melt, the SE relation can predict quite accurately NP motion ($D/D_{SE} \simeq 1$), whereas in the entangled melt an much higher diffusivity than that predicted by the SE was observed ($D/D_{SE} \simeq 250$). In both cases, the NP were larger than the radius of gyration of the chains ($R_N/R_g = 2.5$ in the unentangled melt and $R_N/R_g \simeq 3.2$ in the entangled melt).

Similar results where reported by Omari *et al.*[193] for the diffusion of gold NPs in semidilute solutions of PS in toluene, for the case $R_N \approx \xi < R_g$. The author also found the dependence of D on polymer concentration ϕ to be well described by the phenomenological equation of Phillies[168,169,194],

$$D = D_0 \exp(-\alpha \phi^{\nu}), \tag{137}$$

with $\alpha \simeq 12$ and $\nu \simeq 0.9$.

Kohli and Mukhopadhyay[181] studied the diffusion of gold NPs in semidilute PEG[h]-water, finding a good agreement with CPR theory and identifying R_g as the crossover length scale from the intermediate ($D \propto R_N^{-3}$) to the large size regime ($D_N \simeq D_{SE} \propto R_N^{-1}$).

Grabowski and Mukhopadhyay[195] also studied the diffusion of gold NPs in entangled PBMA melts for NPs in the size range $2R_N/d \simeq 0.3 - 3.5$, a decrease of D as a function of

[g] Poly(n-butyl methacrylate).
[h] Poly(ethylene glycol).

$2R_N/d$ but no trace of the sharp drop predicted by the BWdG theory. The data, however, did not show particularly good agreement neither with CPR theory nor with SCGLE theory, and it was not possible to determine whether activated hopping was relevant.

Very good agreement with the CPR prediction for the intermediate size regime was observed by Poling-Skutvik *et al.*[183], who studied the diffusion of PS NPs in dilute and semidilute solutions of partially hydrolyzed PAM[i] in a very wide size range, $2R_N/\xi_b \simeq 0.4 - 80$. The measured subdiffusive exponent α, however, was significantly higher than the CPR prediction ($\alpha = 1/2$) even for $R_N \gg \xi$; the authors concluded therefore that NP dynamics is not completely coupled to the relaxation modes of the polymers at short/intermediate times, as predicted by CPR theory.

To summarize, it is beyond doubt that the SE relation is violated for small NPs in PNC ($R_N \lesssim R_g$ in unentangled PNCs and $2R_N \lesssim d$ in entangled PNCs). Much remains o be understood, however, regarding the microscopic mechanism of this slowing down.

4.3 POLYMER DYNAMICS

When NPs at high enough volume fraction are dispersed in a polymer liquid, it is observed experimentally that the dynamics of the polymers undergoes noticeable changes. Understanding how NPs influence polymer dynamics in a PNC is, however, a much more difficult task than understanding the dynamics of a single NP in a PNC. This is because: (1) It is not possible, for the polymers, to consider the infinite dilution limit, unless we desire to study dilute solutions containing NPs; (2) as discussed in Sec. 3.4, the dynamics of polymers is much more complex than that of spherical particles, because of the many different length (and time) scales that play a relevant role in the case of polymers. Therefore, the theories which have been proposed to describe polymer diffusion in PNCs are mostly quite crude or semi-empirical.

4.3.1 *Models*

One of the oldest models for polymer diffusion in PNCs is the Maxwell-Fricke model[196,197], which was originally formulated to study electric conductivity in heterogeneous media. This model assumes immobile, impenetrable obstacles (filler) suspended in a mobile solvent continuum[198], and predicts the diffusion coefficient D of the solvent to be[174,198]

$$\frac{D}{D_0} = \frac{1 - (\phi_f + \phi_{nd})}{\left(1 + \frac{\phi_f + \phi_{nd}}{2}\right)(1 - \phi_f)} \tag{138}$$

where D_0 is the diffusion coefficient of pure solvent, ϕ_f is the filler volume fraction and ϕ_{nd} is the volume fraction of non-diffusing solvent. If $\phi_{nd} \simeq 0$, Eq. (138) becomes

$$\frac{D}{D_0} = \frac{1}{1 + \phi_f/2} \tag{139}$$

[i] Polyacrylamide.

However, this model has a very limited applicability, since it works well only for small diffusing molecules and low filler concentrations[174], and it shows poor agreement with the data for realistic PNCs[199].

Muthukumar and Baumgärtner proposed a model for the translocation of polymers trough cubic pores connected by narrow parallelepipedal bottlenecks[200,201], which has been shown to give a good qualitative description of the diffusion of polymers in PNCs containing large, immobile NPs which interact with the polymers only through excluded volume[137]. In this model, polymer diffusion is an activated process, and therefore the diffusivity has an Arrhenius form:

$$\frac{D}{D_0} = \exp\left(-\frac{\Delta F}{k_B T}\right) \tag{140}$$

where $\Delta F = F_c - F_b$ is a free energy barrier, with F_c and F_b are the confinement free energies for a chain in a cavity and in a bottleneck, respectively. Through scaling considerations, the diffusion coefficient can be expressed as[200]

$$\frac{D}{D_0} = \exp\left\{-N\left[f d_b^{-1/\nu} + \left(\frac{1-f}{z} - 1\right) d_c^{-1/\nu}\right]\right\} \tag{141}$$

where N is the chain length, f is the fraction of monomers in the bottleneck, d_b is the bottleneck diameter, ν is the Flory exponent, z is the average number of cavities which contain the $(1-f)N$ unconfined segments per bottleneck and d_c is the cavity diameter[200,201]. This model predicts therefore an exponential decay of D with N.

It has been proposed that this theory could be applied to PNC by identifying d_b with the average interparticle distance h[137], which can be estimated as

$$h \simeq \sigma_N \left[\left(\frac{\phi_N^{\mathrm{M}}}{\phi_N}\right)^{1/3} - 1\right], \tag{142}$$

where σ_N is the NP diameter, ϕ_N is the NP volume fraction and ϕ_N^{M} represents the maximum value that ϕ_N can reach (for $\phi_N = \phi_N^{\mathrm{M}}$, we have $h = 0$).

Meth *et al.*[202] proposed a model in which a PNC containing spherical NPs is represented as a collection of parallel, rigid cylindrical pores, and the polymers as spheres diffusing through these pores. The authors observe that the formal expression for the reduced diffusion coefficient of a solid sphere of radius R_s suspended in a viscous fluid and moving through a cylindrical pore of radius R is formally identical to the partition function $Z(R/R_g)$ of a Gaussian polymer chain confined within a cylinder (R_g = radius of gyration), provided that $R_s = R_g$. They then calculate the reduced polymer diffusion coefficient as

$$\frac{D}{D_0} = (1-\phi_N)\frac{\int_0^\infty Z(x)P(x)x^2\mathrm{d}x}{\int_0^\infty P(x)x^2\mathrm{d}x} \tag{143}$$

where ϕ_N is the NP volume fraction and $P(x)$ is the two-dimensional pore size distribution[203] describing the distribution of diameters of the effective cylinders, expressed as a function

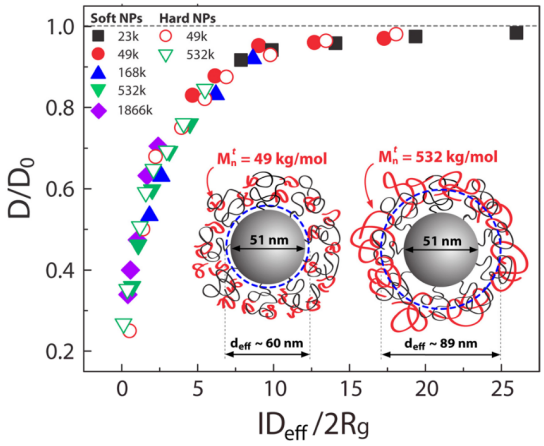

Figura 25 – Reduced polymer diffusion coefficient as a function of the confinement parameter (here ID_{eff} is the effective interparticle distance and d_{eff} is the effective NP diameter) for systems of silica nanoparticles coated either with polymer brushes (soft NPs) or short ligands (hard NPs). From Ref. 157.

of $x = R/R_g$, with R the cylinder radius. This model shows overall a good qualitative agreement with experimental data for several different PNCs containing large, immobile NPs[202]. However, the quantitative agreement with the data is quite poor, and becomes worse at high NP loading. Moreover, the model is expected to fail for polymers smaller than the NPs ($2R_g < \sigma_N$), and it is not clear if it would still be applicable to the case of mobile NPs.

At present, no model has been able to show an excellent quantitative agreement with experimental data or to explain what is the microscopic mechanism behind the slowing down of polymer chains in the presence of NPs. The difficulty, as it is usually the case for PNCs, is that many different characteristics of the system, such as NP to polymer size ratio, NP volume fraction, strength of NP-polymer interaction, presence or absence of entanglements etc., are potentially relevant and must be taken into account.

4.3.2 *Experimental and simulation results*

In general, it is found experimentally that NP slow down polymer diffusion in *unentangled* PNCs, independently of the nature of the polymer-NP interaction (attractive or repulsive)[204]. Composto and coworkers studied polymer dynamics in PNCs extensively, considering spherical silica NPs with both repulsive[137,205] and attractive[141] polymer-NP interactions, spherical polymer-grafted NPs[157,206]. In all cases, a reduction of polymer diffusivity was observed with increasing NP volume fraction, and for spherical NPs it was observed that the data collapse on a master curve when plotted as a function of the *confinement parameter* $h_{eff}/2R_g$ (Fig. 25), where $h_{eff} \equiv h - (\sigma_{N,eff} - \sigma_N)$, where $\sigma_{N,eff}$ is the effective NP diameter (i.e., $\sigma_{N,eff} - \sigma_N$ is the distance of closest approach between the polymer chain and the NP surface). In most of these studies, the NPs were larger than the polymers ($\sigma_N > 2R_g$) and could be considered basically immobile. The authors also studied polymer diffusion in PNCs containing immobile, thin anisotropic NPs, such as nanorods, showing that in these systems polymer diffusivity can change non-monotonically as a function of NP volume fraction ϕ_N, initially decreasing, then reaching a minimum at the NP percolation threshold and finally increasing[207–209].

In entangled PNCs, the presence of the NPs can disentangle the chains, as both expe-

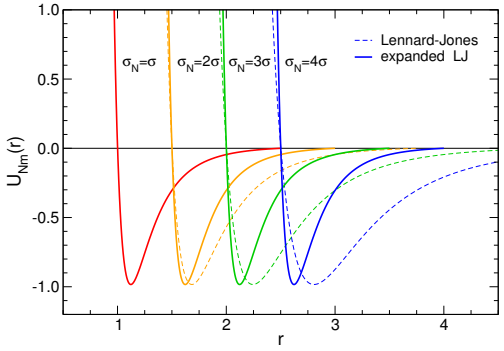

Figura 26 – Monomer-NP potential $U_{Nm}(r)$ (expanded LJ) compared to a standard LJ potential $U_{LJ}(r) = 4[(\sigma_{Nm}/r)^{12} - (\sigma_{Nm}/r)^6]$, where $\sigma_{Nm} = (\sigma_N + \sigma)/2$. The expanded LJ potential is cut and shifted at $2.5\sigma + (\sigma_N - \sigma)/2$ and the LJ potential is cut and shifted at $2.5\sigma_{Nm}$. For $\sigma_N = \sigma$, the two potentials coincide.

riments[210,211] and simulations[212,213] have shown. Chain disentanglement is manifested in an increase of the tube diameter d, and results in a decrease of the disentanglement time $\tau_d \propto N^3 d^{-2}$ (Eq. (71)). However, the long-time diffusion coefficient of the chains is given by the Rouse formula, $D_R \approx k_B T/N\zeta$ (Eq. (52)) and is therefore independent of d. The presence of NPs can therefore reduce τ_d by disentangling the chains, but should not influence the long-time diffusion coefficient (as confirmed by the experiments of Schneider *et al.*[211]). Changes in the long-time chain dynamics have nevertheless been observed in simulations: Li *et al.* observed an increase of the Rouse time $\tau_R \approx R^2/D_R$ with increasing NP volume fraction ϕ_N in PNCs with purely repulsive polymer-NP interactions. A slowing down of chain dynamics with increasing ϕ_N was also observed in several studies of PNCs (both unentangled and entangled) containing weakly attractive NPs[199,213–216]. Desai *et al.*[217], on the other hand, have reported that the polymer diffusion coefficient in a simulated lightly entangled melt ($N = 80, \rho_m = 0.85$) containing repulsive/weakly attractive NPs initially increases with ϕ_N, reaches a maximum around $\phi_N = 4\%$ and decreases for higher values. In a study which considered weakly attractive NPs in a polymer melt at low ϕ_N, Kalathi *et al.* observed, on the other hand, an increase of the chain diffusion coefficient with respect to the neat system. The increase was $\simeq 40\%$ for small NPs, whereas large NPs had basically no effect on the diffusion coefficient of the chains. Although chain lengths from $\simeq 0.2N_e$ to $\simeq 9N_e$ where considered, no significant dependence on chain length was observed.

From these examples, it is clear that the also from the point of view of experiments and simulations, a general understanding of how the presence of NPs influences chain dynamics is still missing. It is clear that the main factors influencing chain dynamics are NP volume fraction/interparticle distance[j] and polymer-NP interaction. Chain length should play a minor role, since even in the case in which the NPs cause the disentanglement of the chains *in itself* does not influence long-time chain diffusivity.

4.4 SIMULATIONS OF PNCS

Computer simulations are an extremely useful tool for the study of PNCs, and these systems have been the object of many Monte Carlo (MC)[218–222] and MD[77,148,179,199,212,215,216,223–232]

[j] These two quantities are related, since $h \simeq \sigma_N[A\phi^{-1/3} - 1]$, where $A > 0$ is a constant (see Sec. 4.1.1).

studies in the past years. Excellent reviews on simulations studies of polymer structure and dynamics in PNCs can be found in Refs. 158 and 233. While Monte Carlo (MC) simulations are very often limited to the study of the structural properties, MD simulations have also access to the dynamical properties, and for this reason are the preferred tool when studying such systems. All-atom MD simulations of PNCs can be performed[228], but only for very limited system sizes and short time scales. For this reason, most MD simulations of PNCs employ coarse-grained models (see also Ch. 3.6.3). The coarse-grained model of choice for the polymers is usually the Kremer-Grest model (see Ch. 3.6.3), whereas for the NPs several models have been used, from simple Lennard-Jones potentials[199,226] to more sophisticated pair potentials which model the NPs as smooth spheres made of uniformly distributed beads[77,217,227,234]. In some cases, NPs are not modeled via a simple pair potential, but instead they are represented as clusters of beads bound together[215,216,223,224]. The most widely used model, however, is the one which we refer to as "expanded Lennard-Jones (LJ)", in which the interaction of the NP with the species α is modeled as[148,164,179,230,235–237]

$$\mathcal{U}_{N\alpha}(r) = \begin{cases} 4\epsilon \left[\left(\frac{\sigma}{r-\Delta_{N\alpha}} \right)^{12} - \left(\frac{\sigma}{r-\Delta_{N\alpha}} \right)^{6} \right] + E_{N\alpha} & r \leq r^c_{N\alpha} + \Delta_{N\alpha} \\ 0 & \text{otherwise,} \end{cases} \tag{144}$$

where for the NP-monomer (bead) interaction $\Delta_{Nm} = (\sigma_N + \sigma)/2 - \sigma = (\sigma_N - \sigma)/2$ and for the NP-NP interaction $\Delta_{NN} = \sigma_N - \sigma$. The addition of $E_{N\alpha}$ insures that $\mathcal{U}(r^c_{N\alpha} + \Delta_{N\alpha}) = 0$. As opposed to the standard LJ potential, in the expanded LJ potential the "softness" (slope) of the potential and the interaction range do not change when the NP size varies, as one can see in Fig. 26. Since experiments have shown that the thickness of the interfacial region surrounding a NP in a polymer matrix changes only weakly with the size of the NP[238], the expanded LJ is a better choice than the standard LJ potential when simulating polymer-NP mixtures.

5

STRUCTURE AND DYNAMICS OF A PNC: INSIGHTS FROM MD SIMULATIONS

Some ideas and figures present in this Chapter have appeared in Ref. 239 and Ref. 240 (addendum to Ref. 239).

As discussed in Sec. 4.4, computer simulations are an invaluable tool for the study of PNCs. Molecular dynamics (MD) simulations are in this respect particularly useful, since –contrary to Monte Carlo (MC) simulations– they can access the dynamical properties of the system in addition to the structural ones. However, with few exceptions[179,199,215] most of the previous simulation studies of polymer-NP mixtures have focused on the dynamics of single NPs, considering the dilute NP regime (low NP volume fraction), in which the NPs can be assumed to interact only weakly with each other and the properties of the polymer solution are expected to be unchanged by the presence of the NPs. Given the scarcity of simulation studies considering the much more challenging regime of finite NP volume fraction, we set out to study the structural and dynamical properties of polymers and NPs in an unentangled, semidilute polymer solution in a wide range of NP volume fractions and NP diameters, up to values where the interaction between NPs cannot be neglected anymore.

5.1 MODEL AND METHODS

We performed NVT molecular dynamics simulations of a system of $N_p = 500$ polymer chains of length $N = 100$ and a variable number N_N of nanoparticles of different diameters σ_N. The polymers are modeled as Kremer-Grest bead-spring chains (FENE+WCA potentials – see Sec. 3.6.3), where the parameters of the FENE potential (Eq. (106)) are $k = 30\epsilon/\sigma^2$ and $r_{\max} = 1.5\sigma$. These values are chosen in order to prevent chain crossing at the thermodynamic conditions considered here. In the present Chapter and in the rest of this work, all quantities are given in Lennard-Jones (LJ) reduced units. The units of energy, length and mass are respectively ϵ, σ and m, where ϵ, and σ are defined by Eq. (104) and m is the mass of a monomer. The units of temperature, pressure, volume fraction and time are respectively $[T] = \epsilon/k_B$, $[P] = \epsilon\sigma^{-3}$, $[\phi] = \sigma^{-3}$ and $[t] = \sqrt{m\sigma^2/\epsilon}$.

For the interaction potentials involving the NPs, we use the "expanded Lennard-Jones" (expanded LJ) potential introduced in Sec. 4.4 (Eq. (144)). With this choice, the "softness" of the NPs is not changed when their diameter σ_N is changed. The cutoff radii are $r^c_{Nm} = 2.5$ for the NP-monomer interaction and $r^c_{NN} = 2^{1/6}$ for the NP-NP interaction. The interaction between monomers and NPs is therefore attractive, while the interaction between NPs is purely repulsive. As discussed in Sec. 5.2.3, a moderate attractive interaction between polymers and NPs is required in order to prevent aggregation (and eventually phase separation) of the

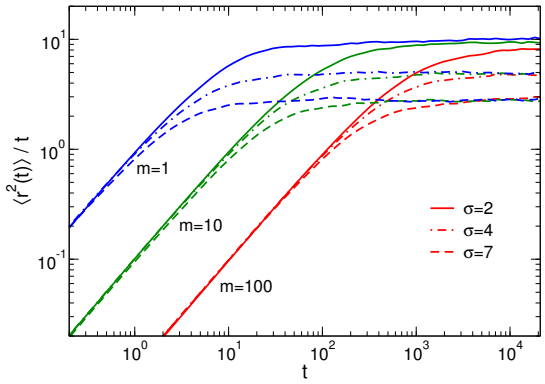

Figura 27 – Mean-squared displacement (divided by time) of a particle of diameter σ and mass m diffusing in pure (implicit) solvent at $T = 1.0$. The long-time diffusion coefficient depends only on σ.

NPs. We considered NP diameters $\sigma_N = 1, 2, 3, 4, 5$, and 7σ. We assume that the NPs have the same mass density as the monomers, $\rho_{\text{mass}} = 6m/\pi\sigma^3$, and therefore the mass of the NPs is $m_N = m(\sigma_N/\sigma)^3$. We define the NP volume fraction as $\phi_N = \pi\sigma_N^3 N_N/6V$, where V is the total volume of the simulation box; the monomer volume fraction ϕ_m is defined in an analogous way. In our simulations, ϕ_m is larger than the overlap volume fraction[5], which can be estimated from the polymer's radius of gyration at infinite dilution (see Sec. 5.3.4) and for the pure polymer system has the value $\phi_m^* = 2.98 \cdot 10^{-2}$. Moreover, as revealed by the analysis of the dynamics of the chains (see Sec. 5.4.1), the system is unentangled.

All the simulations were carried out using the LAMMPS software[241,242]. The simulation box is cubic and periodic boundary conditions are applied in all directions. The initial configurations are prepared by randomly placing the polymers and the NPs in the box; initially, the NPs have diameter equal to that of the monomers ($\sigma_N = \sigma$) and overlaps between particles are allowed. The overlaps are then removed by using a soft potential whose strength is increased over a short amount of time ("fast push-off" method[107]). After the overlaps are removed, the diameter of the NPs is gradually increased until the desired value is reached. After the NP have reached the desired size, we perform an NPT run employing Nosé-Hoover chains[81a] and allow the system to reach pressure $P = 0.1$ at temperature $T = 1.0$. In the pure polymer systems, these parameters correspond to a monomer volume fraction $\phi_m = 0.147$ (monomer density $\rho_m = 0.280$). Finally, in order to have a more realistic dynamics[81], we switch to the NVT ensemble and perform an equilibration run before starting the production run. During the NVT simulations, the pressure fluctuations are always less than 14%. The length of both the equilibration and the production runs is $10^8\delta t = 3 \cdot 10^5$, where $\delta t = 3 \cdot 10^{-3}$ is the integration time step. Time integration is performed with the velocity Verlet algorithm[79]. In all cases, we verified that during the equilibration runs the NPs (resp. polymers) diffused on average over a distance equal to several times their diameter (resp. radius of gyration), and that their motion became diffusive (see Sec. 5.4).

During the NVT runs, the temperature is kept fixed by means of a Langevin thermostat (see Sec. 3.6.1). This thermostat acts as an *implicit solvent*, in which every particle interacts independently with the solvent "molecules", but hydrodynamic interactions between solute

[a] Additional information can be found in the LAMMPS manual page[243]. During the NPT run, the box sides are coupled to each other so that they fluctuate together ($L_x = L_y = L_z = L$).

particles are not accounted for[b]. The force experienced by particle i is therefore

$$m_\alpha \ddot{\mathbf{r}}_{\alpha,i} = -\nabla_i \mathcal{U}(\{\mathbf{r}_{\alpha,k}\}) - m_\alpha \Gamma_\alpha \dot{\mathbf{r}}_{\alpha,i} + \sqrt{2 m_\alpha \Gamma_\alpha k_B T}\, \boldsymbol{\zeta}(t), \tag{145}$$

where α denotes the particle type (m = monomer, N = NP) and $\mathcal{U}(\{\mathbf{r}_{\alpha,k}\})$ is the total interaction potential acting on the particle, with $\{\mathbf{r}_{\alpha,k}\}$ representing the set of coordinates of all the particles in the system. The term $\sqrt{2 m_\alpha \Gamma_\alpha k_B T}\boldsymbol{\zeta}(t)$ is a uniformly distributed random force which represents collisions with solvent molecules, while Γ_α is a viscous friction coefficient, which is related to the viscosity of the implicit solvent η_s by

$$\Gamma_\alpha = \frac{C \eta_s \sigma_\alpha}{m_\alpha}, \tag{146}$$

where σ_α is the diameter of the particle and C a coefficient which depends on the hydrodynamic boundary conditions.

The damping constant for the monomers is $\Gamma_m = 0.1$, while that of the NPs is chosen by imposing that the viscosity of the pure solvent calculated via the Stokes formula (Eq. (146)), i.e.,

$$\begin{aligned} \eta_s &= \frac{\Gamma_m m}{C\sigma} = \frac{\Gamma_N m_N}{C\sigma_N} = \text{const.} \\ &\rightarrow \Gamma_N = \Gamma_m \left(\frac{m\sigma_N}{m_N \sigma}\right) = \Gamma_m \left(\frac{\sigma}{\sigma_N}\right)^2. \end{aligned} \tag{147}$$

With this choice of the friction coefficient, the long-time diffusion coefficient of a particle in the pure (implicit) solvent $D_{s,\alpha}$ follows the Stokes-Einstein law with viscosity η_s:

$$D_{s,\alpha} = \frac{k_B T}{\Gamma_\alpha m_\alpha} = \frac{k_B T}{C \eta_s \sigma_\alpha}. \tag{148}$$

This way, $D_{s,\alpha}$ depends only on the diameter of the particle, and not on its mass, as we can see from Fig. 27, where the mean-squared displacement (divided by time) of particles of various masses and diameters in the pure solvent is shown. We note that since $\Gamma_m = 0.1$ and $m, \sigma = 1$, if we assume stick boundary conditions ($C = 3\pi$), the numerical value of the solvent viscosity is $\eta_s = 0.1/3\pi = 1.06 \cdot 10^{-2}$. Additional details on the simulated systems can be found in Tab. 1 at the end of this Chapter.

5.2 STATIC PROPERTIES: NANOPARTICLES

To give a feeling of what the simulated system looks like, we show in Fig. 28 some snapshots for $\sigma_N = 4$ and different values of the NP volume fraction ϕ_N. We can see how the NP dispersion, which is initially good (Figs. 28a-b), becomes progressively poorer as ϕ_N is increased (Fig. 28c), until eventually large polymer-free regions are formed (Fig. 28d). In order

[b] We note that it has been recently pointed out that hydrodynamic interactions can affect the long-time dynamics of NPs in a polymer solution even at high monomer volume fractions [230], an observation which warrants further investigation.

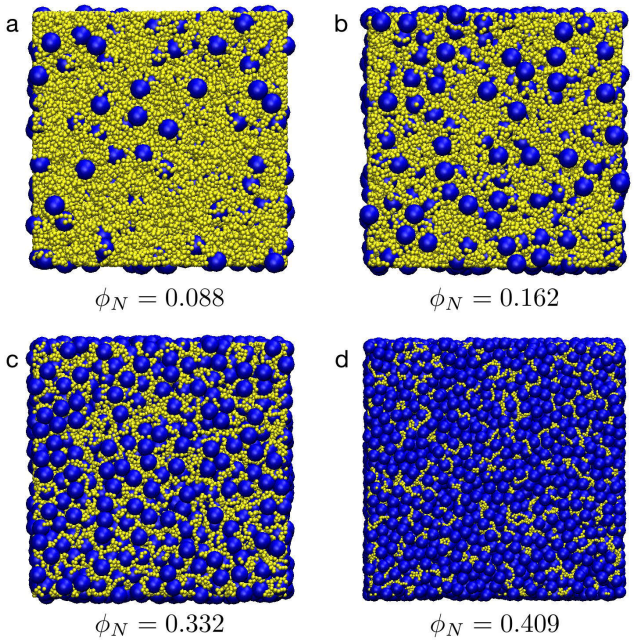

Figura 28 – Snapshots of systems containing NPs of diameter $\sigma_N = 4$ at different volume fractions (yellow spheres: monomers, blue spheres: NPs). In systems (a) and (b), the dispersion of NPs is good, while in (c) and (d) it is poor. In system (d) the formation of large polymer-free regions is evident. The length of the simulation box edges are respectively 57.45 (a), 59.15 (b), 67.13 (c), and 93.57 (d).

to characterize the structure of the systems when σ_N and ϕ_N are varied, we start by analyzing some basic quantities, such as the radial distribution function (RDF) $g(r)$ (Eq. (34)) and the structure factor $S(q)$ (Eq. (32)).

5.2.1 *Radial distribution function*

Figure 29 shows the NP-NP radial distribution function $g_{NN}(r)$ for $\sigma_N = 2$ and 4 and different values of the NP volume fraction ϕ_N. For low values of ϕ_N, g_{NN} shows a peak at

$$r_s \equiv \sigma_N + (2^{7/6} - 1) = \sigma_N + 1.245 \quad \text{(secondary peak)}, \tag{149}$$

which corresponds to twice the distance at the minimum of the monomer-NP potential. This indicates that the NPs are well dispersed in the polymer solution and configurations in which two neighboring NPs are separated by a polymer strand are favored (this kind of configuration is schematically represented in Fig. 29a). We call this peak *secondary peak*.

When ϕ_N increases, another peak appears at

$$r_c \equiv \sigma_N + (2^{1/6} - 1) = \sigma_N + 0.122 \quad \text{(contact peak)}, \tag{150}$$

which corresponds to the cutoff of the NP-NP potential and represents a configuration in which two NPs are touching; we therefore call it *contact peak*. Eventually, the contact peak

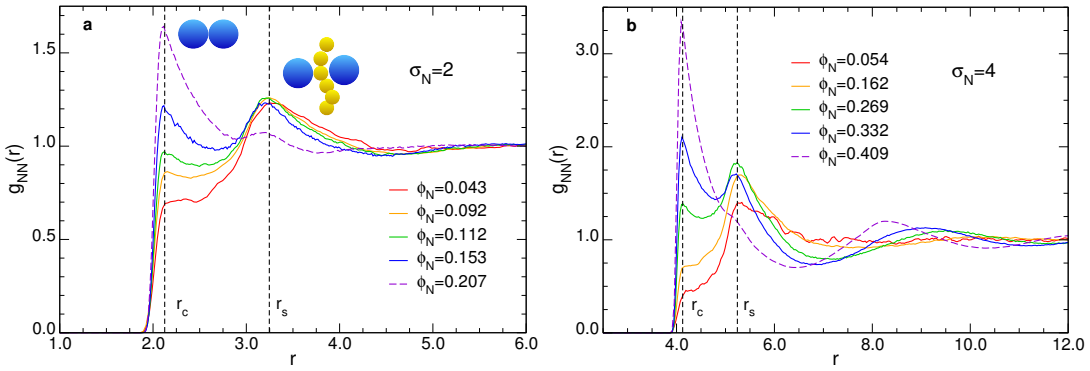

Figura 29 – NP-NP radial distribution function at different NP volume fractions ϕ_N for $\sigma_N = 2$ (a) and $\sigma_N = 4$ (b). The *contact peak* at $r_c = \sigma_N + 0.122$ corresponds to a configuration in which two NPs are touching, while the *secondary peak* at $r_s = \sigma_N + 1.245$ represents a configuration in which two NPs are separated by a polymer strand (a schematic representation of the two cases is shown in (a)): At low and intermediate ϕ_N, this last configuration is favored.

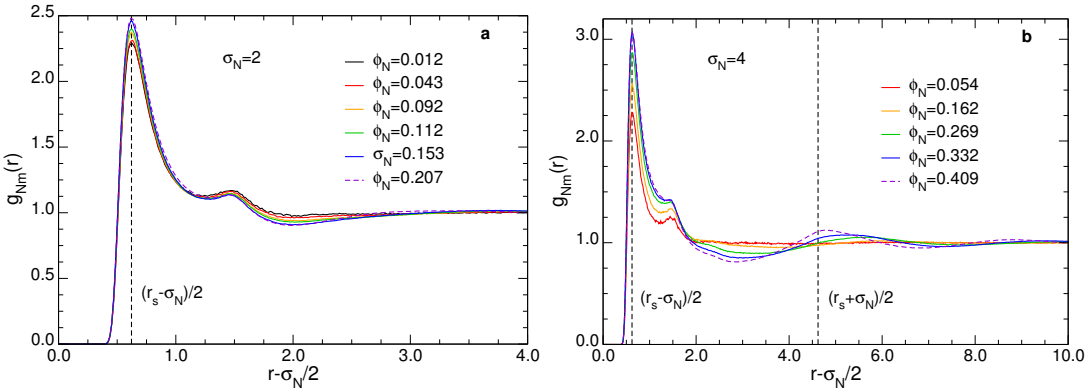

Figura 30 – Monomer-NP radial distribution function at different NP volume fractions ϕ_N for $\sigma_N = 2$ (a) and $\sigma_N = 4$ (b). The position of the main peak, $r_s = \sigma_N + 1.245$, is independent of ϕ_N.

becomes higher than the secondary peak, an evidence of the formation of large polymer-free regions (Fig. 28d).

To gain a better understanding of the distribution of the NPs relative to the polymers, we also study the monomer-NP radial distribution function. The radial distribution function for a binary system containing particles of type a and b can be defined for $a \neq b$ as[244]

$$g_{ab}(r) \equiv \frac{M_a + M_b}{4\pi M_a M_b \rho r^2} \sum_{k=1}^{M_a} \sum_{j=1}^{M_b} \langle \delta(|\mathbf{r} + \mathbf{r}_k - \mathbf{r}_j|) \rangle, \tag{151}$$

where $M_{a(b)}$ is the number of particles of type a (b) and $\rho = (M_a + M_b)/V$ is the total density. Fig. 30 shows the monomer-NP radial distribution function, $g_{Nm}(r)$, for $\sigma_N = 2$ and 4 and different values of the NP volume fraction ϕ_N. For all values of ϕ_N, $g_{Nm}(r)$ shows a sharp main peak at $r_s/2 \simeq \sigma_N/2 + 0.622$, indicating direct contact between monomers and NPs is always favored. Note that this observation is not in contrast with what we discussed above regarding g_{NN}, as the shifting of the main peak from r_s to r_c at high ϕ_N is due to the presence of the polymer-free regions. The smaller peak at $r \simeq r_s/2 + 1$ ($r - \sigma_N/2 \simeq 1.622$) is due to

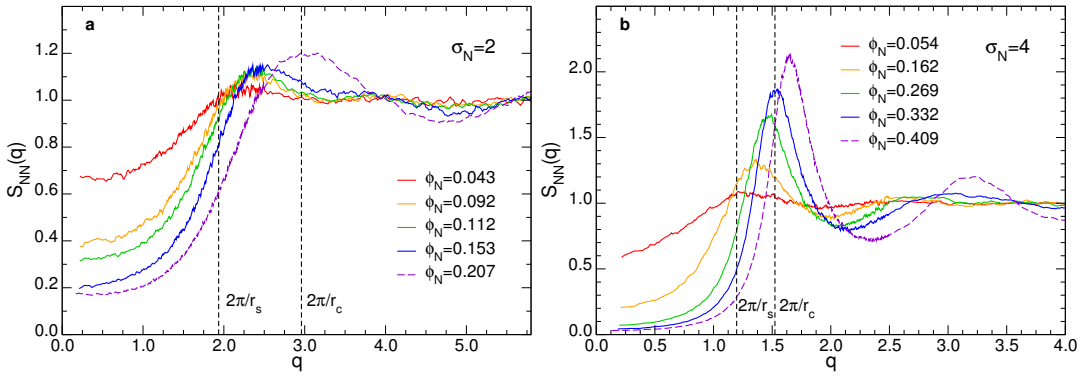

Figura 31 – NP-NP structure factor at different NP volume fractions ϕ_N for $\sigma_N = 2$ (a) and $\sigma_N = 4$ (b).

the second layer of monomers. At larger values of r we observe a periodic modulation of wavelength $\simeq \sigma_N$, which is clearly visible in Fig. 30b.

5.2.2 *Structure factor*

The structure factor was defined in Sec. 3.3. Since $S(q)$ is related to $g(r)$ *via* a Fourier transform (Eq. (35)), we can in principle find in the NP-NP structure factor $S_{NN}(q)$ the same information that we find in $g_{NN}(r)$. If the position of the main peak of $g(r)$ is $r = r_0$, the main peak of $S(q)$ will be at $q_0 \simeq 2\pi/r_0$, although the precise value of q_0 depends on temperature and density[39]. Hence, we expect to find the main peak of $S_{NN}(q)$ at $q \simeq 2\pi/r_s$ at low NP volume fraction and at $q \simeq 2\pi/r_c$ at high NP volume fraction, as we indeed observe in Figs. 31a-b. We also notice that, while in the $g(r)$ we can clearly distinguish two peaks at intermediate values of ϕ_N (Fig. 29), in the $S(q)$ their contributions interfere with each other and result in a single peak that is shifted towards higher wavevectors as ϕ_N is increased. Therefore, interpretation of $S_{NN}(q)$ might not always be straightforward.

5.2.3 *NP dispersion: The interparticle distance*

In the following sections, we will mainly consider those systems in which the NPs are well dispersed in the polymer solution (Fig. 28a-b). As a qualitative criterion, we define a system with good NP dispersion as one where the secondary peak of $g_{NN}(r)$ is higher than or comparable to the contact peak. It should be noticed that the maximum volume fraction that we can reach while keeping a good NP dispersion depends on the NP diameter σ_N. To see this, we consider the *interparticle distance* h[137,141,157,205], which represents the average spacing between the surfaces of neighboring nanoparticles. In the literature, the following expression has often been used to estimate h[137,141,157,205]:

$$h^{\text{th.}} \equiv \sigma_N \left[\left(\frac{\phi_N^{\text{M}}}{\phi_N} \right)^{1/3} - 1 \right], \tag{152}$$

where ϕ_N^{M} is the maximum achievable NP volume fraction, for which $h = 0$[205]. There is however an evident problem with the above expression: It is *a priori* not clear at all what

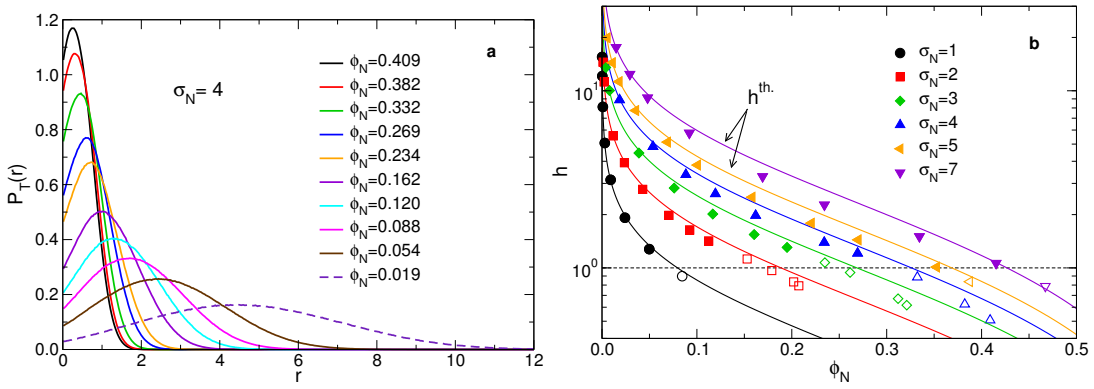

Figura 32 – (a) Pore-size probability density function of the NPs for $\sigma_N = 4$. (b) Interparticle distance as a function of the NP volume fraction ϕ_N. Filled symbols: systems with good NP dispersion. Open symbols: systems with poor NP dispersion. Continuous lines: "theoretical" interparticle distance $h^{\text{th.}}$, calculated from Eq. (152), with $\phi_N^{\text{M}} = 0.637$.

value should be used for ϕ_N^{M}. Taking the NPs to behave approximately as hard spheres (an approximation that in our case is justified by the very steep NP-NP potential), there are several possibilities, like the close-packing value[245] $\phi_{\text{cp}} = \pi/\sqrt{18} \simeq 0.740$, corresponding to an fcc or hcp lattice, or the volume fraction of some other crystal lattice, like the bcc ($\phi_{\text{bcc}} = \pi\sqrt{3}/8 \simeq 0.680$) or the simple cubic ($\phi_{\text{sc}} = \pi/6 \simeq 0.524$). The value $\phi_N^{\text{M}} = \pi/6$ was used in Ref. 246, one of the first to apply Eq. (152) to polymer nanocomposites. More recently, $\phi_{\text{rcp}} \simeq 0.637 \simeq 2/\pi$, that should correspond to a random close packing (RCP) of hard spheres, has often been invoked in the definition of h[137,141,157,205].

However, it has been shown by Torquato *et al.* that the concept of RCP is ill-defined, and that different procedures can result in different values for ϕ_{rcp}, ranging from 0.6 to 0.68[247]. This issue could be solved, as suggested by Torquato *et al.*, by replacing the ill-defined concept of RCP with that of *maximally random jammed* (MRJ) structure[247,248]. For monodispere hard spheres, this redefinition should lead to a unique value, $\phi_{\text{MRJ}} = 0.642$[248]. However, the problem of *a priori* assigning a certain value to ϕ_N^{M} remains.

We propose therefore a different way to define h, which relies on the concept of *pore size distribution* (the definition used here is that of Torquato *et. al.*; see Chapter 8 for more details)[203]. The pore size distribution (PSD) $P_T(r)$ of a system consisting of two phases is defined such that $P_T(r)\text{d}r$ represents the probability that a randomly chosen point in the phase of interest lies at a distance between r and $r + \text{d}r$ of the nearest point on the interface between the two phases[203]. It is clear from this definition that the typical interparticle distance h for the NPs in a polymer nanocomposite should correspond approximately to the typical pore size.

There is another clue that suggests the identification of h with some quantity derived from $P_T(r)$. For a system of randomly distributed overlapping spheres of radius R with number density ρ, the PSD can be computed explicitly[249] (see see Chapter 8):

$$P_T^{\text{os}}(r) = \frac{3\phi}{e^{-\phi}R}\left(\frac{r}{R}+1\right)^2 \exp\left[-\phi\left(\frac{r}{R}+1\right)^3\right]. \tag{153}$$

In this expression, $\phi = \pi(2R)^3\rho/6$ is the "volume fraction" of the spheres (although since the spheres can overlap, this does not correspond to their real volume fraction).

Let us now define r_{max} as the value of r for which $P_T(r)$ is maximized, i.e., $P_T(r_{\text{max}}) =$

$\max_r\{P_T(r)\}$. For this model, we have $r^{\rm OS}_{\rm max} = R[(2/3\phi)^{1/3} - 1]$, and therefore we can define a *typical pore diameter* as

$$2r^{\rm OS}_{\rm max} = 2R\left[\left(\frac{2}{3\phi}\right)^{1/3} - 1\right]. \tag{154}$$

By comparing Eqs. (152) and (154) and making the identifications $2R = \sigma_N$ and $\phi = \phi_N$, we note that $2r^{\rm OS}_{\rm max} = h^{\rm th.}$, provided that we choose $\phi^{\rm M}_N = 2/3 \simeq 0.667$. Given this quite remarkable connection between $2r^{\rm OS}_{\rm max}$ and $h^{\rm th.}$, and given that the definition of $r_{\rm max}$ does not present the same problems that affect Eq. (152), we are naturally lead to define the interparticle distance as

$$h \equiv 2\, r_{\rm max}, \tag{155}$$

where $2r_{\rm max}$ is not computed using Eq (154), which is strictly valid only for the overlapping spheres system, but rather evaluated directly from the PSD $P_T(r)$ obtained from the data. Exhaustive details on how the pore size distribution is calculated will be given in Sec. 8. An example of the PSD is show in Fig. 32a, where we report the PSD of the simulated systems for $\sigma_N = 4$.

In Fig. 32b, we show the interparticle distance calculated from the pore size distribution (Eq. (155)) *versus* the NP volume fraction: filled (open) symbols represent systems with a good (poor) NP dispersion (according to the above defined criterion). We also report for comparison the "theoretical" interparticle distance $h^{\rm th.}$, Eq. (152), with $\phi^{\rm M}_N = 0.637$ (continuous lines); we note that the two quantities are very similar, with $h^{\rm th.}$ being on average slightly larger than h. This means that Eq. (152) can be used to obtain an estimate of the "true" interparticle distance, despite the problems affecting its definition[c]. As we can see, NP dispersion starts to become poor when $h \simeq 1$, i.e., when the average distance between the surface of neighboring NPs becomes comparable with the monomer size, in qualitative agreement with the snapshots shown in Fig. 28c-d.

5.3 STATIC PROPERTIES: POLYMERS

5.3.1 *Radial distribution function*

In Fig. 33, we report the monomer-monomer radial distribution function $g_{mm}(r)$ for $\sigma_N = 2$ and 4. One sees that at low NP volume fraction the most prominent features of $g_{mm}(r)$ are a sharp peak at $r \simeq r_b = 0.96$ (first nearest neighbor distance in a chain) and a smaller one at $r \simeq 2r_b = 1.92$ (second nearest neighbor). When the NP volume fraction is increased, the height of these two peaks increases. The reason is that, while the structure of the chain at the length scale $r \lesssim 2r_b$ remains almost unchanged when ϕ_N increases, the monomer density ρ_m decreases, because the volume increases and the number of monomers is fixed. Since $g_{mm}(r)$ contains a factor ρ_m^{-1} (Eq. (34)), this results in an increase of this function for $r \lesssim 2r_b$.

[c] We note that Li *et al.* in Ref. 212 used Torquato's definition of the PSD to define a quantity which is basically an alternative definition of h (see Supplementary Material of Ref. [212]). At the time of this work, however, we were not aware of this article. Moreover, in Ref. 215 the mean pore radius of a PNC is calculated using the Euclidean distance map. However, to evaluate the interparticle distance they used Eq. (152) with $\phi^{\rm M}_N = 2/\pi$.

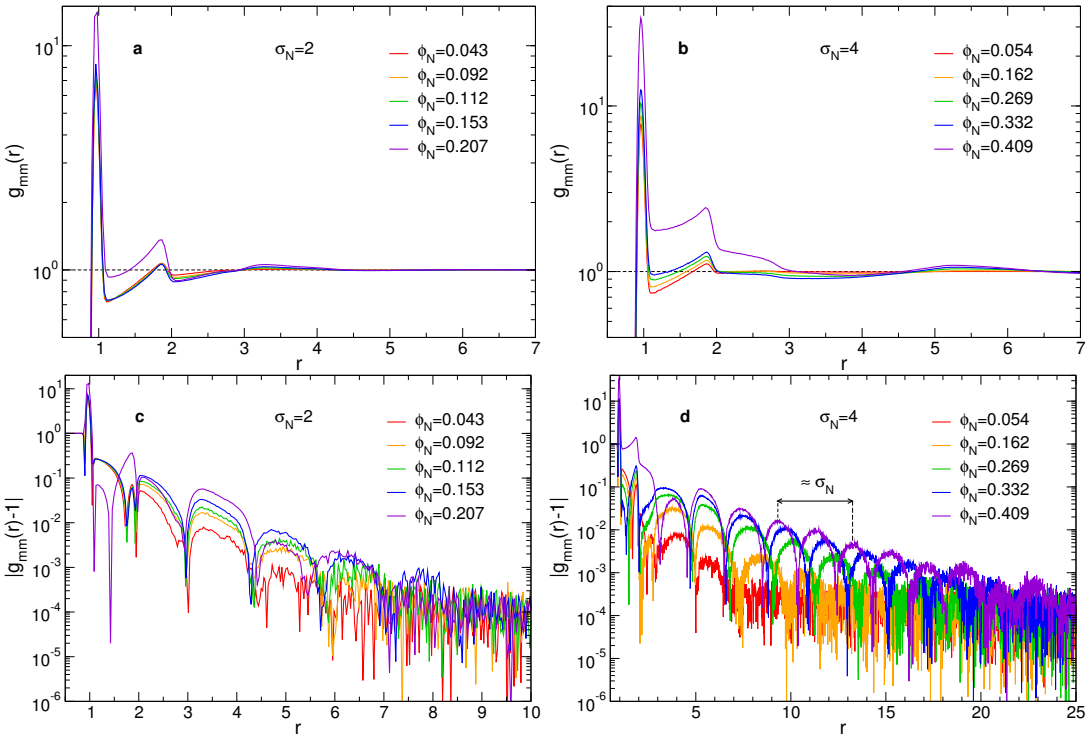

Figura 33 – Monomer-monomer radial distribution function for $\sigma_N = 2$ (a) and $\sigma_N = 4$ (b) and different values of the NP volume fraction ϕ_N.

Since $g_{mm}(r)$ is dominated by the two peaks at r_b and $2r_b$ and shows only very small fluctuations around $g_{mm}(r) = 1$ at larger r, we plot in Figs. 33c-d the function $|g_{mm}(r) - 1|$, hence allowing to detect more easily the structure at large r. For $\sigma_N = 4$, Fig. 33d, $|g_{mm}(r) - 1|$ shows very clearly at intermediate and high ϕ_N a long-range modulation with typical wavelength σ_N, due to the presence of the NPs[d] (compare to Fig. 30). For $\sigma_N = 2$, the presence of this modulation is less clear, because the size of the NPs is close to the monomer size and as a consequence the signal coming from the NPs cannot be distinguished well from the one coming from the monomers themselves.

5.3.2 *Structure factor*

In Fig. 34 we report the monomer-monomer structure factor, $S_{mm}(q)$. Figure 34a, shows $S_{mm}(q)$ for $\sigma_N = 4$. At $\phi_N = 0$ (pure polymer solution), there is a small peak at $q^* \simeq 1.4$ (inset of Fig. 34a), which in real space corresponds to a distance $r^* = 2\pi/q^* \simeq 4.5$. As this peak reveals the presence of a typical length scale in the system[250], one could be tempted to associate r^* to the geometrical mesh size ξ (see Sec. 3.2.2). However, an analysis of the PSD of the monomers $P_G(r)$ (we use here the definition of Gubbins instead of that of Torquato – see Chapter 8 for more details) reveals that the actual mesh size at $\phi_N = 0$, calculated as the average $\langle r \rangle_G$ of the PSD, is

[d] Note that, since we have taken the absolute value, the wavelength must be calculated as the distance between the nth peak and the $(n+2)$th.

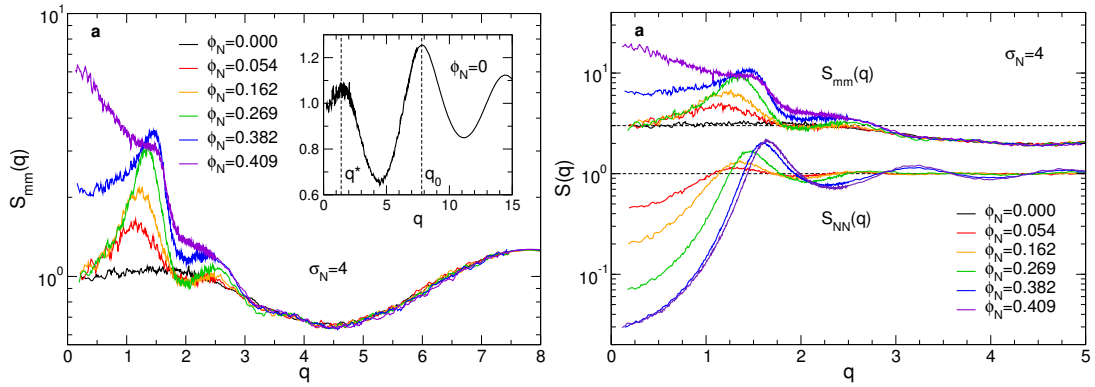

Figura 34 – (a) Monomer-monomer structure factor $S_{mm}(q)$ (log-lin scale) at different NP volume fractions for $\sigma_N = 4$. *Inset*: $S_{mm}(q)$ in the pure polymer solution (linear scale) (b) Comparison between the structure factors of monomers and NPs for $\sigma_N = 4$. For clarity, the curves representing $S_{mm}(q)$ have been shifted up by a factor of 3.

$$\xi_0 \equiv \xi(\phi_N = 0) = 1.04, \tag{156}$$

as shown in Fig. 35. We note that this means that the average *diameter* of the pores is $2\xi_0 = 2.08$[e]. Although ξ_0 and r^* are of the same order of magnitude, the information given by the PSD is much more precise than that given by the structure factor, since the signal at $q^* \simeq 1.4$ results from the superposition of many *a priori* unknown contributions. More details about the estimation of the geometrical mesh size will be given in Chapter 8.

The main peak of $S_{mm}(q)$ is at $q_0 \simeq 7.8$, which is close to $2\pi/r_b = 6.5$, where $r_b = 0.96$ is the average monomer-monomer bond length. For $\phi_N > 0$, the spatial arrangement of the NPs starts to be visible as a modulation in $S_{mm}(q)$, with a main peak appearing approximately at the same wavevector as the main peak of $S_{NN}(q)$, as we can see from Fig. 34b, where $S_{mm}(q)$ is compared to $S_{NN}(q)$. At even higher NP volume fraction, a signal starts to appear at $q = 0$, due to the fact that the polymers are getting far from each other (see Fig. 28d). If ϕ_N was increased even more, eventually the monomer volume fraction would become smaller than the overlap volume fraction (dilute regime) and $S_{mm}(0)$ would saturate to N (see Sec. 3.3.2).

5.3.3 *Single chain radial distribution function*

The structure of the individual polymer chains can be characterized by the function

$$p(r) \equiv \frac{4\pi r^2 \rho g_1(r)}{(N-1)}, \tag{157}$$

where $\rho g_1(r)$ is obtained by applying Eq. (34) to a single polymer chain. The quantity $p(r)\mathrm{d}r$ represents the probability to find a monomer belonging to the same chain at distance between

[e] The PSD, and thus the value of ξ, will in general change when ϕ_N is increased. However, this behavior has not been studied for the simulated systems. We expect, however, that in the presence of well-dispersed NPs of diameter $\sigma_N > 2\xi_0$, ξ will increase. This behavior is likely reversed in the presence of NPs of diameter $\sigma_N < 2\xi_0$, as one can also deduce from the fact that adding well-dispersed NPs of diameter $\sigma_N = 1$ to the system causes a decrease of the system's volume (see Sec. 5.5).

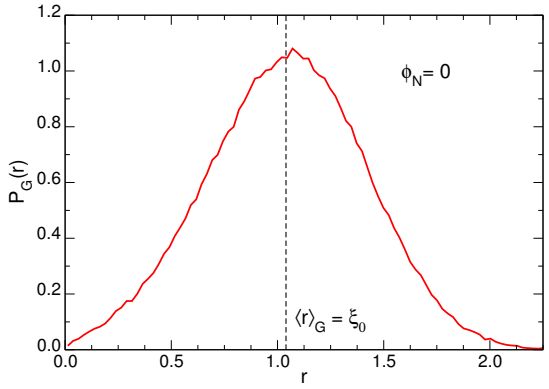

Figura 35 – Pore size distribution of the neat system ($\phi_N = 0$), calculated using Gubbins's definition (see Chapter 8). $\langle r \rangle_G = \xi_0 = 1.04$ is the mean value (geometrical mesh size).

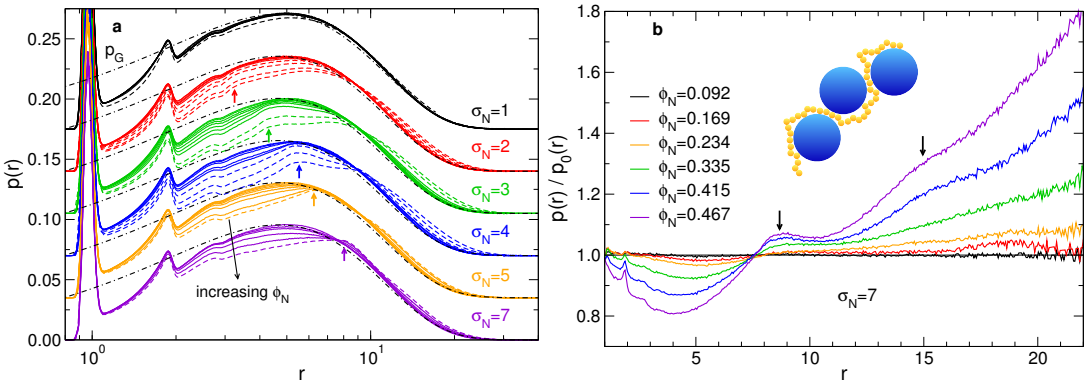

Figura 36 – (a) The function $p(r)$ for different values of the NP diameter σ_N and volume fraction ϕ_N. Continuous lines: good NP dispersion. Dashed lines: poor NP dispersion. Dash-dotted lines: Gaussian chain approximation $p(x) = p_G(x)$ with $R_g = R_g(\phi_N = 0)$. The long black arrow indicates the direction of increasing ϕ_N. The small arrows indicate the "bump" at $r \simeq \sigma_N + 1$. For the sake of clarity, for $\sigma_N \leq 5$ every set of curves has been shifted upwards with respect to the previous set by 0.035. (b) The ratio $p(r)/p_0(r)$ for $\sigma_N = 7$ and different values of ϕ_N. The small arrows help locating the two "bumps" at $r \simeq \sigma_N + 1$ and $2(\sigma_N + 1)$. Cartoon: schematic representation of the polymer structure in the presence of the NPs.

r and $r + \mathrm{d}r$ from a given monomer.

For a Gaussian chain, p has the following expression[30]:

$$p(x) = p_G(x) \equiv \frac{8Nx}{\sqrt{\pi}(N-1)R_g} \left[\frac{\sqrt{\pi}}{2}(1+2x^2)\mathrm{erfc}(x) - xe^{-x^2} \right], \tag{158}$$

where $x = r/2R_g$ and $\mathrm{erfc}(x)$ is the complementary error function[251]. This probability density peaks at $r \simeq 0.74R_g$[30].

In Fig. 36a, we show $p(r)$ for different values of σ_N and ϕ_N, along with p_G for a Gaussian chain, Eq. (158), with $R_{g0} = R_g(\phi_N = 0)$ (dash-dotted line). The dashed lines correspond to systems with poor NP dispersion, while the continuous lines correspond to systems with good NP dispersion. We observe that, for small ϕ_N, p_G provides a good approximation of p at intermediate and large r (at small r, $p(r)$ is dominated by excluded volume interaction between nearest neighbors). For all values of ϕ_N, $p(r)$ shows a very high peak at $r \simeq r_b =$

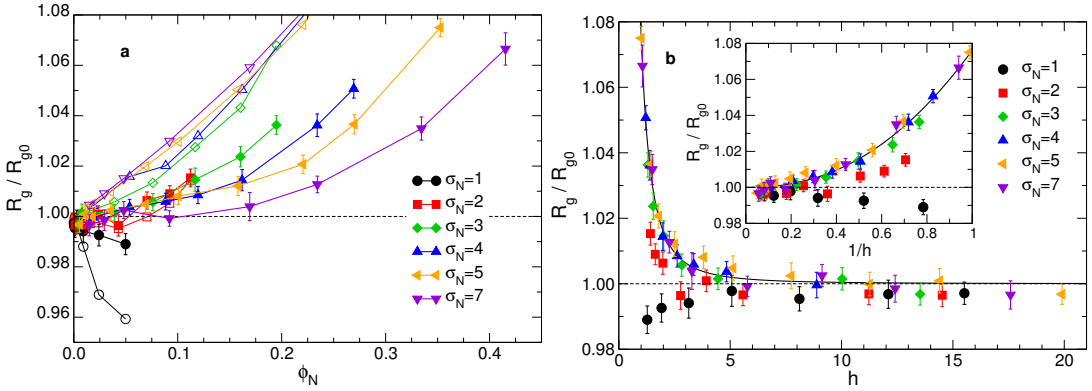

Figura 37 – Reduced radius of gyration of the polymers as a function of the NP volume fraction ϕ_N (a) and of the interparticle distance h (b). Open symbols in (b): $(V/V_0)^{1/3}$. *Inset*: R_g/R_{g0} as a function of the inverse interparticle distance $1/h$. Continuous lines: Eq. (162).

0.96, corresponding to the first nearest neighbor, and a smaller peak at $r \simeq 2r_b = 1.92$, corresponding to the second nearest neighbor. For values of r larger than $2r_b$, this signal gets washed out, and ultimately $p(r)$ decays to zero. When ϕ_N increases, we observe two effects: The third nearest neighbor peak becomes more pronounced and the curve becomes broader. This indicates that the presence of the NPs stretches the chains, causing them to become locally more ordered.

We also note that $p(r)$ shows a modulation of wavelength $\simeq \sigma_N + 1$, the first peak of which is clearly visible in Fig. 36a as a "bump" at $r \simeq \sigma_N + 1$ (colored arrows). The presence of this modulation can be better appreciated by plotting the ratio $p(r)/p_0(r)$, where $p_0(r) = p(\phi_N = 0, r)$. In Fig. 36b, we report $p(r)/p_0(r)$ for $\sigma_N = 7$: As we can see, the effect of the NPs is to produce a "hole" in the range $0 \lesssim r \lesssim \sigma_N + 1$, but also to stretch the chain, increasing $p(r)$ significantly at larger distances. The modulation is clearly visible, with two bumps appearing at $r \simeq \sigma_N + 1$ and $2(\sigma_N + 1)$ (small arrows). As discussed in Sec. 4.1.2, chain swelling in the presence of small NPs ($\sigma_N < 2R_g$) has already been predicted theoretically [164] and observed in both simulations [152] and experiments [140,159,161].

5.3.4 *Radius of gyration*

In order to quantify the expansion of the chains, we measure the radius of gyration $R_g = \sqrt{\langle r_g^2 \rangle}$, where $\langle r_g^2 \rangle$ was defined in Eq. (12). In the pure polymer solution, we have

$$R_{g0} \equiv R_g(\phi_N = 0) = 6.28 \pm 0.02. \tag{159}$$

In Fig. 37a we present the reduced radius of gyration R_g/R_{g0} as a function of NP volume fraction for different values of σ_N. With the exception of $\sigma_N = 1$, there is a modest but clear increase of R_g/R_{g0} with increasing NP volume fraction. Assuming that the expansion of the chain's pervaded volume is uniform and identical to that of the system's volume, we would obtain

$$\frac{R_g}{R_{g0}} = \left(\frac{V}{V_0}\right)^{1/3} \tag{160}$$

where $V_0 = V(\phi_N = 0)$ is the volume of the neat system. This quantity is reported in Fig. 37a (open symbols): One can see that for $\sigma_N > 2$ the observed expansion is significantly smaller than what predicted by this simple assumption, confirming that the chains do not expand uniformly but rather are stretched, as discussed in the previous section. Only for $\sigma_N = 2$ the approximation of Eq. (160) predicts the chain's expansion to a good approximation.

Fig. 37a also shows that for $\sigma_N = 1$, R_g *decreases* with increasing NP volume fraction. The reason is that NPs of this size have the largest surface-to-volume ratio, making the monomer-NP interaction (which scales approximately with the NP surface) very relevant. The consequence is that while in this range of ϕ_N the effect of the excluded volume is small, the effect of the interaction is large: Small NPs produce an effective attractive interaction between the monomers, which results in a decrease of R_g and of the overall monomer volume fraction ϕ_m (we recall that all the simulations were performed at the same average pressure $P = 0.1$; see also Sec. 5.5). We can therefore say that in this range of ϕ_N, the NPs of size $\sigma_N = 1$ act like a poor solvent, promoting chain contraction.

We note that for $\sigma_N > 1$, the increase of R_g is stronger, at fixed volume fraction, for smaller NPs. This behavior can be rationalized by plotting R_g as a function of the interparticle distance h, as shown in Fig. 37b. We observe that for $\sigma_N \geq 3$, the data fall on a master curve, which can be approximated by the empirical expression (continuous line in Fig. 37b)

$$\frac{R_g}{R_{g0}} = 1 + 0.0762 \cdot h^{-2.26}. \tag{161}$$

Approximating h with the expression of Eq. (152), one obtains

$$\frac{R_g}{R_{g0}} \simeq 1 + 0.0762 \cdot \left\{ \sigma_N \left[\left(\frac{\phi_N^{\mathrm{M}}}{\phi_N} \right)^{1/3} - 1 \right] \right\}^{-2.26}. \tag{162}$$

From Eq. (162), we see that at fixed ϕ_N, the increase of R_g will be larger for smaller σ_N. The fact that the behavior of R_g is captured by the interparticle distance h means that for $\sigma_N \geq 3$ chain expansion is a purely geometrical effect, dominated by excluded volume: the NPs force the chains to take less tortuous paths, therefore increasing their effective size. For $\sigma_N = 1$ and 2 the data do not fall on the master curve, for the reasons explained above (high surface-to-volume ratio promotes chain contraction). To provide a better resolution for small values of h, in the inset of Fig. 37b we plot R_g/R_{g0} as a function of $1/h$[164].

We can summarize our results by saying that NPs of size $\sigma_N \geq 2$ act like a good solvent, swelling the polymer chains, while NPs of size $\sigma_N = 1$ act like a poor solvent, causing them to contract. We note that this effect is expected to depend on the strength of the monomer-NP interaction: With stronger interactions, chain contraction could be observed also for $\sigma_N > 1$. Further study is needed in order to clarify this point.

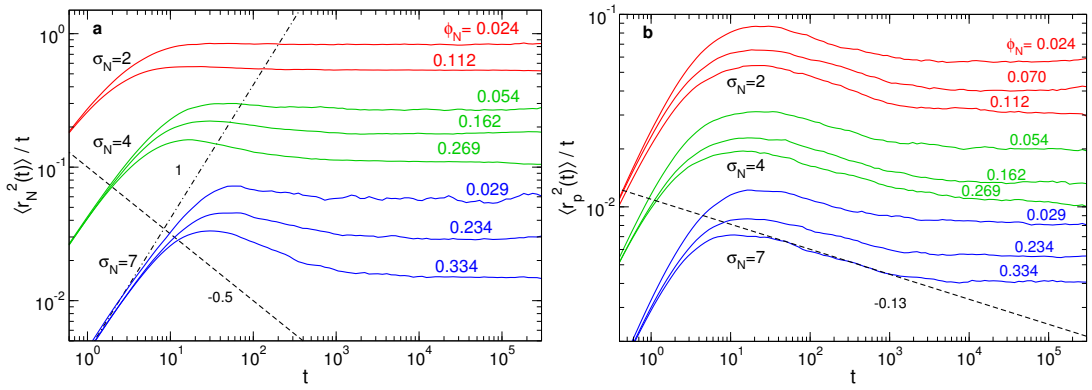

Figura 38 – (a) MSD of the NPs divided by time. Dashed line: $\langle r^2(t)\rangle/t \propto t^{-1/2}$, predicted by the CPR theory (Sec. 4.2.2) for the subdiffusive regime of intermediate size NPs. Dash-dotted line: $\langle r^2(t)\rangle/t \propto t$ (ballistic regime). The curves for $\sigma_N = 7$ have been shifted downwards by a factor 2 to facilitate the visualization. (b) MSD of the centers of mass of the chains divided by time. Dashed line: $\langle r^2(t)\rangle/t \propto t^{-0.13}$, i.e., $\langle r^2(t)\rangle \propto t^{0.87}$ (subdiffusive transient). The curves for $\sigma_N = 4$ have been shifted down by a factor 2 and those for $\sigma_N = 7$ by a factor 8 for clarity.

5.4 DYNAMICS

5.4.1 *Mean squared displacement*

To characterize the dynamics of the system, we study the mean squared displacement (MSD) of the NPs and of the centers of mass (CM) of the chains, which we denote respectively $\langle r_N^2(t)\rangle$ and $\langle r_p^2(t)\rangle$ (see Eqs. (53) and (57)).

In order to clearly identify the transition between the short-time ballistic regime, $\langle r^2(t)\rangle \propto t^2$, and the long time diffusive regime, $\langle r^2(t)\rangle \propto t$, we show in Fig. 38 the MSD divided by time t for the NPs (Fig. 38a) and for the polymers (Fig. 38b). At low ϕ_N, the motion of the NPs shows the same qualitative behavior for all the values of the NP diameter σ_N (Fig. 38a): After the initial ballistic regime, the motion becomes almost immediately diffusive, with the exception of the system with $\sigma_N = 7$, which shows a weak subdiffusive transient, $\langle r^2(t)\rangle \propto t^\beta$ $(0 < \beta < 1)$, between these two regimes. A clear transient subdiffusive regime appears between the ballistic and diffusive regimes at intermediate and high values of ϕ_N. The MSD of the chains, on the other hand, shows a weak subdiffusive transient for all values of ϕ_N and σ_N, with an exponent $\beta \simeq 0.87$ that is not much influenced by the value of ϕ_N (Fig. 38b). This transient, which is most likely due to non-Gaussian dynamics caused by intermolecular correlations[47], has been previously observed in experiments[45–47] and simulations[21,45,47–49,252] of polymer melts, where the measured subdiffusive exponent was $\beta \simeq 0.8$. The fact that in our case the exponent is slightly larger than 0.8 is likely due to the fact that the density considered here is significantly smaller than that of a melt, $\rho \simeq 0.85$. The different regimes (ballistic, subdiffusive, diffusive) and the transitions between them can also be studied systematically through the following quantity, which represents the slope of the MSD in a log-log scale and is a generalization of the subdiffusive exponent β:

$$\beta_\alpha(t) \equiv \frac{\mathrm{d}\log\langle r_\alpha^2(t)\rangle}{\mathrm{d}\log t} = \frac{t}{\langle r_\alpha^2(t)\rangle}\frac{\mathrm{d}\langle r_\alpha^2(t)\rangle}{\mathrm{d}t} \tag{163}$$

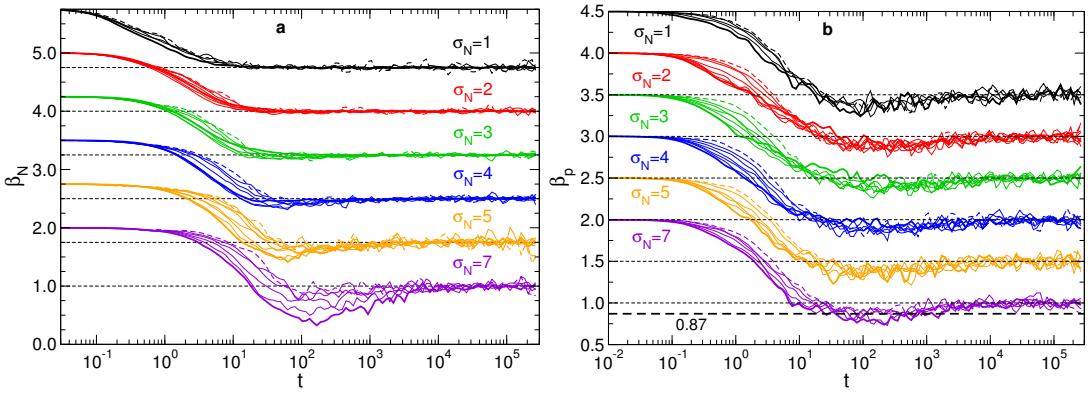

Figura 39 – Slope of the MSD in log-log scale, β_α (Eq. (163)), for the centers of mass of the NPs (a) and for the polymers (b). For the sake of clarity, for $\sigma_N < 7$ every set of curves has been shifted with respect to the previous one, by 0.5 in (a) and by 0.75 in (b). Different curves in the same set correspond to different NP volume fractions ϕ_N. The dashed curves correspond to the lowest ϕ_N, while the thick continuous curves correspond to the highest ϕ_N.

In Fig. 39a we report β_N. As discussed above, the dynamics of the NPs is more strongly influenced by the values of ϕ_N and σ_N than that of the polymers. For $\sigma_N = 5, 7$, we can observe a subdiffusive transient ($\beta_N < 1$) appearing very clearly at intermediate times. For $\sigma_N < 5$, the effect is much smaller. In Fig. 39b we show β_p for the simulated systems. The presence of the transient subdiffusive regime with $\beta_p \simeq 0.87$ is clearly visible. The dynamics of the polymers becomes again diffusive ($\beta_p = 1$) after a time $t \simeq 10^4$, which we identify with the relaxation time of the chain[5]. We can observe that β_p is not much affected by the NP volume fraction ϕ_N and size σ_N.

We now compare our results with the CPR scaling theory (Sec. 4.2.2). Since at low NP volume fraction in our system $\xi \simeq \xi_0 \simeq 2$, based on the predictions of CPR theory one expects the MSD of the NPs of diameter $\sigma_N \gtrsim 2$ to show subdiffusive behavior with exponent $\beta = 1/2$ at small ϕ_N. However, no such behavior is observed for any value of σ_N (Fig. 38). For small NPs, this may be due to the fact that the time window in which the subdiffusive behavior is expected to be present, i.e., $\tau_\xi < t < \tau_{\sigma_N}$, is too small, since $\tau_{\sigma_N} \propto \tau_\xi (\sigma_N/\xi)^4$. For larger NPs, this time window regime should be large enough to observe subdiffusion, and indeed for $\sigma_N = 7$ we observe a very weak subdiffusive transient, but the exponent β is close to 1 (Fig 38a). This is in agreement with previous simulations, which have also found that β is not always equal to $1/2$ in the subdiffusive regime, but rather gradually approaches this value as σ_N is increased[229].

5.4.2 *van Hove function*

In order to investigate the heterogeneity of NP dynamics, we study the van Hove function $G(\mathbf{r}, t)$[1], which is the real-space counterpart[f] of the intermediate scattering function introduced in Sec. 3.4.4. The van Hove function can be written as the sum of a self and a distinct part: $G(\mathbf{r}, t) = G_s(\mathbf{r}, t) + G_d(\mathbf{r}, t)$, where

[f] The two quantities are related by a Fourier transform: $F(\mathbf{q}, t) = \int G(\mathbf{r}, t) e^{-i\mathbf{q}\cdot\mathbf{r}} d\mathbf{r}$.

$$G_s(\mathbf{r},t) = \langle \delta[\mathbf{r} - \mathbf{r}_k(t) + \mathbf{r}_k(0)] \rangle \tag{164}$$

and

$$G_d(\mathbf{r},t) = \frac{1}{M} \sum_{\substack{k=1 \\ j \neq i}}^{M} \langle \delta[\mathbf{r} - \mathbf{r}_j(t) + \mathbf{r}_k(0)] \rangle. \tag{165}$$

The self part of the van Hove function represents the time-dependent spatial autocorrelation of a particle, while the distinct part represents the time-dependent spatial pair correlation. Since the system is isotropic, we will consider the spherical average of these two quantities: $G_s(r,t)$ and $G_d(r,t)$. The function $4\pi r^2 G_s(r,t)$ represents the probability to find a particle at time t a distance r from its original position. We note that $G_s(\mathbf{r},0) = \delta(\mathbf{r})$ and $G_d(\mathbf{r},0) = \rho g(\mathbf{r})$, where $g(\mathbf{r})$ is the pair correlation function[1].

For both small and large values of t, the self part of the van Hove function is a Gaussian[1]:

$$G_s(r,t) = \Gamma_s(r,t) = \left(\frac{3}{2\pi \langle r^2(t) \rangle} \right)^{3/2} \exp\left(-\frac{3r^2}{2\langle r^2(t) \rangle} \right). \tag{166}$$

We can therefore define a rescaled self van Hove function which also preserves the probability with the following change of variables:

$$\begin{aligned} r' &= r \cdot \left(\frac{3}{2\langle r^2(t) \rangle} \right)^{1/2} \\ G_s' &= G_s \cdot \left(\frac{3}{2\langle r^2(t) \rangle} \right)^{-3/2} \end{aligned} \tag{167}$$

If G_s is Gaussian, the result of the transformation (167) is

$$\Gamma_s'(r') \equiv \pi^{-3/2} e^{-r'^2}, \tag{168}$$

i.e., the distribution is independent of time.

In Fig. 40a, we show the rescaled van Hove function for the case $\sigma_N = 1, \phi_N = 0.05$ (but for other parameters we find the same qualitative behavior). In Fig. 40b, we report the ratio between the rescaled self van Hove function $G_s'(r,t)$ of the NPs and the same quantity in the Gaussian approximation $\Gamma_s'(r,t)$, for the same system. We observe that the shape of $G_s'(r,t)$ at short and long times is indeed very close to a Gaussian ($G_s'(r,t) = \Gamma_s'(r,t)$), and that the largest deviation from Gaussian behavior occurs when the dynamics of the NPs starts to be diffusive (in this case, at $t \simeq 1$). These deviations are found to be most pronounced at large r, i.e., the NPs move a bit further than expected from a Gaussian approximation.

To better quantify how dissimilar $G_s(r,t)$ is from a Gaussian, it is customary to define a non-Gaussian parameter[253],

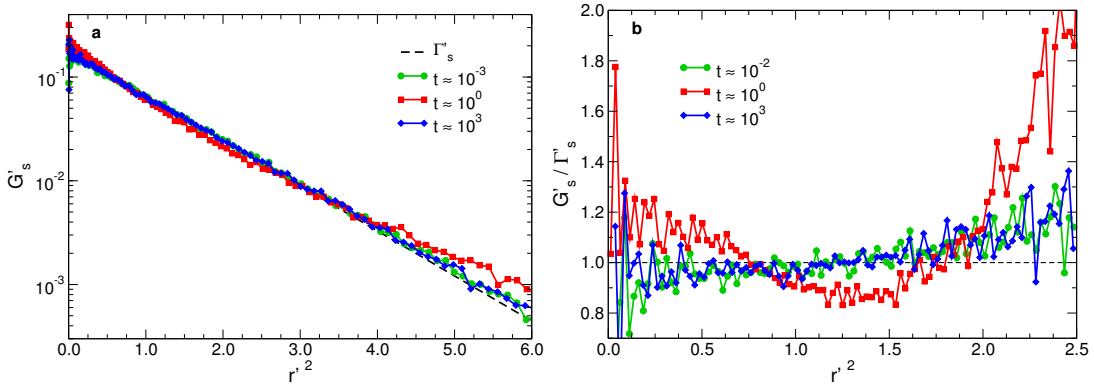

Figura 40 – (a) Rescaled self part of the van Hove function as a function of r'^2 (Eqs.(164)-(167)) for $\sigma_N = 1, \phi_N = 0.05$ (b) Ratio between the rescaled self part of the van Hove function and the same quantity in the Gaussian approximation (Eq. (168)) for the same system.

$$\alpha_2(t) \equiv \frac{3\langle r^4(t)\rangle}{5\langle r^2(t)\rangle^2} - 1, \tag{169}$$

where

$$\langle r^n(t)\rangle \equiv \langle |\mathbf{r}(t) - \mathbf{r}(0)|^n\rangle = 4\pi \int_0^\infty G_s(r,t)\, r^{2+n} \mathrm{d}r. \tag{170}$$

If $G_s(r,t)$ is Gaussian, Eq. (166), we have $\alpha_2 = 0$. Therefore, high values of $|\alpha_2|$ indicate a significant non-Gaussian behavior.

In Fig. 41, we show $\alpha_2(t)$ of the NPs for several values of the NP diameter σ_N and of the NP volume fraction ϕ_N. The largest departure from Gaussian behavior happens when the dynamics of the NPs starts to be diffusive, in agreement with what is observed from $G'_s(r,t)$. Both at short and long times $\alpha_2 \simeq 0$, as expected. We notice that the maximum deviation from Gaussian behavior (the maximum of the curves in Fig. 41) becomes larger when ϕ_N is increased. This trend shows that the structure of the surrounding polymer mesh and the presence of nearby NPs both contribute to the non-Gaussian behavior. Moreover, increasing the NP size at fixed ϕ_N generally reduces the magnitude of α_2. This is reasonable, since a large NP interacts with a large number of monomers and other NPs and thus "feels" an averaged interaction, which results in a reduction of the dynamical fluctuations and therefore of α_2. One exception to this trend is $\sigma_N = 7$ at high NP volume fraction (Fig. 41d). However, the reason for this is likely that the system is approaching crystallization (see Sec 5.5). Apart from the case $\sigma_N = 7, \phi_N = 0.467$, we always have $|\alpha_2| < 0.2$, and we can therefore state that the dynamics of the NPs is, to a good approximation, Gaussian. The non-Gaussian parameter of the polymer chains (not shown) always satisfies $|\alpha_2| < 0.1$, therefore also the dynamics of the polymers is approximately Gaussian. We also mention that in this case no clear dependence of α_2 on ϕ_N and σ_N is observed.

Finally, we show in Fig. 42 the distinct part of the van Hove function, $G_d(r,t)$, of the NPs for some selected systems. The relaxation happens in a way which is very similar to that observed in simple, non-supercooled liquids[253], in that we observe that in all cases the correlation hole at $r = 0$ is slowly filled as t is increased. Since there is no evidence for the

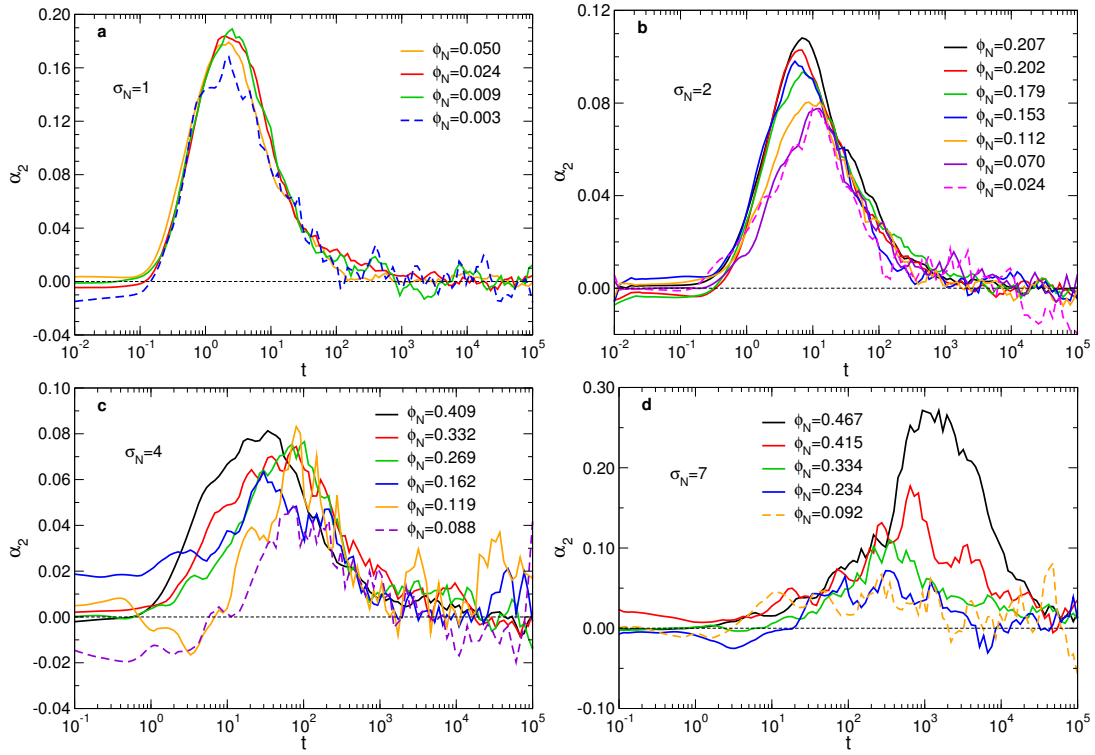

Figura 41 – Non-Gaussian parameter α_2, Eq. (169), for various NP diameters σ_N and NP volume fractions.

presence of a peak at $r = 0$, we conclude that hopping dynamics is absent in the studied systems[254].

5.4.3 *Polymer diffusion*

In order to make a more quantitative characterization of the dynamical properties of the polymers and the NPs as a function of NP diameter σ_N and volume fraction ϕ_N, we now focus on the self diffusion coefficient D (which for simplicity we will refer to as "diffusion coefficient"), which can be obtained from the MSD through Einstein's relation, Eq. (54).

It is known that measurements of D in systems with periodic boundary conditions suffer from finite-size effects because of long-ranged hydrodynamic interactions[255,256]. Although an analytical expression for the correction to D is available[255,256], it is not evident whether it can be applied to the motion of polymer chains and NPs in a concentrated polymer solution. For the NPs, such an expression is most likely not adequate when, as in our case, the NP size is smaller than the polymer size[77]. Therefore, for consistency we choose not to apply any finite size correction to the measured diffusion coefficients.

In the pure polymer system ($\phi_N = 0$), the diffusion coefficient of the CM of the chains is $D_{p0} = (1.14 \pm 0.02) \cdot 10^{-2}$. In Fig. 43a we plot the reduced diffusion coefficient of the polymer chains D_p/D_{p0} as a function of the NP volume fraction ϕ_N. We can observe that D_p/D_{p0} decreases with increasing NP volume fraction, with the decrease being stronger, at fixed ϕ_N, for smaller NPs. The data can be fitted to the empirical functional form[g]

[g] No particular physical meaning should be attributed to this functional form, which is only chosen for mathematical convenience.

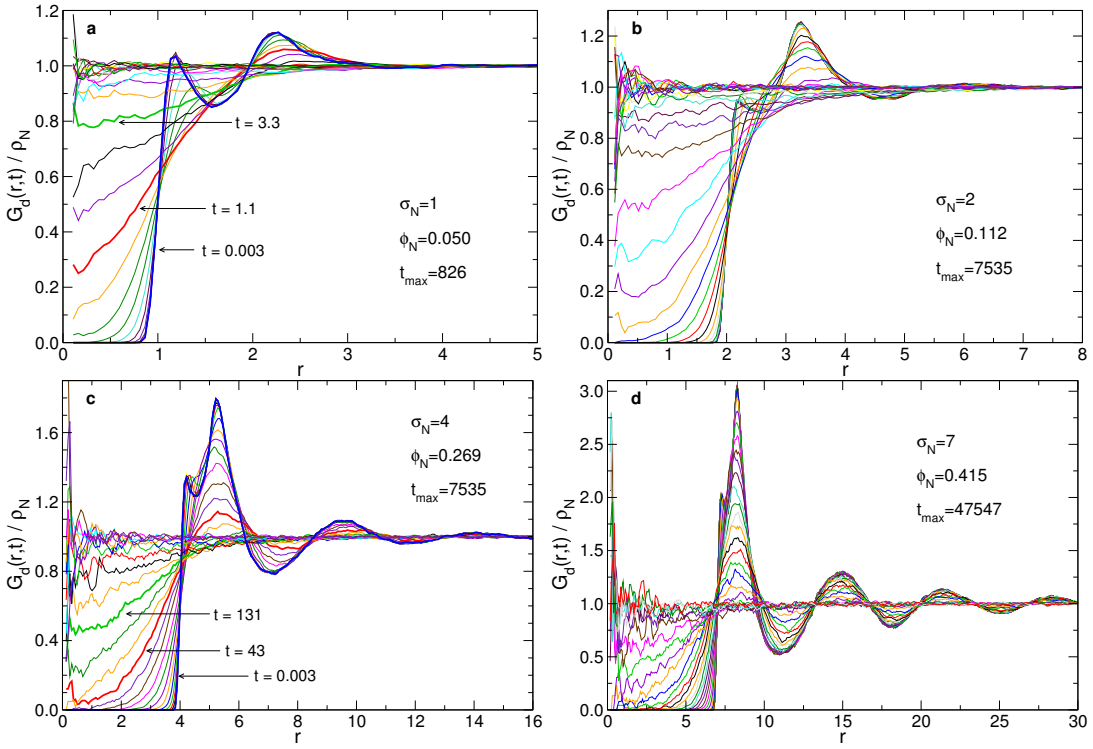

Figura 42 – Distinct part of the van Hove function, Eq. (165), for some selected systems. The curves are equally spaced in logarithmic time (t). In (a) and (c), we have indicated some of the t values associated to the curves. The minimum value of t is for all the figures $t_{\min} = \delta t = 0.003$ (integration time step), while the maximum value, $t_{\max}$, is reported in the legend.

$D_p = D_{p0}[1 - (\phi_N/\phi_{N0})^{\alpha}]$, where α increases weakly with NP size. By using this relation, we can interpolate between the data points and plot D_p/D_{p0} as a function of the NP diameter σ_N for different volume fractions (Fig. 43b) and we observe that D_p/D_{p0} increases monotonically with σ_N at fixed ϕ_N. There are two possible causes (or a combination of the two) that can lead to the slowing down of the chains with increasing NP volume fraction: the increase of the number of obstacles to polymer motion and the increase of polymer-NP interfacial area, which, since the interaction between polymers and NPs is attractive, can result in a reduced chain mobility. A predominance of the first effect would imply that the slowing down of the polymers is a mostly entropic effect, while if the second effect is the most important the dynamics of the polymers is mainly controlled by enthalpy.

Composto and coworkers[137,141,157,205] observed a similar slowing down of chain motion in a series of experimental studies on polymer nanocomposites containing large NPs ($\sigma_N \gtrsim 2R_g$). They found that the reduced diffusion coefficient of the polymers falls on a master curve when plotted *versus* a "confinement parameter", defined as $h/2R_g$, where h is the interparticle distance, which the authors computed using Eq. (152) with $\phi_N^{\mathrm{M}} = 2/\pi$ (see Sec. 4.3.1). Since the collapse of the data was independent of the strength of the polymer-NP interaction[141], the authors concluded that the slowing down of the polymers is entropic in origin, caused by the reduction of chain entropy as the chain passes through bottlenecks formed by neighboring NPs (entropic barrier model)[137]. An analogous reduction in polymer mobility due to the presence of NPs was observed by Li *et al.*[215] in molecular dynamics simulations of

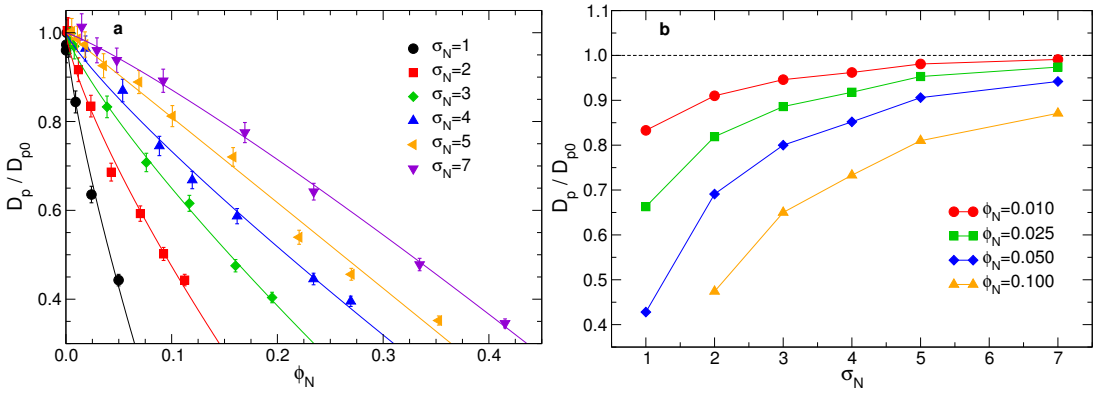

Figura 43 – (a) Reduced diffusion coefficient of the centers of mass (CM) of the chains D_p/D_{p0} as a function of NP volume fraction, where $D_{p0} = D_p(\phi_N = 0)$. Continuous lines: empirical fits with the functional form $D_p = D_{p0}[1 - (\phi_N/\phi_{N0})^{\alpha}]$. The values of ϕ_{N0} are 0.10, 0.23, 0.36, 0.47, 0.52, 0.59, and the values of α are 0.76, 0.77, 0.81, 0.85, 1.00, 1.15 respectively for $\sigma_N = 1, 2, 3, 4, 5, 7$. (b) D_p/D_{p0} as a function of NP diameter σ_N.

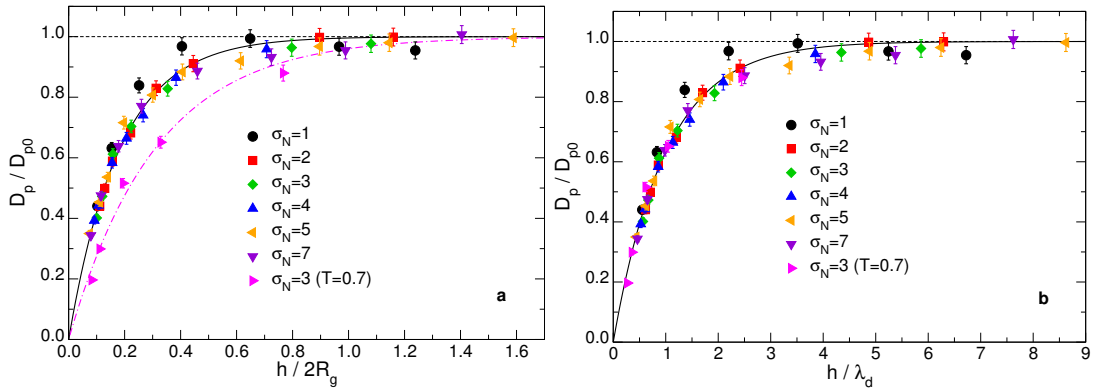

Figura 44 – Reduced diffusion coefficient of the centers of mass (CM) of the chains as a function of the static confinement parameter $h/2R_g$ (a) and of the dynamic confinement parameter h/λ_d (b) for different values of the NP diameter σ_N. Continuous and dash-dotted lines in (a): $D_p = D_{p0}[1 - \exp(-a \cdot h/2R_g)]$, with a respectively equal to 5.44 and to 3.22. Continuous line in (b): Eq. (171).

unentangled melts of short chains ($N = 35, \rho_m = 0.85$) containing repulsive NPs. The slowing down was weaker than that observed by Composto and coworkers in Refs. 137,205, an effect which the authors attributed to the absence of chain entanglements. Karatrantos *et al.*[199] also observed a monotonic decrease in the polymer diffusion coefficient with increasing NP volume fraction in molecular dynamics simulations of NPs in unentangled and weakly entangled melts, and attributed this phenomenon to the increase in the polymer-NP interfacial area. An enhancement of chain diffusivity at low ϕ_N has also been observed in simulations by Kalathi *et al.*[77], possibly because attractive monomer-monomer interactions were considered in their work. It is therefore clear that, despite the fact that some general trends can be identified, the dynamics of the polymers can depend strongly on the details of the system (see also Sec. 4.3.2).

Following Composto and coworkers[137,141,157,205], we plot in Fig. 44a the reduced diffusion coefficient of the chains as a function of the confinement parameter $h/2R_g$. We recall that in our case h is not defined by Eq. (152), but rather computed from the pore size distribution

(Sec. 5.2.3). In addition to the $T = 1.0$ data, we also show the results from simulations at $T = 0.7$ with $\sigma_N = 3$. The first observation is that, with the exception of $\sigma_N = 1$, all the $T = 1.0$ data fall on the same master curve, which is well approximated by the empirical expression $D_p = D_{p0}[1 - \exp(-ah/2R_g)]$, with $a = 5.44$ (continuous line in Fig. 44a). The fact that also in our case D_p/D_{p0} is only a function of the confinement parameter is rather surprising, since Composto and coworkers mainly considered NPs of size comparable to that of the polymers or larger, which could be considered as basically immobile[137,141,157,205], whereas in our case $\sigma_N < 2R_g$ and the NPs diffuse faster than the chains in almost all the systems considered, as it will be shown in Sec. 5.4.7.

We notice, however, two important differences: The first one is that while in our case the diffusion coefficient of the pure polymer solution ($D_p/D_{p0} = 1$) is recovered at $h/2R_g \simeq 1$, in Refs. 137,141,157,205 it is recovered only at much higher values of the confinement parameter, $h/2R_g \simeq 20$. Our finding is similar to what observed by Li *et al.*[215], who attributed the discrepancy between their data and those of Composto and coworkers to the absence of entanglement in their simulated system. The second difference is that the $T = 0.7$ data clearly do not fall on the same master curve. Since a decrease in temperature is approximately equivalent to an increase in the strength of the polymer-NP interaction, this result suggests that in our system the polymer-NP interaction plays a relevant role, in contrast with Ref. 141, where the authors concluded that the confinement parameter captures the polymer slowing down independently of the polymer-NP interactions. We propose in the following a possible solution to these discrepancies.

The confinement parameter $h/2R_g$ is a purely static quantity, which only depends on the spatial configuration of the polymers and the NPs in the system. However, there are several cases in condensed matter physics in which two systems with very similar structure show a completely different dynamics: A well-known example is that of the glass transition, where a supercooled liquid shows structural properties similar to those of a liquid at higher temperature, but completely different dynamical properties[244,257,258]. It seems therefore more appropriate to introduce a *dynamic confinement parameter* h/λ_d, where λ_d is a dynamic length scale which will in general depend on temperature, density and on the details of the system. We have already seen that the $T = 1.0$ data are well approximated by the function $D_p = D_{p0}[1 - \exp(-ah/2R_g)]$, with $a = 5.44$ (continuous line in Fig. 44a); the $T = 0.7$ data are well approximated by the same functional form, but with a different coefficient, $a = 3.22$. In light of what we discussed above, we make the hypothesis that the reduced diffusion coefficient of the polymers can be expressed as

$$D_p = D_{p0}\left[1 - \exp\left(-\frac{h}{\lambda_d(T)}\right)\right], \tag{171}$$

where we have explicitly reported the dependence of λ_d on temperature. Since R_g does not change more than 8% with respect to the pure polymer solution value R_{g0} (see Fig. 37), we can estimate λ_d as $\lambda_d = 2R_{g0}/a$: This gives $\lambda_d(1.0) = 2.31$ and $\lambda_d(0.7) = 3.90$. We show D_p/D_{p0} as a function of h/λ_d in Fig. 44b: In this plot, the data for different temperatures fall on the same master curve, showing that the dynamic confinement parameter h/λ_d is more successful than the "static" confinement parameter $h/2R_g$ in capturing the slowing down of the polymers (Fig. 44a). However, one question remains: What does the dynamic length scale λ_d represent exactly, and why does it increase when temperature is decreased? Our

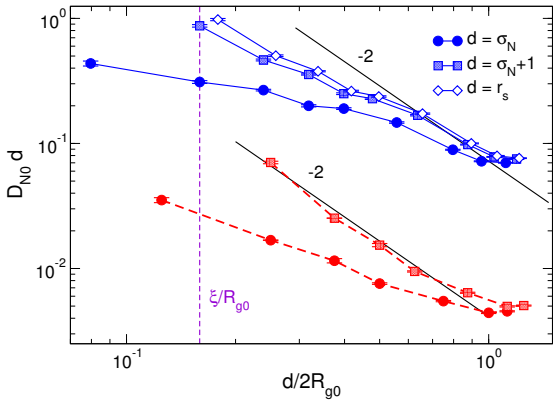

Figura 45 – Single NP diffusion coefficient multiplied by the effective hydrodynamic diameter of the NP d as a function of $d/2R_{g0}$ (blue symbols, above), compared with the results from Ref. 179 (red symbols, below). Circles: $d = \sigma_N$. Squares: $d = \sigma_N + 1$ Diamonds: $d = \sigma_h \simeq \sigma_N + 1.245$. Continuous lines: slope of -2. The dashed vertical line marks the value $\xi_0/R_{g0} \simeq 1/R_{g0} \simeq 0.16$.

answer is that λ_d is a cooperativity length scale, i.e., it represents the typical length scale of the spatial rearrangement needed for a polymer segment to escape its local cage. Similarly to what happens in a supercooled liquid[257,259], this cooperative length scale is expected to increase when T is decreased. In our system, an important role could also be played by the attractive polymer-NP interactions, which become more relevant when T is decreased and could reduce the mobility of polymer segments close to the polymer-NP interface. We also expect λ_d to increase with monomer density, since a higher density naturally leads to a locally more constrained dynamics: This could explain why the data of Li *et al.*[215], who simulate NPs in a dense melt, are compatible with a larger cooperativity length scale. Another factor that is expected to play a major role is the stiffness of the chain, with stiffer chains expected to lead to a larger λ_d.

To summarize, we propose a modification of the confinement parameter theory of Composto and coworkers[137,141,157,205]: our hypothesis is that the dynamics of the polymers is controlled by a dynamic confinement parameter h/λ_d, where λ_d is a cooperativity length scale which will depend in general on the thermodynamic parameters and on the details of the model. Further study is required to test the validity of this hypothesis, and to understand how λ_d depends on the properties of the physical system.

5.4.4 *Single nanoparticle diffusion*

The diffusion coefficient of a hard-sphere probe particle of diameter σ_N in a continuum solvent with shear viscosity η is given by the Stokes-Einstein equation[1]:

$$D_{N0} = \frac{k_B T}{f \pi \eta \sigma_N}, \tag{172}$$

where f is a number between 2 and 3 which depends on the choice of the hydrodynamic boundary conditions: $f = 2$ for pure slip and $f = 3$ for pure stick boundary conditions[176]. If the particle is not a perfect hard sphere, for example because its shape is not perfectly spherical

or because there is adsorption of solvent molecules on its surface, σ_N must be replaced with an effective hydrodynamic diameter σ_h [260,261]. As discussed in Sec. 4.2, Eq. (172) is inadequate to describe the motion of particles smaller than the polymer size in a polymer solution/melt, since the continuum assumption breaks down when the size of the probe particle becomes comparable to the characteristic length scale of the solvent. The mechanism behind the violation of the Stokes-Einstein relation has been discussed in detail in Sections 4.2.1, 4.2.2 and 4.2.3.

To test the validity of the Stokes-Einstein formula, Liu *et al.* [179] have used MD simulations to measure the single particle diffusion coefficient of NPs in a dense, unentangled melt ($N = 60, \rho_m = 0.84$). The results of their simulations are shown in Fig. 45 (red symbols, dashed lines). The authors argued that the effective hydrodynamic radius of the particle, $R_h = \sigma_h/2$, should have the value $R_h = (\sigma_N + 1)/2$, which would correspond to the contact distance between a NP and a monomer if they were hard spheres[h]. By fitting their data in the size range $\sigma_N < 2R_g$ with a power law $D_{N0} \propto R_h^{-\gamma}$, they found $\gamma \simeq 3$ (red squares in Fig. 45), and for diameters $\sigma_N > 2R_g$ they recovered the Stokes-Einstein relation. The results of Ref. 179 are therefore in agreement with the prediction that $D_{N0} \propto \sigma_N^{-3}$ (see Sec. 4.2) if one replaces the NP diameter σ_N with the effective hydrodynamic diameter $\sigma_h = \sigma_N + 1$. However, when plotting D_{N0} as a function of σ_N instead of $\sigma_N + 1$ and fitting with a power law $D_{N0} \propto \sigma_N^{-\gamma}$, one obtains instead $\gamma \simeq 2$ (red circles in Fig. 45). Hence one must conclude that the value of the exponent γ depends on the exact definition of the effective NP diameter, which makes the comparison of simulation data with theoretical predictions a delicate matter, especially when the size of the NP is of the same order of magnitude as the monomer size (for large NPs, $\sigma_N + 1 \simeq \sigma_N$).

Since the identification of $\sigma_N + 1$ with the effective hydrodynamic diameter is rigorously justified only for hard-sphere interactions, we propose instead to define σ_h from the monomer-NP radial distribution, $g_{Nm}(r)$ (see Fig. 30). As discussed in Sec. 5.2.1, for all the values of ϕ_N and σ_N, $g_{Nm}(r)$ displays a main peak at

$$r = \frac{r_s}{2} \equiv \frac{\sigma_N + (2^{7/6} - 1)}{2} \simeq \frac{\sigma_N + 1.245}{2} = \frac{\sigma_N}{2} + 0.622 \tag{173}$$

The position of this peak shows almost no change also when T is changed. Given the robustness of r_s, and the fact that it can be obtained directly by analyzing the configurations (with no assumption on the monomer-NP interaction potential) we propose to define the hydrodynamic diameter of the NPs as

$$\sigma_h = 2R_h \equiv r_s \simeq \sigma_N + 1.245 \tag{174}$$

The choice to define σ_h in this manner instead of simply using the value $\sigma_N + 1$ has implications which are, of course, more conceptual than practical, since the numerical values are very similar.

In order to test the theoretical predictions discussed above, we have performed additional simulations at low NP volume fraction ($\phi_N < 0.015$) for $\sigma_N = 10, 12$, and 14. In Fig. 45 we show $D_{N0}d$ as a function of $d/2R_g$, with d alternatively defined as σ_N, $\sigma_N + 1$ and r_s (blue

[h] The same argument can be found in Ref. 262.

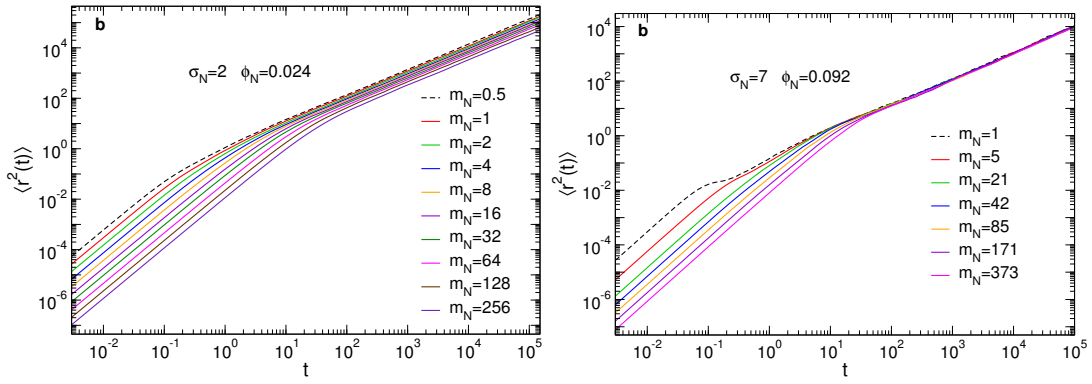

Figura 46 – Mean squared displacement of the NPs when varying the NP mass m_N at fixed diameter σ_N, in the case $\sigma_N = 2, \phi_N = 0.024$ (a) and $\sigma_N = 7, \phi_N = 0.092$ (b).

symbols, continuous lines). Also included are the data from Ref. 179 (red symbols, dashed lines). We can see that D_{N0} decreases continuously for $d < 2R_g$, whereas at $\sigma_h \simeq 2R_g$ Stokes-Einstein behavior, $D_{N0}d = \text{const.}$, is recovered. Taking $d = \sigma_N + 1$ or $d = r_s$, we find in the range $0.6 \lesssim d/2R_g \lesssim 1$ a slope of approximately -2, which agrees with the theoretical predictions. However, the range in which we observe this slope is rather small and hence we cannot claim that our data confirm the theory. However, a *caveat* is in order: We have verified that, as also reported in previous studies [177,179,217], the diffusion coefficient of small NPs decreases when the NP mass increases at fixed NP volume, i.e., when the mass density is increased. The effect becomes progressively weaker as σ_N is increased, and at $\sigma_N = 7$ no mass density dependence is observed. Nevertheless, this effect should be taken into account when comparing the results of simulations to those of experiments or to theoretical predictions. The mass dependence of polymer and NP diffusivities is discussed in detail in the next Section.

Another possibility is that the observed discrepancy between the data and CPR theory is due to the absence of hydrodynamic interactions in our simulations. In Ref. 229, the authors simulated polymer solutions containing spherical NPs using both Langevin dynamics and multi-particle collision dynamics (MPCD), which accounts for hydrodynamic interactions. They found that the agreement between the data and CPR theory is rather poor for the simulations employing Langevin dynamics, whereas it is almost perfect for the MPCD simulations.

5.4.5 *Mass dependence of NP and polymer diffusivities*

In previous studies of polymer nanocomposites [179,217] and binary soft-sphere liquids [177] it has been shown that outside of the Stokes-Einstein regime not only the diameter, but also the mass density of a particle can affect its dynamics. In order to study this effect, we performed some simulations at low NP volume fraction and changed the NP mass while leaving the diameter fixed. The results for the mean squared displacement (MSD) $\langle r^2(t) \rangle$ of the particles are reported in Fig. 46 for the cases $\sigma_N = 2, \phi_N = 0.024$ and $\sigma_N = 7, \phi_N = 0.092$. At short times, the motion of the particles is ballistic and the mass dependence of the MSD follows trivially from the equipartition theorem [263]:

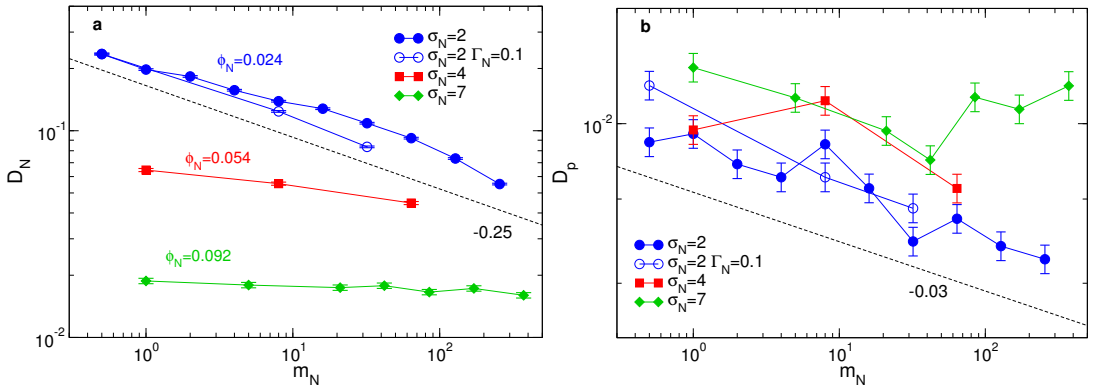

Figura 47 – Diffusion coefficient of the NPs (a) and of the polymers (b) when varying the NP mass m_N at fixed diameter σ_N. The values of the NP volume fraction ϕ_N are $0.024, 0.054$ and 0.092 respectively for $\sigma_N = 2, 4$ and 7. Open symbols: simulation without rescaling of the viscous friction coefficient Γ_N. Dashed lines: slopes -0.25 (a) and -0.03 (b). These slopes are reported only for reference.

$$\langle r_N^2(t)\rangle = \langle v_N^2\rangle t^2 = \frac{3k_BT}{m_N}t^2, \tag{175}$$

where $\langle v_N^2\rangle$ is the mean squared speed of the NPs. At longer times, when the motion becomes diffusive, i.e. $\langle r^2(t)\rangle \propto t$, we can observe a much more interesting effect: While the motion of the larger NPs is unaffected by a change in the mass (Fig. 46b), the motion of smaller NPs presents a clear mass dependence (Fig. 46a).

This result can be better appreciated in Fig. 47a, where we show the NP diffusion coefficient D_N as a function of the NP mass for different values of σ_N and ϕ_N (here also the case $\sigma_N = 4, \phi_N = 0.054$ is shown). One recognizes that the mass dependence of the diffusion coefficient becomes weaker when the NP diameter is increased, and for $\sigma_N = 7$ it has disappeared almost completely. The observation that the mass dependence of the long time diffusion coefficient is stronger for smaller particles is in agreement with previous studies[177,179].

Our interpretation of this result is that large particles are forced to wait for the polymers to relax in order to diffuse through the solution: The constraints on their motion are purely geometric, and mass plays no role. Smaller particles, on the other hand, can slip through the polymeric mesh; the probability that they find a passage to slip through in a certain time interval increases with their average velocity, which at equilibrium decreases as $m_N^{-1/2}$, as it follows from the equipartition of energy[263]: $\langle v_N^2\rangle = 3k_BT/m_N$. We expect this effect to be strongly suppressed when the polymer density is increased, and to be negligible for the motion of NPs of diameter $\sigma_N \gtrsim \sigma$ in a melt.

Although in Refs. 177,179 it was claimed that the mass dependence disappears for high values of m_N, in our case for $\sigma_N = 2$ there is no hint that the mass dependence vanishes for larger mass values. In the case of Ref. 177, however, the disappearance of the mass dependence for high values of the mass is only apparent, as it becomes clear once the data are plotted in double logarithmic instead of linear scale (not shown). We believe that this could also be the case for Ref. 179, since also there the data are only reported in linear scale. From the analysis of our data and of those of Ref. 177, it seems that not only the mass dependence does not disappear when m_N is increased, but on the contrary it becomes

stronger.

The diffusion coefficient of the polymer chains D_p is almost unaffected by changes in the NP mass density, as we can observe from Fig. 47b, although it is possible to see a very weak decrease of D_p for $\sigma_N = 2$. It is possible that the slowing down of the NPs has an effect on the dynamics of the polymers, but this effect is very weak at low NP concentrations. Further study should be dedicated to clarifying this point.

Finally, we have made some tests to determine whether the observed mass dependence is an artifact resulting from the scaling of the friction coefficient of the Langevin thermostat. To this aim, we ran some simulations where the friction coefficient of the NPs, Γ_N, was kept constant and equal to that of the monomers: $\Gamma_N = \Gamma_m = 0.1$. The result is included in Fig. 47 (open blue circles). One sees that the effect of mass density is still present, but using $\Gamma_N = 0.1$ (fixed) has the effect of reducing the diffusion coefficient of the NPs, as one expects since this means that more massive NPs experience a higher solvent viscosity (we recall that $\eta_s \propto \Gamma_N m_N / \sigma_N$).

In conclusion, we have shown that the effect of mass density on the dynamical properties should be taken into careful consideration when performing Langevin dynamics simulations of multi-component systems, such as polymer mixtures, binary fluids and solutions with explicit solvents. A possible way to avoid this effect may be to perform Brownian dynamics (Sec. 3.6.1) , in which inertial effects are absent by construction.

5.4.6 *Nanoparticle diffusion*

In the previous section, we have dealt with the motion of a single NP in the polymer solution, i.e., we have considered the dilute NP limit: We will now discuss the dynamics of NPs at higher NP volume fraction ϕ_N.

Only few simulation studies have considered high NP volume fractions. Liu *et al.*[179] have observed a reduction of the NP diffusion coefficient with increasing ϕ_N, and attributed the phenomenon to polymer-mediated interactions, i.e., to the formation of chain bridges between neighboring NPs that would hinder NP motion; it is not clear, however, what the typical lifetime of such bridges should be, and thus whether this explanation is correct. Karatrantos *et al.*[199] have observed a similar reduction in NP mobility and argued that it is due "*to both nanoparticle-polymer surface area and nanoparticle volume fraction*"[199], implying that pure geometry and polymer-NP attraction both play a role. The importance of polymer-NP interaction in NP dynamics is beyond dispute: Patti[226] showed that the diffusion coefficient of NPs in an unentangled melt decreases monotonically when the strength of the polymer-NP interaction is increased, with the decrease being stronger for smaller NPs. A monotonic decrease of NP diffusivity with the strength of the polymer-NP interaction was also observed by Liu *et al.*[179]. We mention, however, that this trend can be reversed (NP diffusivity *increasing* with increasing interaction strength) in strongly entangled systems, where the dynamics of the NPs is dominated by density fluctuations on length scales of the order of the tube diameter[187].

In Fig. 48a, we show the reduced diffusion coefficient of the NPs, D_N / D_{N0}, where D_{N0} is the diffusion coefficient of a single NP in the polymer solution, as a function of the NP volume fraction ϕ_N; also shown are data for $\sigma_N = 3$ and $T = 0.7$. Similarly to the diffusion coefficient of the chains, D_N decreases with increasing NP volume fraction. The decrease of D_N / D_{N0} with the NP volume fraction is rather quick: Already at the modest volume fraction

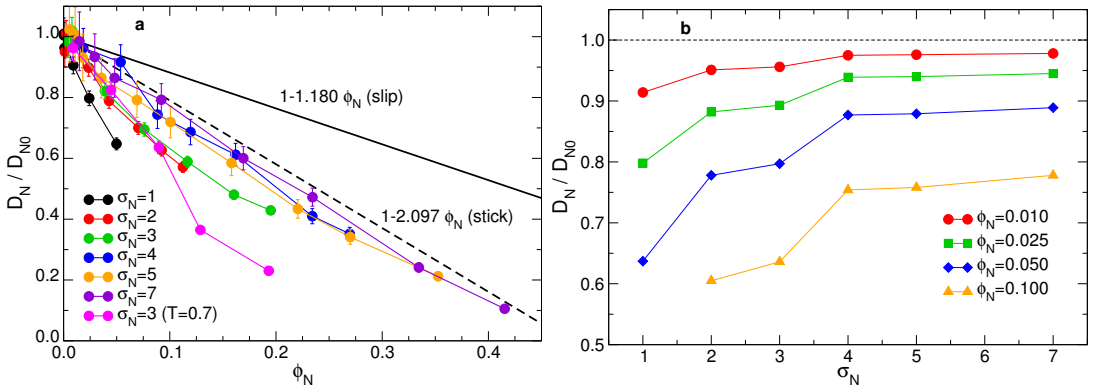

Figura 48 – Reduced NP diffusion coefficient as a function of the NP volume fraction ϕ_N (a) and of NP diameter σ_N (b). The continuous line and the dashed line in (a) represent Eq. (176), with $C = -1.180$ (slip BC) and $C = -2.097$ (stick BC), respectively.

of $\phi_N = 0.1$, the diffusion coefficient is reduced by $\simeq 40\%$ for NPs of diameter $\sigma_N = 2$ and 3, and by $\simeq 30\%$ for NPs of diameter $\sigma_N \geq 3$.

Cichocki and Felderhof[264] calculated the self diffusion coefficient of hard spheres performing Brownian motion in an incompressible fluid, finding for low ϕ_N

$$D = D_0(1 - C\phi_N), \tag{176a}$$

where C is a constant that has value $C = -2.097$ for pure stick boundary conditions (BC) and $C = -1.180$ for pure slip BC. We compare these predictions with our data in Fig. 48a. One can see that Eq. (176) gives a good approximation of the data for low ϕ_N and large σ_N when the value of C corresponding to stick BC is chosen, whereas the agreement is poor for the value corresponding to slip BC. This is reasonable, since the monomer-NP interaction is attractive. When σ_N is decreased, the agreement between Eq. (176) and the data becomes progressively poorer: This is also reasonable, since when the size of the NP becomes comparable to the monomer size we cannot treat the polymer solution as a continuum, as we have also seen in Sec. 5.4.4. Despite this, for large σ_N Eq. (176) gives a surprisingly good description of the data for small ϕ_N.

In order to study the dependence of D_N/D_{N0} on σ_N at fixed ϕ_N, we interpolated between the points in Fig. 48a in order to obtain approximately the reduced NP diffusion coefficient as a function of the NP diameter σ_N at constant ϕ_N. The result is shown in Fig. 48b: The ratio $D_N(\sigma_N)/D_{N0}$ shows an initial increase with increasing σ_N, then an inflection point at $\sigma_N \simeq 2.5$, and finally it reaches a plateau for $\sigma_N \gtrsim 4$. Such a peculiar behavior can be interpreted in the following manner: At $\sigma_N \simeq 1$, increasing the NP diameter at fixed volume fraction has the effect of reducing the total polymer-NP interface, and therefore decreasing the interaction energy between polymers and NPs, resulting in an enhanced NP diffusion. When the NP size becomes larger than the average poer diameter $2\xi \simeq 2.1$ (the exact value depends on ϕ_m), the motion of NPs starts to be geometrically hindered by the polymer segments[175,184], and as a result the dependence of D_N/D_{N0} on the NP size weakens. Then, when the NPs become large enough, since the surface-to-volume ratio becomes smaller, the importance of the energetic contribution to the diffusion coefficient starts to decrease, resulting in another

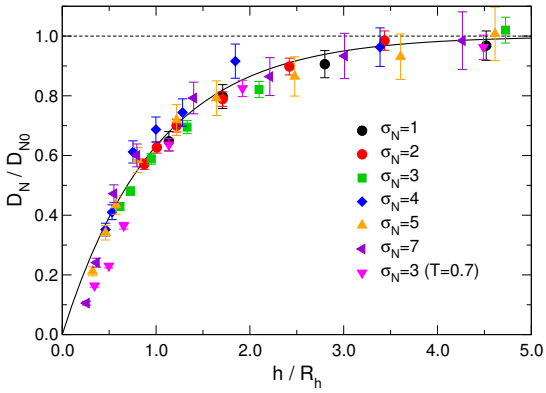

Figura 49 – Reduced NP diffusion coefficient D_N/D_{N0} as a function of h/R_h, where h is the interparticle distance and $R_h = (\sigma_N + 1.245)/2$ is the hydrodynamic radius of the NPs.

increase in the diffusion coefficient. Finally, for large NPs energy becomes irrelevant and D_N/D_{N0} is completely controlled by geometry, and therefore is constant at constant NP volume fraction.

In Sec. 5.4.3, we showed that the reduced diffusion coefficient of the polymers D_p/D_{p0} collapses on a master curve when plotted as a function of h/λ_d, where h is the interparticle distance and λ_d is a fit parameter depending on temperature, which should be interpreted as a dynamic length scale associated to polymer motion. Applying the same line of reasoning to the NP diffusion coefficient, we fitted D_N/D_{N0} to the expression $1 - \exp(-h/\lambda_d^N)$. We found that this expression fits the data rather well, and that the best fit parameter is $\lambda_d^N \simeq \sigma_N + 1.2$. We argue that this value should be interpreted as the hydrodynamic radius of the NPs, i.e., $\lambda_d^N = R_h$ (defined in Eq. (174)). In Fig. 49a we show D_N/D_{N0} as a function of h/R_h. The continuous line is the expression

$$D_N = D_{N0}\left[1 - \exp\left(-\frac{h}{R_h}\right)\right]. \tag{177}$$

We stress that here R_h was not used as a fit parameter to produce the graph of Fig. 49, but instead it was calculated from Eq. (174). However, we would also like to clarify, in the absence of any theoretical model that justifies it, that we believe that Eq. (177) should be considered as no more than a good approximation (much like Eq. (171)).

5.4.7 *Comparison of polymer and NP diffusivities*

In Fig. 50a, we show the ratio D_N/D_p. One sees that, in almost all the systems we considered, $D_N/D_p > 1$, i.e. the NPs diffuse faster than the polymer chains. An exception is $\sigma_N = 7$ at high densities; however, we know that at higher NP volume fraction the NPs form in this case a crystal (see next Section) and therefore D_N becomes very small.

Figure 50b shows the NP diffusion coefficient D_N as a function of the polymer center of mass diffusion coefficient D_p. One can observe that there is a strong correlation between D_N and D_p, which can be approximated by a power law, $D_N \propto D_p^{\alpha}$, where α increases with increasing NP diameter (inset of Fig. 50b). This correlation suggests that there is a coupling between the long time diffusivities of the NPs and of the centers of mass of the polymers, as

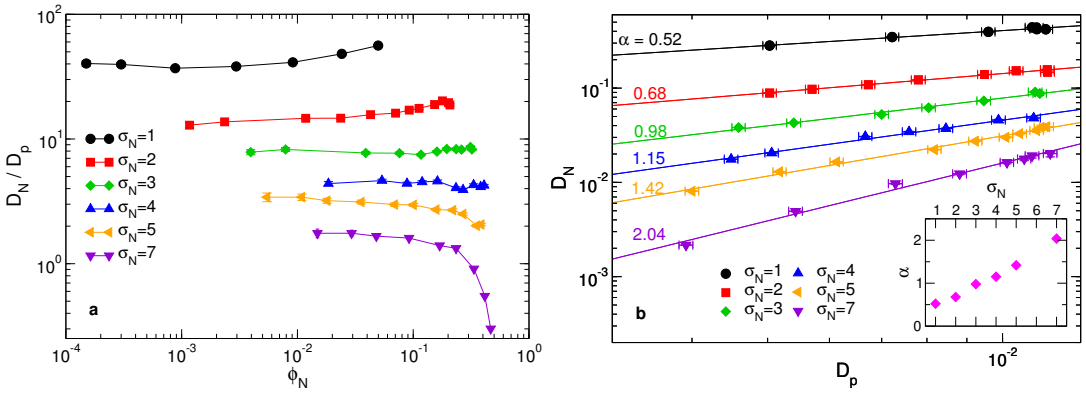

Figura 50 – (a) Ratio between the NP and polymer diffusion coefficients as a function of the NP volume fraction and for different values of the NP diameter σ_N. (b) NP diffusion coefficient D_N *versus* the chain CM diffusion coefficient D_p. The correlation between D_N and D_p takes the form of a power law, $D_N \propto D_p^{\alpha}$, where α increases with the NP diameter. *Inset*: α as a function of the NP diameter.

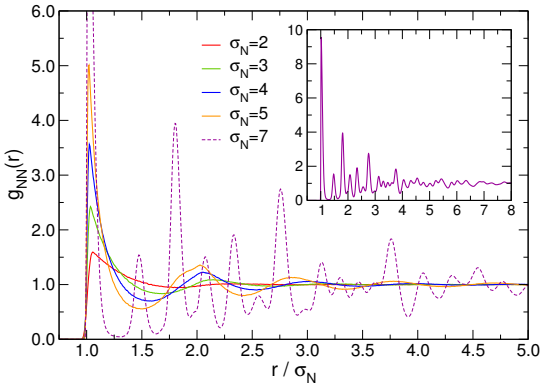

Figura 51 – NP-NP radial distribution function, $g_{NN}(r)$, of systems purely composed of NPs ($N_N = 10^4$) of different diameter σ_N at $T = 1.0$ and $P = 0.1$. *Inset*: $g_{NN}(r)$ for $\sigma_N = 7$, shown for a wider range of r/σ_N values.

it was proposed by Chen *et al.*[229].

5.5 HIGHER NANOPARTICLE VOLUME FRACTIONS

If we keep increasing the number of NPs N_N while keeping pressure and number of polymers constant, the volume of the simulation box will eventually start to increase proportionally to N_N. As a consequence, the NP volume fraction ϕ_N will reach a plateau, $\phi_N = \phi_N^{\max}(\sigma_N)$ (see Fig. 52b below), which corresponds to the value of ϕ_N for a pure NP system at temperature $T = 1.0$ and pressure $P = 0.1$. This situation corresponds approximately to the one depicted in Fig. 28d. If a standard LJ potential was used for the NP-NP interaction, $\phi_N^{\max}$ would not depend on σ_N, since the interaction potential would only depend on the ratio σ_N/r and all systems would be equivalent apart from a trivial distance rescaling. However, the expanded LJ potential, Eq. (144), does not simply depend on σ_N/r; therefore, pure NPs systems with the same T and P are *not* equivalent.

This is shown in Fig. 51, where we show the NP-NP radial distribution function, $g_{NN}(r)$,

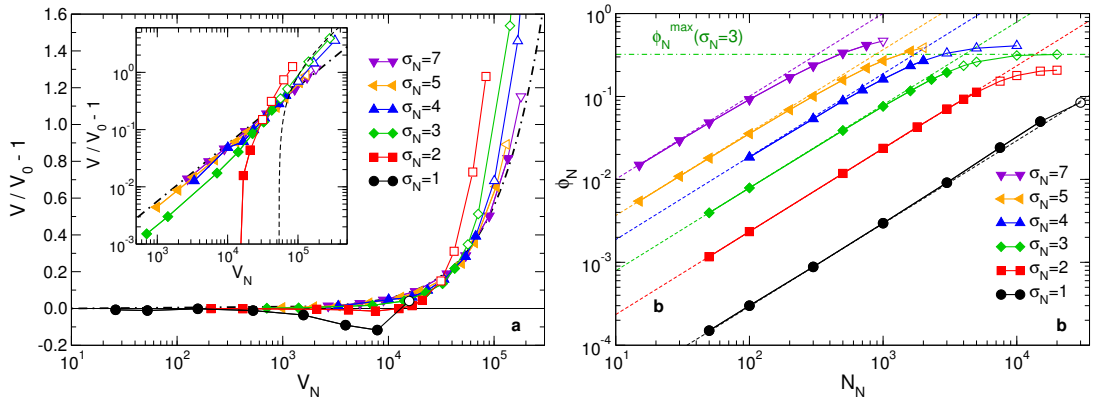

Figura 52 – (a) Expansion factor $(V - V_0)/V_0$, with $V_0 \equiv V(\phi_N = 0)$ and V the volume of the simulation box, as a function of the total NP volume $V_N \equiv N_N \pi \sigma_N^3/6$. Dash-dotted line: Eq. (178). *Inset*: Same plot as in the main figure, but in double-logarithmic scale. Data for $\sigma_N = 1$ are not shown for clarity. Dash-dotted line: Eq. (178). Dashed line: Eq. (179) for $\sigma_N = 3$ ($\phi_N^{\max} \simeq 0.3$). (b) NP volume fraction as a function of the number of NPs N_N. Dashed lines: $\phi_N = \pi \sigma_N^3 N_N/6V_0$. Dash-dotted line: $\phi_N^{\max}(\sigma_N = 3)$.

of systems purely composed of NPs ($N_N = 10^4$) of different diameter σ_N at $T = 1.0$ and $P = 0.1$. We note a pure NP system can be interpreted as the result of taking limit $N_N \to \infty$ in the nanocomposite; this is because, as discussed above, $V \propto N_N$ for large N_N and the number of polymers is constant, and therefore $\lim_{N_N \to \infty} \phi_m = 0$. For $\sigma_N = 2$ and 3, the RDF shows the typical structure of a liquid, with a peak at $\sigma_N = r_c$ (see Sec. 5.2.1) followed by a periodic modulation of wavelength r_c. As σ_N is increased, the value of $g_{NN}(r_c)$ increases, and for $\sigma_N = 5$ reaches the value $g_{NN}(r) \simeq 5$, while at the same time a shoulder appears in the second neighbor peak at $2r_c$, signaling that the system is very dense (although still a liquid). The $\sigma_N = 7$ system, on the other hand, clearly crystallizes, as we can see from the extremely high value of $g_{NN}(r_c)$ and from the sequence of peaks typical of long range order (see also the inset of Fig. 51).

In Fig. 52a, we show the expansion factor $(V - V_0)/V_0$, where $V_0 \equiv V(\phi_N = 0)$ (volume of the neat system) and V is the volume of the simulation box, as a function of the total NP volume $V_N \equiv N_N \pi \sigma_N^3/6 = V\phi_N$, for different values of σ_N. For small V_N, we expect that the system's volume is simply $V = V_0 + V_N$, and therefore

$$\frac{V - V_0}{V_0} \simeq \frac{V_N}{V_0}. \tag{178}$$

Eq. (178) is represented in Fig. 52a by the dash-dotted line. As one can see, for $\sigma_N \geq 4$ this approximation describes the data very well, meaning that in this range of NP diameters the expansion of the system is purely due to the excluded volume of the NPs. This is also shown in the inset of Fig. 52a, where we show $(V - V_0)/V_0$ as a function of V_N in double-logarithmic scale. For $\sigma_N = 3$, the observed expansion is smaller than what predicted by Eq. (178). For $\sigma_N = 2$, and even more so for $\sigma_N = 1$, the behavior is qualitatively very different, as there is a range of V_N values in which we observe a *decrease* in volume, an effect which we ascribe to the greater relevance of the polymer-NP interaction for this NP sizes. The behavior of the system's volume should be compared with the one of the radius of gyration, which was discussed in Sec. 5.3.4. We recall that chain expansion was observed for $\sigma_N \geq 2$ and chain

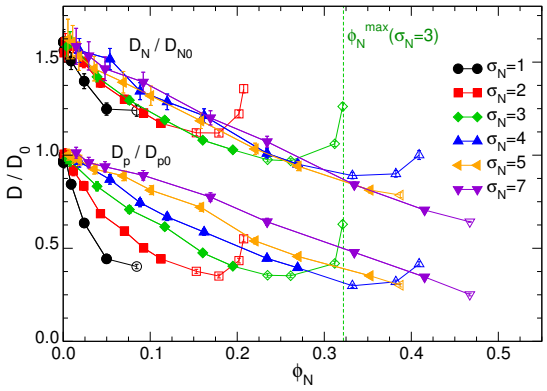

Figura 53 – Normalized diffusion coefficient of NPs and polymers as a function of NP volume fraction for different values of the NP diameter σ_N. Filled symbols: good NP dispersion. Open symbols: poor NP dispersion. Dashed line: approximate value of $\phi_N^{\max}$ for $\sigma_N = 3$. The data for D_N/D_{N0} have been shifted up by 0.6 for clarity.

contraction for $\sigma_N = 1$, so that the behavior of the single chains is qualitatively similar to the behavior of the whole system.

For large V_N, we can neglect the volume of the polymers. The system's volume is thus $V \simeq V_N/\phi_N^{\max}$, where $\phi_N^{\max}$ is the volume fraction of a pure NP system at temperature $T = 1.0$ and pressure $P = 0.1$. We have therefore

$$\frac{V - V_0}{V_0} \simeq \frac{V_N}{\phi_N^{\max} V_0} - 1. \tag{179}$$

Eq. (179) is represented in the inset Fig. 52a by the dashed line for $\sigma_N = 3$, for which $\phi_n^{\max} \simeq 0.3$ (see Fig. 52b). In Fig. 52b we show the NP volume fraction ϕ_N as a function of N_N. Initially, the expansion is very small and therefore $\phi_N \simeq \pi\sigma_N^3 N_N/6V_0$ (dashed lines). Then, for larger values of N_N, the volume starts to increase proportionally to N_N and ϕ_N reaches the plateau $\phi_N = \phi_N^{\max}(\sigma_N)$.

Since the number of polymer chains is constant, the increase of the volume at large N_N results in a decrease of polymer volume fraction ϕ_m, and therefore in a decrease of the polymer-NP interface per unit volume. This in turn causes a weakening of the polymer-mediated attractive interaction between NPs and consequently an increase of the free volume $V_{\text{free}} = V[1 - (\phi_N + \phi_m)]$. Both of these mechanisms result in an increase in the polymer and NP diffusivities. We can observe this effect in Fig. 53, where we show the normalized diffusion coefficient of both polymers and NPs for all the simulated systems, including those where good NP dispersion is not realized (open symbols): D/D_0 reaches a minimum corresponding to the value of ϕ_N at which the volume starts to increase, and it continues to grow as $\phi_N^{\max}$ is approached. We note however that for $\sigma_N = 7$, D/D_0 shows a monotonic decrease. While in all the other cases we found that the pure NP system at $T = 1.0$ and $P = 0.1$ is a liquid, for $\sigma_N = 7$ it is a crystal, which means that as we approach $\phi_N^{\max}$ the ratio D/D_0 will decrease and eventually settle to a very small value.

Table 1: Details of the simulated systems. N_N: number of NPs. σ_N: NP diameter. L: simulation box length. ϕ_m: monomer volume fraction. ϕ_N: NP volume fraction. D_N: NP diffusion coefficient. D_p: polymer diffusion coefficient. R_g: radius of gyration. h: interparticle distance. Systems in which there is poor NP dispersion (p.d.) are denoted by an asterisk in the last column.

N_N	σ_N	L	ϕ_m	ϕ_N	D_N	D_p	R_g	h	p. d.
0	–	56.32	0.1466	0.0000	–	0.0114	6.282	–	-
30000	1	57.08	0.1408	0.0845	0.2793	0.0046	6.4681	0.8980	*
15000	1	54.03	0.1660	0.0498	0.2824	0.0050	6.2133	1.2760	
7500	1	54.57	0.1611	0.0242	0.3477	0.0072	6.2358	1.9194	
3000	1	55.64	0.1520	0.0091	0.3949	0.0096	6.2452	3.1421	
1000	1	56.11	0.1482	0.0030	0.4221	0.0111	6.2688	5.0730	
300	1	56.28	0.1468	0.0009	0.4199	0.0114	6.2535	8.1108	
100	1	56.11	0.1482	0.0003	0.4380	0.0111	6.2621	12.0997	
50	1	56.18	0.1476	0.0001	0.4400	0.0109	6.2639	15.5146	
20000	2	73.92	0.0648	0.2074	0.1174	0.0063	7.1314	0.7926	*
15000	2	67.76	0.0842	0.2020	0.0964	0.0049	6.9420	0.8338	*
10000	2	61.64	0.1118	0.1789	0.0805	0.0040	6.6559	0.9663	*
7500	2	59.00	0.1275	0.1530	0.0807	0.0043	6.4846	1.1229	*
5000	2	57.13	0.1404	0.1123	0.0886	0.0050	6.3783	1.4177	
4000	2	56.61	0.1443	0.0923	0.0971	0.0057	6.3390	1.6361	
3000	2	56.31	0.1466	0.0704	0.1085	0.0067	6.3218	1.9785	
1800	2	56.05	0.1487	0.0428	0.1222	0.0078	6.2599	2.7735	
1000	2	56.18	0.1477	0.0236	0.1392	0.0095	6.2879	3.9275	
500	2	56.23	0.1472	0.0118	0.1526	0.0104	6.2609	5.5744	
100	2	56.30	0.1467	0.0023	0.1566	0.0114	6.2632	11.2290	
50	2	56.31	0.1466	0.0012	0.1473	0.0114	6.2605	14.5222	
20000	3	95.84	0.0297	0.3212	0.0589	0.0071	7.6393	0.6161	*
10000	3	76.81	0.0578	0.3120	0.0410	0.0048	7.2650	0.6705	*
5000	3	64.66	0.0968	0.2614	0.0329	0.0040	6.7890	0.9414	*
4000	3	62.21	0.1087	0.2348	0.0334	0.0040	6.5920	1.0718	*
3000	3	60.14	0.1204	0.1950	0.0382	0.0046	6.5102	1.3057	
2300	3	58.75	0.1291	0.1604	0.0428	0.0054	6.4311	1.5429	
1600	3	57.87	0.1351	0.1167	0.0524	0.0070	6.3742	2.0149	
1000	3	57.07	0.1408	0.0761	0.0618	0.0080	6.3179	2.8246	
500	3	56.64	0.1441	0.0389	0.0731	0.0095	6.2917	4.4527	
100	3	56.37	0.1461	0.0079	0.0908	0.0110	6.2921	10.0294	
50	3	56.35	0.1463	0.0040	0.0875	0.0112	6.2624	13.5295	
10000	4	93.57	0.0320	0.4090	0.0200	0.0047	7.7135	0.5071	*
5000	4	75.96	0.0597	0.3823	0.0150	0.0036	7.2264	0.6233	*
3000	4	67.13	0.0865	0.3323	0.0145	0.0034	6.8100	0.8860	*
2000	4	62.90	0.1052	0.2694	0.0176	0.0045	6.6007	1.2091	

1600	4	61.18	0.1143	0.2342	0.0205	0.0051	6.5100	1.3929	
1000	4	59.15	0.1265	0.1619	0.0306	0.0067	6.3726	1.9771	
700	4	58.12	0.1334	0.1195	0.0343	0.0076	6.3358	2.6185	
500	4	57.45	0.1381	0.0884	0.0372	0.0085	6.3197	3.3626	
300	4	57.21	0.1398	0.0537	0.0458	0.0099	6.3056	4.8379	
100	4	56.56	0.1447	0.0185	0.0481	0.0110	6.2800	8.8842	
2000	5	69.65	0.0775	0.3874	0.0071	0.0034	6.9309	0.8357	*
1600	5	66.72	0.0882	0.3526	0.0081	0.0040	6.7538	1.0106	
1000	5	62.36	0.1080	0.2699	0.0130	0.0052	6.5122	1.4406	
750	5	60.60	0.1176	0.2206	0.0165	0.0061	6.4122	1.7888	
500	5	59.15	0.1265	0.1581	0.0222	0.0082	6.3587	2.5069	
300	5	57.99	0.1342	0.1007	0.0273	0.0092	6.3333	3.8062	
200	5	57.44	0.1381	0.0691	0.0301	0.0101	6.3126	5.1301	
100	5	56.87	0.1423	0.0356	0.0329	0.0105	6.2973	7.7382	
50	5	56.59	0.1444	0.0181	0.0354	0.0111	6.2820	11.2616	
30	5	56.48	0.1453	0.0109	0.0383	0.0112	6.2879	14.4058	
15	5	56.40	0.1459	0.0055	0.0389	0.0114	6.2622	19.9009	
1000	7	72.71	0.0681	0.4672	0.0009	0.0029	6.9195	0.7881	*
750	7	68.71	0.0807	0.4153	0.0022	0.0039	6.7000	1.0633	
500	7	64.51	0.0975	0.3345	0.0049	0.0054	6.5015	1.5040	
300	7	61.26	0.1139	0.2344	0.0097	0.0073	6.3621	2.2690	
200	7	59.65	0.1234	0.1692	0.0123	0.0088	6.3070	3.2795	
100	7	58.00	0.1341	0.0920	0.0162	0.0101	6.2774	5.7758	
50	7	57.17	0.1401	0.0481	0.0177	0.0107	6.2980	9.1238	
30	7	56.83	0.1426	0.0294	0.0191	0.0109	6.2728	12.4074	
15	7	56.57	0.1446	0.0149	0.0202	0.0115	6.2612	17.5854	

6

STRUCTURE, DYNAMICS AND ELASTICITY OF POLYDISPERSE DISORDERED NETWORKS

The data and considerations presented in this Chapter are the result of ongoing research and are thus in some parts incomplete, and/or will be subject to revision. Simulations and data analysis have been carried out in collaboration with Andrea Ninarello, Lorenzo Rovigatti and Josè Ruiz-Franco and will be the subject of one or more future publications[265]. The primitive path analysis data shown in Fig. 67 have been provided by Cristian Micheletti. Walter Kob, Emanuela Zaccarelli and Virginie Hugouvieux supervised this project and contributed with very useful discussion.

As discussed in Chapter 4, understanding the physical mechanisms governing the diffusion of nanoparticles in polymer systems is fundamental not only for the obvious technological application, but also for the insights it allows us to gain on biological systems. One obvious example is the diffusion of proteins and other biomolecules in the crowded cellular environment, which is fundamental for its strong influence on cellular functions, such as enzymatic reactions and self-assembly of cellular structures[123,124]. As we have seen, in the past years many steps have been taken towards a comprehensive understanding of this problem. Computer simulations, in particular, have proven fundamental for the insight that they provide in the microscopic structural and dynamical properties of polymer nanocomposites (PNC), shedding light on the role played by properties which are difficult to control precisely in experiments, such as the interaction between the nanoparticles and the polymeric matrix. Most of these simulation studies, however, focused on PNCs containing free linear chains, whereas much less attention has been given to systems of chemically or physically crosslinked polymers, despite the ubiquity of polymeric networks and gels in synthetic and biological systems. Examples of biological systems include the actin and chromatin networks in cells[266–268], the bacterial matrix in biofilms[269], the extracellular matrix in living tissues[270], whereas hydrogels are of prime importance when considering technological applications[271–275].

The main issue when simulating the diffusion of probe particles in a polymer network is to determine which kind of structure to adopt for the network. In some of the earliest studies, the network was simply modeled as an array of fixed obstacles[276], which is clearly very far from a physically realistic description. Other authors attempted to incorporate connectivity and flexibility in the network model, but most of them resorted to regular structures, in which the crosslinks are placed on the vertices of a regular lattice and connected either by chain segments[277,278] or directly by springs[279–281]. In the latter case, the resulting system can be hardly called a "polymer network", since there is no actual strand connecting the crosslinks, and therefore strand dynamics and entanglement effects are not accounted for. Moreover, real-life networks are usually disordered and polydisperse, with a continuous (in the thermodynamic limit) distribution of strand lengths. A notable exception is provided by Ref. 282, where the motion of a single particle in a disordered, polydisperse tetravalent network[283] has been

studied *via* Brownian dynamics simulations of a system with spherical boundary conditions (SBC)[284]. It would be desirable, however, to have a model which does not rely on SBC, since periodic boundary conditions are the *de facto* standard for simulations of polymer systems, as confirmed also by the fact that the more widely used molecular dynamics packages, as LAMMPS[241] and ESPResSo[285], currently do not support SBC. Models of polymer networks which overcome all or some of the above mentioned shortcomings (monodispersity, ordered structure, absence of chain dynamics, absence of entanglement effects) have been proposed over the years[76,286–295]: However, to the best of our knowledge, none of these models have been used to study the problem of nanoparticle diffusion.

In the present Chapter we will introduce a novel model of disordered, polydisperse and defect-free network of bead-spring chains, which has originally been developed for the study of microgels[296–301], and use molecular dynamics simulations to study its static, dynamic and elastic properties for different system parameters. In Chapter 7, we will show how the same model can be used effectively to study the problem of nanoparticle diffusion in disordered polymeric networks.

6.1 MODEL AND METHODS

There are several possible methods to generate a model polymer network. One possibility is starting with a system of (mono- or polydisperse) precursor chains and then crosslink them through some procedure. The crosslinking can be allowed only between chain ends[76,288,292–295] (*end-linking*) or between any pair of monomers[286,287] (*random crosslinking*). However, these methods suffer from kinetic limitations, in that it can be quite difficult to reach a perfect (fully-bonded) configuration because of the slow dynamics of the chains[76,288,294]. *Ad hoc* methods can be used to increase the number of bonded sites[76,294]. Using these methods is however not completely satisfactory, since the final structure will in principle depend on the exact method that was used to force the formation of more bonds. Another option is to impose some lattice connectivity, like the diamond lattice[277,289–291,302,303]. Several of these “lattice networks" can then be randomly superimposed in order to obtain a disordered structure[289–291]. Even in this case, however, these systems present an underlying ordered connectivity and monodisperse strand length, contrary to most experimental systems.

In order to overcome the shortcomings of these methods, we generate a polydisperse network *via* the method described in Ref. 296. This method was originally developed for MD simulations of microgels[296,299], but can be trivially generalized to the case of a bulk network. The starting point is a mixture of two different species of *patchy particles*, i.e., spheres of identical size and mass decorated by a certain number of interaction sites (the “patches") arranged in regular configurations. The number of patches a particle possesses is called the *valence*. We consider systems of M_2 bivalent particles and M_f f-valent particles, with $f = 3, 4$: Bonding is only allowed between pairs of bivalent particles and between bivalent particles and f-valent particles. The f-valent particles act therefore as crosslinkers, bonding to the bivalent particles to form branched structures.

The interaction potential between a pair of particles is

$$\mathcal{U}(\mathbf{r}_i, \mathbf{r}_j, \{\mathbf{p}_i\}, \{\mathbf{p}_j\}) = \mathcal{U}_{\mathrm{WCA}}(r_{ij}) + \sum_{\mu \in \{\mathbf{p}_i\}} \sum_{\nu \in \{\mathbf{p}_j\}} \mathcal{U}_{\mathrm{patch}}(r_{\mu\nu}), \tag{180}$$

where $\mathbf{r}_i, \mathbf{r}_j$ are the position vectors of the two particles, $r_{ij} \equiv |\mathbf{r}_i - \mathbf{r}_j|$ and $\{\mathbf{p}_i\}$, $\{\mathbf{p}_j\}$ are the sets of unit vectors identifying respectively the patches of particle i and those of particle j, with $r_{\mu\nu}$ the distance between patch μ on particle i and patch ν on particle j. The potential $\mathcal{U}_{\text{WCA}}$ is the usual purely repulsive WCA potential[a] (Sec. 3.6.3), while the patch potential has the following form:

$$\mathcal{U}_{\text{patch}}(r_{\mu\nu}) = \begin{cases} 2\epsilon_{\mu\nu}\left(\frac{\sigma_p^4}{2r_{\mu\nu}^4} - 1\right)\exp\left(\frac{\sigma_p}{r_{\mu\nu}-r_c} + 2\right) & r < r_c \\ 0 & \text{otherwise,} \end{cases} \tag{181}$$

where σ_p sets the position of the attractive well (of depth $\epsilon_{\mu\nu}$) and r_c is chosen by imposing $\mathcal{U}_{\text{patch}}(r_c) = 0$. Here, $\sigma_p = 0.4$, $r_c = 1.5\sigma_p = 0.6$; with this choice of values, the minimum of the potential is at $r_{\min} = \sigma_p$, as shown in Fig. 54. The interaction energy $\epsilon_{\mu\nu}$ is $\epsilon_{\mu\nu} = 1$ for all pairs of patches, with the exception of pairs of patches belonging to a pair of f-valent particles, for which $\epsilon_{\mu\nu} = 0$, so that the bonding of two f-valent particles (crosslinkers) is forbidden. The patches are arranged on the poles, equidistant on the equator and on a tetrahedron for bi-, tri- and tetrafunctional particles, respectively. In all cases, the distance between the patch and the center of the particle is $1/2$. The pair potential given in Eq. (181) is complemented by a three-body potential $\mathcal{U}_{\text{triplet}}$ acting on triplets of close patches[304]:

$$\mathcal{U}_{\text{triplet}} = w\,\epsilon_{\mu\nu} \sum_{\lambda,\mu,\nu} \mathcal{U}_3(r_{\lambda,\mu})U_3(r_{\lambda,\nu}), \tag{182}$$

where

$$\mathcal{U}_3(r) = \begin{cases} 1 & r < \sigma_p \\ -U_{\text{patch}}(r)/\epsilon_{\mu\nu} & r_{\min} < r < r_c \end{cases} \tag{183}$$

The term (182) has a twofold effect: On one hand it enforces the single-bond-per-patch condition: a given patch cannot be involved in more than one bond at a time. On the other hand, the three-body term also provides an efficient bond-swapping mechanism that makes it possible to easily equilibrate the system at extremely low temperatures. The parameter w appearing in Eq. (182) can be used to tune the amplitude of $\mathcal{U}_{\text{triplet}}$, in order to favor ($w \simeq 1$) or hamper ($w \gg 1$) bond swapping[304].

Starting from a cubic box with periodic boundary conditions containing M_2 bivalent particles and M_f crosslinkers, a molecular dynamics simulation is run at constant volume and temperature $T_{\text{assembly}} = 0.05$ (NVT ensemble). For these simulations, we use a GPU implementation of the oxDNA software[305,306]. At this very low temperature, the system approaches the ground state, where all the bonds are satisfied (fully-bonded state). Since the bonds can break and reform with an efficiency that is greatly improved by the above mentioned bond-swapping potential, the system can quickly reach equilibrium. Once the majority of the bonds ($> 99.8\%$) are formed, the simulation is stopped and the particles which do not belong to the percolating cluster (at most 4% of the total in all the simulated systems) are removed. We note that, although we chose for practical reasons to stop the reaction before reaching

[a] The parameters σ and ϵ of the WCA potential fix, as usual, the length and energy scales.

the fully-bonded ground state of the system, reaching this state is in principle possible by making a greater computational effort.

The system obtained from this procedure contains only a small number of dangling ends, i.e., it is an almost-perfect network. However, since it is known that a dangling end of length N has a relaxation time of order e^N [89], and since we observe slow relaxation processes in the system in the presence of dangling ends (see below), we decide to remove all the (simple and branched) dangling ends in the system, so that a perfect, fully-bonded network is obtained.

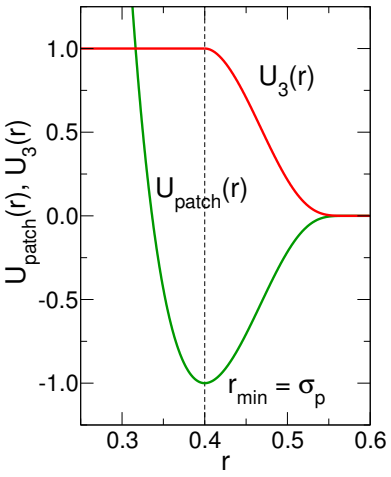

Figura 54 – Patch potential (Eq. (181)) and $\mathcal{U}_3$ potential (Eq. (183)).

Once the dangling ends are removed, the interaction potential is changed from Eq. (180) to the Kremer-Grest potential (Sec. 3.6.3), with parameters $k = 30$ and $r_0 = 1.5$. The reversible bonds of the patchy system are therefore replaced by permanent FENE bonds[b], so that the initial topology is fixed (i.e., the system is a chemical gel). MD simulations are then run using the LAMMPS package [241,242]. The system is initially allowed to relax to pressure $P = 0$ at constant temperature $T = 1.0$; then, NPT simulations are run at these T, P values. Temperature and pressure are kept constant by Nosé-Hoover chains of three thermostats and three barostats [81], and the three dimensions of the box, L_x, L_y and L_z, are allowed to fluctuate independently. The equations of motion are those of Shinoda *et al.* [307], which combine the hydrostatic equations proposed by Martyna *et al* [308] with the strain energy proposed by Parrinello and Rahman in Ref. 309. The integration time step is $\delta t = 0.003$ for all the simulations. Additional information can be found in the LAMMPS manual page [243]. The Nosé-Hoover chain method insures a correct sampling of the NPT ensemble [310].

The method described above allows to generate a network which is naturally disordered and almost perfect (fully-bonded). Moreover, since bond-swapping is allowed, the system can quickly reach equilibrium: therefore, for a given T_{assembly}, the properties of the final state are uniquely determined by only three parameters (as it will be shown below): the fraction of crosslinks, the initial density and the crosslink valence.

We considered systems containing an initial number of particles (before the assembly of the network) $M_{\text{tot}} \equiv \sum_\alpha M_\alpha = M_2 + M_f = 5 \cdot 10^4$, with initial crosslinker fractions $c = M_f/(M_f + M_2) = 0.01, 0.05, 0.1$ and crosslinker functionalities (valences) $f = 3, 4$. For $c = 0.05$ and 0.1, we built the network starting from initial number densities $\rho_{\text{init}} = 0.05, 0.1, 0.2, 0.3, 0.4, 0.5$, whereas for $c = 0.01$ we only considered $\rho_{\text{init}} = 0.05, 0.1$ and 0.2. For each system, we have considered two independent realizations in order to improve the statistics. Moreover, for $c = 0.05, 0.1$ and $\rho_{\text{init}} = 0.1, 0.2$ we have also considered systems of $4 \cdot 10^5$ particles in order to check for the presence of finite size effects. For the structural and dynamic quantities considered in this work, no significant finite size effects were found. In Fig. 55 we show snapshots of some of the simulated systems taken after equilibration.

In Tab. 2, we report the details of the systems of $5 \cdot 10^4$ particles, containing respectively trivalent ($f = 3$) and tetravalent ($f = 4$) crosslinks. We have introduced here the mean functionality F,

[b] We note that when the patchy bonds are replaced by FENE bonds, the bond directionality is lost.

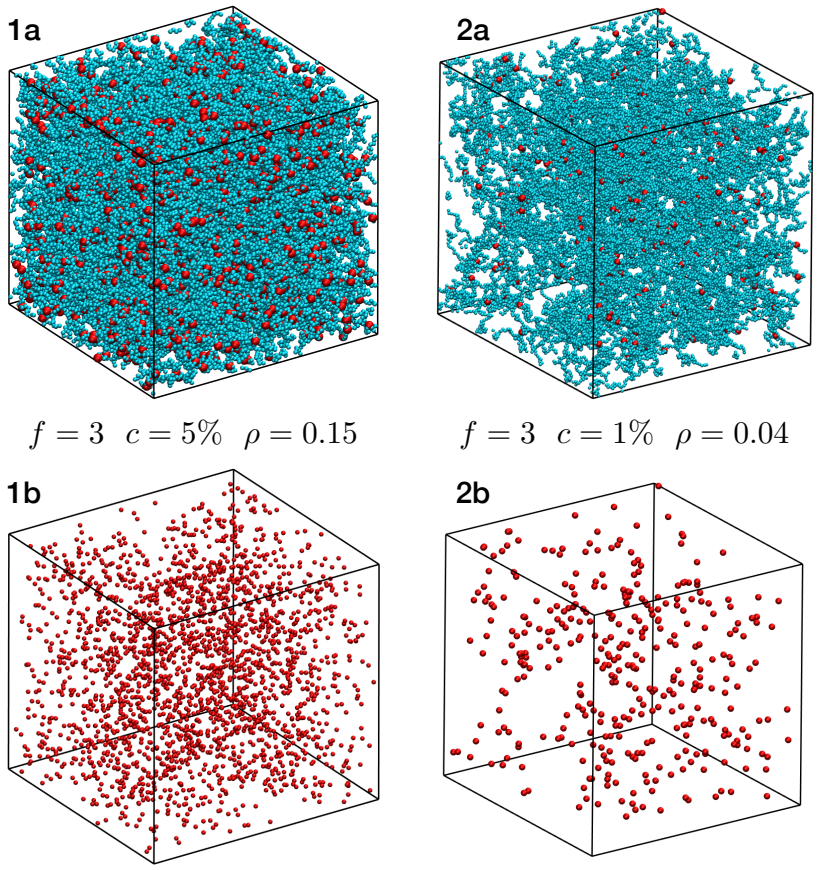

Figura 55 – Snapshots of two of the simulated systems. 1a-b: $f = 3, c = 5\%, \rho = 0.15$. 2a-b: $f = 3, c = 1\%, \rho = 0.04$. Bifunctional particles are shown in blue, while crosslinks are shown in red. In the 1b and 2b, only the crosslinks are shown. In 2a-b and 1a, the crosslinks are shown as having double the size of the bifunctional particles in order to improve the visualization.

Tabella 2 – Properties of the trivalent (a) and tetravalent (b) networks after the removal of the dangling ends. M_{tot}: total n. of particles. M_4: n. of tetravalent particles. M_3: n. of trivalent particles. M_2: n. of bivalent particles. $c \equiv (M_4 + M_3)/M_{\text{tot}}$: crosslinker concentration. F: mean valence, Eq. (184). $\rho \equiv M_{\text{tot}}/\langle V \rangle$: average density. All the values are averaged over two independent realizations of the system.

M_{tot}	M_3	M_2	c	F	ρ
48773.0	4845.0	43928.0	0.0993	2.099	0.1270
49388.5	4907.0	44481.5	0.0994	2.099	0.1929
49636.0	4940.0	44696.0	0.0995	2.100	0.2908
49731.5	4953.5	44778.0	0.0996	2.100	0.3758
49803.0	4966.0	44837.0	0.0997	2.100	0.4630
49797.5	4968.5	44829.0	0.0998	2.100	0.5398
47023.0	2346.0	44677.0	0.0499	2.050	0.0936
48508.0	2394.0	46114.0	0.0494	2.049	0.1498
48976.0	2434.0	46542.0	0.0497	2.050	0.2469
49243.5	2454.0	46789.5	0.0498	2.050	0.3327
49439.0	2465.0	46974.0	0.0499	2.050	0.4141
49469.0	2465.0	47004.0	0.0498	2.050	0.4812
36368.5	352.0	36016.5	0.0097	2.010	0.0425
41791.0	405.0	41386.0	0.0097	2.010	0.0872
46047.5	441.0	45606.5	0.0096	2.010	0.1789

(a) Properties of the systems with trivalent ($f = 3$) crosslinks.

M_{tot}	M_4	M_3	M_2	c	F	ρ
48952.0	4821.5	176.0	43954.5	0.1021	2.201	0.1593
49568.5	4901.5	98.5	44569.0	0.1009	2.200	0.2487
49748.0	4924.5	75.0	44748.5	0.1005	2.199	0.3563
49792.5	4948.0	52.0	44792.5	0.1004	2.200	0.4472
49804.5	4958.0	42.0	44804.5	0.1004	2.200	0.5255
49888.0	4970.0	29.0	44889.0	0.1002	2.200	0.6123
47464.5	2319.5	163.0	44982.0	0.0523	2.101	0.1258
48946.5	2408.5	91.0	46447.0	0.0511	2.100	0.1924
49469.0	2441	58.5	46969.5	0.0505	2.100	0.2908
49439.0	2450.5	49.0	46939.5	0.0506	2.100	0.3750
49620.0	2462.0	37.5	47120.0	0.0504	2.100	0.4617
49700.5	2466.0	34.0	47200.5	0.0503	2.100	0.5399
39123.5	373.5	105.0	38645.0	0.0122	2.022	0.0597
44301.5	419.0	72.0	43810.5	0.0111	2.021	0.1137
46274.5	438.0	58.0	45778.5	0.0107	2.020	0.1977

(b) Properties of the systems with tetravalent ($f = 4$) crosslinks.

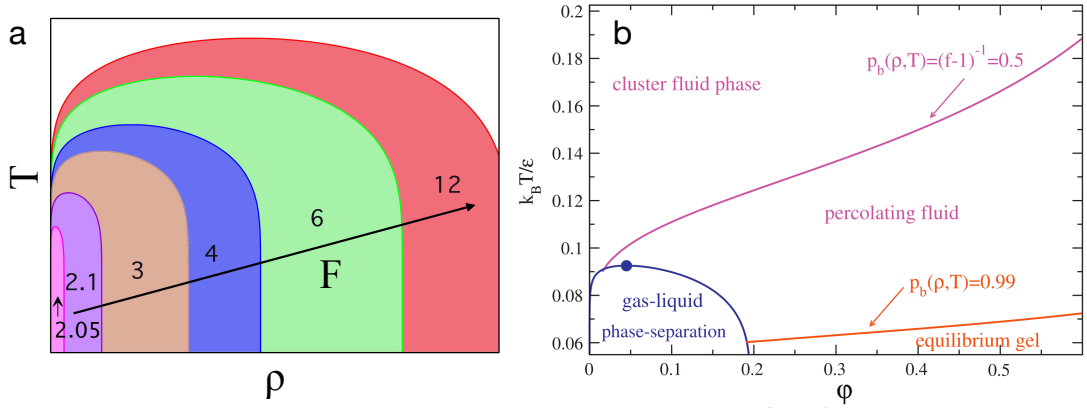

Figura 56 – (a) Qualitative phase diagram of mixtures of limited valence particles with different mean valence F (numbers). The different colors denote the coexistence regions for systems with different values of F. We note that the coexistence region disappears in the limit $F \to 2$. Adapted with permission from Ref. 64. Original image courtesy of F. Sciortino. (b) Phase diagram of a system of trivalent ($f = 3$) particles. Here ϕ is the volume fraction. We note that the coexistence region lies inside the percolation region. From Ref. 64

$$F \equiv \frac{\sum_\alpha \alpha M_\alpha}{\sum_\alpha M_\alpha} = \frac{\sum_\alpha \alpha M_\alpha}{M_{\text{tot}}}, \tag{184}$$

where M_α is the number of particles with valence α.

The density ρ is defined as $\rho \equiv M_{\text{tot}}/\langle V \rangle$, where $V = L_x L_y L_z$ is the volume of the box, which depends on time since the simulations are performed in the NPT ensemble. For each value of the system's parameters, the properties reported in Tabs. 2a and 2b are averaged over the two realizations of the system. Here M_{tot} refers to the number of particles after all the dangling ends have been removed (all the systems are in the fully-bonded state, with no dangling ends). We note that for the systems with the tetravalent crosslinkers (Tab. 2b), the removal of the dangling ends has the side effect of introducing a certain number of trivalent crosslinks in the system, since when a dangling end is cut a crosslinker loses a bond. In this case, the crosslink fraction must be calculated as $c = (M_3 + M_4)/(M_2 + M_3 + M_4)$. However, we note that for all the systems considered with the exception of the system with $c \simeq 0.01$, we have $M_3 \ll M_4$ and therefore the presence of the trivalent crosslinks can be neglected. When only one kind of crosslinker is present, we obtain a simple relation between c and the mean functionality:

$$F = \frac{f M_f + 2M_2}{M_f + M_2} = 2 + (f-2)c. \tag{185}$$

The quantities c, F and ρ reported in Tab. 2b, however, have been calculated taking into account the presence of the trivalent particles.

Before concluding this section, we should remark that a homogeneous percolating network is not going to form for arbitrary values of f, c and of the initial monomer density ρ_{init}[c]. This is due to the fact that when the mean functionality F is larger than 2, systems of limited

[c] We note that ρ_{init} refers to the value after the removal of the dangling ends.

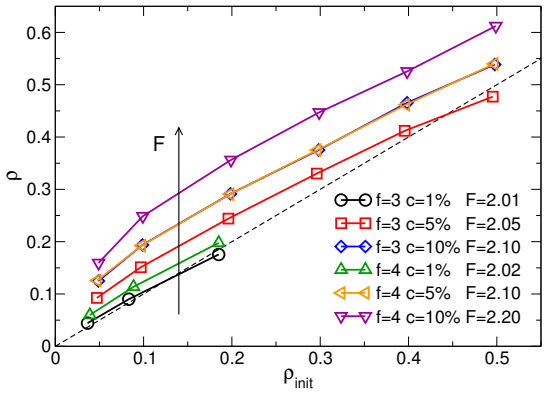

Figura 57 – Average density, $\rho \equiv M_{\text{tot}}/\langle V \rangle$, as a function of the initial density of the system, for different values of the crosslinker valence f and of the crosslinker concentration c. $F = 2 + (f-2)c$ is the mean valence.

valence particles like the one used to generate the network present a gas-liquid coexistence region[60,64,311,312], as predicted by Wertheim's theory for fluid with directional attractive interactions[313–316]. This is shown qualitatively in Fig. 56. If ρ_{init} is chosen such that the state point $(\rho_{\text{init}}, T_{\text{assembly}})$ lies in the coexistence region, the system will undergo phase separation. The area of the coexistence region in the T, ρ plane is an increasing function of the mean valence F[64] (Fig. 56a); therefore, the higher the values of f and c, the higher the density at which the system will undergo phase separation. Since the coexistence region lies inside the percolation region (Fig. 56b), a percolating network might still form, but it would lack homogeneity.

6.2 STATIC PROPERTIES

As discussed in Sec. 6.1, the network is initially built at constant N, V and T. Then, after the dangling ends have been removed and the interaction potential has been changed from patchy to Kremer-Grest, the system is allowed to relax to $P = 0$. The final mean density of the system, $\rho \equiv M_{\text{tot}}/\langle V \rangle$, will in general be different from the initial density ρ_{init}.

In Fig. 57, we show ρ as a function of ρ_{init} for different values of c and f. One can see that for most of the systems $\rho > \rho_{\text{init}}$ (i.e., the network contracts), with only two of the systems here considered[d] having $\rho < \rho_{\text{init}}$. This is due to the fact that the average distance between two bonded patchy particles is $\simeq 1.2$ at $T = 1.0$ in the explored ρ_{int} range, whereas the Kremer-Grest model has an equilibrium bond length $\simeq 0.96$. We also note that the curves for $f = 4, c = 5\%$ and $f = 3, c = 10\%$ superimpose perfectly, implying that the parameter controlling ρ is the mean valence F. Indeed, it can be verified that all these systems have $F \simeq 2.1$ (see also Tabs. 2a and 2b).

6.2.1 *Strand length distribution*

One of the most relevant properties of the network is the strand length distribution, where a strand is a segment of bifunctional particles between two crosslinks. Although, as discussed in Sec. 6.1, some of the $f = 4$ systems actually contain a certain number of trivalent cros-

[d] $f = 3, c = 5\%, \rho_{\text{init}} \simeq 0.5$ and $f = 3, c = 1\%, \rho_{\text{init}} \simeq 0.2$

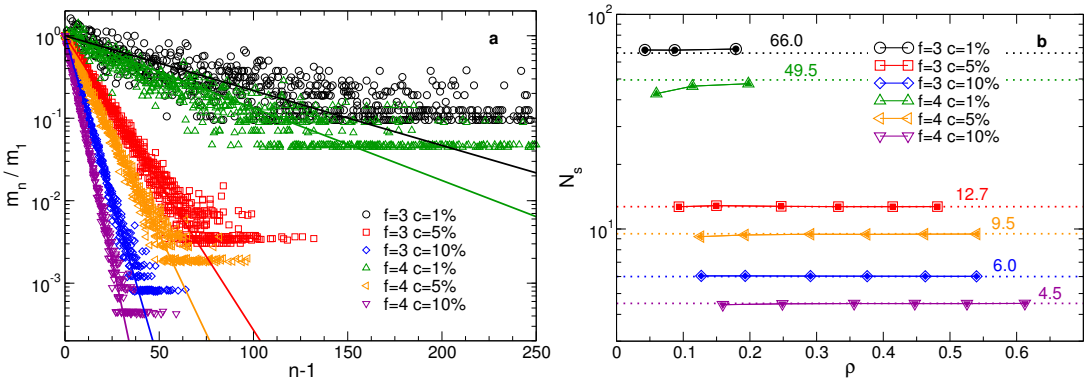

Figura 58 – (a) Number of strands of length n, m_n, normalized by the number of strands of unitary length, m_1. Points: simulation data for all the densities considered (see Tabs. 2a and Tab. 2b). Lines: theoretical prediction (Eq. (187)). (b) Mean strand length N_s as a function of monomer density ρ. Open symbols: data. Filled symbols: Eq. (191). Dotted lines (with labels): N_s calculated from Eq. (190) assuming that c takes the exact values 1, 5 and 10% and that F is given by Eq. (185).

slinkers, for the systems considered here this number can be neglected. Therefore, in the following we will assume that the system contains only one type of crosslinker.

The number m_n of network strands of length n can be estimated using the Flory-Stockmayer (FS) result, Eq. (87). However, since bonding is not allowed between pairs of crosslinkers, m_n deviates from the FS theory. A more precise expression, which takes into account the fact that the crosslinkers can only bind to bivalent particles, has been given by Rovigatti *et al.*[297]:

$$\begin{aligned} m_n &= M_2 \left(\frac{1-p_2p_b}{p_2p_b}\right)^2 \left(\frac{2p_2p_b-1}{p_2p_b}\right)^{n-1} \\ &= M_2 \left(\frac{1-p_2p_b}{p_2p_b}\right)^2 \exp\left[(n-1)\ln\left(\frac{2p_2p_b-1}{p_2p_b}\right)\right] \end{aligned} \tag{186}$$

In Eq. (186) the fraction of bonding sites belonging to α-valent particles, is $p_\alpha = \alpha M_\alpha/(fM_f + 2M_2)$, with $\alpha = 2, f$, and the bond probability $p_b = N_b/N_b^{\max}$, where N_b is the number of bonds and $N_b^{\max} = (fM_f + 2M_2)/2$ is the maximum number of bonds (all these quantities are the same as those defined in Sec. 3.5.1).

Taking the limit $p_b \to 1$ (which is justified by the fact that the network is almost fully bonded) in Eq. (186), we obtain

$$\begin{aligned} m_n &= M_2 \left(\frac{fM_f}{2M_2}\right)^2 \exp\left[(n-1)\ln\left(1-\frac{fM_f}{2M_2}\right)\right] \\ &= m_1 \exp\left\{(n-1)\ln\left[1-\frac{f}{2}\left(\frac{c}{1-c}\right)\right]\right\}. \end{aligned} \tag{187}$$

Therefore, in the fully-bonded limit the slope of the exponential only depends on f and on c. This is shown in Fig. 58a, where we show m_n/m_1 for systems with different f, c and density $\rho = (M_f + M_2)/V$: As we can see, data for different ρ collapse on the same master curves controlled by f and c.

From Eq. (186) we can also calculate the average strand length N_s, defined as $\langle n \rangle_n$, where $\langle \cdot \rangle_n$ denotes the weighted average over the strand lengths:

$$N_s \equiv \langle n \rangle_n = \frac{1}{M_s} \sum_{n=1}^{\infty} m_n n \tag{188}$$

where $M_s \equiv \sum_{n=1}^{\infty} m_n$ is the total number of strands[e] . The result is

$$N_s = \frac{p_2 p_b}{1 - p_2 p_b}. \tag{189}$$

In the limit $p_b \to 1$, we have

$$N_s = \frac{p_2}{1 - p_2} = \frac{p_2}{p_f} = \frac{2M_2}{fM_f} = \frac{2}{f}\left(\frac{1-c}{c}\right) = \frac{F}{fc} - 1. \tag{190}$$

We note that using the FS expression we would get $N_s = F/fc$: the difference between the two expressions is therefore more relevant when the value of $\langle m_n \rangle$ is small, as expected.

In Fig. 58b we compare the data for N_s with the theoretical prediction of Eq. (190). Since all the systems are in the fully-bonded state, we have $p_b = 1$. As discussed in 6.1, the removal of the dangling ends has the effect of converting a small number of tetravalent crosslinkers into trivalent ones. This must be taken into account when calculating N_s from Eq. (190):

$$N_s = \frac{p_2}{1 - p_2} = \frac{p_2}{p_3 + p_4} = \frac{2M_2}{3M_3 + 4M_4}. \tag{191}$$

As one can see, the agreement between Eq. (191) and the data is basically perfect: In all the systems considered, the relative error made when using Eq. (191) is smaller than 10^{-4}.

6.2.2 *Strand conformation*

In order to study the conformation of the strands, we study the radius of gyration of the strand segments $R_g(n)$, where n is is the chemical length of a strand segment. We note that $R_g(1) = 0$ and $R_g(2) = l_b/2$, where $l_b \simeq 0.97$ is the RMS bond length, $l_b = \sqrt{\langle (\mathbf{r}_{i+1} - \mathbf{r}_i)^2 \rangle}$, with $i, i+1$ denoting consecutive monomers belonging to the same chain[f]. For large values of n, we expect $R_g(n) \propto (n-1)^{\nu}$, with $\nu \simeq 0.588$, since our model corresponds to chains in an athermal solvent. In Fig. 59a we show $R_g(n)$ for the systems with $f = 3$ and those with $f = 4$. One can see that for large values of n, we indeed observe $R_g(n) \propto (n-1)^{\nu}$. We also note that at fixed n, $R_g(n)$ is with very good approximation independent of the crosslinker concentration c and of the crosslinker valence f, and only depends on the density of the system. For small values of n, $R_g(n)$ *increases* with increasing ρ, as one can see from Fig. 59b, where we represent the mean squared radius of gyration $R_g^2 \equiv \langle R_g^2(n) \rangle_n$, normalized by

[e] For a fully-bonded network ($p_b = 1$), $M_s = \frac{1}{2}\sum_{f>2} M_f f = M_{\text{tot}}\langle f \rangle/2$, where $\langle f \rangle \equiv \sum_{f>2} f M_f$ is the mean crosslink functionality. This is because to every f-valent crosslinks are connected $f/2$ strands.

[f] The parameter l_b actually depends on ρ, f and c; however, these dependences are very weak and therefore l_b can be considered as constant.

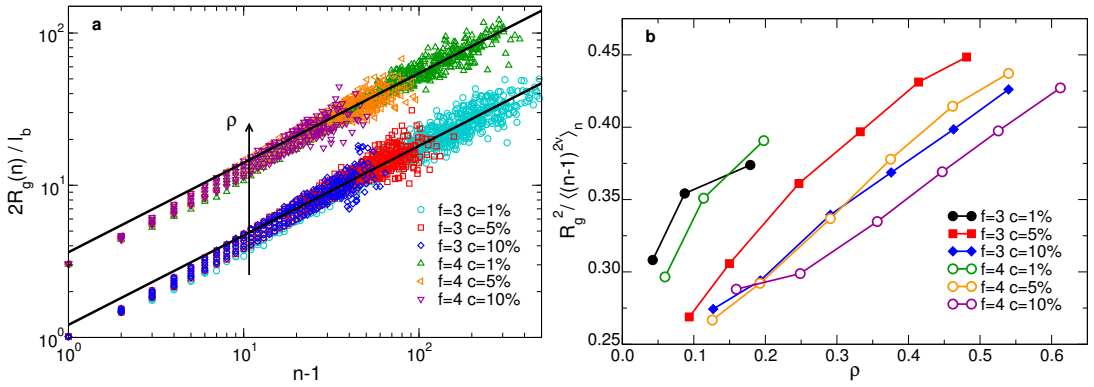

Figura 59 – (a) Mean radius of gyration of the strands of length n, $R_g(n)$, normalized by $R_g(2) = l_b/2$, as a function of $n-1$. Continuous lines are power laws $R_g(n) \propto (n-1)^\nu$, with $\nu = 0.588$. The data for $f = 4$ have been shifted up by a factor 3 in order to improve visualization. Note that for each pair of f, c values, all the densities considered are included in the plot. (b) Mean strand radius of gyration $R_g^2 \equiv \langle R_g^2(n) \rangle_n$, normalized by $\langle (n-1)^{2\nu} \rangle_n$, as a function of density, for different values of f and c.

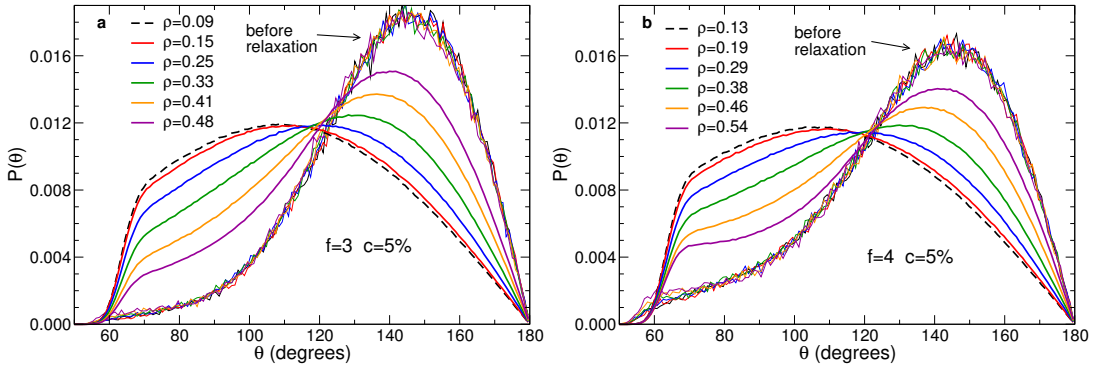

Figura 60 – Bond angle distribution $P(\theta)$ for $f = 3, c = 5\%$ (a) and $f = 4, c = 5\%$ (b). Thin lines: bond angle distribution before the system is allowed to relax to zero pressure.

$\langle (n-1)^{2\nu} \rangle_n$, as a function of ρ. From Fig. 59b, we can also see that in the systems $f = 4, c = 5\%$ and $f = 3, c = 10\%$, which have the same mean functionality F, the strands have basically the same conformation. The same qualitative behavior is observed when considering the end-to-end distance R_e (not shown).

The fact that R_g increases with increasing density may appear paradoxical, since in polymeric systems with free chains R_g usually *decreases* with increasing ρ (cf. Eq. (24)). This behavior, however, can be understood qualitatively by analyzing the bond angle distribution of the strands, $P(\theta)$ (see Sec. 8.2.3). In Fig. 60 we report $P(\theta)$ for $f = 3, 4$ and $c = 5\%$ (the other systems show the same qualitative behavior), compared with the same quantity calculated before changing the interaction potential from patchy to Kremer-Grest and allowing the system to relax to $P = 0$ (thin lines). Before the system is brought to $P = 0$, $P(\theta)$ displays a peak at $\theta \simeq 142°$, which comes from the form of the patchy potential. We note that at this stage, $P(\theta)$ only depends on f and c and not on ρ_{init}. When the system relaxes to $P = 0$, the chains are allowed to relax: As a result, the curve assumes a more gentle profile, and the peak shifts to lower values of θ. For high ρ, $P(\theta)$ retains a shape which is quite similar to the shape it had before relaxation, signaling the presence of strong topological constraints

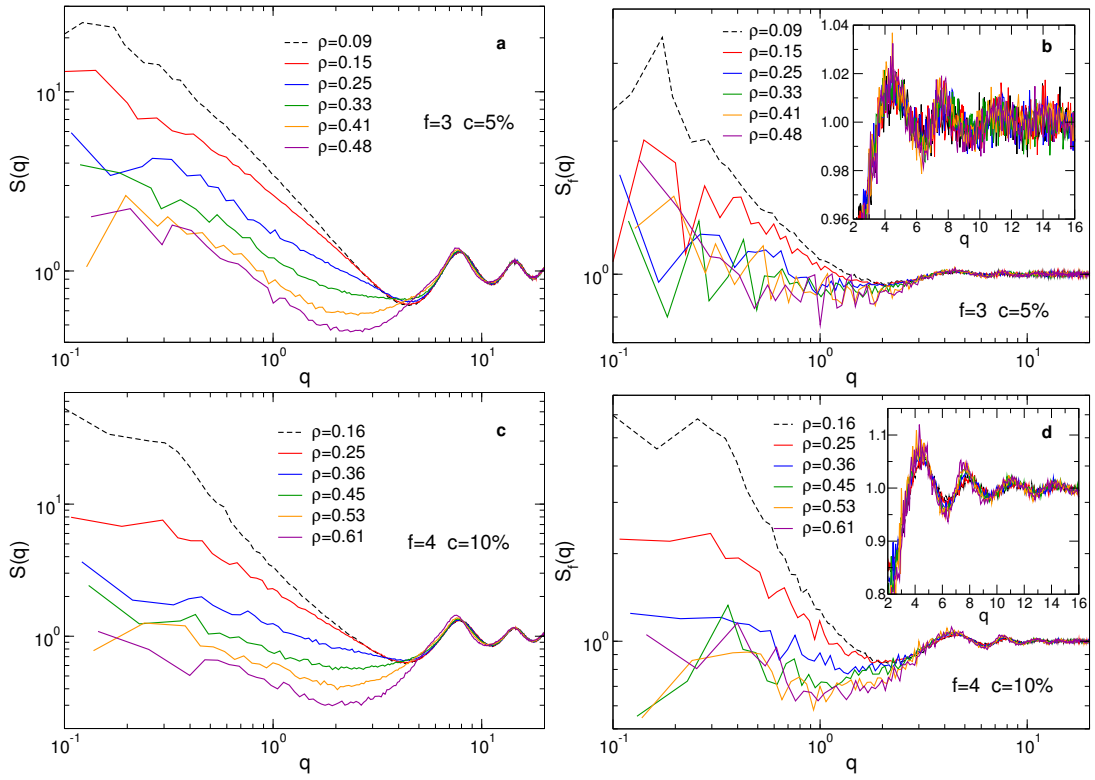

Figura 61 – Total structure factor $S(q)$ (a,c) and structure factor of the crosslinks $S_f(q)$ (b,d) for the systems $f = 3, c = 5\%$ and $f = 4, c = 10\%$. *Insets of Figs. b and d*: $S_f(q)$ in linear scale.

(entanglement), which were formed during the building of the network and are a result of the non-crossability of the strands. For low ρ, the network can completely relax and $P(\theta)$ assumes a form identical to that of chains in a dilute solution (cf. Fig. 98). We note that $P(\theta)$ drops to zero for $\theta \lesssim 60°$ because of the excluded volume interaction. We can see that for both systems, the average bond angle $\langle\theta\rangle$ increases with increasing density: This results in an increase of the persistence length of the strands, and therefore an increase of $R_g(n)$[g].

6.2.3 *Structure factor*

To gain insight into the global structure of the network, it is useful to study the structure factor $S(q)$. In Fig. 61, we report the total structure factor $S(q)$ (61a-c) and the structure factor of the crosslinks $S_f(q)$ (61b-d) for $f = 3, c = 5\%$, $f = 4, c = 10\%$ and different values of the monomer density ρ. The structure factors of the other systems display the same qualitative features. All the systems display a rather large isothermal compressibility $\kappa_T = S(0)/\rho k_B T$, which increases with decreasing density. For small values of q, $S(q)$ decreases approximately as a power law, $S(q) \propto q^{-\alpha}$[h]. The value of α decreases with increasing monomer densities; for the systems studied here, it was found that $0.5 \lesssim \alpha \lesssim 1.3$. This behavior results from the existence of holes on all length scales, i.e., from a fractal void space[76,317]. For larger q, $S(q)$ behaves very similarly to the structure factor of a polymer solution (cf. Fig. 99), with a

[g] Although it is possible to conceive cases for which an increase in $\langle\theta\rangle$ causes a *decrease* of the persistence length (e.g., a rigid "accordion-like" chain), nothing seems to suggest that this is the case here.

[h] The same behavior was observed by Russo and Sciortino in a trivalent patchy-particle network[61].

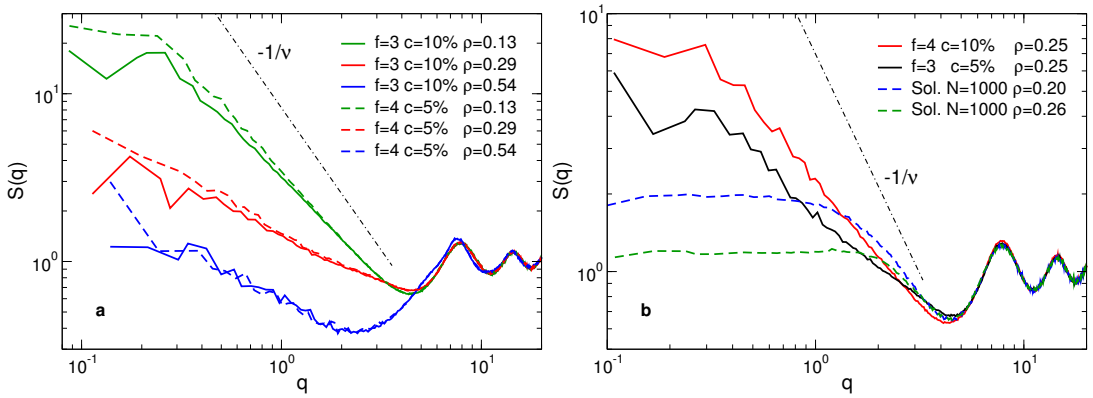

Figura 62 – (a) Comparison between the structure factor $S(q)$ of the $f = 3, c = 10\%$ system and that of the $f = 4, c = 5\%$ system for different densities. We note that these systems have the same mean valence F and the same density ρ (see also Fig. 57). (b) Comparison between the structure factor of two selected systems which have the same density $\rho = 0.25$, but different F (continuous lines). We also show for reference $S(q)$ for a polymer solution of chains of length $N = 1000$ for $\rho = 0.20$ and 0.26.

contact peak[i] at $q \simeq 8 \simeq 2\pi/\sigma$ followed by periodical oscillations.

In Figs. 61b-d, we show the structure factor of the crosslinks, $S_f(q)$, for the same systems. The qualitative behavior of $S_f(q)$ is very similar to that of $S(q)$, with a peak at small q which decays similarly to a power law, followed at larger q by a liquid-like oscillatory behavior. The height of the small-q peak is however much lower than that of $S(q)$, and also the oscillations have much smaller amplitude, signaling that the spatial distribution of the crosslinks is significantly more homogeneous than that of all the monomers. We also note that the contact peak of $S_f(q)$ is found at $q \simeq 4$, which is approximately half the value at which the contact peak of $S(q)$ is found, as it is clearly shown in the insets of Figs. 61b-d. The reason for this behavior is that two f-valent particles cannot bind, so that there is always at least a bifunctional particle between two crosslinks. The distance of closest approach between two crosslinks is therefore $r_c \simeq 2\sigma$, and therefore the contact peak of $S_f(q)$ is found at $q \simeq 2\pi/r_c \simeq \pi/\sigma$ instead of $q \simeq 2\pi/\sigma$.

In Fig. 62a we compare the total structure factors $S(q)$ of the systems $f = 4, c = 5\%$ and $f = 3, c = 10\%$ for different values of the total density ρ. As noted at the beginning of this Chapter, the systems $f = 4, c = 5\%$ and $f = 3, c = 10\%$ have approximately the same mean valence F and therefore they also have the same ratio ρ/ρ_{init}. One can see that curves corresponding to similar densities superimpose almost perfectly, suggesting that $S(q)$ is controlled either by ρ alone or by ρ and F. In Fig. 62b we compare $S(q)$ for two systems with very similar density but different F: The two curves are quite different, suggesting that the behavior of $S(q)$ is determined by both F and ρ. These two structure factors are also compared with the $S(q)$ of a solution of chains of length $N = 1000$ at similar densities. One can see that, due to the presence of the crosslinks, the network has a much higher compressibility. Moreover, the power-law behavior of the network's $S(q)$ at small q suggests that the structure of the network is significantly more heterogeneous than that of the solution.

[i] We use here the same terminology that was introduced in Sec. 5.2.1.

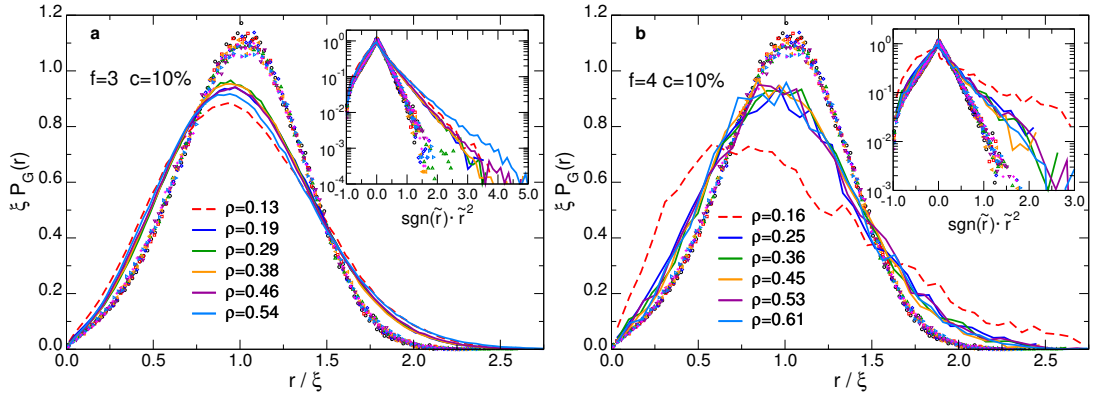

Figura 63 – Gubbins's pore size distribution (PSD) as a function of the rescaled variable r/ξ (lines), with $\xi \equiv \langle r \rangle_G$, for $f = 3, c = 10\%$ (a) and $f = 4, c = 10\%$ (b). Symbols denote the PSD for a solution of linear chains of length $N = 50$ in the density range $0.11 \leq \rho \leq 0.64$. *Insets*: PSD as a function of the rescaled variable $\tilde{r} \equiv r/\xi - 1$ (semi-logarithmic scale).

6.2.4 *Pore size distribution*

To probe the properties of the void space in the system, we calculated Gubbins's pore size distribution (PSD) $P_G(r)$ (see Ch. 8 for the details on how this quantity is calculated). In Fig. 63, we report the rescaled PSD for $f = 3, c = 10\%$ and $f = 4, c = 10\%$. Here $\xi \equiv \langle r \rangle_G$; as discussed in Ch. 8, this quantity can be identified with the geometrical mesh size of the network. The data are compared with the rescaled PSD for a solution of 200 polymer chains of length $N = 50$ in the density range $0.11 \leq \rho \leq 0.64$ (symbols). For $N = 50$, the overlap density is $\rho^* \simeq 0.11$ (Tab. 5); Therefore, all these data points are for systems in the semidilute or concentrated ($\rho > \rho^{**} = 0.3$) regime.

We observe that the rescaled PSD of the network is significantly broader than the one of the solution, indicating that the network is more heterogeneous. For $f = 3, c = 10\%$ (Fig. 63a), all the curves fall basically on the same master curve. The structure of the pore space depends therefore only very weakly on ρ, as for a semidilute/concentrated solution. Also for $f = 4, c = 10\%$ (Fig. 63b) the curves collapse on a master curve, with the exception of the one for the lowest density, $\rho = 0.16$, which is significantly broader. As it will be discussed below, this might indicate that we are approaching a phase separation (cf. also with the corresponding data point in Figs. 64a-b).

In order to better visualize the tails of the PSD, we report in the insets of Fig. 63a-b the PSD as a function of $\mathrm{sgn}(\tilde{r}) \cdot \tilde{r}^2$, where $\tilde{r} \equiv r/\xi - 1$, in semi-logarithmic scale. One sees from these plots that the decay of $P_G(r)$ is approximately Gaussian –a straight line in semi-logarithmic scale– both for the solution and for the network (cf. also with Sec. 8.4.3), although the PSD of the network has a much broader tail.

In Fig. 64a, we report ξ as a function of the monomer density ρ for the simulated networks and for the solutions of linear chains studied in Ch. 8 (chain lengths $N = 1000, 200$ and 50), in the density range $0.04 < \rho < 0.64$. We recall that the expected scaling behavior for ξ is given by Eq. (30)[j]. We observe that ξ behaves very similarly in the solution and in the network, with the network value being slightly ($\simeq 7\%$) larger than the value in solution. This is likely

[j] The overlap densities and radii of gyration at infinite dilution are given in Tab. 5

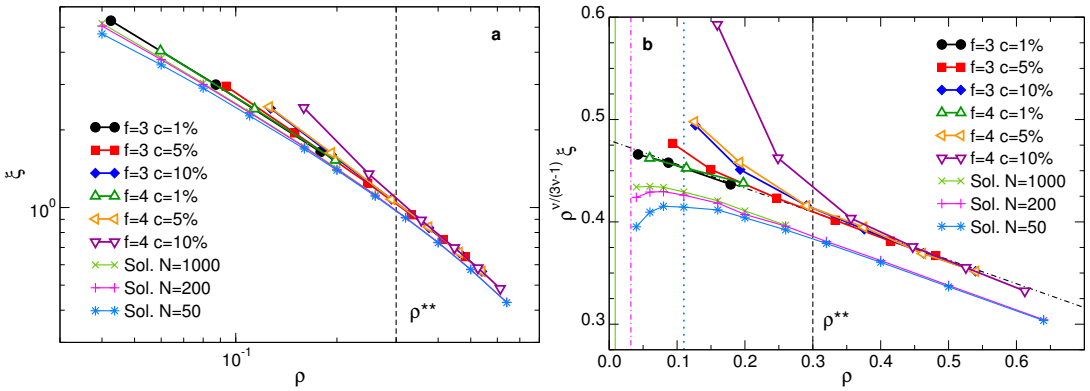

Figura 64 – (a): Mesh size $\xi \equiv \langle r \rangle$ as a function of monomer density ρ for the simulated networks and for solution of linear chains of length $N = 1000, 200$ and 50. $\rho^{**} = 0.3$ is the overlap density for a system of linear chains. (b): Same as (a), but for the rescaled mesh size $\rho^{\nu/(3\nu-1)}\xi$. The dash-dotted line is a linear fit: $0.480 - 0.234\rho$. The continuous, dash-dotted and dotted vertical lines represent estimates of the overlap densities ρ^* respectively for $N = 50$ ($\rho^* \simeq 0.11$), $N = 200$ ($\rho^* \simeq 0.032$) and $N = 1000$ ($\rho^* \simeq 0.0089$).

due to the action of the crosslinks, which cause a local increases in the density field and consequently are responsible for the presence of slightly larger holes.

In Fig. 64b, we report $\rho^{\nu/(3\nu-1)}\xi$ as a function of ρ: For a polymer solution in the semidilute regime, this quantity is expected to be a constant[k] (Eq. (30)). One can clearly see that most data points for the network mesh size fall on a master curve, which is well approximated by a linear function (dash-dotted line). When ρ is decreased, however, some points leave the master curve and display significantly higher values. We observe that the density at which the data leave the master curve decreases with decreasing mean valence F, as it's clear from the fact that the data sets for $f = 3, c = 10\%$ and $f = 4, c = 5\%$, which have the same F, superimpose perfectly. We interpret this phenomenon as a result of the system approaching a gas-liquid phase separation. As discussed in Sec. 6.1, the system of patchy particles used to assemble the network has, for $F > 2$, a gas-liquid coexistence region whose area in the T, ρ plane increases with increasing F (Fig. 56a). Systems with larger F will therefore undergo phase separation at higher ρ for fixed T. We interpret therefore the increase in ξ observed upon lowering of ρ as a signal of the fact that we are entering the coexistence region. We observe that the qualitative change of the PSD when entering the coexistence region is much more apparent that the change in the structure factor (cf. Figs. 61 and 62).

6.3 DYNAMICS AND ELASTIC PROPERTIES

6.3.1 *Mean-squared displacement and localization length*

In order to probe the dynamics of the systems, we will consider the mean-squared displacement (MSD) of: (1) all the particles in the system (2) the crosslinks (3) the central monomers of the strands. Since the simulations are carried out in the NPT ensemble, one has to choose

[k] This behavior can be observed in the semidilute regime, i.e., for density $\rho^*(N) < \rho < \rho^{**}$, where ρ^* is the overlap density. However, the transitions from dilute ($\rho < \rho^*$) to semidilute and that from semidilute to concentrated ($\rho > \rho^{**}$) are both quite broad. Moreover, $\xi \propto \rho^{-\nu/(3\nu-1)}$ can only be properly observed for large values of N. For these reasons, only for $N = 1000$ and $\rho \lesssim 0.1$ we can actually observe a region in which $\rho^{\nu/(3\nu-1)}\xi$ is with good approximation constant in Fig. 64b. More details will be given in Chapter 8.

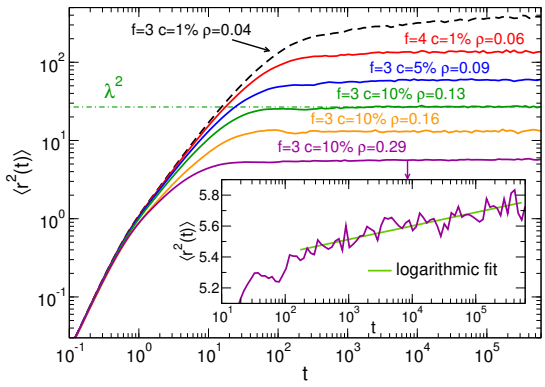

Figura 65 – MSD of all the particles for some selected systems. Dash-dotted line: λ^2, Eq. (192), for $f = 3$, $c = 10\%$, $\rho = 0.13$. *Inset*: Detail of the MSD of the system $f = 3, c = 10\%, \rho = 0.29$. Green line: logarithmic fit.

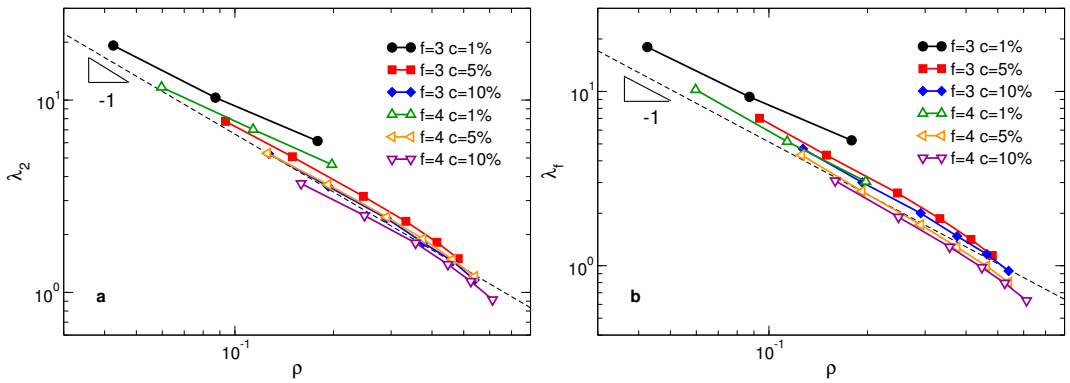

Figura 66 – Localization length of the bifunctional particles (a) and of the crosslinks (b) as a function of ρ. The dashed lines, drawn for reference, are power laws with slope -1.

whether to include the affine "breathing" motion of the simulation box when computing the MSD. We decide to remove this affine motion, i.e., the x coordinate is rescaled as follows: $\tilde{x}(t) = [x(t)/L_x(t)] \cdot \langle L_x \rangle$, where L_x is the box length in the x direction (the y and z coordinates are rescaled analogously). In addition to the rescaling, we also remove the center of mass motion. We note, however, that because of the large system size the breathing motion of the box has such a small amplitude that there is almost no difference if the coordinates are not rescaled.

In Fig. 65 we show the MSD of all the particles for some selected systems. The MSD of the other systems displays the same qualitative behavior. After the initial ballistic regime, $\langle r^2(t) \rangle \propto t^2$, the MSD shows a crossover towards a plateau, a behavior which is typical of networks[60,61,318]. The square root of the MSD in the plateau region, λ indicates the *localization length*, i.e., the typical length scale of the motion the particles perform around their equilibrium positions. For the simulated systems, we can define λ as

$$\lambda^2 \equiv \lim_{t \to \infty} \langle r^2(t) \rangle. \tag{192}$$

One sees that λ increases with decreasing ρ, going from $\lambda \simeq 1$ for $\rho = 0.29$ to $\lambda \simeq 20$ ($\lambda^2 \simeq 400$) for $\rho = 0.04$. These values should be compared with those typical of glass forming liquids, where $\lambda \simeq 0.1$ due to the fact that localization is mainly determined by local packing constraints[244,253]. The considerable difference in value observed here is due to the fact that in the studied systems localization is determined by the connectivity of the network and the non-crossability of the chains rather than by packing constraints. The global topology of the system is fixed, but the particles can still participate in large amplitude breathing modes involving large sections of the network[60,61,318]. We note that the approach to the plateau happens on very long time scales, especially at low density. Even for the denser systems, a closer inspection reveals that in most of the cases the MSD is not really flat, but rather it increases logarithmically. An example of such behavior is shown in the inset of Fig. 65. We conclude therefore that even in the absence of dangling ends these networks can have extremely long relaxation times, most likely due to the fact that the longest strands can take a very long time to explore the whole configuration space.

Despite this very slow relaxation process, it is possible to estimate λ with good accuracy for all the studied systems. We note that λ can be expressed as

$$\lambda^2 = \frac{M_f \lambda_f^2 + M_2 \lambda_2^2}{M_f + M_2} = c\lambda_f^2 + (1-c)\lambda_2^2 \tag{193}$$

where λ_f and λ_2 are the localization lengths of the crosslinks and of the bifunctional particles, respectively. Therefore, it is useful to consider separately λ_2 and λ_f. We note however that since c is relatively small in our systems, $\lambda \simeq \lambda_2$.

In Fig. 66a we show λ_2 as a function of the monomer density ρ. We observe that for $c = 5\%$ and 10%, λ_2 decreases approximately as ρ^{-1} in the studied density range. We also note that the curves for $f = 4, c = 5\%$ and $f = 3, c = 10\%$, which have the same mean valence F, superimpose almost perfectly. This demonstrates that the dynamics of the system is controlled by the pair (F, ρ), as also the strand conformation (Fig. 59b) and the structure (Fig. 62). If the chains could pass through each other, as in the phantom network model

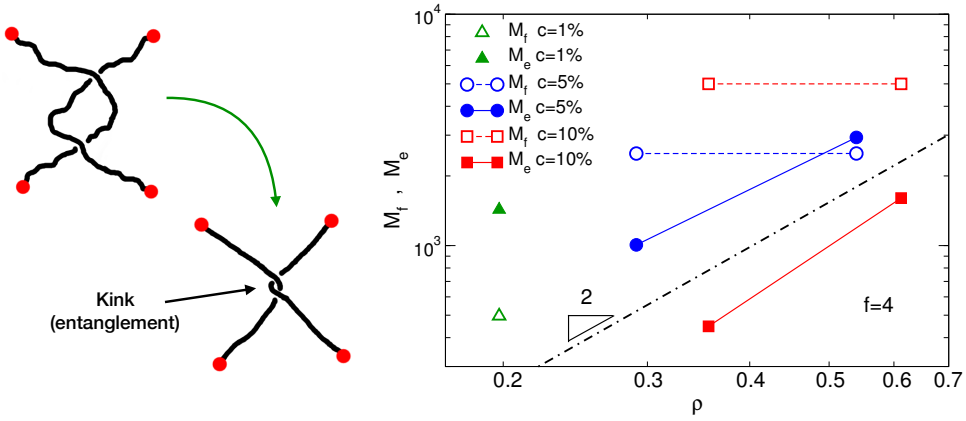

Figura 67 – Number of crosslinks (M_f) and entanglements (M_e) as a function of monomer density ρ for some simulated systems with tetravalent crosslinks ($f = 4$). Cartoon: reduction to the primitive paths for two entangled strands. Red dots represent the crosslinks.

(Sec. 3.5.2), we would expect $\lambda_2^2 \approx R_e^2 \approx b^2 N_s$[74,76], and therefore, since N_s is independent of density (see Sec. 6.2.1), λ_2 would not depend on ρ[1], in contrast with our results. This can be understood by realizing that the excluded volume interaction prevents the chains from interpenetrating: Therefore, the dynamics of the strands is more appropriately described by the reptation model (Sec. 3.4.3), and strands of length $n > N_e$, with N_e the entanglement length, are confined in a tube-like region[76]. For $t \to \infty$, the strand monomers fluctuate along the primitive path (the axis of the tube), with a mean amplitude which depends on the mean strand length N_s and on N_e. Since N_s is independent of ρ, we attribute the decrease of λ_2 with increasing density to a decrease of the entanglement length.

In Fig. 66b we show the localization length λ_f of the crosslinks as a function of density. One sees that λ_f behaves very similarly to λ_2: Indeed, we will see below that we have $\lambda_f \simeq 2\lambda_2/f$. It was argued by Duering *et al.*[76], following Vilgis and Boué[319] that for a network of identical strands of length N_s,

$$\lambda_f^2 \simeq \left(\frac{1}{2R_g^2(N_e)} + \frac{A}{N_s} \right)^{-1}, \tag{194}$$

where A is a constant and $R_g^2(N_e) \approx b^2 N_e$, where b is the effective bond length. For $N_s \gg N_e$, Eq. (194) reduces to $\lambda_f^2 \simeq 2R_g^2(N_e) \approx b^2 N_e \approx d_e^2$, where d_e is the diameter of the entanglement tube. The interpretation is that the crosslinks are only weakly pulled into the strands' tubes, and therefore oscillate around their equilibrium position with an average amplitude given by the diameter of the entanglement tube. In our systems, N_s is fixed, but N_e, as observed above, depends on density. Since λ_f is approximately proportional to ρ^{-1}, Eq. (194) would suggest that in the studied density range N_e decreases approximately as ρ^{-2}.

This result is in agreement with preliminary results from the primitive path analysis, which are shown in Fig. 67. Using the primitive path analysis algorithm of Everaers *et al.*[75,320], we counted the number M_e of entanglement points for some selected system with tetravalent crosslinks. The procedure is as follows: (1) The crosslinks are fixed in space, then (2) the

[1] Although we won't show it here, this is (almost) exactly what happens if we turn off all the excluded volume interactions except for those between nearest neighbors.

inter-chain excluded volume interactions are turned off, while the intra-chain interactions are kept, and finally (3) the system is cooled to $T = 0$[75]. Since inter-chain excluded volume interactions are disabled, the chains are straightened; however, the intra-chain interaction still prevents the chains from passing through each other, and thus the topology is conserved. The network is thus reduced to a mesh of primitive paths. M_e can then be calculated by counting the number of kinks which are formed when two entangled chains are straightened (cartoon in Fig. 67).

Since to every entanglement point are associated on average two entanglement strands[mn], we have

$$M_e \simeq \frac{M_{\text{tot}}}{2N_e} \tag{195}$$

Even though the analysis was carried out only for two systems for $c = 5\%$ and $c = 10\%$, one can see from Fig. 67 that the behavior of M_e as a function of ρ is compatible with a power law with exponent 2, which would be in agreement with $N_e \propto \rho^{-2}$. We also note that for $c = 10\%$ the number M_f of crosslinks is larger than M_e in the whole density range considered. For $c = 5\%$, on the other hand, we have $M_f > M_e$ at low density, but there is a crossover density ρ_{cross} such that for $\rho > \rho_{\text{cross}}$ we have $M_e > M_f$. For $c = 1\%$, only density $\rho = 0.20$ was considered, and it was found that the M_e is significantly larger than M_f. Knowing wether the density of crosslink M_f/V is larger than the density of entanglements M_e/V is relevant in many situations, and notably when considering the diffusion of nanoparticles in polymer networks, as we discussed in Sec. 4.2.4. It is important to stress that in our systems an increase in ρ is not equivalent to that which we would obtain by simply compressing the system (i.e., by collapsing the network). The reason is that our networks are *generated* at different densities, and this influences the way the strands entangle.

In Fig. 68 we compare the MSD of the crosslinks, $\langle r_f^2(t)\rangle_{f=3,4}$, with the MSD of the bifunctional particles, $\langle r_2^2(t)\rangle$, for the systems with $c = 5\%$ and $c = 10\%$. We find that the ratio $\langle r_f^2(t)\rangle / \langle r_2^2(t)\rangle$ is well approximated by the expression

$$\frac{\langle r_f^2(t)\rangle}{\langle r_2^2(t)\rangle} = \frac{2}{f}. \tag{196}$$

To show this, in Fig. 68 the MSD of the bifunctional particles is multiplied by a factor $2/f$. One can see that Eq. (196) is satisfied to a very good approximation, with the agreement being better for intermediate values of ρ[o].

To test the generality of Eq. (196), we also run some simulations of networks with pentavalent ($f = 5$) crosslinks. In Fig. 69a we compare the MSD of the crosslinks and that of the

[m] Two strands can have more than one entanglement. In that case, there can be fewer than two entanglement strands per entanglement point. When writing Eq. (195), we make the assumption that these configurations are rare.

[n] The corresponding relation for the number of crosslinks is $M_f = 2M_{\text{tot}}/(\langle f\rangle N_s)$, since there are on average $\langle f\rangle/2$ strands per crosslinks.

[o] The same relation was found in simulations of trivalent ($f = 3$) networks by Russo *et al.*[61]. The authors, however, claimed that the general form of this relation, derived from the phantom network model (PNM), is $\langle r_f^2(t)\rangle / \langle r_2^2(t)\rangle = 6/f^2$. Unfortunately, although $6/f^2 = 2/f$ for $f = 3$, this relation is incorrect even in the framework of the PNM (see Appendix B). Values approximately verifying Eq. (196) were also found in a simulation study by Kenkare *et al.*[294].

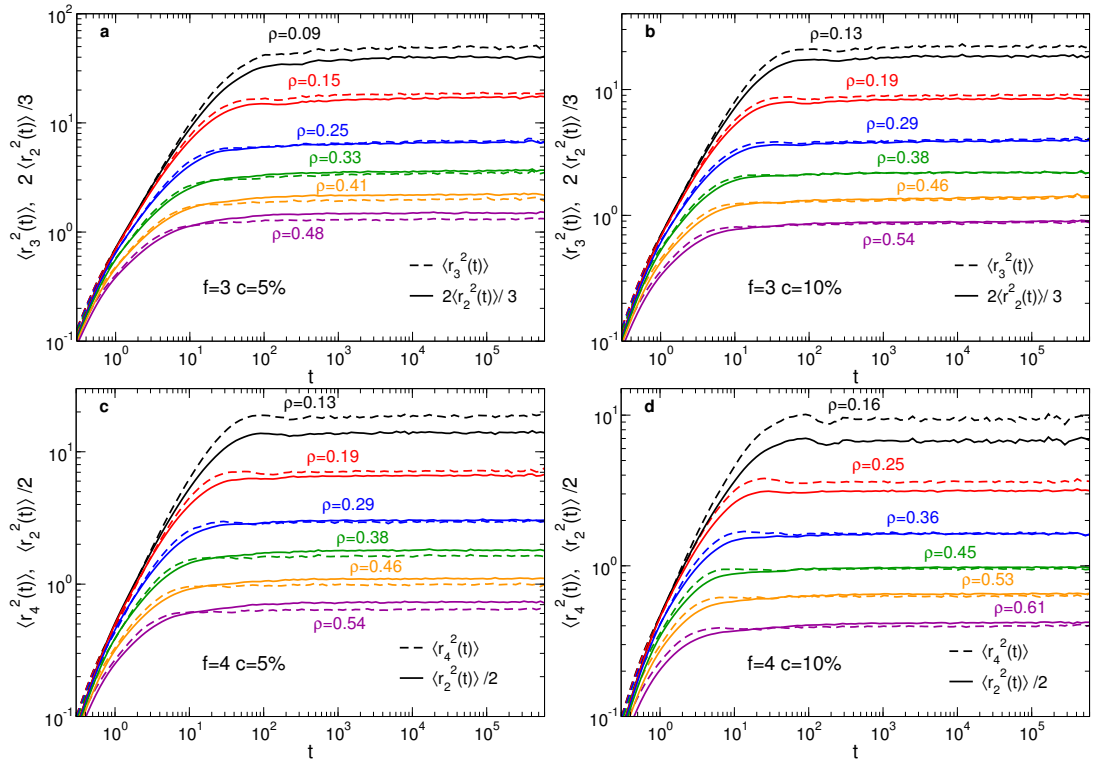

Figura 68 – Comparison between the MSD of the crosslinks, $\langle r_f^2(t)\rangle$, and that of the bifunctional particles, $\langle r_2^2(t)\rangle$, for some selected simulated systems. (a) $f = 3, c = 5\%$ (b) $f = 3, c = 10\%$ (c) $f = 4, c = 5\%$ (d) $f = 4, c = 10\%$. In all cases, the MSD of the bifunctional particles has been rescaled according to Eq. (196).

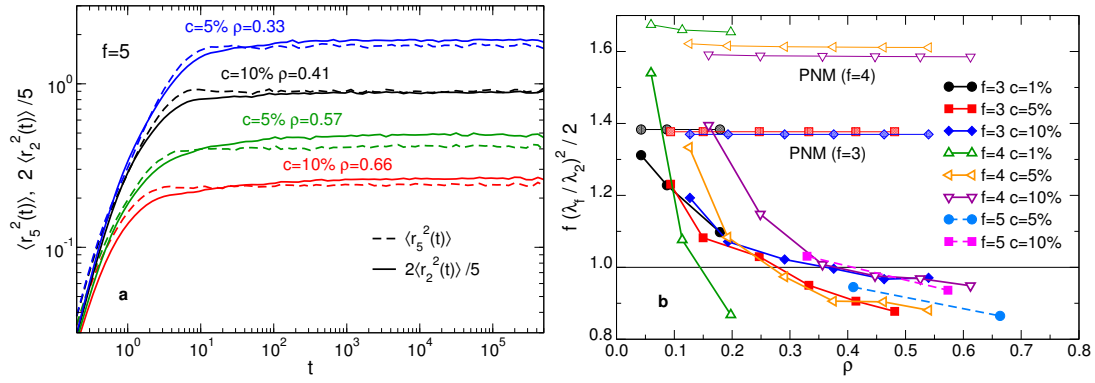

Figura 69 – (a) Comparison between the MSD of the crosslinks, $\langle r_f^2(t)\rangle$, and that of the bifunctional particles, $\langle r_2^2(t)\rangle$, for some selected systems with pentavalent ($f = 5$) crosslinks. In all cases, the MSD of the bifunctional particles has been rescaled according to Eq. (196). (b) $f(\lambda_2/\lambda_f)^2/2$ (cf. Eq. (198)) as a function of monomer density ρ. λ_2 and λ_f are the localization lengths of the bifunctional particles and of the crosslinks, respectively.

bifunctional particles for these systems. One can see that also in this case Eq. (196) gives with very good approximation the correct relation between $\langle r_f^2(t)\rangle$ and $\langle r_2^2(t)\rangle$.

Eq. (196) can be understood by considering the MSD $\langle r_{\mathcal{N}}^2\rangle$ of an harmonic oscillator attached to $\mathcal{N}$ identical springs with spring constant K: From the equipartition theorem[263], we obtain

$$\langle r_{\mathcal{N}}^2\rangle = \frac{3k_BT}{\mathcal{N}K} \tag{197}$$

By taking the ratio of Eq. (197) with $\mathcal{N} = f$ and $\mathcal{N} = 2$, we immediately obtain Eq. (196). In the limit $t \to \infty$, Eq. (196) becomes

$$\lim_{t\to\infty} \frac{\langle r_f^2(t)\rangle}{\langle r_2^2(t)\rangle} = \frac{\lambda_f^2}{\lambda_2^2} = \frac{2}{f} \;\longrightarrow\; \frac{f}{2}\left(\frac{\lambda_f}{\lambda_2}\right)^2 = 1, \tag{198}$$

where λ_2 and λ_f are the localization lengths respectively of the bifunctional particles and of the crosslinks. In Fig. 69b we show $f(\lambda_f/\lambda_2)^2/2$ as a function of monomer density ρ. We observe from this plot that the relation (196) works better for higher crosslink concentrations c and for higher densities, whereas for low c, ρ theagreement between the formula and the date gets significantly worse. In particular, we observe that for $f = 3, 4, 5$ and $c = 10\%$, $f(\lambda_f/\lambda_2)^2/2$ tends approximately to 0.95, whereas for $c = 5\%$ it tends to a somewhat smaller value. For $c = 1\%$, the available data do not allow to reach any conclusion regarding the high-ρ behavior.

In order to compare the data with and analytical expression, we have also calculated $(\lambda_f/\lambda_2)^2$ in the framework of the phantom network model (PNM – see Sec. 3.5.2). The result is (see Appendix B)

$$\frac{f}{2}\left(\frac{\lambda_f}{\lambda_2}\right)^2 = \frac{f}{2}\left[1 + \frac{(f-2)^2}{f-1}\left(\frac{N_s+2}{6(N_s+1)}\right)\right]^{-1} \quad \text{(PNM)}. \tag{199}$$

The values of $f(\lambda_f/\lambda_2)^2/2$ for $f = 3$ and $f = 4$ calculated from Eq. (199) are reported in Fig. 69b. We see that in the limit $\rho \to 0$, $f(\lambda_f/\lambda_2)^2/2$ tends with good approximation to the PNM result. At present, it is not clear if the PNM result is really recovered in the limit $\rho \to 0$, and if it is recovered, what is the exact cause. We have also performed simulations of "phantom chains", removing the excluded volume interactions except that for the bonded particles[p] (data not shown). These simulation revealed that even in these systems $f(\lambda_f/\lambda_2)^2/2$ displays the same qualitative behavior observed in Fig. 69b for the systems with excluded volume, i.e., $f(\lambda_f/\lambda_2)^2/2 \simeq 1$ for large ρ and an approach towards the PNM result when ρ is decreased. This suggests that the reason for the recovery of the PNM result at low ρ is not simply the fact that the excluded volume interaction are less relevant at low density. Further investigations, which will be carried out in future work, are needed in order to clarify this point.

In order to better understand the collective dynamics of the strands, we have studied the MSD $\langle r^2_{(n+1)/2}(t)\rangle$ of the central monomers of the strands[q]. The results are shown in Fig. 70 for $f = 3, c = 10\%, \rho = 0.25$ and $f = 4, c = 10\%, \rho = 0.36$. In order to improve the statistics,

[p] These simulations are performed in the NVT ensemble, with $V = \langle V\rangle$, otherwise the system would collapse.
[q] For the central monomers to be well-defined, we only considered strands of uneven length.

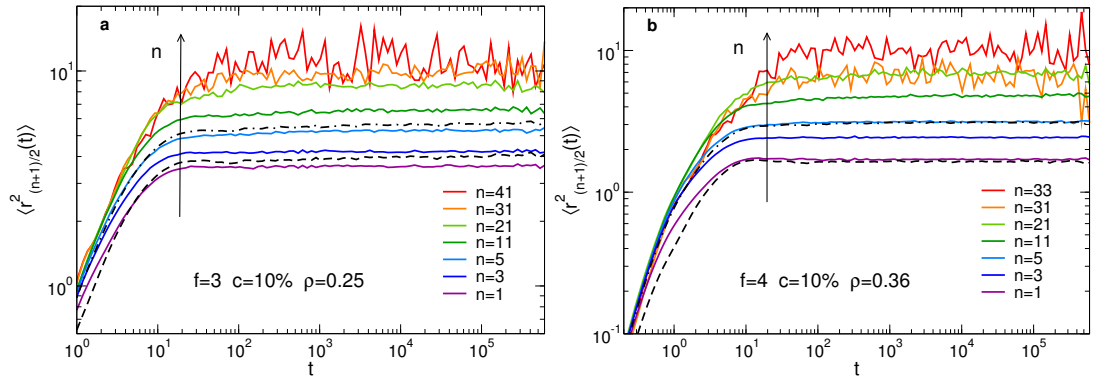

Figura 70 – MSD of the middle monomers of the strands of length n. (a) $f = 3, c = 10\%, \rho = 0.25$ (b) $f = 4, c = 10\%, \rho = 0.36$. Dashed lines: MSD of the crosslinks. Dash-dotted lines: MSD of all the particles.

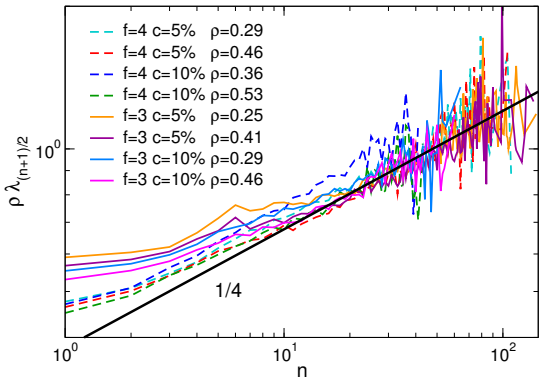

Figura 71 – Localization length of the central monomers of the strands $\lambda_{(n+1)/2}$, multiplied by the monomer density ρ, as a function of the strand length.

we show here the data for the systems of $4 \cdot 10^5$ particles instead of those of $5 \cdot 10^4$. We observe that the localization length $\lambda_{(n+1)/2}$ of the central monomers, which for $n = 1$ is very similar to that of the crosslinks, increases monotonically with increasing strand length n, reaching for large n values much higher than that of the mean localization length λ. As previously discussed, the strands of length $n > N_e$ are confined in a tube whose contour length is $\mathcal{L}_T \approx d(n/N_e) \approx bnN_e^{-1/2}$ (see Sec. 3.4.3). At long times, the middle monomers will fluctuate along the primitive path (the "axis" of the tube), and since the tube itself is a random walk we will have[76]

$$\lambda_{(n+1)/2} \propto \mathcal{L}_T^{1/4} \propto n^{1/4} \quad (n > N_e). \tag{200}$$

This result is illustrated in Fig. 71, where we show $\rho\lambda_{(n+1)/2}$[r] as a function of n for the systems of $4 \cdot 10^5$ particles. One clearly sees that, whereas the small-n behavior of $\rho\lambda_{(n+1)/2}$ depends on f[s], the large-n behavior is basically independent of f and $\rho\lambda_{(n+1)/2} \propto n^{1/4}$.

[r] The ρ prefactor is justified by the fact that λ is approximately proportional to ρ^{-1}, see Sec. 6.3.1.
[s] The dependence on c is much weaker.

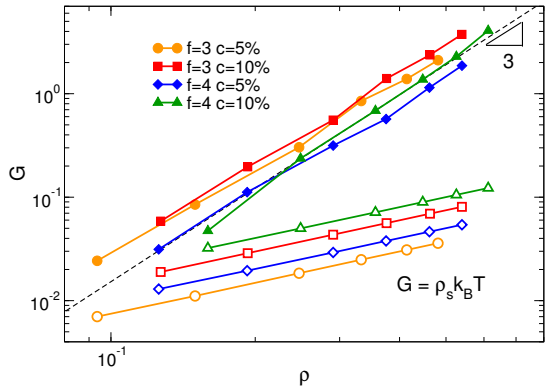

Figura 72 – Shear modulus G of the network as a function of monomer density for crosslink concentration $c = 5\%$ and $c = 10\%$. Filled symbols: simulation data. Open symbols: affine network model prediction.

6.3.2 *Shear modulus*

In order to characterize the elastic properties of the network, we study the shear modulus G (Sec. 3.5.2) in the linear regime. To measure G, we use the method used in Ref. 300, which we briefly describe in Appendix C. Even though in Ref. 300 this method was used to measure the shear modulus of microgel particles, it can readily be applied to bulk systems such as those studied here.

In Fig. 72, we show G as a function of the total density ρ. In Sec. 3.5.2, we briefly discussed two simple models of rubber elasticity and their predictions for G: The affine model predicts $G = \rho_s k_B T$, where ρ_s is the strand density, whereas the phantom network model predicts $G = \rho_s k_B T(1 - 2/\langle f \rangle)$. Since $\rho_s = \rho/N_s$, both models predict therefore that G scales linearly with monomer density, i.e., $G \propto \rho$. We can see, however, that this is not the case, as the shear modulus of the studied systems scales approximately as ρ^3 (dashed line in Fig. 72). This behavior can be rationalized by taking into account the presence of the entanglements. When entanglements are present, G can be approximated as $G \simeq k_B T \rho_s^{\text{eff}}$, where ρ_s^{eff} is an effective strand density resulting from the combined effect of the crosslinks and of the entanglements (see Sec. 3.5.2):

$$\rho_s^{\text{eff}} \approx \rho \left(\frac{1}{N_s} + \frac{1}{N_e(\rho)} \right). \tag{201}$$

From Eq. (201) and the data shown in Fig. 72, we deduce that in the density range here considered the entanglement length follows approximately $N_e \propto \rho^{-2}$[t]. We note the same relation was found from considerations on the behavior of the localization length λ_f of the crosslinks as a function of density and is compatible with the preliminary results of primitive path analysis (Sec. 6.3.1).

[t] It is interesting to note that the same dependence of N_e on ρ can be obtained via simple scaling considerations applied to melts of monodisperse chains[321], where it is found that $N_e \propto \rho^{-2}(R_e^2/N)^{-3}$ (N = chain length), although a melt has usually a very specific density (usually $0.84 - 0.85$ in simulations of the Kremer-Grest model) and therefore the ρ appearing in this relation should be considered in principle as a constant prefactor.

7

NANOPARTICLE DIFFUSION IN POLYMER NETWORKS

The data and considerations presented in this Chapter are the result of ongoing research and are thus in some parts incomplete, and/or will be subject to revision. The ideas and results presented will be the object of a future publication[322].

As discussed in Chapter 6, understanding the dynamical properties of NPs embedded in polymer networks is a problem of great interest in many different fields, from material science[271–275] to biophysics[266–270]. In Sec. 4.2.4 we have discussed how the presence of crosslinks (or entanglements) influences NP diffusion in a polymer system in a radical way, by fixing the topology of the system and therefore turning off the constraint release mechanism. When the confinement parameter C, defined as the ratio between the NP diameter σ_N and the effective tube diameter d (Eq. 97), becomes significantly larger than 1, the NPs are trapped in the mesh and can only move through the non-Gaussian process of activated hopping. The two main theories of hopping, i.e., the Dell-Schweizer (DS) theory[191] and the CPR theory of hopping[185] give qualitatively different predictions regarding the behavior of the NP diffusion coefficient D as a function of the confinement parameter in the hopping regime ($C \gtrsim 1$). According to the DS theory, D is approximated by Eq. (132), while according to CPR theory it follows either Eq. (134) or Eq. (136), depending on whether $N_e > N_x$ (unentangled regime) or $N_x > N_e$ (entangled regime). Here N_x is the mean length of the elastically active strands and N_e the entanglement length. Simulations can provide a useful tool to determine which theory gives the best description of this kind of systems: However, while the diffusion of NPs in polymer solutions and melts has been the object of numerous simulation studies in the past years[77,148,179,199,215,226–232], much fewer works dealt with the problem of NP diffusion in crosslinked networks[276–282]. In the present Chapter, we will study the diffusion of spherical NPs in the same polydisperse, disordered networks which were the subject of Chapter 6, trying to shed some light on the fundamental mechanism governing the motion of NPs in polymeric systems in which constraint release has been turned off.

7.1 MODEL AND METHODS

We consider spherical NPs of diameter σ_N ranging from $\sigma_N = 2$ to $\sigma_N = 8$ in a polymer network of $M \simeq 4 \cdot 10^5$ monomers with trivalent ($f = 3$) crosslinks at concentration $c = 10\%$ (mean valence $F = 2.1$). We consider three different networks, with monomer densities $\rho_{m0} = 0.183$, 0.286 and 0.370 in the neat state. To simulate the NPs, we use the expanded Lennard-Jones potential (Eq. (144)), described in Sec. 4.4, with $\Delta_{Nm} = (\sigma_N + \sigma)/2 - \sigma = (\sigma_N - \sigma)/2$ and $\Delta_{NN} = \sigma_N - \sigma$. This potential is the same that was used in the simulations described in Chapter 5. However, in the present work we choose cutoff radii $r^c_{Nm} = r^c_{NN} = 2^{1/6}$, so that

Tabella 3 – Properties of the simulated systems. σ_N: NP diameter. $\rho_{m0} = M/\langle V \rangle_0$: monomer number density in the neat system (we note that this value does not depend on σ_N). N_N: Number of NPs. ρ_m: monomer number density in the filled system. $\phi_m = \pi \rho_N \sigma^3/6$: monomer volume fraction. $\phi_N = \pi N_N \sigma_N^3/(6V)$: NP volume fraction. $C_r \equiv \sigma_N/\lambda_f$: Confinement ratio (see Sec. 7.4.2).

σ_N	ρ_{m0}	N_N	ρ_m	ϕ_m	ϕ_N	C_r
2.0	0.183	9755	0.1513	0.0792	0.0165	0.641
3.0	0.183	2890	0.1653	0.0866	0.0181	0.962
4.0	0.183	1219	0.1706	0.0893	0.0186	1.282
5.0	0.183	624	0.1732	0.0907	0.0189	1.603
6.0	0.183	361	0.1747	0.0915	0.0191	1.923
7.0	0.183	228	0.1756	0.0920	0.0192	2.244
8.0	0.183	152	0.1761	0.0922	0.0192	2.564
2.0	0.286	6538	0.2596	0.1359	0.0181	0.997
3.0	0.286	1937	0.2694	0.1411	0.0188	1.496
3.5	0.286	1220	0.2719	0.1424	0.0190	1.745
4.0	0.286	817	0.2731	0.1430	0.0191	1.994
4.5	0.286	574	0.2745	0.1437	0.0192	2.244
5.0	0.286	418	0.2753	0.1441	0.0192	2.493
6.0	0.286	242	0.2769	0.1450	0.0193	2.991
2.0	0.370	5028	0.3452	0.1807	0.0187	1.327
3.0	0.370	1490	0.3537	0.1852	0.0191	1.991
3.5	0.370	938	0.3550	0.1859	0.0192	2.323
4.0	0.370	629	0.3564	0.1866	0.0193	2.655
4.5	0.370	441	0.3574	0.1871	0.0193	2.987
5.0	0.370	322	0.3574	0.1871	0.0193	3.319

both the NP-monomer interaction and the NP-NP interaction are purely repulsive. In the simulations described in Chapter 5, a cutoff radius $r^c_{Nm} = 2.5$ was chosen for the NP-monomer interaction, since an attractive interaction was needed in order to prevent NP aggregation and phase separation. In the network, however, the global structure of the polymer strands is fixed, and therefore the entropy gain that would result from NP aggregation is much more limited. Moreover, we only consider very small NP volume fractions, a factor which ulteriorly inhibits aggregation. We assume that the NPs have the same mass density as the monomers, $\rho_{\text{mass}} = 6m/\pi\sigma^3$, and therefore the mass of the NPs is $m_N = m(\sigma_N/\sigma)^3$.

All the simulations were carried out using the LAMMPS software[241,242]. The simulation box is cubic and periodic boundary conditions are applied in all directions. Initially, the NPs are inserted at random positions in the network, allowing for overlaps. The overlaps are then removed using the "fast push-off" method[107], and the NP size is gradually increased until the diameter reaches the value σ_N. We note that this method is identical to the one described in Chapter 5. After the NP have reached the desired size, we perform an NPT run with Nosé-Hoover chains[81] and allow the system to reach pressure $P = 0$ at temperature $T = 1.0$. During the NPT run, the box sides are coupled to each other so that they fluctuate together ($L_x = L_y = L_z$). After the system has adjusted to $P = 0$, we perform a short run in the NPT ensemble, where the mean volume V is measured. Then, we switch to the NVT ensemble by fixing the system's volume to V and perform an equilibration run before starting production. Since the Nosé-Hoover thermostat doesn't produce a realistic dynamics[81], we switch to a Langevin thermostat identical to the one described in Sec. 5.1. The monomer friction coefficient is $\Gamma_m = 0.1$, whereas the NP friction coefficient is $\Gamma_N = \Gamma_m(m\sigma_N/m_N\sigma) = \Gamma_m(\sigma/\sigma_N)^2$, so that an isolated monomer and an isolated NP experience the same solvent viscosity (see Sec. 5.1). For the NVT simulations, we use a velocity Verlet integrator[79]. The integration time step is $\delta t = 0.003$ for equilibration and $\delta t = 0.006$ for production. During the NVT equilibration run (of duration $3 \cdot 10^5$) the NP mass is set to $m_N = 1$, in order to speed up their dynamics and accelerate the exploration of the phase space. After equilibration, we set m_N to its final value, $m_N = \sigma_N$ and perform a short run of duration $3 \cdot 10^4$ which allows us to estimate the time needed for the NP motion to become diffusive and therefore to choose the duration of the production run. We then start the production run, whose duration is between $6 \cdot 10^4$ and $1.2 \cdot 10^6$ depending on the NP diameter and on the monomer density. For larger values of σ_N and ρ_m, longer runs are performed. Based on the discussion of Sec. 4.2.4, we expect the relaxation time of the simulated systems increases *at least* exponentially with the confinement parameter $C = \sigma_N/d$, where σ_N is the NP diameter and d is the dynamical confinement length scale, resulting from both topological entanglements and crosslinks (4.2.4). Therefore, even a small increase of σ_N can mean an enormous increase in the relaxation time. As a consequence, some of the simulated systems didn't fully equilibrate during the equilibration run. We decide nevertheless to report data on the behavior of these systems, since we believe that this can help shed some light on the physics governing the diffusion of NPs in polymer networks. Moreover, the very steep increase of the relaxation time with the confinement parameter means even in experimental systems it will be extremely difficult to reach thermodynamic equilibrium. Therefore, these data can also prove useful in interpreting experimental results.

In order to limit the effect of NP addition on the structural and dynamical properties of the network and to limit inter-NP interactions, we embed in the network a small number of NPs N_N. The value of N_N is chosen in such a way that the total NP volume, $V_N \equiv \pi N_N \sigma_N^3/6$, is 2%

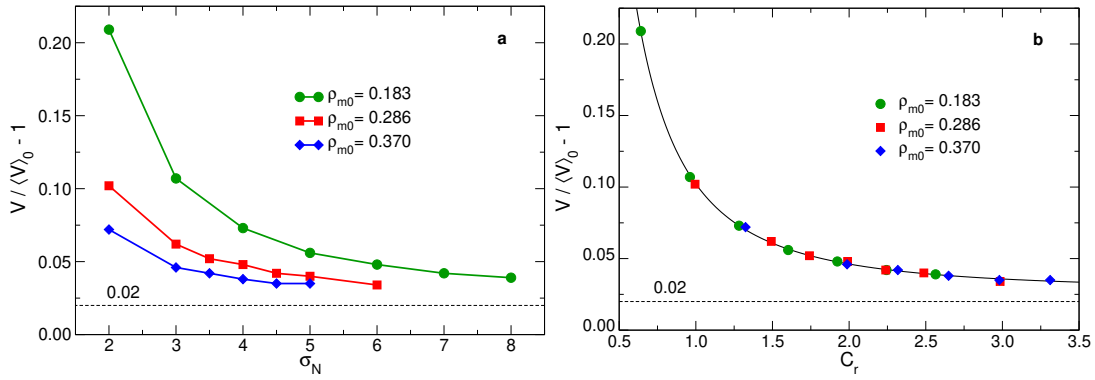

Figura 73 – (a) Expansion factor $V/\langle V\rangle_0 - 1$ as a function of NP diameter σ_N for systems with different monomer densities ρ_{m0} in the neat state. V is the volume of the filled system, whereas $\langle V_0\rangle$ is the mean volume of the neat system, measured in NPT simulations. The dashed line marks the value the expansion factor would have if the expansion was only due to the excluded volume of the NPs. (b): The same quantity as a function of the confinement ratio C_r (see Sec. 7.4.1). Continuous line: Eq. (203) with $A = 2.73 \cdot 10^{-2}$ and $B = 7.48 \cdot 10^{-2}$.

of the mean volume of the neat system, $\langle V\rangle_0$, which was measured in the NPT simulations described in Sec. 6.1. We have therefore

$$N_N = \left\lfloor 0.02 \cdot \frac{6\langle V\rangle_0}{\pi\sigma_N^3} \right\rfloor \simeq \left\lfloor 0.038 \cdot \frac{\langle V\rangle_0}{\sigma_N^3} \right\rfloor . \tag{202}$$

We note that in general $\langle V\rangle_0 \neq V$, since the addition of NPs causes a swelling of the network. This is illustrated in Fig. 73a, where we show the expansion factor $(V - \langle V\rangle_0)/\langle V\rangle_0$ as a function of σ_N for the three networks considered in this work. This quantity is positive for all values of σ_N and ρ_{m0}, signaling an expansion of the system. If the expansion was only due to the excluded volume of the NPs, we would have $(V - \langle V\rangle_0)/\langle V\rangle_0 \simeq 0.02$ (dashed line in Figs. 73a-b), since the total NP volume is $V_N \simeq 0.02\langle V\rangle_0$ (Eq. (202)). However, one sees that the expansion factor is significantly higher than this value for all values of σ_N, and that it increases markedly with decreasing σ_N and ρ_{m0}.

We observe that the data fall on a master curve when plotted as a function of the confinement ratio C_r, as shown in Fig. 73b. This parameter, which will be introduced in Sec. 7.4.1, is defined as the ratio between the NP diameter and the localization length λ_f of the crosslinks (see Sec. 6.3.1). The degree of swelling of the network upon the addition of the NPs depends therefore only on the ratio between the NP size and the typical size of the entanglement mesh. The master curve is very well described by the following functional form (continuous line in Fig. 73b):

$$\frac{V - \langle V\rangle_0}{\langle V\rangle_0} = A + BC_r^{-2} \tag{203}$$

with $A = 2.73 \cdot 10^{-2}$ and $B = 7.48 \cdot 10^{-2}$. We note that Eq. (203) can be rewritten as

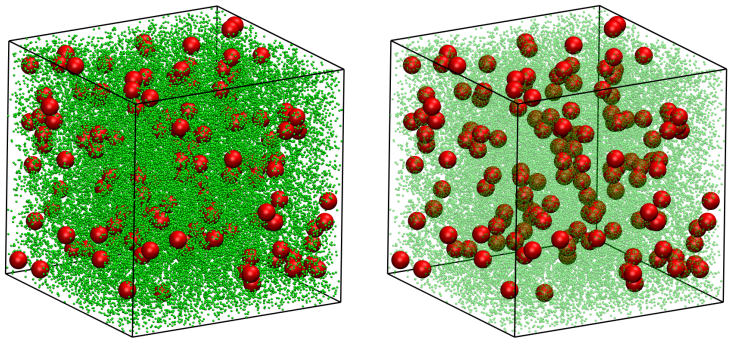

Figura 74 – Snapshot of the system $\rho_{m0} = 0.370$, $\sigma_N = 8.0$ after equilibration. For clarity, only the crosslinks (green) and the NPs (red) are shown. On the left, the crosslinks are shown as transparent to help visualize the NPs.

$$\frac{V - \langle V \rangle_0}{\langle V \rangle_0} = A + B \left(\frac{\lambda_f S_N}{0.12 \langle V \rangle_0} \right)^2 \tag{204}$$

where $S_N = N_N \pi \sigma_N^2$ is the total surface of the NPs. Indeed, from Eq. (202) one obtains $S_N \simeq 0.12 \langle V \rangle_0 \sigma_N^{-1}$, which alongside Eq. (203) gives Eq. (204). The expansion is therefore larger the larger the total surface of the NPs.

The final values of the density are reported in Tab. 3 alongside other relevant parameters. Since ρ_m is not independent of σ_N, we will therefore use the value ρ_{m0} of the density in the neat state to identify unambiguously the three different networks here considered. From the data reported in Tab. 3, one can also see that in all the systems, the final NP volume fraction, $\phi_N = \pi \sigma_N^3 N_N / (6V)$, is between 1.65% and 1.93%. To give the reader a feeling of what the simulated systems look like, we report in Fig. 74 a snapshot of one of the $\rho_{m0} = 0.370$ containing NPs of diameter $\sigma_N = 8.0$.

7.2 STATIC PROPERTIES: NETWORK

The addition of NPs to the system will in general affect the structural properties of the network. The magnitude of the changes induced by the NPs will depend on many factors, such as the NP diameter σ_N, their volume fraction ϕ_N and the monomer-NP interaction. We expect, however, that in the limit $\phi_N \to 0$ the structure of the network will remain basically unchanged upon the addition of NPs.

7.2.1 *Structure factor*

In Fig. 75, we report the monomer-monomer structure factor $S_{mm}(q)$ for the three networks here considered (monomer density in the neat state $\rho_{m0} = 0.183, 0.286$ and 0.370) and for different values of the NP diameter σ_N. We note that the NP volume fraction in each system is $\phi_N \simeq 0.02$ (see Tab. 3). For comparison, we also include the structure factor of the neat systems (thick black lines), measured in the NPT simulations described in Chapter 6[a]. We

[a] We recall that the network studied in Chapter 6 contained $M \simeq 5 \cdot 10^4$ monomers, whereas the systems described here contain $M \simeq 4 \cdot 10^5$ monomers.

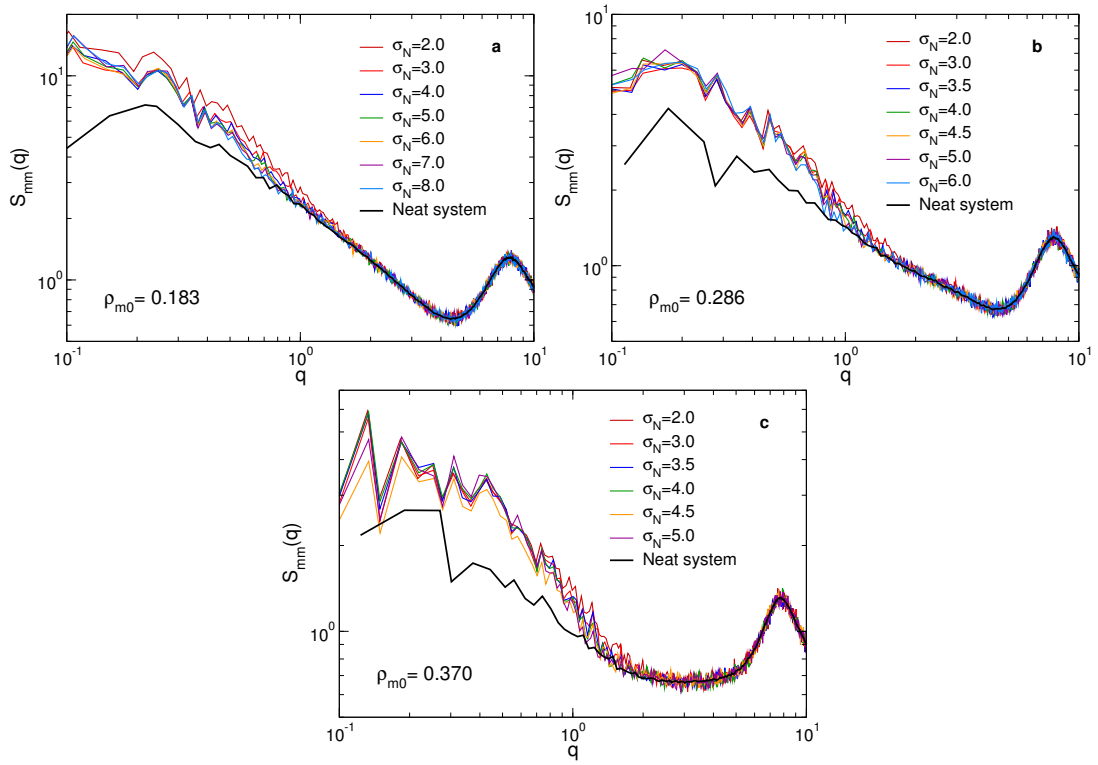

Figura 75 – Monomer-monomer structure factor $S_{mm}(q)$ for networks containing NPs, with monomer density in the neat state $\rho_{m0} = 0.183$ (a) 0.286 (b) and 0.370 (c). Continuous black line: $S_{mm}(q)$ for the neat system, measured in NPT simulations (see Chapter 6).

observe that upon the addition of the NPs, $S_{mm}(q)$ remains basically unchanged for $q \gtrsim 1$. Since $q \approx 2\pi/r$, where r is a distance, this means that the structure of the network changes only slightly for distances $r \lesssim 2\pi$. For $q \lesssim 1$, however, there is a marked increase, which we interpret as resulting from the NPs filling and stretching the holes in the network. A similar effect was observed for NPs dispersed in a polymer solution in Sec. 5.3.2; in that case. however, the NPs were uniformly dispersed and this resulted in a well defined peak in the structure factor at $q \simeq 2\pi/\sigma_N$. In the present case, the increase happens for all $q \lesssim 1$, i.e., for $r \gtrsim 2\pi$, and in a way which is basically independent of σ_N, implying that all the holes of size $r \gtrsim 2\pi$ are stretched in a similar way independently of the size of the NPs. This can be understood by considering that the larger holes can be filled by more than one NP at the same time, and therefore to a first approximation the stretching of the holes will only depend on the NP volume fraction ϕ_N, which is basically independent of σ_N (cf. Tab. 3).

7.3 STATIC PROPERTIES: NANOPARTICLES

7.3.1 *Radial distribution function*

In Fig. 76a-c we report the NP-NP radial distribution function (RDF) $g_{NN}(r)$ for the three networks and for different values of the NP diameter σ_N. In order to facilitate the comparison between different diameters, we plot $g_{NN}(r)$ as a function of the rescaled distance r/σ_N. We observe that $g_{NN}(r)$ displays a peak at $r_c = \sigma_N + (2^{1/6} - 1) = \sigma_N + 0.122$ (contact distance).

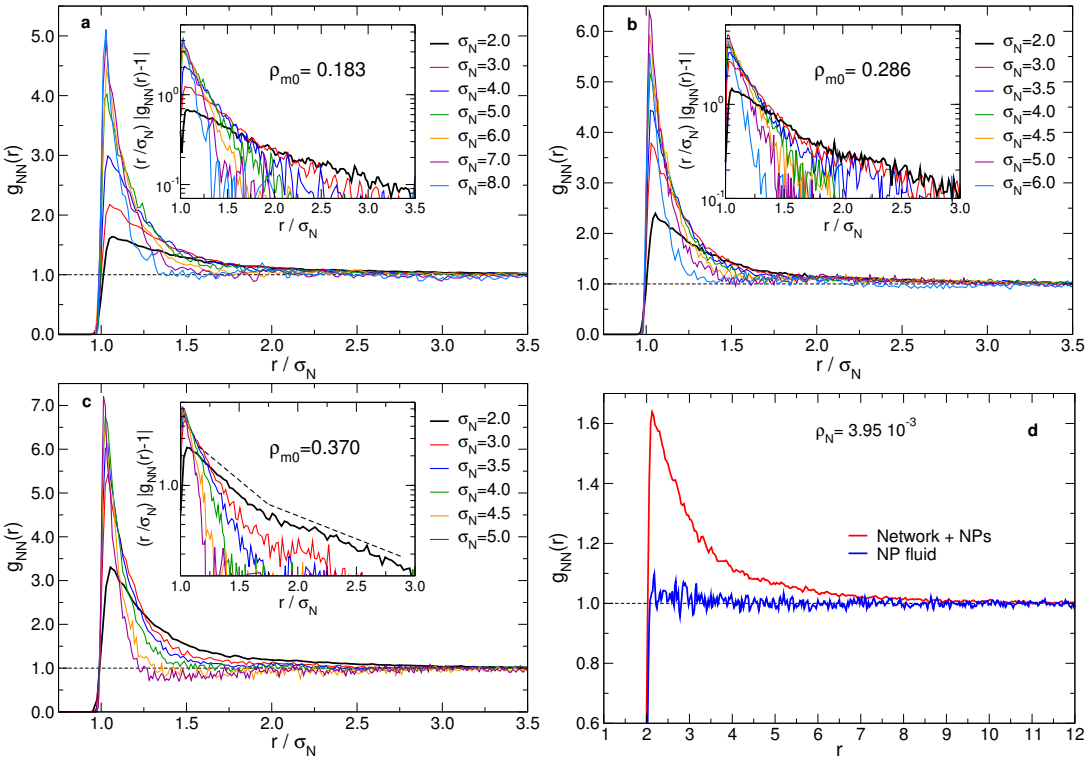

Figura 76 – NP-NP radial distribution function $g_{NN}(r)$ for NPs embedded in a polymer network with monomer density in the neat state $\rho_{m0} = 0.183$ (a) 0.286 (b) and 0.370 (c), as a function of the rescaled distance r/σ_N. The dashed lines in (c) are shown to help visualize the two exponential decays. (d): $g_{NN}(r)$ for the system $\sigma_N = 2$, $\rho_{m0} = 0.186$, compared with the same quantity for a NP fluid at the same density ($\rho_N = 3.95 \cdot 10^{-3}$).

From the rather large value of $g_{NN}(r_c)$ one can deduce that the probability to find two NPs in contact with each other is significantly higher than in a NP fluid with the same density ρ_N. This is exemplified in Fig. 76d, where we compare $g_{NN}(r)$ for the system $\sigma_N = 2$, $\rho_{m0} = 0.186$ ($\rho_N = 3.95 \cdot 10^{-3}$) with the RDF of a NP fluid at the same ρ_N. While the fluid has basically no structure (i.e., it is a gas), the RDF of the NPs embedded in the network displays a marked peak. We note that $g_{NN}(r_c)$ increases significantly when ρ_m or σ_N are increased. The decay of the peak is well described by the function $e^{-r/\Lambda}/r$, with $\Lambda > 0$[42,43], as one can see from the insets of Fig. 76a-c, where we report $(r/\sigma_N) \cdot |g_{NN}(r) - 1|$ in semi-logarithmic scale. This initial decay ($r/\sigma_N < 1$) is followed by a second one (cf. dashed lines in Fig. 76c), which is well described by the same functional form as the first one, although with a larger decay length Λ. We observe that the peak becomes sharper when σ_N or ρ_m are increased.

These behaviors can be interpreted by considering the dynamical behavior of the NPs in the network (which will be discussed in detail in Sec. 7.4). When diffusing through the network, the NPs regularly end up trapped in cages formed by the local entanglement mesh [b]. The time needed to escape the cage is a steeply increasing function of the confinement parameter $C = \sigma_N/d$: Therefore, the NPs can get trapped in these cages for very long times. A single cage can trap two or more NPs at the same time, acting effectively as a local attractive potential well for the NPs: This results in the strong signal observed in the RDF for $r_c \simeq \sigma_N$. It is evident from this qualitative picture that the strength of the signal will increase with increasing C, i.e., when either σ_N or ρ_m is increased (as an increase of ρ_m causes a decrease of d). The fact that the peak of the RDF is sharper for larger NPs or higher monomer densities also follows from the above explanation, since when σ_N is larger or d smaller it is rare for more than two NPs to be simultaneously trapped in the same cage, and therefore $g_{NN}(r)$ decays to 1 for smaller values of r/σ_N.

7.3.2 *Structure factor*

In Figs. 77a-c we report the NP-NP structure factor $S_{NN}(q)$ for the three networks and for different values of σ_N. Also in this case, in order to facilitate the comparison between different diameters, we show $S_{NN}(q)$ as a function of the rescaled variable $q\sigma_N/2\pi$. The behavior of $S_{NN}(q)$ is similar to that of a dilute liquid, with a "contact peak" at $q_c \simeq 2\pi/r_c \simeq 2\pi/\sigma_N$ (where r_c is the position of the peak of $g(r)$), followed by weak oscillations of period $\simeq q_c$. However, differently from a dilute liquid, $S_{NN}(q)$ displays a peak at $q \simeq 0$, which signals the presence of NP clustering. As discussed in Sec. 7.3.1, this clustering is driven by the trapping of NPs in entanglement cages. The difference between this NP-NP structure factor and that of a NP fluid at the same density is shown in Fig. 77d for the system $\sigma_N = 2$, $\rho_{m0} = 0.186$ ($\rho_N = 3.95 \cdot 10^{-3}$). The height of the peak, however, it too small to conclude that a macroscopic phase separation is taking place. The overall shape of $S_{NN}(q)$ as a function of the rescaled wavevector $q\sigma_N/2\pi$ depends only weakly on σ_N, implying that the spatial distribution of the NPs has approximately the same qualitative feature independently on the NP size. We observe however that the contact peak is shifted to smaller q_c for small σ_N and that the peak at $q \simeq 0$ becomes significantly smaller for large σ_N. However, the latter effect could be due to the fact that the systems with large NPs have not yet equilibrated.

[b] With the term "entanglement mesh", we will refer in the present Chapter to the mesh formed by both the crosslinks and the entanglements.

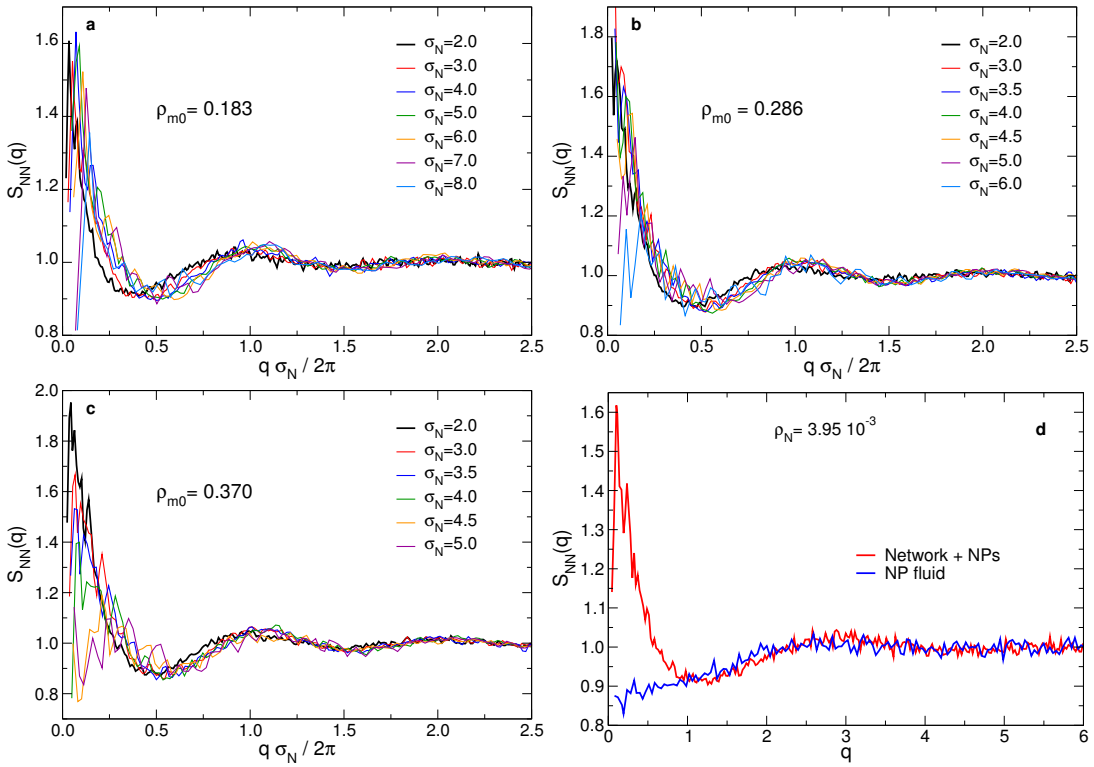

Figura 77 – NP-NP structure factor $S_{NN}(q)$ for NPs embedded in a polymer network with monomer density in the neat state $\rho_{m0} = 0.183$ (a) 0.286 (b) and 0.370 (c), as a function of the rescaled wavevector $q\sigma_N/2\pi$. (d): $S_{NN}(q)$ for the system $\sigma_N = 2$, $\rho_{m0} = 0.186$, compared with the same quantity for a NP fluid at the same density ($\rho_N = 3.95 \cdot 10^{-3}$)

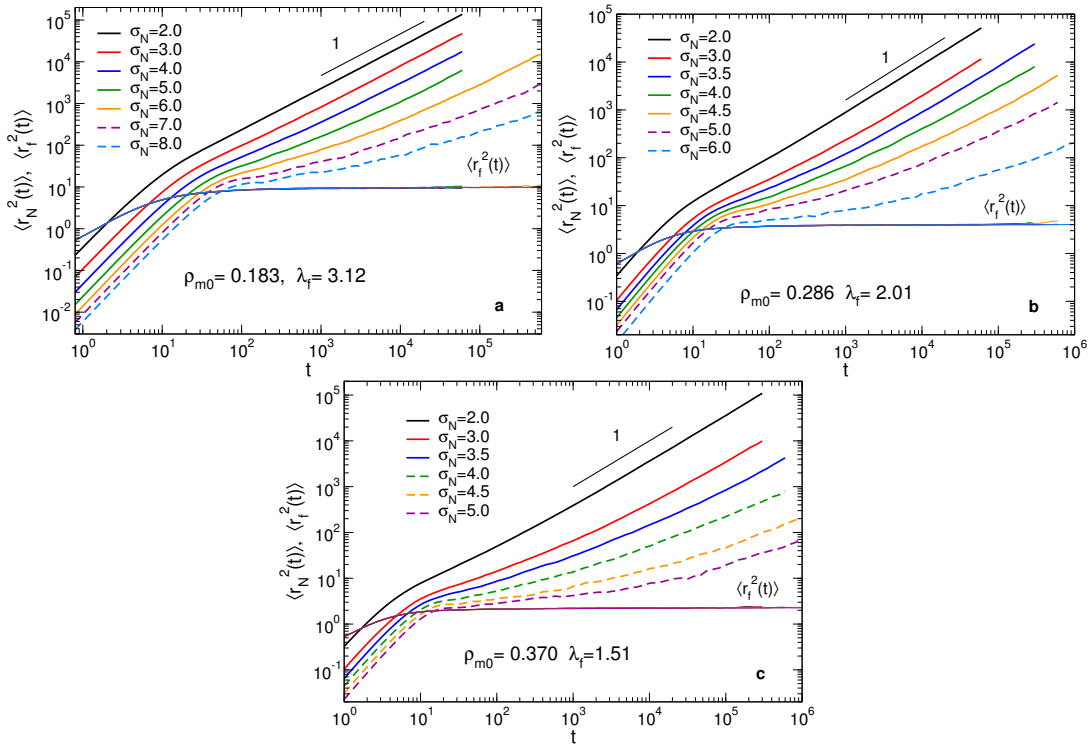

Figura 78 – Mean-squared displacement (MSD) of NPs, $\langle r_N^2(t)\rangle$, and of the crosslinks, $\langle r_f^2(t)\rangle$, in a polymer network with monomer density in the neat state $\rho_{m0} = 0.183$ (a) 0.286 (b) and 0.370 (c). Dashed lines: systems where the NPs haven't reached the diffusive regime. $\lambda_f = (\lim_{t\to\infty}\langle r_f^2(t)\rangle)^{1/2}$ is the localization length of the crosslinks.

7.4 NANOPARTICLE DYNAMICS

In Sec. 4.2.4 we discussed the dynamics of NPs in polymer systems with crosslinks and topological entanglements. Although the existing theories make qualitatively different predictions, they agree upon the fact that the central quantity controlling NP dynamics is the confinement parameter $C = \sigma_N/d$, where d is the dynamical confinement length scale, which results from the presence of both the crosslinks and the entanglements. Intuitively, when C becomes significantly larger than 1, we expect the NPs to be trapped by the entanglement mesh. Since the constraint release mechanism is turned off by the presence of the crosslinks, the NPs can only escape their local cage by the hopping mechanism, whose typical time scale τ_h increases at least exponentially in C. We expect therefore the dynamics of the NPs to be strongly suppressed when σ_N or ρ_m are increased.

7.4.1 *Mean-squared displacement*

In Fig. 78a-c we show the mean-squared displacement (MSD) of the NPs, $\langle r_N^2(t)\rangle$, for the three networks and for different values of σ_N. For comparison, we also show the MSD of the crosslinks, $\langle r_f^2(t)\rangle$. For small values of σ_N and ρ_m, the motion of the NPs becomes diffusive ($\langle r_N^2(t)\rangle \propto t$) immediately after the initial ballistic behavior ($\langle r_N^2(t)\rangle \propto t^2$). When σ_N or ρ_m are increased, however, a subdiffusive transient $\langle r_N^2(t)\rangle \propto t^{\beta(t)}$ $(0 < \beta(t) < 1)$ appears between the ballistic and the diffusive regime. For high values of σ_N and ρ_m, the MSD shows almost a

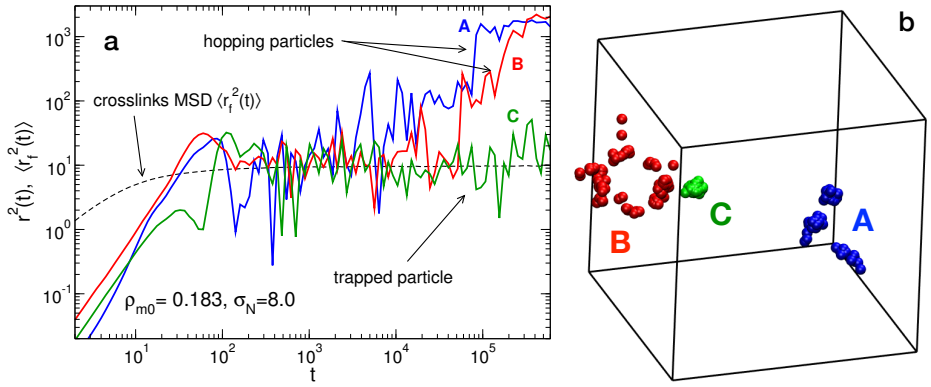

Figura 79 – (a) Squared displacement of three NPs denoted A,B and C (continuous lines) and of the crosslinks (dashed line) for $\rho_{m0} = 0.183$ and $\sigma_N = 8.0$. (b) Trajectories of the NPs A,B and C, created by taking snapshots of the NP position at regular time intervals of length $\Delta t = 6 \cdot 10^3$. To facilitate visualization, the NPs are represented with a smaller diameter ($\sigma_N = 4.0$).

plateau (i.e., $\beta(t) \simeq 0$), meaning that most of the NPs are trapped by the entanglement mesh. By comparing $\langle r_N^2(t)\rangle$ for large σ_N to $\langle r_f^2(t)\rangle$ and by extrapolating from the available data the behavior of $\langle r_N^2(t)\rangle$ for very large σ_N, we deduce that the expected plateau height λ_N for $\langle r_N^2(t)\rangle$, i.e., the *localization length* of the NPs, is approximately equal to λ_f, the localization length of the crosslinks. The estimated values of λ_f for $\rho_{m0} = 0.183, 0.286$ and 0.370 are respectively $3.12, 2.01$ and 1.51. We recall that $\lambda_f \approx d$, where d is the effective tube diameter [c], as discussed in Sec 6.3.1. We can therefore conclude that the localization length of the NPs is also of the order of the tube diameter:

$$\lambda_N \approx \lambda_f \approx d \tag{205}$$

This can be better seen from Fig. 79, where we compare the squared displacement (SD) $r^2(t)$ of three NPs (labeled A, B and C) with the MSD of the crosslinks. One can see that particle C is trapped by the mesh, displaying a completely flat SD, with localization length equal to the localization length of the crosslinks, λ_f. Also the particles A and B are initially trapped by the mesh, but eventually manage to escape. Their SD consists in a series of abrupt "jumps", each of one is followed by a flat region. This type of jerky motion is one of the typical signatures of hopping. For comparison, we show in Fig. 79 snapshots of the particles taken at regular time intervals: $t = 0, \Delta t, 2\Delta t, \ldots, t_{\max}$, with $\Delta t = 6 \cdot 10^3$. A close observation of these "stroboscopic" snapshots also reveals the existence of hopping motion, as the positions of the mobile particles A and B at different times form well-separated clusters.

These properties of the NP trajectories is shown more clearly in Fig.80, where we show the same kind of "stroboscopic snapshots" for the $\rho_{m0} = 0.183$ network containing NPs of diameters $\sigma_N = 8$. In order to help the visualization, we only show the trajectories of 15 particles, and we represent each particle as having diameter $\sigma_N = 2$ instead of $\sigma_N = 8$. One can clearly see that the NP trajectories form clusters: For the NPs which are trapped by the

[c] In our systems, there is no unique strand length, but rather an exponential distribution of strand length, as discussed in Sec. 6.2.1. It is therefore much more difficult to disentangle the contributions of the crosslinks and those of the entanglements, and it is more appropriate to talk of an effective tube diameter resulting from a combination of these effects.

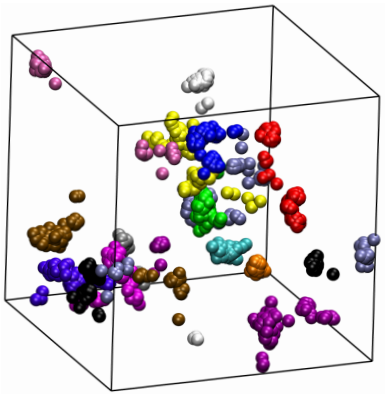

Figura 80 – Trajectories of 15 NPs of diameter $\sigma_N = 8.0$ embedded in the $\rho_{m0} = 0.183$ network, created by taking snapshots of the NP position at regular time intervals of length $\Delta t = 6 \cdot 10^3$. To facilitate visualization, the NPs are represented with a smaller diameter ($\sigma_N = 4.0$).

mesh up to time $t_{\max}$, the trajectory forms a single cluster, whereas for the mobile NPs it forms well separated clusters, which allow us to locate the cages in which the particles are temporarily trapped between the hopping events.

To better study the transition from subdiffusive to diffusive motion, we also study the time dependence of the exponent $\beta(t)$, which was defined in Eq. (163). In Fig. 81, we report $\beta(t)$ for the three networks and for different NP diameters. After the initial ballistic regime ($\beta = 2$), β decreases abruptly, reaching values very close to zero for the largest NPs. In the more confined cases, such as $\rho_{m0} = 0.370, \sigma_N = 5$, this initial decrease is followed by a plateau region, in which β is essentially flat and approximately zero. At longer times, β increases approximately logarithmically, $\beta(t) \simeq a + b \ln(t)$ until eventually it saturates to 1 (diffusive regime). We note that this implies that in the subdiffusive regime[d]

$$\langle r_N^2(t) \rangle \simeq c t^{a + b \ln(t)/2} \tag{206}$$

The value of b (slope of $\beta(t)$ in linear-logarithmic scale) is basically independent of σ_N, and has value $b \simeq 0.05$. This suggests that, despite the fact that larger NPs are more strongly confined (smaller a value in Eq. (206)), the mechanism governing the approach to the diffusive regime is independent of NP size.

7.4.2 *Diffusion coefficient*

The NP diffusion coefficient D_N can be obtained through Einstein's relation, Eq. (54), by fitting $\langle r_N^2(t) \rangle$ in the diffusive regime with a linear function. Unfortunately, in some systems the simulation time was not long enough to reach the diffusive regime, as we can see from Figs. 78 and 81. However, for those systems where the diffusive regime is not reached, it is still possible to give an upper bound for the diffusion coefficient.

In Fig. 82a we show D_N as a function of the NP diameter σ_N (semi-logarithmic scale) for the three networks considered here. Open symbols represent the upper bounds on D_N for those systems where the diffusive regime was not reached. One can see that increasing

[d] The factor $b/2$ (instead of b) in the exponent of t is a consequence of the definition of $\beta(t)$ Eq. (163)).

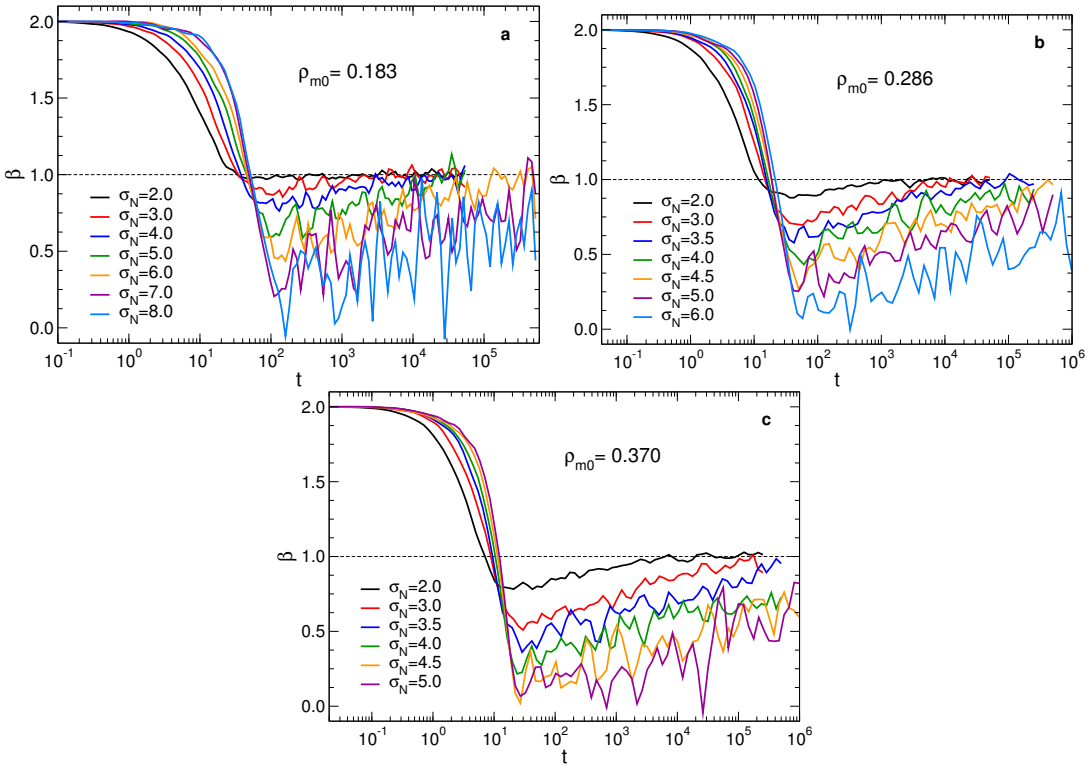

Figura 81 – Exponent β, Eq. (163), from the MSD of the NPs, for polymer network with monomer density in the neat state $\rho_{m0} = 0.183$ (a) 0.286 (b) and 0.370 (c) and different NP diameters σ_N.

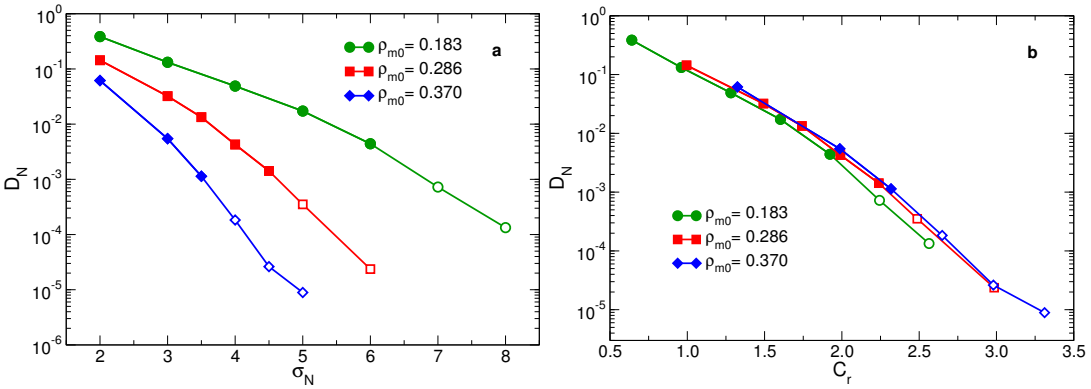

Figura 82 – Diffusion coefficient D_N of the NPs as a function of the NP diameter σ_N (a) and of the confinement ratio $C_r \equiv \sigma_N/\lambda_f$ (b). Open symbols represent upper bounds for D_N for the systems in which the diffusive regime was not reached.

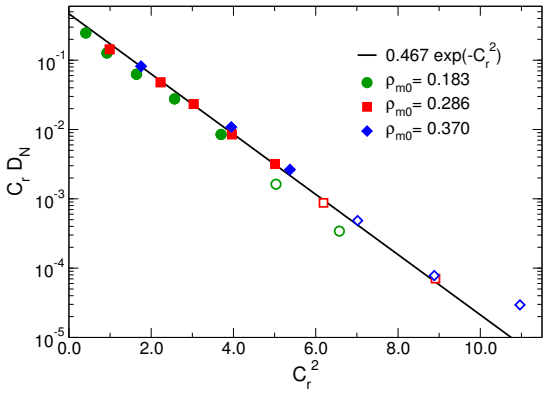

Figura 83 – Scaling plot of the NP diffusion coefficient, Eq. (207), with C_r the confinement ratio, Eq. (208). Continuous line: Eq. (207) with $A = 0.467$. Open symbols represent upper bounds for D_N for the systems in which the diffusive regime was not reached.

σ_N causes an extremely strong decrease of the diffusion coefficient, and that the decrease becomes steeper when ρ_m increases. For $\rho_{m0} = 0.286$, for example, increasing σ_N from 2 to 5 causes a two orders of magnitude drop in D_N. In Sec. 7.4.1, we have seen that the spatial extent of NP localization is controlled by the localization length λ_f of the crosslinks, which is proportional to the effective tube diameter d: $\lambda_f \approx d$. From the definition of the confinement parameter, we have therefore $C \approx \sigma_N/\lambda_f$. The values of σ_N/λ_f for the simulated systems are reported in Tab. 3. Since the available theories on NP diffusion in polymer networks predict that D_N is controlled by C [185,191], it seems therefore natural to plot D_N as a function of σ_N/λ_f, as we do in Fig. 82b. Upon rescaling σ_N this way, the data fall almost perfectly on a master curve; we stress that no fit parameter was used to produce this plot. One sees that D_N decays faster than an exponential in σ_N/λ_f. Indeed, we find that the expression

$$D_N = A\left(\frac{\lambda_f}{\sigma_N}\right)\exp\left[-\left(\frac{\sigma_N}{\lambda_f}\right)^2\right] = \frac{A}{C_r}e^{-C_r^2} \tag{207}$$

fits the data extremely well, as we show in Fig. 83, where Eq. (207) (with $A = 0.467$) is shown as a continuous line. In Eq. (207) we have introduced the *confinement ratio*[e],

$$C_r \equiv \frac{\sigma_N}{\lambda_f}\,. \tag{208}$$

Eq. (207) is formally identical to that found in Eq. (134) from the CPR theory of activated hopping [185]. In the CPR theory, this equation gives the NP diffusion coefficients for the case in which the crosslink density in the network is higher than the entanglement density, and therefore the trapping of the NPs is dominated by the crosslinks. It is surprising that Eq. (207) gives such a good description of the data without any multiplicative prefactor in the argument of the exponential, i.e., $D_N \propto e^{-aC_r^2}$ with $a = 1$. This suggests that C_r is indeed the relevant confinement parameter which controls the dynamics of the NPs in the simulated systems.

[e] This nomenclature was chosen to distinguish it form the confinement parameter $C = \sigma_N/d$.

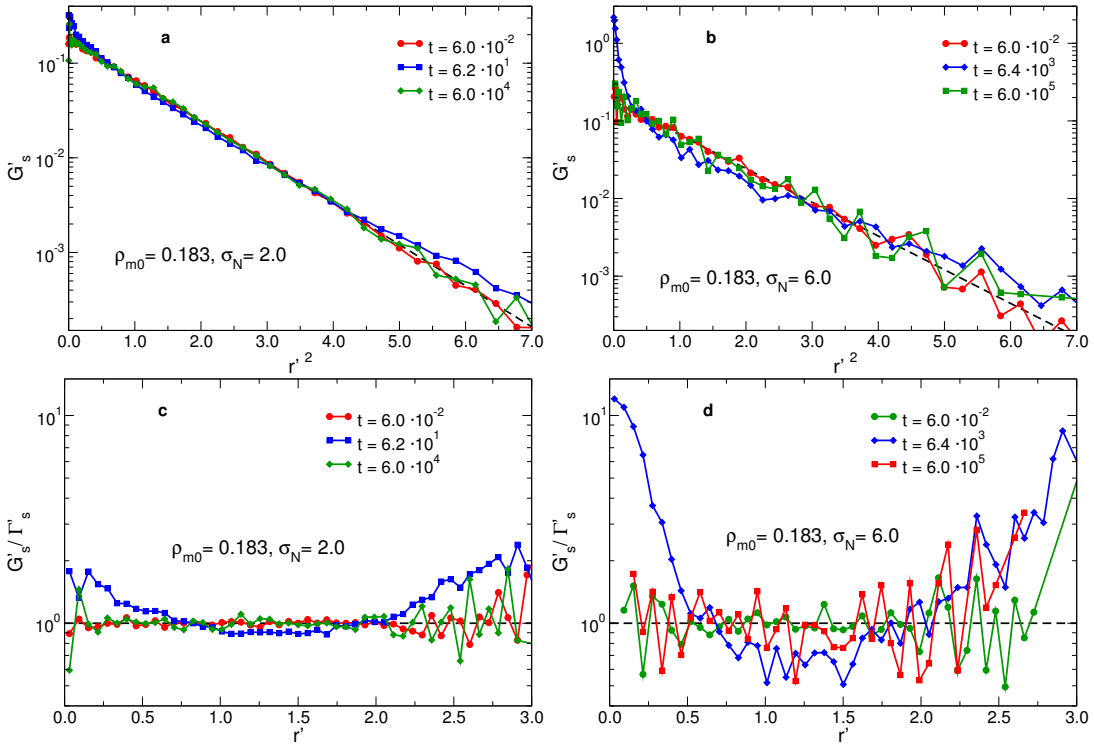

Figura 84 – (a-b): Rescaled self van Hove function $G'(r',t)$ for NPs of diameter $\sigma_N = 2.0$ (a) and $\sigma_N = 6.0$ (b) embedded in the network with density in the neat state $\rho_{m0} = 0.183$. (c-d) Ratio between $G'(r',t)$ and $\Gamma'_s(r') = \pi^{-3/2}e^{-r'^2}$ (Gaussian approximation).

7.4.3 *van Hove function*

In the previous section, we have deduced by studying the squared displacement of single particles that large NPs perform hopping motion from one entanglement cage to the other. The presence of hopping can be detected by investigating the van Hove function of the NPs, which was defined in Sec. 5.4.2.

In Fig. 84 we report the self part of the van Hove function $G_s(r,t)$ for NPs of diameters $\sigma_N = 2$ and 6 embedded in the $\rho_{m0} = 0.183$ network. To facilitate the comparison with theory, we define the rescaled self van Hove function $G'_s(r',t)$ as done in Sec. 5.4.2 (Eq. (167)). We recall that when $G_s(r,t)$ is Gaussian, $G'_s(r',t)$ is simply given by $G'_s(r',t) = \Gamma'_s(r') = \pi^{-3/2}e^{-r'^2}$ (Eq. (168)). At short times, $G_s(r,t)$ is always a Gaussian.

From Fig. 84a, one can see that for $\sigma_N = 2$, $G'_s(r',t)$ is very well described by a Gaussian: Small deviations are only observed for $t = \mathcal{O}(10)$, which is the time at which the NPs enter the diffusive regime (cf. Fig. 78a). This is also apparent from Fig. 84c, where we show the ratio $G'_s(r',t)/\Gamma'_s(r')$: this quantity is almost flat at both short and long times, with significative deviations appearing at both small and large r' only for $t = \mathcal{O}(10)$. This behavior is qualitatively the same as that observed in Sec. 5.4.2 for the NP diffusion in unentangled polymer solutions. We can conclude therefore that in this system, NPs of size $\sigma_N = 2.0$ are not trapped by the entanglement mesh and can diffuse freely.

The situation is very different, however, for $\sigma_N = 6$ as one can see from Fig. 84b. Indeed, we observe that at $t = \mathcal{O}(10^3)$, a peak appears at small r'. The presence of this peak, which is accentuated when plotting $G'_s(r',t)/\Gamma'_s(r')$ (Fig. 84d), shows that at intermediate times

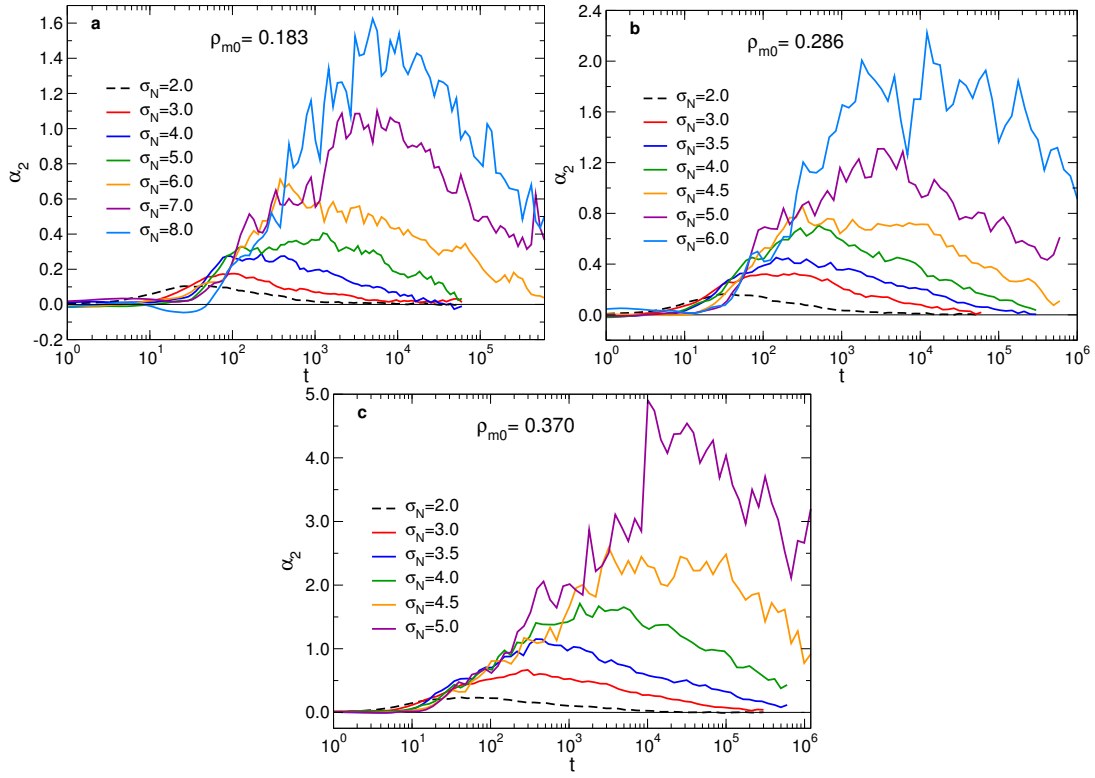

Figura 85 – Non-Gaussian parameter α_2, Eq. (169), for NPs of different diameters σ_N embedded in a polymer network with monomer density in the neat state $\rho_{m0} = 0.183$ (a) 0.286 (b) and 0.370 (c).

a significant fraction of the NPs have moved significantly less than what predicted by the Gaussian approximation, whereas another significant fraction has moved significantly more. This is the clear signal of transient trapping of the NPs by the entanglement mesh and of hopping motion. At $t = \mathcal{O}(10^5)$, the NPs have broken free from their cages and the Gaussian approximation is recovered.

To quantify the dissimilarity between $G_s(r,t)$ and a Gaussian, it is useful to calculate the non-Gaussian parameter $\alpha_2(t)$ (Eq. (169)), which we report in Fig. 85 for the three networks considered in the present work and different NP diameters. All the systems considered share the same qualitative behavior. At short times, $\alpha_2 \simeq 0$, i.e., the dynamics of the NPs is Gaussian. This regime is followed by an increase in α_2, which corresponds to the onset of the subdiffusive regime in the MSD. For small σ_N/small ρ_m, this increase is very modest, and α_2 remains of order 10^{-1}. However, for large σ_N, α_2 reaches values significantly larger than 1. These values are comparable to those measured in simulations of deeply supercooled liquids[253] or in experimental studies of polymer networks containing NPs[323]. In the presently studied systems, as in experimental systems[323], such strong dynamical heterogeneity originates from the structural heterogeneity of the network on the scale of the NP size: Some NPs freely diffuse through the gaps in the network, whereas other NPs end up trapped in the mesh. At long times, some of the systems return to a Gaussian behavior ($\alpha_2 \simeq 0$), whereas others are not able to do so during the duration of the simulation (these are the same systems where the diffusive regime is not reached).

To conclude the analysis of the van Hove function, we also consider its distinct part,

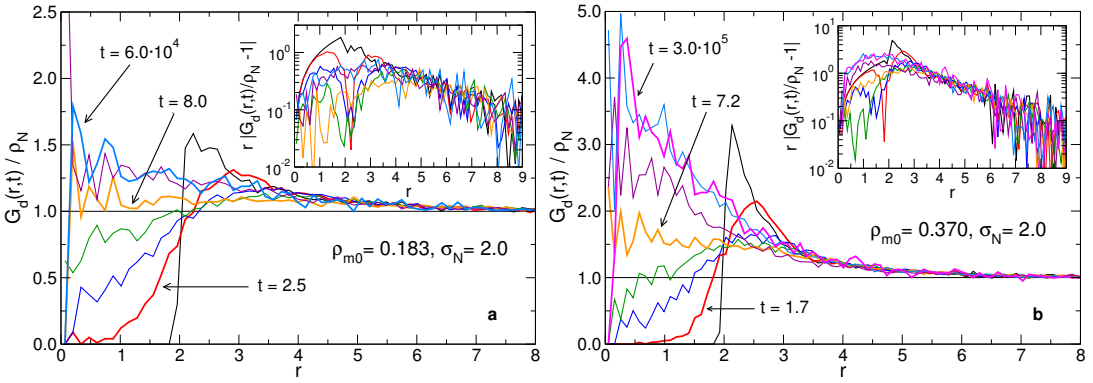

Figura 86 – Distinct van Hove function $G_d(r,t)$ of NPs of diameter $\sigma_N = 2.0$ embedded in the $\rho_{m0} = 0.183$ (a) and 0.370 (b) networks. *Insets*: $r|G_d(r,t) - 1|$.

$G_d(r,t)$ (Sec. 5.4.2). In Fig. 86 we show $G_d(r,t)/\rho_N$ for NPs of diameter $\sigma_N = 2$ embedded in the networks $\rho_{m0} = 0.183$ (a) and $\rho_{m0} = 0.370$ (b). In all cases, we observe that with increasing t the correlation hole at small r is slowly filled and the contact peak ($\sigma_N \simeq 2$) is washed out, a behavior which resembles that of well-dispersed NPs in a polymer solution (cf. Fig. 42). However, whereas in a NP liquid $G_d(r,t)/\rho_N \simeq 1$ at long enough times, in the presently studied system correlations persist during the whole duration of the simulation. In particular, we observe from the insets of Figs. 86a-b that the tail of the contact peak (cf. Fig. 76) remains basically unchanged for all values of t, even though the NPs reach the diffusive regime (Fig. 78) and the dynamics is Gaussian with very good approximation (Figs. 84 and 85). The reason for this behavior is that, although the NPs can freely diffuse through the gaps in the network, they are not able to explore the whole simulation box. Indeed, in some parts of the system the local mesh size will be so small that the NPs won't be able to pass through. The existence of these "impenetrable" zones is at the origin of the persisting correlations observed in $G_d(r,t)$.

This behavior is shown qualitatively in Fig. 87, where we show the trajectories of the NPs in the system $\rho_{m0} = 0.370$, $\sigma_N = 2.0$. As for Figs. 79 and 80, we show snapshots of the particles taken at regular time intervals of length Δt from $t = 0$ to $t = t_{\max}$; here, $\Delta t = 3 \cdot 10^3$. In order to facilitate the visualization, we only show the trajectories of 200 NPs and each NP is simply represented as a point. The NPs trajectories are clearly not homogeneously distributed in the whole sample, and one can distinguish regions with a high density of points and regions with a low density of points. These snapshots confirm therefore qualitatively the above interpretation of the behavior of $G_d(r,t)$. We also observe that at long times a peak appears at $r = 0$. Since $4\pi r^2 \rho_N G_d(r,t)dr$ represents the probability to find, at time t, a given particle at a distance r from the position occupied by some other particle at time 0, the appearance of this peak implies that there is a strong probability that a NP occupies a position which was previously occupied by another one. Therefore, we interpret this peak as a clear signal of the presence of hopping motion [253,324].

When the confinement parameter increases (because σ_N or the network density increases), hopping motion becomes even more relevant. This appears clearly from Fig. 88, where we report $G_d(r,t)/\rho_N$ for NPs of diameter $\sigma_N = 4$ embedded in the networks $\rho_{m0} = 0.286$ (a) and $\rho_{m0} = 0.370$. Even tough the worse statistics doesn't allow us to study accurately the behavior of $G_d(r,t)$ for $r > \sigma_N$, we clearly observe the appearance of a peak at $r \simeq 0$. At long

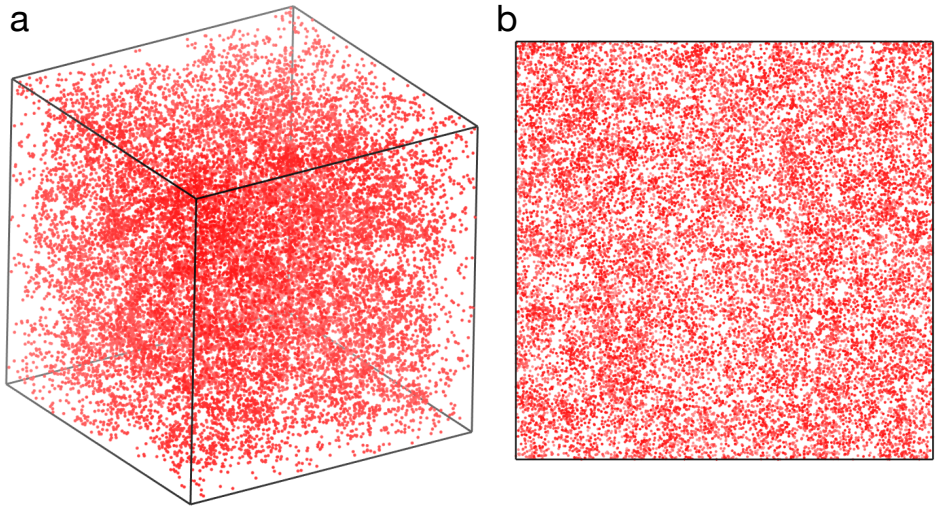

Figura 87 – Trajectories of 200 NPs in the system $\rho_{m0} = 0.370$, $\sigma_N = 2.0$, created by taking snapshots of the particles at regular time intervals of length Δt from $t = 0$ to $t = t_{\max}$, with $\Delta t = 3 \cdot 10^3$. To facilitate visualization, the NPs are represented as points. (a): Side view. (b): Front view.

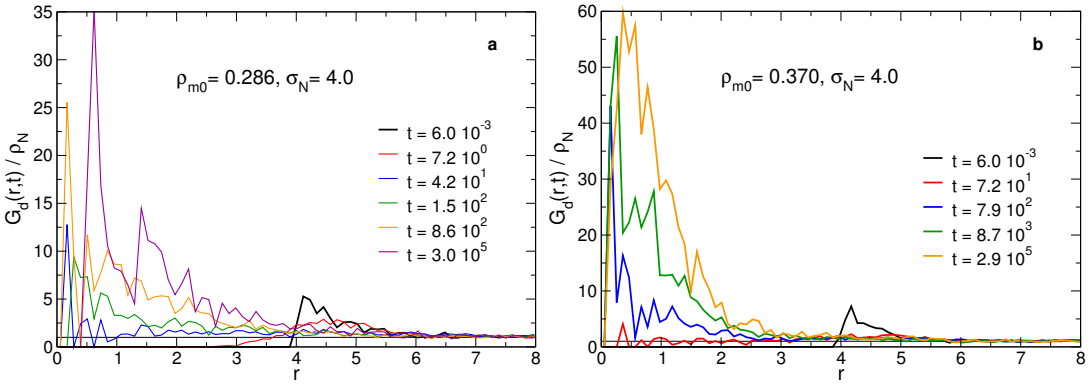

Figura 88 – Distinct van Hove function $G_d(r,t)$ of NPs of diameter $\sigma_N = 4.0$ embedded in the $\rho_{m0} = 0.286$ (a) and 0.370 (b) networks.

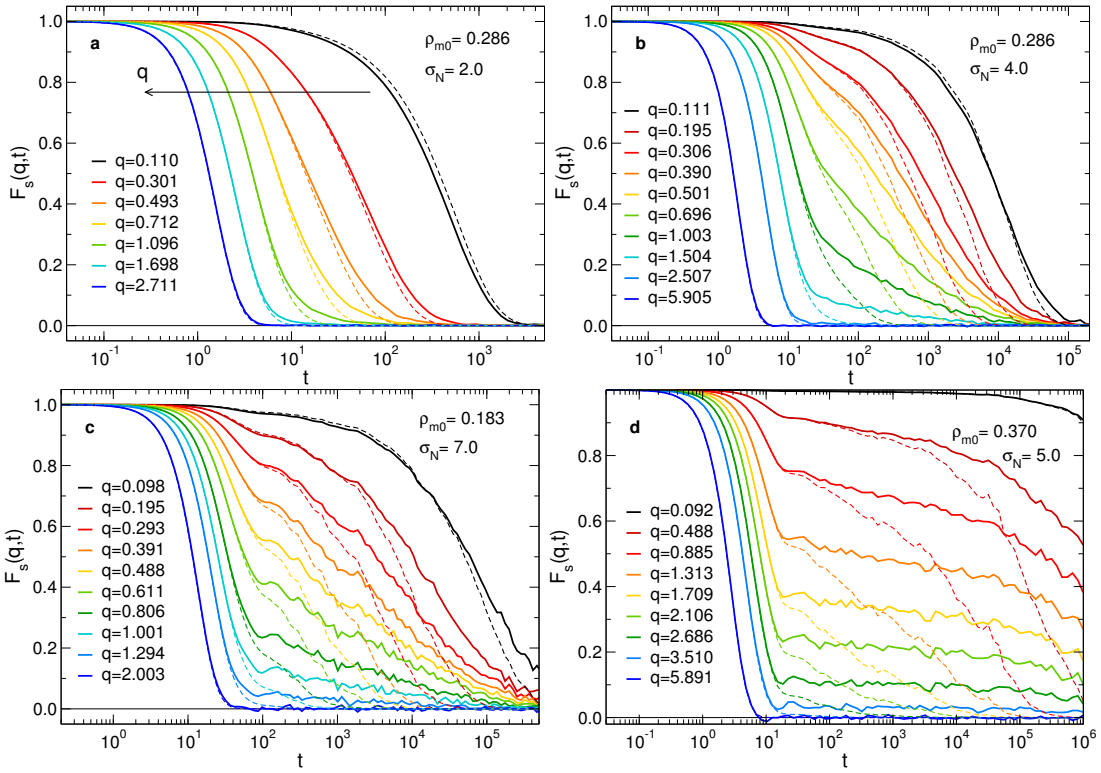

Figura 89 – Self intermediate scattering function $F_s(q,t)$ of the NPs for the systems $\rho_{m0} = 0.286, \sigma_N = 2.0$ (a), $\rho_{m0} = 0.286, \sigma_N = 4.0$ (b), $\rho_{m0} = 0.183, \sigma_N = 7.0$ (c), $\rho_{m0} = 0.370, \sigma_N = 5.0$ (d). In all the figures, q increases going from right to left. Dashed lines: Eq. (210).

times, this peak grows enormously, signaling that NP motion is dominated by hopping.

7.4.4 *Self intermediate scattering function*

Additional insights on the dynamics of the NPs can be gained by considering the self intermediate scattering function $F_s(\mathbf{q},t)$, which is the Fourier transform of the self part of the van Hove function [1,53]:

$$F_s(\mathbf{q},t) \equiv \langle \exp[-i\mathbf{q}\cdot(\mathbf{r}_k(t) - \mathbf{r}_k(0))]\rangle = \int G_s(\mathbf{r},t) e^{-i\mathbf{q}\cdot\mathbf{r}} d\mathbf{r}. \tag{209}$$

We have seen in Sec. 7.4.4 that in the regime of weak confinement (low σ_N and/or ρ_m), the self part of the van Hove function is well described by a Gaussian. Since the Fourier transform of a Gaussian is also a Gaussian, it follows that in this regime $F_s(\mathbf{q},t)$ is a Gaussian. Indeed, from Eqs. (166) and (209) we obtain

$$F_s(q,t) = \Phi(q,t) \equiv \exp\left(-\frac{q^2}{6}\langle r^2(t)\rangle\right). \tag{210}$$

In Fig. 89, we report the intermediate scattering function of the NPs for four selected systems (continuous lines), compared with the Gaussian approximation $\Phi(q,t)$ (dashed lines). At

short times (ballistic regime), the dynamics of the NPs is Gaussian and $F_s(q,t) = \Phi(q,t)$. In particular, since $\langle r^2(t)\rangle = 3k_BTt^2/m_N$ (equipartition theorem[263]), with m_N the mass of the NP, we have

$$F_s(q,t) = \Phi(q,t) = \exp\left(-\frac{k_BTq^2t^2}{2m_N}\right). \tag{211}$$

The behavior of $F_s(q,t)$ after this initial ballistic regime depends on the degree of confinement. For $\sigma_N = 2.0$, $\rho_{m0} = 0.183$ (Fig. 89a), the NPs are weakly confined, and $F_s(q,t)$ is very well descibed by the Gaussian approximation, i.e., $F_s(q,t) \simeq \Phi_s(q,t)$. Since the motion of the NPs becomes diffusive immediately after the ballistic regime (cf. Fig. 78), we have $\langle r^2(t)\rangle \simeq 6Dt$ and the decay of $F_s(q,t)$ is essentially a simple exponential:

$$F_s(q,t) \simeq \Phi(q,t) \simeq e^{-Dq^2t}. \tag{212}$$

For stronger confinements, however, the qualitative behavior of $F_s(q,t)$ changes drastically, as a shoulder appears after the initial ballistic regime (Figs. 89b-d). This behavior is reminiscent of the one of supercooled liquids , which show an initial quasi-exponential decay, followed by a shoulder and then a second "stretched exponential" decay (α-relaxation)[1,244] [f]:

$$F_s(q,t) \simeq A\exp[-(t/\tau)^\beta] \quad (0 < \beta < 1). \tag{213}$$

We can also see from Figs. 89b-d that in the strong confinement regime, the Gaussian approximation $F_s(q,t) = \Phi(q,t)$ gives a poor description of the data at intermediate times, in agreement with what observed in Sec. 7.4.3 from the function $G_s(r,t)$.

In the case of supercooled liquids, the control parameter for the emergence of the two-step relaxation described above is temperature, whereas in our case it is the confinement parameter $C = \sigma_N/d$. This is illustrated in Fig. 90, where we show $F_s(q \simeq 2\pi/\sigma_N, t)$, where $2\pi/\sigma_N$ is the position of the contact peak of the NP-NP static structure factor (Sec. 7.3.2).

In Fig. 90a, we show $F_s(q \simeq 2\pi/\sigma_N, t)$ for particles of diameter $\sigma_N = 5.0$ embedded in the three different networks. We observe that when ρ_m is increased, the shape of $F_s(q,t)$ changes drastically, going from a single-step relaxation for $\rho_{m0} = 0.183$ to a two-step relaxation for higher densities. For $\rho_{m0} = 0.286$ and 0.370, the α-relaxation is well described by Eq. (213), with an exponent $\beta \simeq 0.23 - 0.24$ which depends very weakly on ρ_m. One of the most important qualitative difference between our $F_s(q,t)$ and those of a supercooled liquid is that for the latter the height of the shoulder depends only weakly on temperature, whereas in our case there is a marked dependence on the degree of confinement. This can be explained by the fact that the shoulder height is related to the localization length λ_N of the MSD [g]. Indeed, at the time t^* of appearance of the shoulder we have

[f] In order to conform to the literature, we use the letter β for the α-relaxation exponent. This should not be confused, however, with the exponent β of the MSD.

[g] Here we refer to the localization length in a loose sense, as the value of $(\langle r_N^2(t)\rangle)^{1/2}$ at the beginning of the subdiffusive regime.

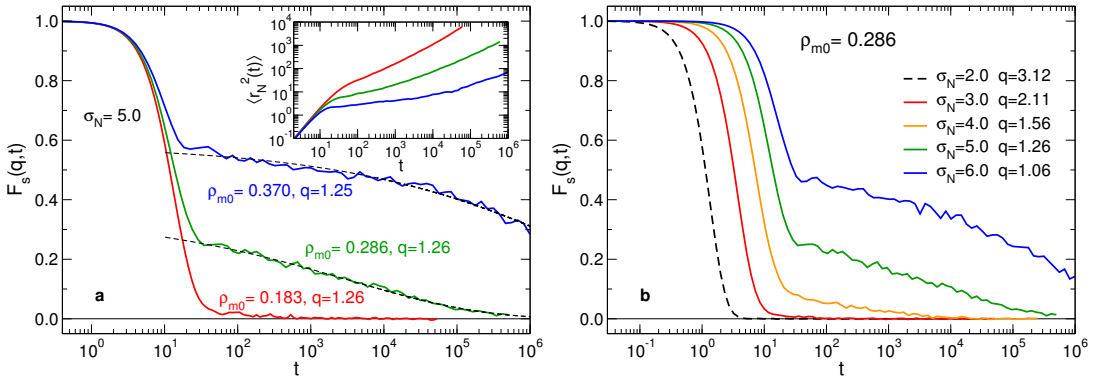

Figura 90 – (a) Self intermediate scattering function $F_s(q,t)$ for NPs of diameter $\sigma_N = 5.0$ embedded in the three networks studied here. $F_s(q,t)$ was calculated at $q \simeq 2\pi/\sigma_N = 1.25$. Dashed lines: Fits with a stretched exponential (Eq. (213)). The values of the fit parameter are for $\rho_{m0} = 0.370$: $A = 0.585$, $\tau = 7.71 \cdot 10^6$, $\beta = 0.226$. For $\rho_{m0} = 0.286$: $A = 0.352$, $\tau = 3.34 \cdot 10^3$, $\beta = 0.239$. *Inset:* NP mean-squared displacement for the same systems. (b) $F_s(q,t)$ for NPs of different diameters embedded in a network with density in the neat state $\rho_{m0} = 0.286$. As for (a), $F_s(q,t)$ was calculated at $q \simeq 2\pi/\sigma_N$.

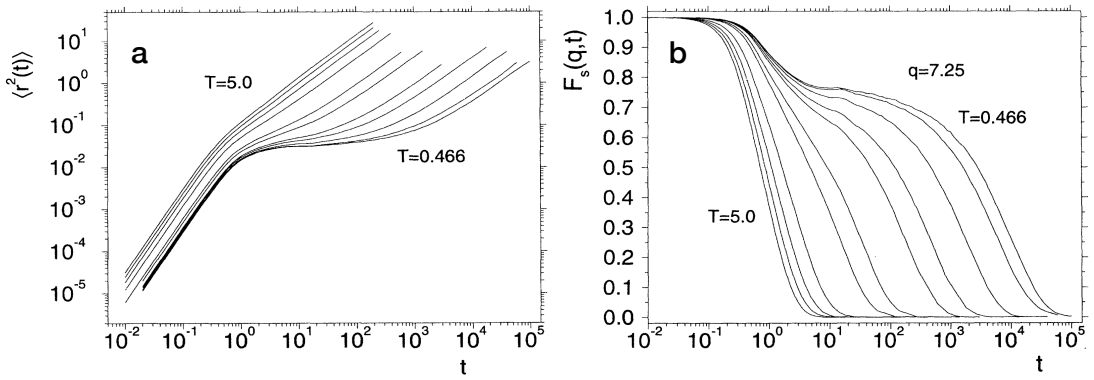

Figura 91 – MSD (a) and self intermediate scattering function (b) of the A particles in a simulation of a Kob-Andersen liquid. The self intermediate scattering function was calculated at a wavevector q corresponding to the position of the main peak of the A-A static structure factor $S_{AA}(q)$. Adapted from Refs. 253 (a) and 325 (b).

$$F_s(q,t^*) \simeq \Phi(q,t^*) \simeq \exp\left(-\frac{q^2}{6}\lambda_N^2\right). \tag{214}$$

In supercooled molecular liquids, the value of λ_N is given by the spatial extent of the vibrations of the particle inside its cage, and depends only weakly on T. This is evidenced in Fig. 91, where we report $\langle r^2 \rangle$ and $F_s(q,t)$ for the A particles in a simulation of a Kob-Andersen liquid[253,325]. In our system, $\lambda_N \approx \lambda_f$, and we have seen in Sec. 6.3.1 that λ_f decreases approximately as ρ_m^{-1}: Therefore, the height of the shoulder of $F_s(q,t)$ will depend rather strongly on ρ_m.

In Fig. 90b, we show $F_s(q \simeq 2\pi/\sigma_N, t)$ for particles of various diameters embedded in the $\rho_{m0} = 0.286$ network. We observe that, despite the fact that all the systems have approximately the same ρ_m (see Tab. 3), there is a clear dependence of the shoulder height of $F_s(q,t)$ on σ_N. This is because small NPs can move farther inside their local cage before feeling the

confinement effect, and therefore they have a larger localization length.

8

CHARACTERIZING THE MESH SIZE IN A POLYMER SOLUTION

Some ideas and figures present in this Chapter have appeared in Ref. 326.

We have seen in Sec. 4.2.2, when discussing the CPR theory, that the geometrical mesh size ξ (Sec. 3.2.2) is a fundamental quantity in the problem of the diffusion of nanoparticles in polymer liquids. This is also apparent when considering other models, such as those based on geometric obstruction[165–167] and hydrodynamics[168–173]. The mesh size is also a fundamental quantity when considering the diffusion of particles in polymer networks and gels[174,185,191,323,327–329].

When considering the diffusion of a probe particle in a polymer solution, it is clear that the relevant "mesh size" should be nothing else than the average geometrical size of the pores, or holes, in the solution, i.e., those regions which are filled only with solvent. In view of applications to diffusion problems, we will in the present work adopt this intuitive concept of ξ as the average pore size of the polymer solution. This also allows to extend the intuitive definition of ξ proposed by de Gennes, as the average size of the transient mesh in a semidilute solution[2], to the dilute and concentrated regimes: In the dilute regime the chains do not overlap, but a mesh size still exists as an average geometric distance between neighboring chains. In the concentrated regime the chains overlap so strongly that there is no clear mesh structure, but we can still measure the size of the pores.

We are, however, immediately confronted with the question: How exactly should we measure ξ? Usually, ξ is either estimated using scaling calculations, or measured from the monomer density fluctuation correlation length, ξ_c (Sec. 3.3). An example of scaling estimate is Eq. (22), where ρ^* is often estimated by considering the chains as spheres of radius R_{g0} (radius of gyration at infinite dilution), i.e. $\rho^*(N) \simeq 3N/4\pi R_{g0}^3$.(cf. Eq. (18)). This approximation is written explicitly as

$$\xi \simeq R_{g0}\left(\frac{4\pi\rho R_{g0}^3}{3N}\right)^{-\nu/(3\nu-1)} . \tag{215}$$

Scaling arguments are useful and allow to obtain easily an estimate of ξ; however, by construction they can only give the quantity of interest up to an unknown multiplicative factor, which is very inconvenient in cases where a precise knowledge of ξ is required. Estimates based on the correlation length –which can be obtained from scattering experiments– are also useful: However, as discussed in Sec. 3.3.2, the correlation length is not the same quantity as the mesh size, and taking them to be the same object can lead to apparently nonsensical results, such as ξ increasing when the polymer concentration is increased[41].

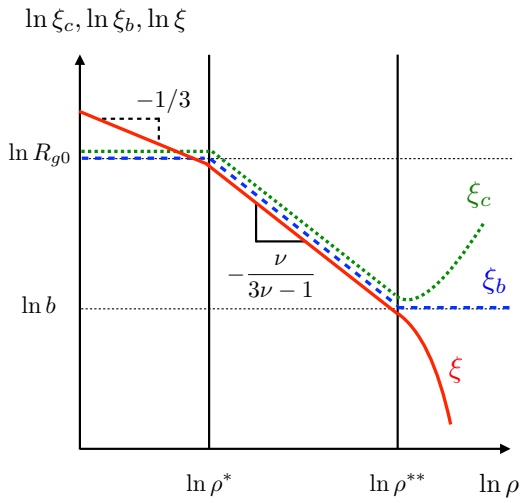

Figura 92 – Theoretical predictions for the blob size ξ_b, the correlation length ξ_c and the geometrical mesh size ξ as functions of density, respectively Eqs. (25), (51), and (30).

In the present chapter, we discuss how molecular dynamics simulations of coarse-grained polymers have been used to perform a systematic comparison of the different conventional ways to measure ξ, i.e., those based on scaling theory and those based on static correlation functions in Fourier and real space. We show that these techniques have serious limitations, can lead to apparently contradictory behaviors and can provide at best an approximate value for the average mesh size in the semidilute regime. To overcome these problems, we propose a different method to estimate ξ, based on the concept of pore size distribution[203,330–338]. One version of the pore size distribution, due to Torquato, has been already mentioned in Sec. 4.1.1, were it was used to compute the average interparticle distance between NPs in a PNC. We will show that, if the coordinates of the monomers are known, the pore size distribution allows to measure ξ reliably at any density, and also to obtain not only an average value, but the *distribution* of mesh sizes. This last feature can be particularly relevant, since it is known that particles diffusing in systems with the same average mesh size can display completely different dynamical behaviors[323], i.e., the heterogeneity of the polymer medium plays a relevant role in particle diffusion.

In Sec. 3.2 and 3.3 we have introduced the concepts of blob size ξ_b, geometrical mesh size ξ and monomer density fluctuation correlation length ξ_c, discussing their expected behaviors in the dilute, semidilute and concentrated regime. The main results of this analysis are summarized in the Eqs. (25), (30) and (51). In order to make these equations dimensionless, we also introduced the scaling variable χ, Eq. (27) (see Eqs. (28) and (31)). In Fig. 92, we schematically represent the predicted behaviors of ξ_b, ξ and ξ_c as a function of monomer density ρ. We can summarize the key predictions as follows:

- *Dilute regime* ($\rho < \rho^*$): The blob size and the correlation length are both approximately equal to the chain size, $\xi_b \approx \xi_c \approx R_{g0}$, where R_{g0} is the infinite dilution limit of the (RMS) radius of gyration, $R_{g0} \equiv \lim_{\rho\to 0} R_g$ [a]. The geometrical mesh size $\xi \propto (\rho/N)^{-1/3}$, i.e., the average distance between neighboring chains.

[a] Since we are making scaling estimates, other measures of chain size can be equivalently used, as for example the RMS end-to-end distance R_e.

- *Semidilute regime* ($\rho^* < \rho < \rho^{**}$): The three length scales are all equivalent in a scaling sense: $\xi_b \approx \xi_c \approx \xi$. In this regime, the whole system is described by a single relevant length scale.

- *Concentrated/melt regime* ($\rho > \rho^*$): The blob size reduces to the effective bond length, $\xi_b \approx b$, whereas ξ_c increases with increasing density as in every dense liquid. The geometrical mesh size, on the other hand, goes to zero with increasing density.

8.1 MODEL AND METHODS

We have performed NVT molecular dynamics simulations (MD) of a system of N_c coarse-grained polymer chains of length (degree of polymerization) N at different monomer densities $\rho = NN_c/V = M/V$. The model chosen to simulate the chains is the bead-spring model of Kremer and Grest (FENE+WCA potentials – see Sec. 3.6.3), where the parameters of the FENE potential (Eq. (106)) are $k = 30\epsilon/\sigma^2$ and $r_0 = 1.5\sigma$. Since non-bonded interactions are purely repulsive, this model mimics the behavior of polymers in an athermal solvent[5,41]. As usual, all quantities reported in the following are in reduced units: The units of energy, length and mass are respectively ϵ, σ and m, where ϵ, and σ are defined by Eq. (104) and m is the mass of a monomer. The units of temperature, pressure, density and time are respectively $[T] = \epsilon/k_B, [P] = \epsilon\sigma^{-3}, [\rho] = \sigma^{-3}$ and $[t] = \sqrt{m\sigma^2/\epsilon}$.

We considered chain lengths $N = 50, 200$, and 1000. For $N = 50$ and $N = 200$, we consider $N_c = 200$ and $N_c = 50$ chains respectively, so that the total number of monomers is $M = N_cN = 10^4$. For $N = 1000$, we simulated both a system of 10 chains ($M = 10^4$) and a larger one, consisting of 50 chains ($M = 5 \cdot 10^4$), in order to check for the presence of finite-size effects. For the system of 10 chains, five independent simulations were performed in order to improve the statistics. No relevant difference was found in all the studied quantities between the systems with $M = 10^4$ and those with $M = 5 \cdot 10^4$.

The range of monomer densities ρ for the different systems are reported in Tab. 4. While many of these densities are meant to represent a polymer solution, we do not take into account hydrodynamic interactions between the monomers, since we focus on static quantities, which are unaffected by hydrodynamic interactions.

All the simulations were carried out using the LAMMPS software[242]. The temperature was kept constant at $T = 1.0$ by means of a Langevin thermostat (Sec. 3.6.1) with damping coefficient $\Gamma = 0.1$. The simulation box is cubic and periodic boundary conditions are applied in all directions. In all the simulations, the MD integration time step is $\delta t = 3 \cdot 10^{-3}$. The initial configurations are prepared by randomly placing the polymers in the box; for every set of values (N, N_c, ρ) a different initial configuration is created. Initially, overlaps between the monomers are allowed. The overlaps are then removed by using a soft potential whose strength is increased over a short amount of time ("fast push-off" method[107]). After the overlaps have been removed, we switch to the WCA potential, Eq. (104), and perform an equilibration run of duration t_e (corresponding to $t_e/\delta t$ MD integration steps) before starting the production run. Since the relaxation time of a polymer chain scales as N^2 for unentangled chains and as $N^{3.4}$ for entangled chains, longer equilibration time were chosen for the system with longer chains. For each system, we checked that the equilibration time t_e was larger than the longest relaxation time of the system by studying the mean-squared displacement

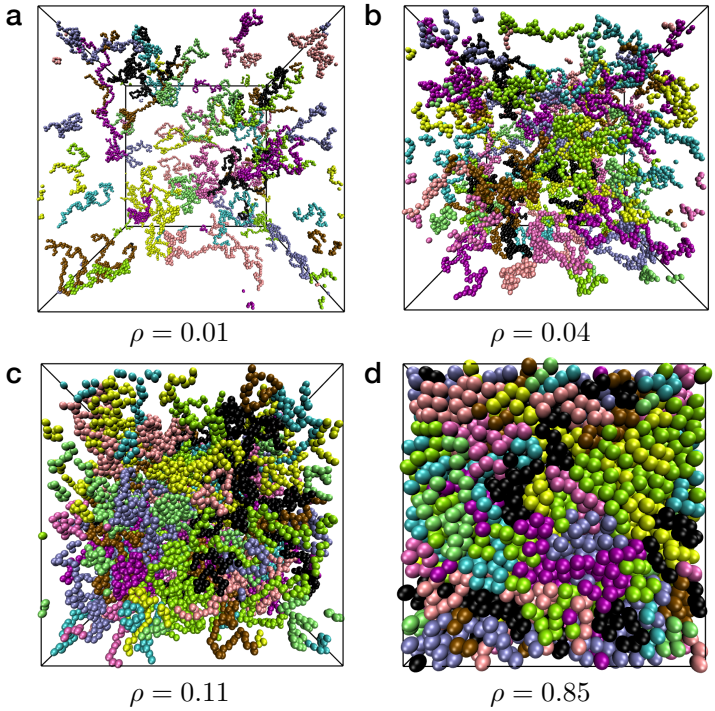

Figura 93 – Snapshots of the system $N = 200, N_c = 50$ and different densities ρ. For this system, $\rho^*(N = 200) \simeq 0.032$ and $\rho^{**} \simeq 0.3$. The lengths of the simulation box edges are respectively $L = 100$ (a) $L = 63.00$ (b) $L = 44.96$ (c) and $L = 22.74$ (d).

of the monomers and of the center of mass of the chains (Sec. 8.2.1 below). The values of t_e for the different systems are reported in Tab. 4.

Tabella 4 – Details of the simulated systems: chain length N, number of chains N_c, number of monomers M, monomer density ρ, equilibration time t_e.

N	N_c	$M = N_c N$	ρ (range)	t_e
50	200	$1 \cdot 10^4$	$[0.001, 1.00]$	$1.5 \cdot 10^5$
200	50	$1 \cdot 10^4$	$[0.001, 0.85]$	$4.5 \cdot 10^5$
1000	10	$1 \cdot 10^4$	$[0.001, 0.26]$	$3.0 \cdot 10^6$
1000	50	$5 \cdot 10^4$	$[0.001, 0.26]$	$3.0 \cdot 10^6$

In Fig. 93 we show four snapshots of the $N = 200$ system at different monomer densities. We note that for this model, $\rho^*(N = 200) \simeq 0.032$, and $\rho^{**} \simeq 0.3$ (see below). Therefore, the system in Fig. 93a is in the dilute regime; the one in Fig. 93b is in the semidilute regime, but very close to ρ^*; the one in Fig. 93c is in the semidilute regime and far from ρ^*; finally, the system in Fig. 93d is a melt.

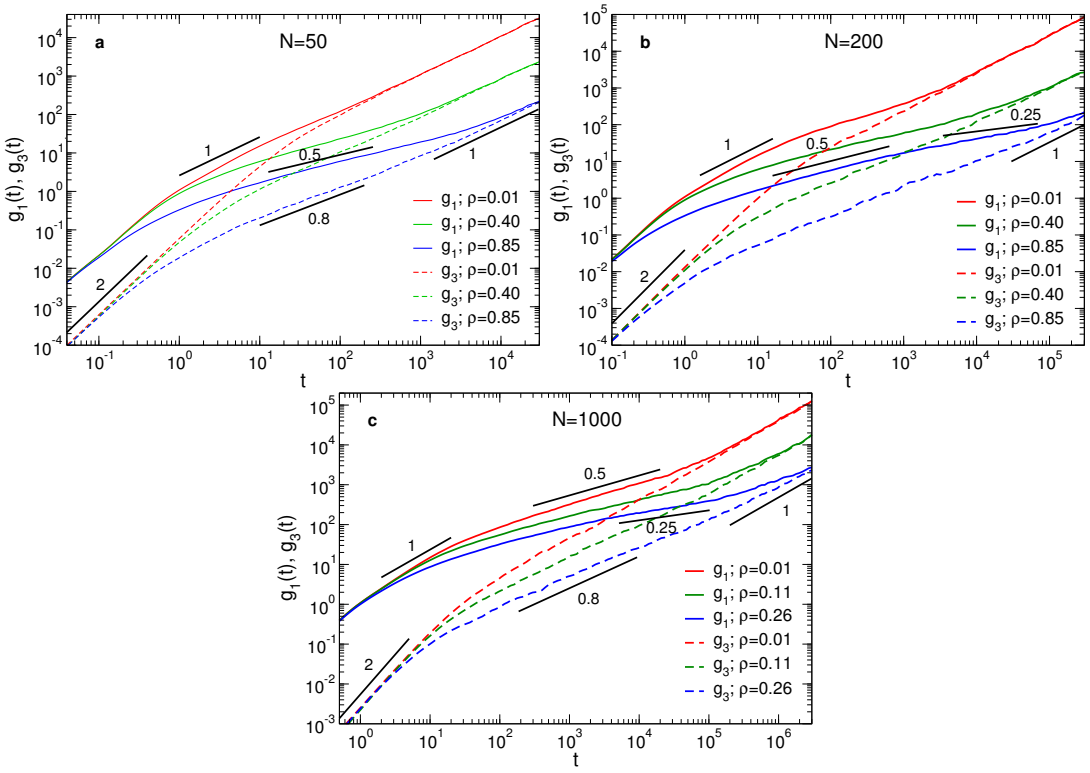

Figura 94 – Diffusion coefficient of the monomers, g_1, and of the centers of mass of the chains, g_3, for chain length $N = 50$ (a), $N = 200$ (b) and $N = 1000$ (c) and different monomer densities ρ.

8.2 PRELIMINARY ANALYSES

8.2.1 *Mean-squared displacement*

In order to check that the equilibration time is long enough, we consider two quantities: the mean-squared displacement (MSD) of the monomers, $g_1(t)$, and the MSD of the center of mass of the chains, $g_3(t)$ (Sec. 3.4). In order to suppress fluctuations caused by chain ends, only the $N/2+1$ monomers in the middle of each chain are considered when calculating g_1[52]:

$$g_1(t) \equiv \frac{1}{(N/2+1)} \sum_{i=N/4}^{3N/4} \langle [\mathbf{r}_i(t) - \mathbf{r}_i(0)]^2 \rangle. \tag{216}$$

In the present work, the motion of every monomer is governed by the Langevin equation, but hydrodynamic interactions between monomers are neglected. Therefore, the Rouse model (Sec. 3.4.1) describes the dynamics of the polymers to a very good approximation. We recall that the longest relaxation time, which is τ_R for unentangled systems and τ_d for entangled systems, is reached when $g_1(t) = g_3(t)$. We can therefore check that the system has equilibrated by verifying that this condition is met for long enough times.

In Fig. 94, we show $g_1(t)$ and $g_3(t)$ for different values of N and ρ. For the fully-flexible Kremer-Grest model here employed, the value of N_e is $\simeq 85$ at $\rho = 0.85$ ($T = 1.0$)[339], and it scales approximately as ρ^{-2} in the concentrated regime[321,340,341]: Therefore, the $N = 50$ system is unentangled for all densities and we expect its dynamics to be described by the Rouse model, Eqs. (56) and (58). From Fig. 94a, we can see that this is indeed the case. Moreover, the subdiffusive transient $g_3(t) \propto t^{\beta}$, with $\beta \simeq 0.8$, is clearly visible at $\rho = 0.85$. For $N = 200$, Fig. 94b, the system is lightly entangled; $N/N_e \simeq 200/85 = 2.35$ at $\rho = 0.85$, and the value becomes smaller with decreasing densities. The dynamics at high density is therefore described by the reptation model, Eqs. (73) and (72). Even at $\rho = 0.85$, we see however the $g_1(t) \propto t^{1/4}$ regime is still not perfectly developed, as also the $g_3(t) \propto t^{1/2}$ regime. The second $g_1(t) \propto t^{1/2}$ regime is not observable: Longer chains are probably needed[52]. For $N = 1000$, Fig. 94c, the system is entangled. Already at density $\rho = 0.26$ the regime $g_1(t) \propto t^{1/4}$ starts to show. The $g_3(t) \propto t^{1/2}$ regime, on the other hand, is not yet developed. For all values of N and ρ considered, we observe that the longest relaxation time, for which $g_1(t) = g_3(t)$, is smaller than the equilibration time t_e (see Tab. 4), and therefore the systems are well equilibrated.

8.2.2 *Chain form factor*

In order to check that the conformation of the chains corresponds to the equilibrium one, we study the chain form factor $S_1(q)/N$, where $S_1(q)$ is the single chain structure factor, whose predicted behavior as a function of density is given by Eq. (44). In Fig. 95, we show $S_1(q)/N$ for different values of $N = 50, 200$, and 1000 and for different values of the monomer density ρ. The swollen chain behavior $S_1(q)/N \propto q^{-1/\nu}$ and the ideal chain behavior $S_1(q)/N \propto q^{-2}$ are clearly observable respectively at low and high densities for $N = 50$ and $N = 200$. At intermediate densities, we expect the form factor to change from a q^{-2} dependence to a $q^{-1/\nu}$ dependence at $q \approx 1/\xi_c$[2,5]. Since $S_1(q)/N$ assumes values from $\approx 1/N$ to 1, this transition is

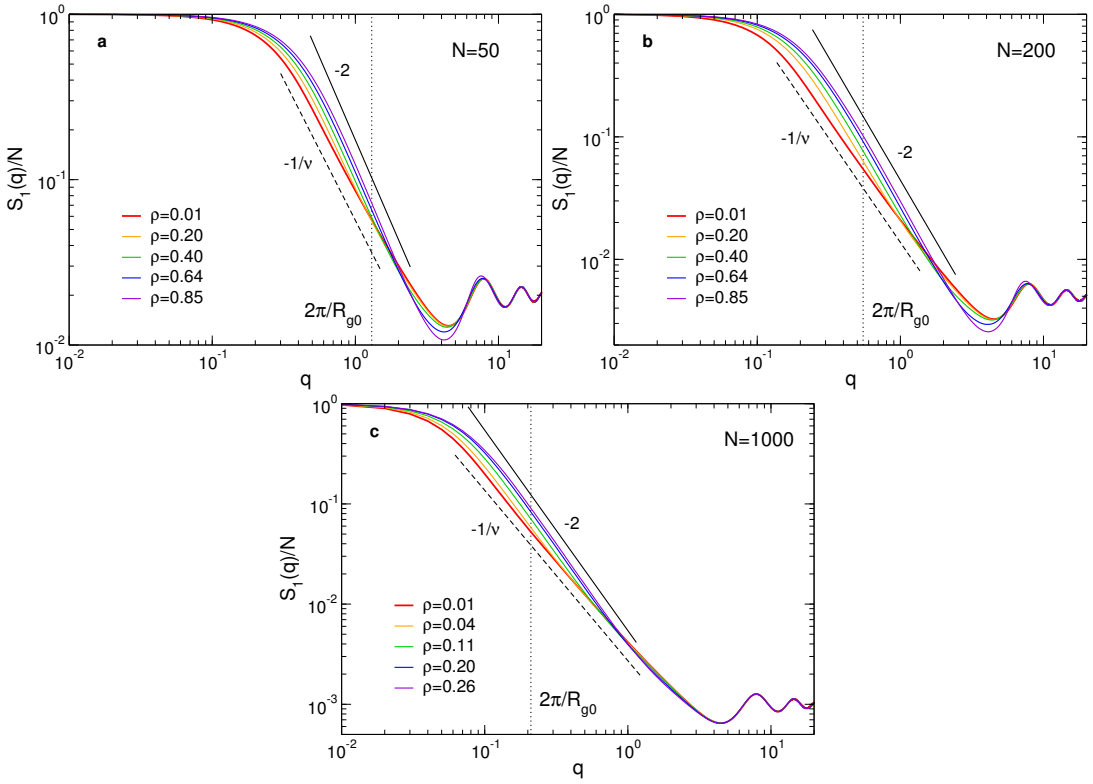

Figura 95 – Single chain form factor for chain length $N = 50$ (a), $N = 200$ (b) and $N = 1000$ (c) and different monomer densities ρ. Continuous lines: slope -2 (ideal chain). Dashed lines: slope $-1/\nu \simeq -1.70$ (swollen chain).

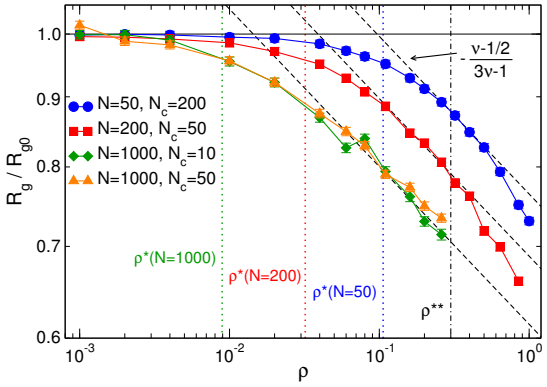

Figura 96 – Normalized polymer radius of gyration as a function of monomer density ρ. The dashed lines have slope $-\frac{\nu-1/2}{3\nu-1} \simeq -0.115$ ($\nu \simeq 0.588$).

more easily observable for the longer chains: $N = 200$ and $N = 1000$.

8.2.3 *Radius of gyration and bond angle distribution*

As an additional preliminary analysis of the structural properties of the simulated systems, we studied the behavior of the (RMS) radius of gyration $R_g = \sqrt{\langle r_g^2 \rangle}$ (Eq. (12)) as a function of monomer density ρ. The predicted scaling behavior for R_g is given by Eq. (26).

In Fig. 96, we report R_g/R_{g0} as a function of ρ, with the dashed lines representing power laws with exponent $-\frac{\nu-1/2}{3\nu-1} \simeq -0.115$. The radius of gyration in the dilute limit, R_{g0}, was computed by simulating a single polymer chain at very low density ($\rho = 10^{-3}$ for $N = 50, 200$ and $\rho = 10^{-4}$ for $N = 1000$): The results are reported in Tab. 5, alongside with the resulting estimate for the overlap density, given by Eq. (18). Figure 96 shows that R_g/R_{g0} follows the scaling predictions for all values of N up to the density $\rho \simeq 0.3$. For $\rho \gtrsim 0.3$, the decrease is steeper than what is predicted by scaling theory. This is likely due to the fact that in this density range the persistence length is density-dependent, an effect which scaling theory does not take into account.

The ρ-dependence of the persistence length can be understood by studying the bond-bond correlation function $\langle \cos(\theta_s) \rangle$, where $\cos(\theta_s)$ is defined as[342]

$$\cos(\theta_s) \equiv \frac{\mathbf{b}_n \cdot \mathbf{b}_{n+s}}{|\mathbf{b}_n| \, |\mathbf{b}_{n+s}|} \quad (s = 1, \ldots, N-n), \tag{217}$$

where $\mathbf{b}_n \equiv \mathbf{r}_{n+1} - \mathbf{r}_n$ is the n-th bond vector, with $\mathbf{r}_n$ the monomer's position vector. For very long chains, $\langle \cos(\theta_s) \rangle$ is expected to have the following behavior[342–344]:

$$\langle \cos(\theta_s) \rangle \propto \begin{cases} s^{-2(1-\nu)} & l_p/l_b < s \ll N_b(\rho) \\ s^{-3/2} & N_b(\rho) \ll s \ll N, \end{cases} \tag{218}$$

where l_p is the persistence length[5], $l_b = \sqrt{\langle \mathbf{b}_n \rangle}$ is the RMS bond length and N_b is the number of monomers in a blob (see Eq. (20)). For the fully flexible Kremer-Grest model considered here, $l_p \approx l_b$[52]. Since in the dilute regime $N_b \approx N$, we expect in this regime $\langle \cos(\theta_s) \rangle \propto$

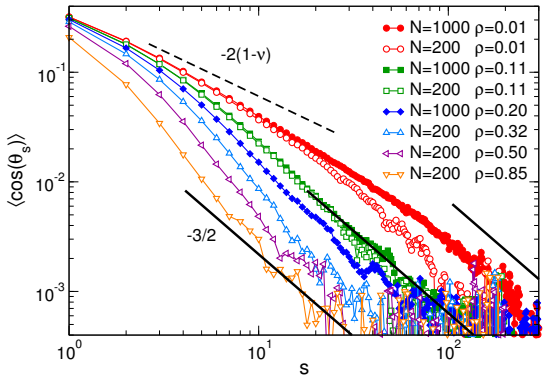

Figura 97 – Bond-bond correlation function $\langle \cos(\theta_s) \rangle$, Eq. (217), for $N = 200$ and 1000 and for different values of ρ. The dashed line indicates the predicted theoretical behavior for small s, whereas the continuous lines indicate the predicted high-s behavior (see Eq. (218)). We note that $2(1-\nu) \simeq 0.824$.

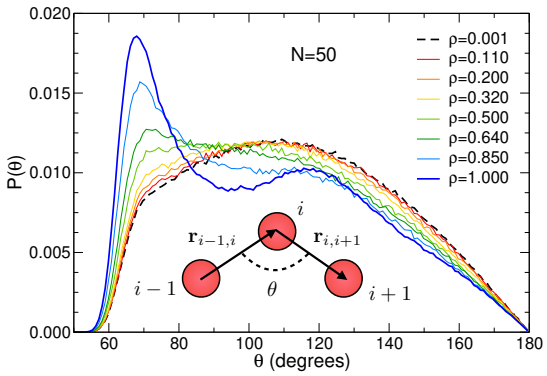

Figura 98 – Bond angle distribution for $N = 50$ and different monomer densities ρ. The bond angle θ is defined by Eq. (219). Cartoon: schematic representation of how θ is defined.

$s^{-2(1-\nu)}$ $\forall s > l_p/l_b \approx 1$. Analogously, since in the concentrated regime $N_b \approx 1$, we expect $\langle \cos(\theta_s) \rangle \propto s^{-3/2}$ $\forall s \ll N$.

In Fig. 97 we report $\langle \cos(\theta_s) \rangle$ for $N = 200$ and 1000 and different densities (for $N = 50$ we find similar results). The chains considered here are too short to clearly observe the small-s regime $s^{-2(1-\nu)}$ (dashed line). On the other hand, the large-s behavior is compatible with the theoretical prediction $\langle \cos(\theta_s) \rangle \propto s^{-3/2}$, as illustrated by the continuous lines. Although it is difficult to precisely quantify the persistence length outside of the melt regime for highly flexible and rather short chains as those considered here[344], the marked reduction of $\langle \cos(\theta_s) \rangle$ with increasing ρ observed for small value of s is compatible with a reduction of the persistence length l_p.

A reduction of l_p with increasing density can also be inferred by considering the distribution of the bond angle $\theta \equiv \pi - \theta_1$, i.e.,

$$\theta \equiv \arccos\left(-\frac{\mathbf{r}_{i-1,i} \cdot \mathbf{r}_{i,i+1}}{|\mathbf{r}_{i-1,i}| \, |\mathbf{r}_{i,i+1}|} \right). \tag{219}$$

In Fig. 98 we report the bond angle distribution $P(\theta)$ for $N = 50$ and different densities (for larger N, the results are basically the same). At low density, $P(\theta)$ shows a maximum

N	R_{g0}	$3N/4\pi R_{g0}^3$
50	4.83 ± 0.02	$1.1 \cdot 10^{-1}$
200	11.44 ± 0.07	$3.2 \cdot 10^{-2}$
1000	29.9 ± 0.2	$8.9 \cdot 10^{-3}$

Tabella 5 – N-dependent properties of the simulated systems: Radius of gyration in the dilute limit, R_{g0} and approximate overlap concentration (Eq. (18)).

at $\theta \simeq 112^\circ$ and falls to zero rather sharply at $\theta \simeq 60^\circ$ because of the excluded volume interaction. When ρ is increased past $\rho \simeq 0.3$, the shape of $P(\theta)$ starts to change significantly in that it develops a peak at $\theta \simeq 70^\circ$, signaling that the chains are compressed. Overall, the average bond angle decreases by $\simeq 8\%$ when going from the dilute regime to density $\rho \gtrsim 0.85$. This effect is also observable in the average bond length (not shown), although the decrease is in this case only $\simeq 1\%$. Although it is possible to conceive chain conformations with a small $\langle\theta\rangle$ but a high persistence length (e.g., an "accordion-like" rigid polymer), the fact that up to very high ρ the form factor is compatible with the scaling predictions for chains in a concentrated solution (Sec. 8.2.2) suggests that the reduction of $\langle\theta\rangle$ corresponds to a reduction of the persistence length.

8.3 DENSITY FLUCTUATION CORRELATION LENGTH

As discussed in Sec. 3.3.2, the correlation length ξ_c can be measured either from the monomer structure factor $S(q)$, Eq. (32), or from the monomer radial distribution function $g(r)$, Eq. (34). Since the system is isotropic, we will consider the spherically averaged structure factor, $S(q)$, which depends only on $q \equiv |\mathbf{q}|$ (Eq. (33)).

In Fig. 99 we show the monomer structure factor for $N = 50, 200$ and 1000 and different densities. In the dilute regime, we expect (see Sec. 3.3)

$$S(q) \simeq S_1(q) = \begin{cases} N/(1 + q^2 R_{g0}^2/3) & q \ll R_{g0}^{-1} \\ C q^{-1/\nu} & R_{g0}^{-1} \ll q \ll b^{-1} \\ \mathcal{O}(1) & q \gg b^{-1}, \end{cases} \tag{220}$$

where $S_1(q)$ is the single chain structure factor and $C > 0$ is a constant. In Fig. 99a-c, we show as thin continuous lines $S_1(q)$ for $\rho = 10^{-3}$. For $N = 50$ and 200, we see that $S(q) = S_1(q)$ at this density, meaning that the system is already in the infinite dilution limit, whereas for $N = 1000$ this limit is still not reached. In the semidilute regime, the behavior of $S(q)$ is predicted to follow Eq. (45). From our data, we can observe at intermediate q the slope $-1/\nu \simeq -1.70$; as expected, this regime is more clearly observable for the longest chains, $N = 1000$ (Fig. 99c).

As ρ is increased, the isothermal compressibility $\kappa_T = S(0)/\rho k_B T$ decreases, and eventually, for $\rho \geq 0.85$, the structure becomes virtually indistinguishable from that of a dense liquid [1,39]. Comparing $S(q)$ for different chain lengths, we note that for densities $\rho > 0.11 \simeq \rho^*(N = 50)$, $S(q)$ becomes independent of N (Fig. 100). This is in agreement with the prediction that in the semidilute and concentrated regimes, $\rho > \rho^*$, the global structure of the system does not depend on N [5].

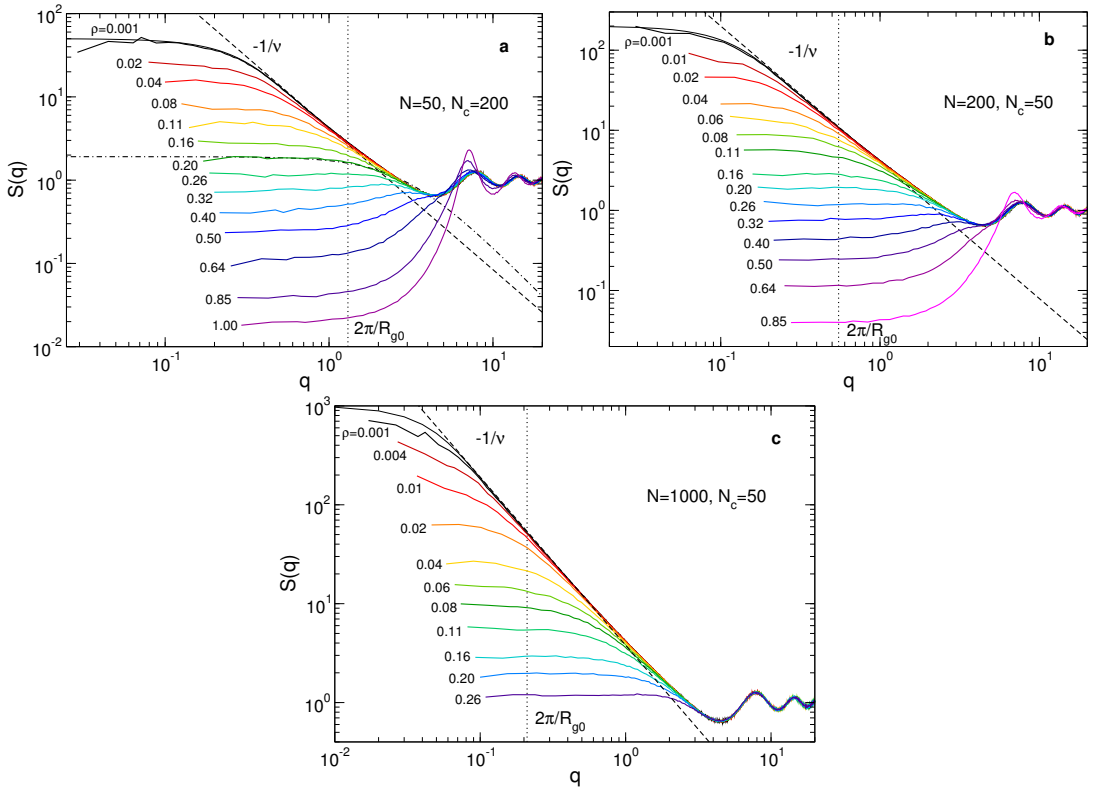

Figura 99 – Monomer structure factor for $N = 50, N_c = 200$ (a), $N = 200, N_c = 50$ (b) and $N = 1000, N_c = 50$ (c), at different monomer densities. Thin continuous lines: $S_1(q)$ for $\rho = 10^{-3}$. Dashed lines: slope $-1/\nu \simeq -1.70$ ($\nu \simeq 0.588$). Dash-dotted curve in (a): fit with the Ornstein-Zernike function, Eq. (46).

The correlation length ξ_c can be measured by fitting $S(q)$ in the low-q range with the Ornstein-Zernike expression, Eq. (46). It is clear, however, that this expression only gives a good description of the data for densities $\rho \lesssim 0.3 = \rho^{**}$. To circumvent this limitation, we consider the radial distribution function of the monomers, $g(r)$, given by Eq. (34). The expected asymptotic expression of $g(r)$ at low and high ρ is given by Eqs. (47) and (50). At low ρ, we can therefore obtain ξ_c from $g(r)$ by fitting it with an exponential, while at higher ρ we fit the exponential envelope of the function[41]. This method is illustrated in Fig. 101, where we show $r|g(r) - 1|$ for $N = 200$ and different values of ρ, with the slopes resulting from the fit (dashed lines). One can see that the low-ρ form works well up to density $\rho \simeq 0.11$, while the high-ρ one gives a good description of the data starting from $\rho \simeq 0.64$. For densities in-between, neither of these two expressions gives a really satisfactory description of the data. We decide nevertheless to fit the data with an exponential also in this intermediate range, as shown in Fig. 101, in order to have at least an estimate of ξ_c.

The values of ξ_c obtained by fitting $S(q)$ and $g(r)$ are reported in Fig. 102a as a function of ρ. We note that the two estimates give almost identical results for $\rho < 0.2$. For $\rho \geq 0.26$, i.e., when we start to approach $\rho^{**} = 0.3$ we cannot fit reliably the structure factor with the Ornstein-Zernike function, Eq. (46), and we have to rely on the radial distribution function. We note that ξ_c reaches a minimum at $\rho \simeq 0.3 = \rho^{**}$ and increases for larger ρ. The increase of ξ_c with ρ is due to local packing constraints, and it is a typical behavior for any dense liquid[41].

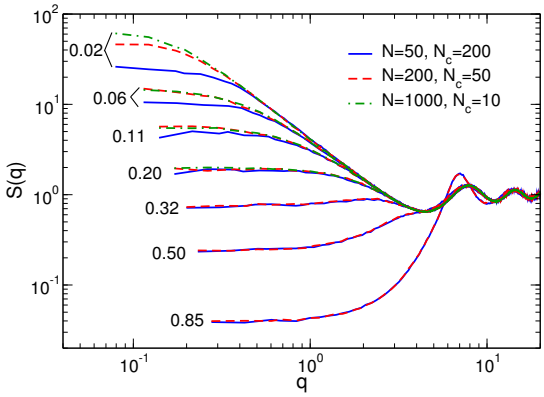

Figura 100 – Comparison between the monomer structure factors $S(q)$ of systems with different chain lengths N at the same monomer density ρ. For densities $\rho > 0.11 \simeq \rho^*(N = 50)$, $S(q)$ becomes independent of N.

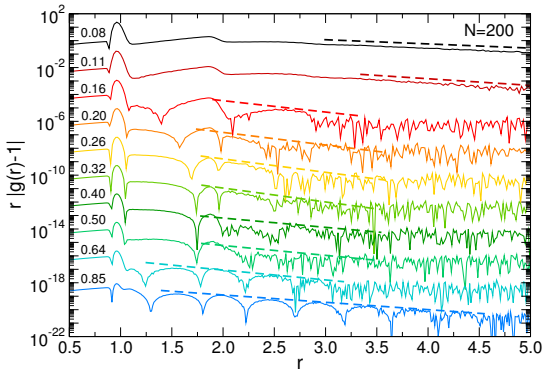

Figura 101 – The function $r|g(r) - 1|$, with $g(r)$ = radial distribution function), for $N = 200$ and different monomer densities. To facilitate the visualization, every curve starting from $\rho = 0.08$ was shifted by a factor 100 with respect to the previous, except for $\rho = 0.85$, which is shifted by a factor 200. The dashed lines are exponential fits.

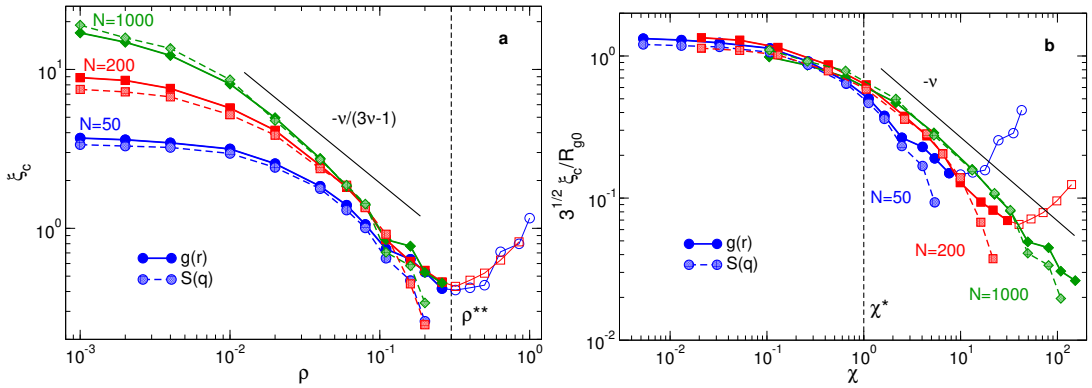

Figura 102 – The length ξ_c measured from $g(r)$ (dark symbols, continuous lines) and from $S(q)$ (light symbols, dashed lines), as a function of monomer density (a) and the scaling variable χ, Eq. (27) (b). Continuous lines represent the slopes predicted by scaling theory for the semidilute regime. Open symbols denote densities $\rho > 0.3$ (concentrated regime).

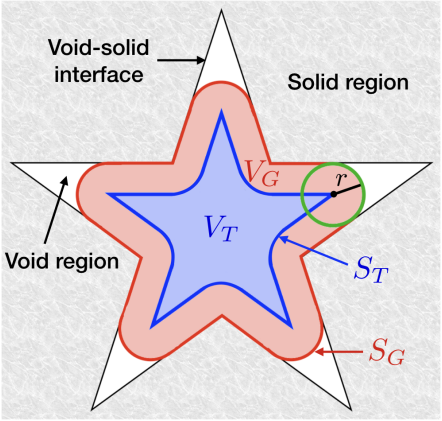

Figura 103 – Example of a porous medium with a single star-shaped pore. V_T is the volume of the portion of void space which is accessible to the center of a spherical probe particle of radius r. This volume is enclosed in the surface S_T followed by the center of the particle as the particle slides over the void-solid interface. V_G is the volume which is coverable by spheres of radius r or smaller, and it is enclosed in the Connolly (or reentrant) surface S_G.

In Fig. 102b, we plot $\sqrt{3}\ \xi_c/R_{g0}$ as a function of the scaling variable χ, Eq. (27). At low densities, $\sqrt{3}\ \xi_c/R_{g0} \simeq 1$, in agreement with the theoretical predictions (Eq. (48)). We observe that in the semidilute regime, ξ_c follows approximately the predictions of scaling theory Eq. (51), i.e. $\xi_c \propto \rho^{-\nu/(3\nu-1)}$ (Fig. 102a), or equivalently $\xi_c \propto \chi^{-\nu}$ (Fig. 102b). The agreement with the theory becomes better with increasing N, as expected from the fact that $\lim_{N\to\infty} \rho^* = 0$, or analogously $\lim_{N\to\infty} \chi^{**} = \infty$.

8.4 ESTIMATING THE GEOMETRICAL MESH SIZE VIA THE PORE SIZE DISTRIBUTION

8.4.1 *Definitions*

We have seen in the previous section how to estimate the monomer correlation length ξ_c. As discussed in Sec. 3.2, only in the semidilute regime we have $\xi_c \approx \xi$. In the dilute regime, $\xi_c \approx R_{g0}$, while $\xi \propto (\rho/N)^{-1/3}$; in the concentrated regime, ξ_c increases, while ξ is expected to decrease. In order to get the actual geometrical mesh size, we therefore need a way to measure directly the size of the pores in the system. With this objective in mind, we turn to a concept that was developed in order to measure the distribution of pore sizes in solid porous media: the *pore size distribution* (PSD)[203,330–338].

We will consider two different definitions of the PSD: The first one, although introduced by others[330,331], was formalized and extensively studied by Torquato and coworkers[203,332–334], while the second one was introduced by Gubbins and coworkers[335–338]. We will in the following consider a generic porous medium in three dimensions, but all the definitions can be extended to any two-phase system and any number of spatial dimensions. Our presentation closely follows the one given by Torquato[203,332–334]. A porous medium is a three-dimensional domain of volume V which is composed by two sub-domains: a void (or pore) region, of volume V_p and volume fraction $\phi_p \equiv V_p/V$ (also called the *porosity*), and a solid region of volume $V_s = V - V_p$ and volume fraction $\phi_s \equiv V_s/V = 1 - \phi_p$. In Fig. 103, we show a schematic example of a porous medium with a single star-shaped pore.

Following Torquato, we start by defining the quantity $V_T(r)$ as the pore volume accessible

to the center of a spherical particle with radius r. With reference to Fig. 103, this is the volume inside the surface S_T followed by the center of the particle when the particle slides over the interface void-solid interface. Naturally, $V_T(r) \leq V_p$. We can then define the *fraction* of pore volume which is accessible to the particle as $F_T(r) \equiv V_T(r)/V_p$. It is clear from the definition that

$$F_T(0) = 1; \quad \lim_{r\to\infty} F_T(r) = 0. \tag{221}$$

Torquato's PSD is then defined as the probability density function[203,332–334]

$$P_T(r) \equiv -\frac{\mathrm{d}F_T(r)}{\mathrm{d}r}. \tag{222}$$

Thus, $P_T(r)dr$ represents the probability that a randomly chosen point in the pore region lies at a distance between r and $r + dr$ from the nearest point on the pore-solid interface. From (221) and (222) it follows that

$$F_T(r) = \int_r^\infty P_T(x)\mathrm{d}x, \tag{223}$$

and that $P_T(r)$ is normalized to unity:

$$\int_0^\infty P_T(x)\mathrm{d}x = 1. \tag{224}$$

Moreover, $P_T(r)$ must clearly vanish for $r \to \infty$.

The definition of Gubbins differs from that of Torquato by a simple, yet significant detail. Instead of considering the part of pore volume which is accessible to the *center* of a spherical particle of radius r, we consider the part which is accessible to *any point* of the particle. In other words, we define $V_G(r)$ as the pore volume coverable by spheres of radius r or smaller, i.e., the set of all the points $\mathcal{P}$ in the pore space such that we can construct a sphere of radius r that contains $\mathcal{P}$ but does not contain any point belonging to the solid phase[335] (Fig. 103). The surface S_G in which V_G is enclosed is sometimes called *Connolly surface* or *reentrant surface*[336,345].

Therefore, $P_G(r)dr$ represents the probability that a randomly chosen point in the pore space is coverable by spheres of radius r but *not* by spheres of radius $r + \mathrm{d}r$[335] [b]. Once $V_G(r)$ is defined, all the other quantities can be defined exactly as done above for Torquato's definition. We note that analogous definitions of V_T and V_G have been given by other authors[336,345,347,348].

The PSDs $P_T(r)$ and $P_G(r)$, obtained respectively from $V_T(r)$ and from $V_G(r)$, can differ significantly from each other. To see this, let's consider the simple case of a solid material

[b] Other definitions of the PSD are possible. In the definition of Do *et al.*[346], for example, the void-solid interface is the boundary of the region $\mathcal{D}$ such that if the center of the probe particle is in $\mathcal{D}$, the solid-probe interaction energy is zero. If the solid-probe interaction potential is taken to be a hard-sphere interaction, this definition is equivalent to the one of Torquato. Despite the arbitrariness deriving from the choice of the solid-probe potential, this method can indeed be more suitable than the one of Torquato in situations where the solid-probe interaction cannot be approximated as a hard-sphere interaction (e.g., in the presence of soft potentials).

containing any number of disconnected spherical pores of radius R. It is easy to see that in this case[331]:

$$F_T(r) = \left(\frac{R-r}{R}\right)^3; \quad P_T(r) = \frac{3(R-r)^2}{R^3} \quad (r \leq R), \tag{225}$$

while

$$F_G(r) = \begin{cases} 1 & r \leq R \\ 0 & r > R \end{cases}; \quad P_G(r) = \delta(r-R), \tag{226}$$

where δ is Dirac's delta distribution. It is clear that in this case the size R of the pores is most readily identified by considering P_G, which is nothing else than a delta distribution centered at R, whereas P_T goes to zero at R. We will see below that also when dealing with more realistic systems, P_G often conveys the information regarding the typical size of the pore in a much clearer manner than P_T.

In order to compute P_T and P_G from the simulation data, we first need to divide the sample in a pore region and in a solid region. For simplicity, we assume that the interaction potential between the probe particle of radius r and the monomers is hard-sphere like, i.e.,

$$\mathcal{U}(d) = \begin{cases} \infty & d < r + r_m \\ 0 & d \geq r + r_m, \end{cases} \tag{227}$$

where d is the distance between the probe particle and the monomer and r_m is the radius of the monomer when it is approximated as a hard sphere. In the present work, we choose $r_m = \sigma/2 = 0.5$ [c]. Once this assumption is made, we can proceed to the calculation of the PSD, following the two definitions. The algorithms used to calculate P_T and P_G are described in Sec. 8.4.2

In Fig. 104, we show the PSDs P_G, P_T and the complementary cumulative distribution functions F_G, F_T for $N = 200$ and different densities. In both graphs, r has been normalized with the length of the simulation box L in order to make the plot more readable. We find that F_T drops to zero much more quickly than F_G, and that their shapes are quite different. As a consequence, also the distributions P_T and P_G are very different.

In Fig. 105 we show $P_G(\tilde{r})$, where $\tilde{r} \equiv r/\langle r \rangle_G - 1$, where $\langle r \rangle_G$ is the mean value of r calculated using Gubbins's PSD, for $N = 200$ and different densities. One can see that at high density, the distribution is very similar to a Gaussian. This becomes clearer when plotting $P_G(\tilde{r})$ as a function of $\mathrm{sgn}(\tilde{r}) \cdot \tilde{r}^2$ (with sgn the sign function) in semi-logarithmic scale, as shown in the inset of Fig. 105. Only at density $\rho < \rho^*$ we observe significative deviations from Gaussianity, with the left-side tail displaying a markedly exponential decay (dashed line in the inset of Fig. 105). The small shoulder observable at low ρ for small values of $\tilde{r}$ (indicated by the arrow in the inset of of Fig. 105) comes from distances inside the pervaded volume of the chain.

[c] We note that different choices of r_m will lead to different PSDs. However, given two different values r_m and r'_m, we expect the difference between the PSDs computed using these two values to be relevantt only when the average pore size is comparable to, or smaller than, $|r_m - r'_m|$.

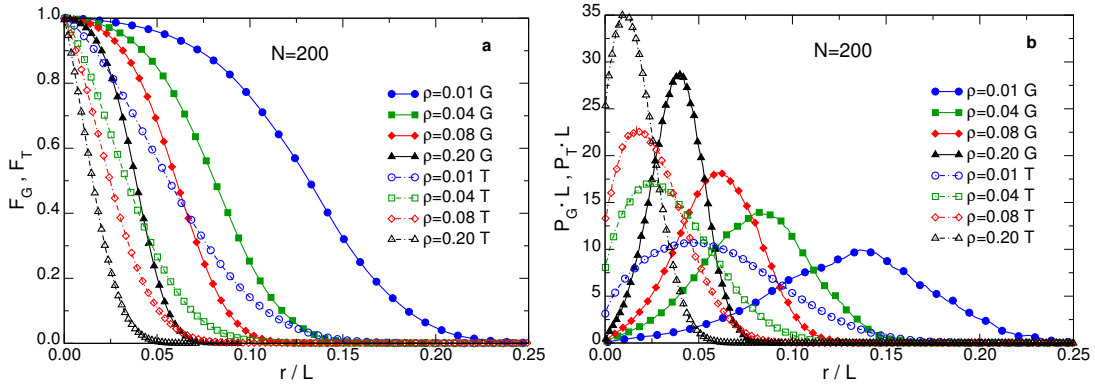

Figura 104 – Complementary cumulative distributions $F_\alpha(r)$ ($\alpha = T, G$) (a) and PSDs $P_\alpha(r)$ (b), as obtained using the definitions of Torquato (filled symbols, continuous lines) and of Gubbins (open symbols, dash-dotted lines). The variable r has been rescaled to the length L of the simulation box in order to facilitate visualization.

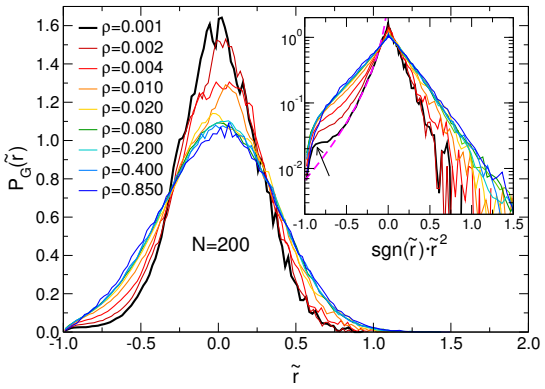

Figura 105 – Gubbins's PSD, $P_G(\tilde{r})$, for $N = 50$ and at different densities ρ, as a function of $\tilde{r} \equiv r/\langle r \rangle_G - 1$. *Inset*: The same quantity as a function of $\mathrm{sgn}(\tilde{r})\ \tilde{r}^2$ in semi-logarithmic scale. Dashed line: exponential fit. The arrow is discussed in the text.

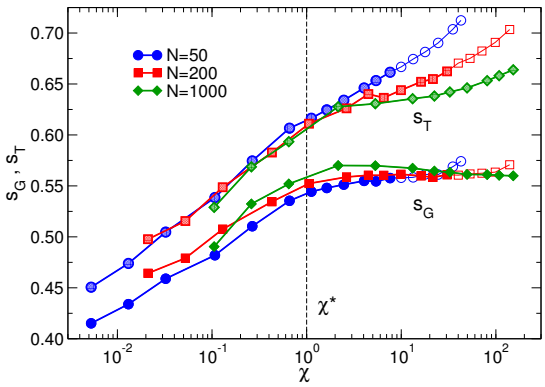

Figura 106 – Relative standard deviation s_α ($\alpha = G, T$), Eq. (228), as a function of the scaling variable χ. s_G was shifted up by 0.2 to facilitate the comparison with s_T. Open symbols denote densities $\rho > \rho^{**} = 0.3$

We note that the width of $P_G(\tilde{r})$ increases with increasing density, indicating that the pore space becomes more heterogeneous on the length scale of the mean pore size $\langle r \rangle_G$. Moreover, although the shape of $P_G(\tilde{r})$ changes quite significantly when ρ is increased in the dilute regime, it remains almost unchanged for $\rho > \rho^* \simeq 0.032$. This effect can be better appreciated by considering the relative standard deviation,

$$s_\alpha \equiv \sqrt{\frac{\langle r^2 \rangle_\alpha}{\langle r \rangle_\alpha^2} - 1} \quad (\alpha = T, G), \tag{228}$$

which is a measure of the width of the PSD relative to its mean value.

In Fig. 106, we show s_G and s_T as a function of the scaling variable χ. One can see that s_G increases with increasing χ up to the beginning of the semidilute regime at $\chi = \chi^* = 1$, where it reaches a plateau. The transition from dilute to semidilute behavior is quite sharp if compared with that of ξ_c (Fig. 102b) or R_g (Fig. 96), suggesting that P_G can be used to determine ρ^* in a more precise way. In addition, s_G is almost independent of N for a given value of χ.

The relative standard deviation s_T of Torquato's PSD behaves quite differently, showing a marked dependence on N at fixed χ for $\chi > 1$. Only for $N = 1000$ a behavior similar to that of s_G, with an increase up to $\chi = 1$ followed by a pleateau, is recovered. These observations suggest that P_G may be more suitable than P_T to probe the pore structure of the system. This will also be argued below based on different considerations. Additional details on P_T will be given in Sec. 8.4.4.

8.4.2 *Calculating the PSD*

Torquato's definition

The algorithm to compute Torquato's PSD is described in Ref. 203. First of all, as mentioned in Sec. 8.4.3, we have to divide the sample in a "pore" region and a "solid" region. In order to do so, we approximate the monomers as hard spheres of diameter σ. The procedure to calculate $P_T(r)$ is then as follows:

1. A random point $\mathbf{r}$ is chosen in the pore phase.

2. The smallest distance $r_{\min}$ between $\mathbf{r}$ and the center of a monomer is calculated. The distance between $\mathbf{r}$ and the nearest interface is calculated as $r = r_{\min} - \sigma/2$.

This procedure is repeated many times, until a large number $\mathcal{N}$ of r values is recorded. In the limit of large $\mathcal{N}$, the normalized histogram of these values is equivalent to $P_T(r)$.

Gubbins's definition

In order to calculate $P_G(r)$, we have used the algorithm proposed by Bhattacharya and Gubbins in Ref. 338. This algorithm is based on the observation that the problem of finding the largest sphere containing $\mathbf{r}$ and which does not overlap with any monomer can be reformulated as the problem of maximizing the function

$$r(\mathbf{r}_c) \equiv \min_{i=1,\dots M}\{s_i\} - \sigma/2, \tag{229}$$

subject to the constraint

$$|\mathbf{r}_c - \mathbf{r}| - r(\mathbf{r}_c) \leq 0, \tag{230}$$

where $\mathbf{r}_c$ is the position of the sphere's center and s_i is the distance between $\mathbf{r}_c$ and the centers $\mathbf{r}_i$ of the monomers: $s_i = |\mathbf{r}_c - \mathbf{r}_i|$. If the maximization of the function (229) is carried out for a large enough number of points $\mathbf{r}$, the resulting (normalized) histogram of r values will converge to $P_G(r)$.

The problem of calculating $P_G(r)$ reduces therefore to a nonlinear optimization problem, which can be solved with a standard algorithm[349]. We have used the open-source Sbplx algorithm of the NLopt library[350], which is a re-implementation of Subplex[351]. Other choices are possible, although one has to make sure that the chosen algorithm can handle discontinuous objective functions[338].

8.4.3 *Estimating the geometrical mesh size via the pore size distribution*

Once the PSD has been determined, we need to extract from it a quantity that we can compare with ξ_c and with the theoretical expectations for ξ. The most natural choice is to consider the mean pore radius,

$$\langle r\rangle_\alpha \equiv \int_0^\infty x\, P_\alpha(x)\mathrm{d}x = \int_0^\infty F_\alpha(x)\mathrm{d}x \quad (\alpha = T, G). \tag{231}$$

Although other choices are possible, such as the position of the peak of $P(r)$, we found that the main results do not depend significantly on this choice.
In Fig. 107 we show $\langle r\rangle_G/R_{g0}$ and $\langle r\rangle_T/R_{g0}$ as a function of the scaling variable χ for different values of N. These two quantities are compared with ξ_c/R_{g0}, where ξ_c is measured from the radial distribution function (points for $\rho > 0.3$ not shown), and with the scaling estimate of Eq. (215). We observe that, despite the fact that $\langle r\rangle_G > \langle r\rangle_T$, both quantities show a remarkably good agreement with the scaling prediction, Eq. (31). Moreover, above the dilute regime, i.e., $\chi \gtrsim 1$, $\langle r\rangle_T \simeq \xi_c$, likely because the calculation of both quantities involves averaging over distances which are of similar magnitude.

To better see that $\langle r\rangle_\alpha$ ($\alpha = T, G$) follow the scaling prediction, we show in Fig. 108a $\langle r\rangle_\alpha$ multiplied by χ^ν (points corresponding to $\rho > 0.3$ not shown): For $\chi \gtrsim 1$, they reach a plateau, the length of which increases with increasing N implying that $\langle r\rangle_\alpha$ is indeed proportional to $\chi^{-\nu}$. Moreover, we also see that for low χ the function tends towards the predicted behavior $\chi^{-\nu+1/3}$, corresponding to the average distance between neighboring chains, Eq. (31). In Fig. 108b we show the ratio $\langle r\rangle_G/\langle r\rangle_T$ as a function of χ (points corresponding to $\rho > 0.3$ not shown). For $\chi < 1$, the ratio increases logarithmically with increasing χ and is independent of N. This demonstrates that in the dilute regime $\langle r\rangle_G$ and $\langle r\rangle_T$ are directly related to each other via an N-independent function. For $\chi > 1$ the $N = 50$ data follows this logarithmic

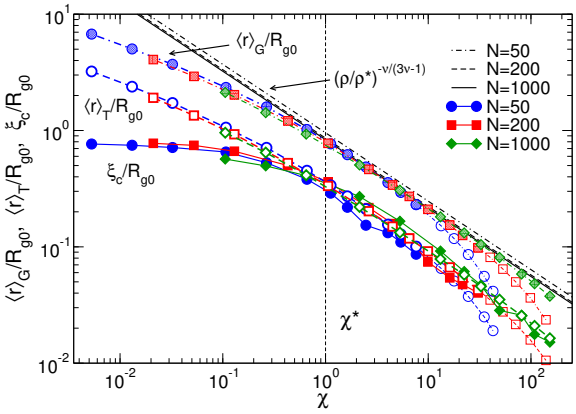

Figura 107 – Comparison between the average pore sizes, the density fluctuation correlation length ξ_c and the scaling estimate of Eqs. (22), with ρ^* estimated using Eq. (215) (ρ was expressed as a function of χ using Eq. (27)), as a function of the scaling variable χ. Dark filled symbols with continuous lines: ξ_c/R_{g0}. Thick-bordered open symbols with dashed lines: $\langle r\rangle_T/R_{g0}$. Light filled symbols with dash-dotted lines: $\langle r\rangle_G/R_{g0}$. Thin-bordered open symbols denote densities $\rho > \rho^{**} = 0.3$. Thick black lines: scaling estimate for $N = 50$ (dash-dotted) $N = 200$ (dashed) and $N = 1000$ (continuous).

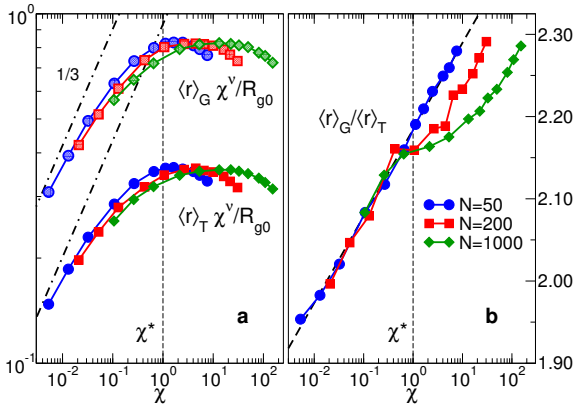

Figura 108 – (a) $\chi^\nu \cdot \langle r\rangle_\alpha/R_{g0}$ ($\alpha = G, T$) as a function of the scaling variable χ. Dash-dotted lines: Predicted slopes in the dilute limit, Eq. (31). (b) Ratio $\langle r\rangle_G/\langle r\rangle_T$ as a function of χ. Thick dashed line: $2.18 + 0.0458\ln(\chi)$. Points corresponding to $\rho > \rho^{**} = 0.3$ are not shown.

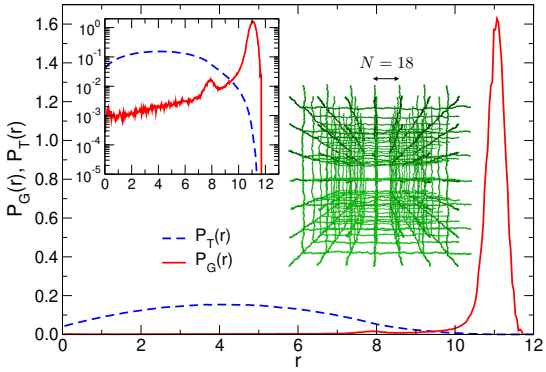

Figura 109 – PSD for a model polymer gel (cubic lattice with strand length $N = 18$; a snapshot of the system is reported in the main figure). Dashed blue line: Torquato's PSD. Continuous red line: Gubbins's PSD. *Inset:* double logarithmic plot of the same PSDs.

dependence whereas the larger systems show a plateau the width of which increases with N, and only for larger χ the ratio increases again. In summary one can conclude that this ratio displays a surprisingly weak dependence on χ, changing only by $\simeq 15\%$ over several decades in χ.

To summarize, we have two possible estimators for the mesh size, which are both in excellent agreement with the scaling prediction and differ from each other by a multiplicative factor $\simeq 2$. This factor is of course irrelevant if we are only interested in order-of-magnitude estimates of the mesh size, but it is relevant when more precise information about the size of the pores is needed. In other words, it is important to understand which PSD, P_G or P_T, gives us a more precise information about the "real" size of the pores. In the following we will therefore discuss how to interpret the PSD, and which estimator to choose between $\langle r \rangle_G$ and $\langle r \rangle_T$ when more quantitative information about the mesh size is required.

When considering the case of a solid material containing disconnected spherical pores, Eqs. (225) and (226), one can see that it is much more straightforward to infer the value of R from $P_G(r)$ than from $P_T(r)$. Indeed, using Eq. (225) we find $\langle r \rangle_T = R/4$, whereas from Eq. (226) one obtains $\langle r \rangle_G = R$. Thus already this simple example hints that $\langle r \rangle_G$ is a better indicator for the "real" pore size than $\langle r \rangle_T$. In order to consider a somewhat less artificial example, we simulated a simple model of a polymer gel: Polymer strands of length $N = 18$ are placed on the edges of a cubic lattice and connected to each other at the vertices (see snapshot in Fig. 109). Initially, the distance between each pair of bonded monomers is $r = 1$. The network is then allowed to relax at constant volume. In order to grant additional flexibility to the chains, we set the k parameter in the FENE potential, Eq. (106), to $k = 20$. By construction, the mesh size of this system is $\xi \simeq N$, and therefore the "ideal" PSD should have a strong signal at $r \simeq N/2 = 9$. More precisely, taking into account the tri-dimensionality of the system and the finite diameter of the monomers, $2r_m = 1$, we expect a strong signal between $(N-1)/2 = 8.5$ (edge of the cubic cell) and $(\sqrt{2}N - 1)/2 \simeq 12.2$ (face diagonal of the cubic cell).

In Fig. 109, we show $P_T(r)$ and $P_G(r)$ for this model gel. We observe that, while $P_T(r)$ displays a broad profile which peaks at $r \simeq 4$, $P_G(r)$ has a negligible value over the whole r range, except for a very sharp peak at $r \simeq 11 \simeq (\sqrt{2}N - 1)/2$. The information about the mesh size is not, however, completely absent from $P_T(r)$, but it is "hidden" in the value of $r_{\max}$ at which $P_T(r_{\max}) = 0$ (the largest pore size), as it becomes clear when plotting $P_T(r)$ in

semi-logarithmic scale (inset of Fig. 109). From this semi-logarithmic plot, one can also see that $P_G(r)$ has a secondary peak (much smaller than the main one) at $r \simeq 8 \simeq (N-1)/2$, which originates from the portion of pore space in the vicinity of the surface of the lattice cells. Furthermore, we note that also for this idealized system the ratio $\langle r \rangle_G / \langle r \rangle_T$ is close to 2 ($\langle r \rangle_G / \langle r \rangle_T \simeq 2.6$), and this remains true also when other densities are considered (not shown). This is a consequence of the fact that for all the systems studied $P_T(r)$ is fairly symmetrical, and $P_G(r)$ peaks close to $r_{\max}$ (the maximum of $P_T(r)$). The precise value of $\langle r \rangle_G / \langle r \rangle_T$ will however depend on the relative forms of P_T and P_G.

From these two examples, we conclude that $P_G(r)$ is the quantity that gives a more immediate and easy to interpret information on the pores in the system. This does not mean that $P_T(r)$ should not be used, but only that care should be taken in its interpretation.

8.4.4 *$P_T(r)$: Comparison with analytical models*

In the previous section we have shown how the PSD can be connected to the geometrical mesh size and have compared the PSD of Torquato, $P_T(r)$, to that of Gubbins, $P_G(r)$. In this section, we will discuss some analytical results which can be used to gain insight into $P_T(r)$. We focus on this distribution because quasi-exact results are available for it[203,332–334], whereas this is not the case for $P_G(r)$.

Torquato and coworkers have studied extensively the properties of porous media, and in particular the PSD of systems of identical particles interacting via an arbitrary potential. For a system of hard spheres (HS) of radius R at density ρ, they demonstrated that[203,332–334]

$$P_T^{\text{HS}}(x) = \frac{3\eta}{R} F_T^{\text{HS}}(x)(a_0 x^2 + 2a_1 x + 4a_2), \tag{232}$$

with

$$F_T^{\text{HS}}(x) = \exp[-\eta(a_0 x^3 + 3a_1 x^2 + 12a_2 x + a_3)]. \tag{233}$$

Here $x \equiv (r+R)/R$, $\eta \equiv 4\pi R^3 \rho/3$ is a dimensionless density which for hard spheres is equivalent to the solid volume fraction ϕ_s, and a_i, $i = 0, 1, 2, 3$ are functions of η only, whose explicit expressions are[203,334d]:

$$a_0 = \frac{1 + \eta + \eta^2 - \eta^3}{(1-\eta)^3} \tag{234a}$$

$$a_1 = \frac{\eta(3\eta^2 - 4\eta - 3)}{2(1-\eta)^3} \tag{234b}$$

$$a_2 = \frac{\eta^2(2-\eta)}{2(1-\eta)^3} \tag{234c}$$

$$a_3 = -(a_0 + 3a_1 + 12a_2) \tag{234d}$$

[d] We note that all the a_i diverge at $\eta = 1$. This divergence is unphysical for hard spheres, since the close-packing value is $\eta = \pi/(3\sqrt{2}) \simeq 0.740$[245]. This unphysical divergence is due to the fact that the Carnahan-Starling approximation is used to derive these coefficients[203,334].

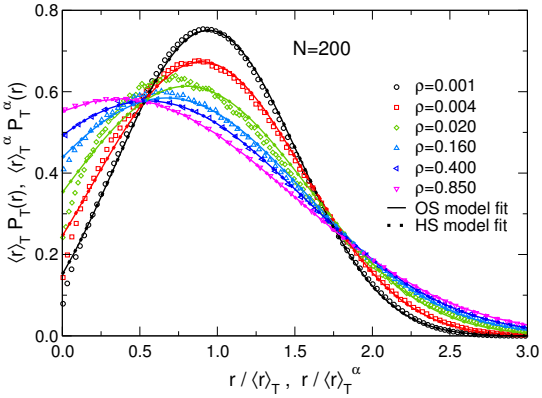

Figura 110 – Torquato's PDS, $P_T(r)$, for $N = 200$ and at different densities (open symbols), compared with the fit results $P_T^{\alpha}(r)$ (with $\alpha =$ OS or HS) employing the HS (Eq. (232), points) and OS (Eq. (235), lines) models. The HS and OS fits superimpose almost perfectly.

For overlapping spheres (OS), i.e., spheres which can overlap with no energy penalty, they found [203,333]

$$P_T^{\mathrm{OS}}(x) = \frac{3\eta}{R} x^2 \exp\left[-\eta(x^3-1)\right]. \tag{235}$$

Note that in this case, η is not equivalent to the particle volume fraction ϕ_s, and indeed it can be shown that $\phi_s = 1 - e^{-\eta}$ [203,333]. For small values of η, Eq. (232) reduces to Eq. (235), i.e., the HS model is equivalent to the OS model [203,333].

We make the assumption that the measured PSD $P_T(r)$ can be fitted by one of the two functional forms (232)-(235), with R and ρ as fit parameters. In other words, we assume that it is possible to map our system on a system of hard (resp. overlapping) spheres with radius $R_{\mathrm{HS}}(\rho, N)$ (resp. $R_{\mathrm{OS}}(\rho, N)$) and density $\rho_{\mathrm{HS}}(\rho, N)$ (resp. $\rho_{\mathrm{OS}}(\rho, N)$).

In Fig. 110 we compare for $N = 200$ and different monomer densities the calculated PSD, with the result of the fits using the HS model, $P_T^{\mathrm{HS}}(r; R_{\mathrm{HS}}, \rho_{\mathrm{HS}})$, and with the OS model $P_T^{\mathrm{OS}}(r; R_{\mathrm{OS}}, \rho_{\mathrm{OS}})$. It is virtually impossible to distinguish $P_T^{\mathrm{HS}}(r; R_{\mathrm{HS}}, \rho_{\mathrm{HS}})$ from $P_T^{\mathrm{OS}}(r; R_{\mathrm{OS}}, \rho_{\mathrm{OS}})$ via a simple visual inspection, since the two curves superimpose almost perfectly. An analysis of the squared difference between the calculated and the fitted function (not shown) reveals however that the HS model fits the data slightly better for all densities, except $\rho = 0.85, 1.00$.

In Figs. 111a and b we show, respectively, $R_{\mathrm{HS}}, R_{\mathrm{OS}}$ and $\rho_{\mathrm{HS}}/\rho, \rho_{\mathrm{OS}}/\rho$ as function of the monomer density. Through an extrapolation of the low density behavior, we deduce that in the limit $\rho \to 0$, $R_{\mathrm{HS}}, R_{\mathrm{OS}} \to R_{g0}(N)$, and $\rho_{\mathrm{HS}}, \rho_{\mathrm{OS}} \to \rho/N$ (dashed horizontal lines in Figs 111a and 111b). In other words, in the dilute regime $P_T(r)$ is well described by the PSD of a system of spheres with radius R_{g0}, and density equal to the chain density ρ/N. This is valid independently of the model used (OS or HS), since, as mentioned above, both models give the same result in the limit $\eta \to 0$, or equivalently $\rho \to 0, R = \text{const}$.

In the semidilute regime $\rho^*(N) < \rho < \rho^{**}$, both R_α and ρ_α ($\alpha =$ OS,HS) tend towards a power-law behavior with increasing N. Since in the semidilute regime the only relevant length scale is the mesh size ξ, we make the hypothesis that for large N these quantities will show the following scaling behavior:

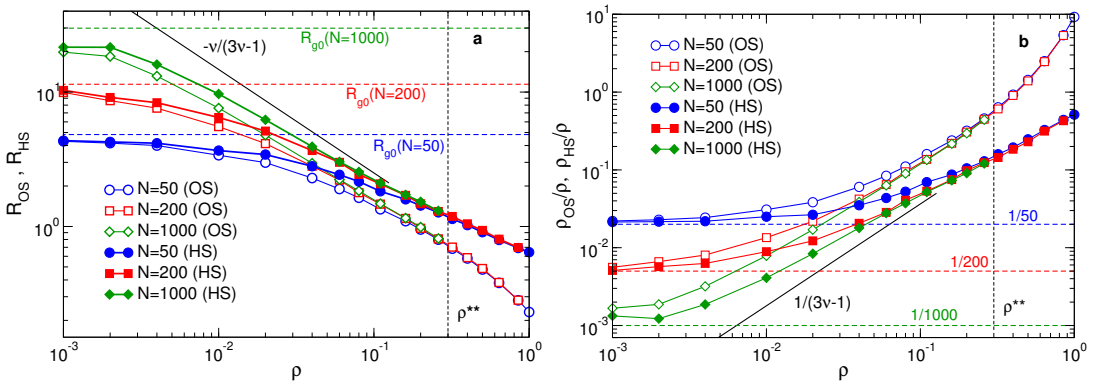

Figura 111 – Fit parameters as a function of monomer density ρ for the fit of the PSD $P_T(r)$ with the HS (Eq. (232), filled symbols) and OS (Eq. (235), open symbols) models. (a): Effective radius. (b): Effective density divided by ρ.

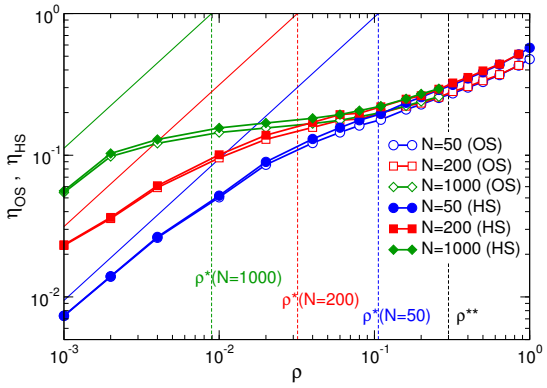

Figura 112 – Dimensionless densities η_{OS} (open symbols) and η_{HS} (filled symbols), Eq. (237), calculated using the fit parameters from the OS and HS model fits, as a function of monomer density. Continuous lines: $\eta_c(0,N) = 4\pi R_{g0}^3 \rho/3N$ (see Eq. (238)). The approximate values of the overlap densities $\rho^*(N)$ have been estimated using Eq. (18).

$$\begin{aligned} R_\alpha &\propto \xi \approx \rho^{-\nu/(3\nu-1)} \\ \rho_\alpha &\propto \xi^{-3} \approx \rho^{3\nu/(3\nu-1)}. \end{aligned} \qquad (\alpha = \text{OS,HS}) \tag{236}$$

This *ansatz* is motivated by the fact that the PSD is a purely geometrical object and hence has to scale with the intrinsic length scales of the system.

In Fig. 112 we show the dimensionless density

$$\eta_\alpha \equiv \frac{4}{3}\pi R_\alpha^3 \rho_\alpha \quad (\alpha = \text{OS,HS}) \tag{237}$$

as a function of ρ. We note that both η_{HS} and η_{OS} depend basically only on (ρ, N), with η_{OS} being slightly smaller than η_{HS}. At low ρ, both η_{OS} and η_{HS} approach the asymptotic expression $\eta_c(0,N) = 4\pi R_{g0}^3 \rho/3N$ (continuous lines), where η_c is in general defined as

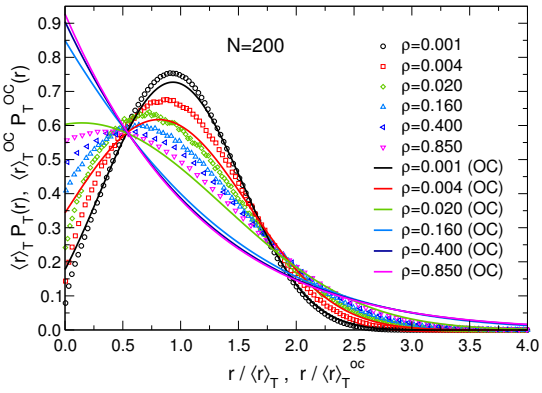

Figura 113 – Torquato's PSD for $N = 200$ and at different densities (open symbols), compared with the OC model prediction, Eqs. (235)-(239).

$$\eta_c(\rho, N) \equiv \frac{4\pi R_g^3}{3N}, \tag{238}$$

i.e., the dimensionless density the chains would have were they spheres of radius R_g. Importantly, we observe that when N increases, η_{OS} and η_{HS} develop a plateau in the semidilute regime: This corroborates the hypothesis that for large N Eq. (236) is valid, since this equation implies $\eta_\alpha \approx$ const.

We have seen in the preceding paragraph that at low ρ the polymer solution can be mapped on a system of overlapping spheres of radius R_g and density equal to the chain density, ρ/N. Inspired by this result, we introduce the *overlapping chains* (OC) model, by assuming that the PSD of the system is approximated *for all* ρ by Eq. (235), with

$$\begin{cases} R_{\text{OS}} = R_g(\rho, N) \\ \rho_{\text{OS}} = \rho/N \\ \eta_{\text{OS}} = \eta_c. \end{cases} \tag{239}$$

This approximation fails at intermediate and high ρ, as it is clear from Fig. 111a-b. This is also illustrated in Fig. 113, where the calculated PSD for $N = 200$ and different densities is compared with the one predicted by the OC model and one sees that already for ρ as low as 0.02 the two PSDs are qualitatively very different. However, given the simplicity of the OC model, we decide nevertheless to compare the computed average pore size, $\langle r \rangle_T$, with the one that the model predicts.

From the PSD (235) one can compute the average pore size with the result

$$\langle r \rangle_T^{\text{OS}} = \frac{R}{3} \exp(\eta) E_{2/3}(\eta), \tag{240}$$

where $E_n(\eta)$ is an exponential integral[251],

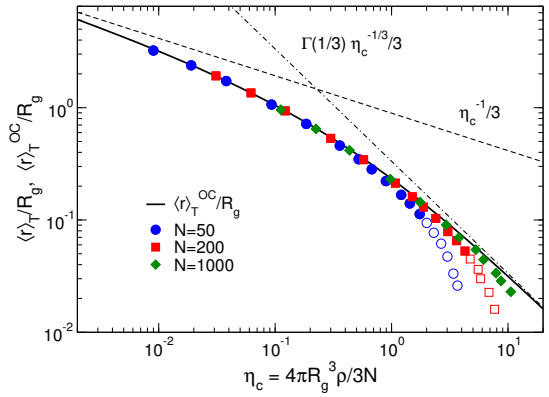

Figura 114 – Reduced average pore size $\langle r\rangle_T/R_g$ (symbols) compared with the OC model prediction $\langle r\rangle_T^{\rm OC}/R_g$ (thick line), Eq. (239), as a function of η_c. Open symbols correspond to densities $\rho > 0.3$ (concentrated regime). Dashed (dash-dotted) line: Low (high) density behavior predicted by the OC model, Eq. (245).

$$E_n(\eta) = \int_1^\infty \frac{e^{-\eta x}}{x^n} \mathrm{d}x. \tag{241}$$

The OC model result is obtained simply by applying Eqs. (239) to Eq. (240), i.e.,

$$\langle r\rangle_T^{\rm OC} = \frac{R_g(\rho, N)}{3} \exp(\eta_c) E_{2/3}(\eta_c). \tag{242}$$

In Fig. 114, we compare the measured average pore size $\langle r\rangle_T$ with the OC model result $\langle r\rangle_T^{\rm OC}$. One observes that, except for the points corresponding to the concentrated regime ($\rho > 0.3$), the prediction of the OC model is in surprisingly good agreement with the data, without using any fit parameter. This is a striking result, since we have seen that the calculated PSD starts to diverge from the theoretical prediction already at relatively low density (Fig. 113).

Another related surprising result is the following. The scaling behavior of R_g is[2,5,30]

$$R_g \approx \begin{cases} R_{g0} & \chi < \chi^* \\ R_{g0}\chi^{-\nu+1/2} & \chi^* < \chi < \chi^{**}. \end{cases} \tag{243}$$

This implies, given the definition of η_c, that

$$\eta_c \approx \begin{cases} \chi^{3\nu-1} & \chi < \chi^* \\ \chi^{1/2} & \chi^* < \chi < \chi^{**}. \end{cases} \tag{244}$$

The function appearing on the right hand side of Eq. (242) can be expanded for $\eta_c \to 0$ and $\eta_c \to \infty$ via a Puiseux series[352]; the leading terms are

$$\exp(\eta_c)E_{2/3}(\eta_c) = \begin{cases} \Gamma\left(\frac{1}{3}\right)\eta_c^{-1/3} + O(1) & \eta_c \to 0 \\ \eta_c^{-1} + O(\eta_c^{-2}) & \eta_c \to \infty, \end{cases} \tag{245}$$

where Γ is the Gamma function, and therefore

$$\frac{\langle r\rangle_T^{\text{OC}}}{R_g} \approx \begin{cases} \eta_c^{-1/3} & \eta_c \to 0 \\ \eta_c^{-1} & \eta_c \to \infty. \end{cases} \tag{246}$$

From Eqs (243), (244), (246), along with the fact that $\lim_{N\to\infty}\chi^{**}(N) = \infty$, we obtain for infinitely long chains

$$\frac{\langle r\rangle_T^{\text{OC}}}{R_{g0}} = \frac{\langle r\rangle_T^{\text{OC}}}{R_g}\frac{R_g}{R_{g0}} \approx \begin{cases} \chi^{-\nu+1/3} & \chi < \chi^* \\ \chi^{-\nu} & \chi^* < \chi. \end{cases} \tag{247}$$

We thus find that for very long chains, $\langle r\rangle_T^{\text{OC}}/R_{g0}$ behaves exactly as ξ/R_{g0}, Eq. (31), for all values of χ. We stress, however, that while $\lim_{N\to\infty}\chi^{**}(N) = \infty$, ρ^{**} is independent of N: Therefore, when considering functions of density instead of functions of χ, we must be aware that the approximation $\langle r\rangle_T \simeq \langle r\rangle_T^{\text{OC}}$ will always break down for $\rho \geq \rho^{**} = 0.3$.

It is not evident whether there is a deep reason behind the fact that $\langle r\rangle_T$ and $\langle r\rangle_T^{\text{OC}}$ are so similar even if $P_T(r)$ and $P_T^{\text{OC}}(r)$ are qualitatively very different. Nonetheless, this remarkable fact allows to estimate $\langle r\rangle_T$ for $\rho < \rho^{**}$ with good accuracy by knowing only R_g and ρ. Since we have seen that $\langle r\rangle_G \simeq 2\langle r\rangle_T$ (Sec. 8.4.3), this means that we are also able to estimate with reasonable accuracy the average value of the PSD of Gubbins. This is a useful result for estimating ξ in real systems, since measuring the PSD experimentally is not an easy task[249].

9

SUMMARY AND CONCLUSIONS

In this thesis, I have shown how molecular dynamics simulations can be used to gain a deep understanding of polymer nanocomposites (PNC), systems of polymers containing nanoparticles (NP). In particular, we have focused on the case of spherical NP, embedded either in dense solutions (Ch. 5) or in crosslinked networks (Ch. 7). In addition, a significant portion of this work was dedicated to the characterization of the static and dynamic properties of these systems, particularly the geometrical mesh size of polymer solutions (Ch. 8) and the dynamic properties of networks (Ch. 6). We report here a brief summary of the thesis, highlighting the main results and discussing the questions which are still open and the possible future lines of research in the field of PNCs.

STRUCTURE AND DYNAMICS OF A PNC

In Chapter 5, we have studied the static and dynamic properties of a dense unentangled polymer solution containing NPs. Whereas most of the previous simulation studies focused on the regime of small NP volume fraction ϕ_N, we considered a very broad range of ϕ_N values, from $\phi_N \simeq 10^{-4}$ to $\phi_N \simeq 0.5$. We also considered a broad range of NP diameters σ_N, from $\sigma_N = \sigma$ (monomer size) to $\sigma_N \simeq R_g \simeq 6\sigma$ (polymer's radius of gyration). The size regime $\sigma_N \lesssim 2R_g$, called the "nanoparticle" or "protein" regime, is the most theoretically challenging, since the action of the polymers on the NPs cannot be easily described through an effective potential as in the "colloid" limit $\sigma_N \gg 2R_g$. In order to insure that the NPs were uniformly dispersed in the polymeric matrix and did not form aggregates, we introduced a weakly attractive interaction between the NPs and the monomers.

In agreement with previous experimental observations[140,159,161] and theoretical predictions[164], we found that uniformly dispersed NPs of size $\sigma_N > \sigma$ cause a swelling of the chains, acting like a good solvent. We also found, however, that NPs of the size of the monomers ($\sigma_N = \sigma$) cause a *contraction* of the chains. We interpreted this as resulting from a competition between excluded volume (entropic effect) and the attractive monomer-NP interaction (enthalpic effect). When a large NP enters in a chain's pervaded volume, it locally swells the chain by forcing it to take a less tortuous path. Small NPs, on the other hand, are easily accommodated in the chain's pervaded volume, where they distribute uniformly and cause chain contraction acting like an effective attractive potential between the monomers. There is therefore a (model-dependent) "critical NP diameter" σ_N^* such that chain expand for $\sigma_N > \sigma_N^*$, whereas they contract for $\sigma_N < \sigma_N^*$. To the best of our knowledge, it is the first time that this effect is observed. We note that the above described phenomenology is probably invalid for NPs larger than the polymers ($\sigma_N > 2R_g$): In this case, the chain could be partially

"flattened" on the NP surface and their R_g would decrease as a result (the size of a swollen real chain in 2D scales as $N^{3/4}$, whereas it scales as $N^{0.588}$ in 3D).

At low volume fraction, the diffusion coefficient D_N of NPs doesn't follow the Stokes-Einstein (SE) relation, i.e., $D_N \propto k_B T/\eta\sigma_N$, in qualitative agreement with CPR theory[184] (Sec. 4.2.2). Despite the fact that the SE relation is recovered for $\sigma_N > 2R_g$ (as revealed by simulating NPs of size $\sigma_N = 10, 12$ and 14), we do not find, for $\sigma_N < 2R_g$, the $D_N \propto \sigma_N^{-2}$ relation predicted by the CPR theory. There are many possible reasons for this discrepancy, from inertial effects in NP motion to the absence of hydrodynamic interactions in our simulations. We note, however, that the relation $D_N \propto \sigma_N^{-2}$ should actually work for the *hydrodynamic diameter* σ_h, which is however troublesome to define since the SE is violated. We tried different definitions, showing that the agreement between data and theory depends rather significantly on the definition used.

Regarding polymer dynamics, we found that the reduced diffusion coefficient of the polymers, D_p/D_{p0}, falls on a master curve when plotted as a function of $h/2R_g$ (*confinement parameter*), where h is the interparticle distance, i.e., the average distance between the surfaces of neighboring NPs. The same result had been previously observed in several experiments[137,141,157,205]. However, most of these works considered NPs of size larger or comparable to that of the polymers, which could be considered as basically immobile on the time scale of polymer diffusion: It is therefore surprising to find the same result in our system, in which the NPs are smaller and diffuse faster than the polymer.

We also found, however, that when temperature is lowered the data don't fall on the same master curve anymore. Since a decrease of temperature is basically equivalent to an increase of the polymer-NP interaction, this result is in contrast with a precedent experimental study[141], which found that attractive interactions didn't significantly affect polymer diffusion. We show that the data can still be made to collapse on a master curve if the $2R_g$ appearing in the confinement parameter is replaced with a fit parameter λ_d. This parameter increases with decreasing temperature, suggesting that it could be associated to some sort of cooperativity length scale similar to the one found in supercooled liquids[257]. However, at present we haven't been able to find a satisfactory interpretation of this length scale, nor to find a measurable quantity which could correspond to it.

The problem of nanoparticle diffusion in dense solutions is still far from being completely understood. In general, a deeper characterization of the structural and dynamic properties of PNCs at high NP loading is necessary. Moreover, most of the simulation studies up to now have only considered melt PNCs, and much less attention has been given to solutions. This is mainly because below a certain monomer density hydrodynamic interactions (HI) cannot be neglected, but simulating systems with HI is challenging. However, theoretical predictions exists for the solution regime[184], which should be tested in simulations.

In addition to these observations, we believe that the following questions are especially worth of attention: (1) What is the general mechanism controlling chain expansion/contraction in a PNC, and how does it depend on $\sigma_N/2R_g$ and on the strength of the polymer-NP interaction? (2) In which range of T, ρ, N and ϵ_{mN} (strength of the monomer-NP interaction) does the diffusion coefficient of the polymers collapse on a master curve when plotted as a function of h/λ_d, where λ_d is a conveniently chosen parameter? Can we formulate a microscopic model that explains this collapse? What is the interpretation of λ_d? (3) In which range of T, ρ, N and ϵ_{mN} does the diffusion coefficient of the NPs collapse on a master curve when plotted as a function of h/R_h? Can we formulate a microscopic model that explains this collapse?

(4) Why don't we observe, in the dilute NP regime, the $D_N \propto \sigma_N^{-2}$ scaling predicted by the CPR theory? Finally, even though it was not explored in this work: (5) What is the effect of a high NP loading on the entanglement mesh in entangled solutions and melts? How does it depend on $\sigma_N/2R_g$ and on the polymer-NP interaction? Previous simulation studies exist, but only a limited range of sizes and interactions has been explored at present[212,225].

STRUCTURE, DYNAMICS AND ELASTICITY OF POLYDISPERSE DISORDERED NETWORKS

In Chapter 6, we studied *via* molecular dynamics simulations the structural, dynamic and elastic properties of polydisperse, disordered, defect-free networks. The networks are assembled starting from a mixture of bifunctional and f-functional "patchy" particles (crosslinkers)[296,299]. Thanks to an efficient bond-swapping potential[304], an almost-fully bonded network is formed, with $> 99.8\%$ of satisfied bonds and $< 4\%$ of the particles belonging to dangling ends. In order to avoid the exponential relaxation times associated to the dangling ends, these are removed by hand. Since the assembly of the network reaches equilibrium, the structure of the network depends only on the crosslink valence f, on the crosslink fraction c and on the initial density. In particular, the distribution of strand lengths only depends on f and c: Therefore, networks with the same crosslink fraction and valence but assembled at different densities will have the same mean strand length N_s, but, in general, a different mean entanglement length N_e.

Once the network was assembled and the free ends removed, we ran NPT simulations at $T = 1$ and $P = 0$. We found that the dynamics of the network is qualitatively well described by the reptation model of Edwards and de Gennes[3]. In particular, the localization length $\lambda_{(n+1)/2}$ of the central monomers of the strands scales as $n^{1/4}$, where n is the strand length, in the limit of long strands, as predicted by the model. We also found that at high ρ the ratio between the MSD, $\langle r_f^2(t)\rangle$, and that of the bifunctional particles, $\langle r_2^2(t)\rangle$, satisfies to good approximation the relation $\langle r_f^2(t)\rangle / \langle r_2^2(t)\rangle \simeq 2/f$. This relation (which was verified with very good accuracy for $f = 3, 4$ and 5) can be understood by considering each monomer as an harmonic oscillator attached to $\mathcal{N}$ identical springs, with $\mathcal{N} = f$ for the crosslinks and $\mathcal{N} = 2$ for the strand monomers. Indeed, the equipartition of energy gives for this simple system $\langle r_{\mathcal{N}}^2\rangle \propto \mathcal{N}^{-1}$, from which the above mentioned relation follows immediately. At low density, $\langle r_f^2(t)\rangle / \langle r_2^2(t)\rangle$ approaches the phantom network model (PNM) result: However, it is not clear whether this is due to the fact that excluded volume interactions become less important or to other factors, since the relation $\langle r_f^2(t)\rangle / \langle r_2^2(t)\rangle \simeq 2/f$ was also found in simulation of "phantom" chains in which all the excluded volume interactions are turned off except those between bonded neighbors. Further investigations are therefore needed in order to clarify this point. Another interesting result from the simulations of these disordered phantom networks is that the data don't agree with the PNM prediction for the shear modulus G, whereas the agreement is almost perfect for monodisperse diamond-lattice phantom networks at high density. These observations suggest that the PNM doesn't give a good description of polydisperse, disordered networks, even when the excluded volume interactions are absent.

Regarding the systems with the excluded volume interactions, we also found that the localization length λ_f of the crosslinks scales as ρ^{-2}. Since λ_f scales as the tube diameter $d_e \propto N_e^{1/2}$, this observation suggests that in these networks the entanglement length scales as $N_e \propto \rho^{-2}$. This is also in agreement with the behavior of the shear modulus G as a function of density and with preliminary results from primitive path analysis.

In conclusion, we proposed a model of a polymer network which is polydisperse, disordered and without dangling ends, whose global structure is entirely determined by the crosslink valence f, the crosslink fraction c and the initial density. In particular, the average strand length is a function only of f and c. Moreover, we have shown that the entanglement length N_e depends on the system's density in a rather simple way, i.e., $N_e \propto \rho^{-2}$. These properties give access to disordered, polydisperse polymer networks where the entanglement length can be tuned by changing the initial density, whereas the mean strand length N_s remains fixed, since it only depends on f and c. These networks are therefore ideal to study how the properties of the network change from a crosslink-dominated state ($N_s < N_e$) to an entanglement-dominated one ($N_s > N_e$).

NANOPARTICLE DIFFUSION IN POLYMER NETWORKS

In Chapter 7 we used molecular dynamics simulations to study the diffusion of spherical NPs in the same networks which were the subject of Chapter 6. We considered trivalent networks containing a volume fraction $\phi_N < 2\%$ of NPs with diameters ranging from $\sigma_N = 2$ to $\sigma_N = 8$. We have found that the parameter controlling NP diffusion is the *confinement ratio* $C_r = \sigma_N / \lambda_f$, where λ_f is the localization length of the crosslinks, which is of the order of the effective tube diameter ($\lambda_f \approx d$). Whereas small particles ($C_r < 1$) can freely diffuse through the network, larger particles ($C_r > 1$) are trapped by the entanglement mesh. This results in a subdiffusive regime in their mean-squared displacement, $\langle r_N^2(t) \rangle \propto t^{\beta(t)}$ ($\beta < 1$), which for strong confinement (C_r significantly larger than 1) leads to the formation of a plateau. The height of this plateau, i.e., the localization length of the NPs, is of order λ_f, suggesting that NP localization is mainly controlled by the crosslinks. This is also confirmed by the fact that the NP diffusion coefficient D_N is well described by the expression $D_N = A \exp(-C_r^2)/C_r$, with $A > 0$, which was proposed in Ref. 185 to describe the diffusion coefficient of a NP in a network with high crosslink density (compared to the density of entanglements).

In addition to these observations, an analysis of the squared displacement of single NP trajectories and of the van Hove function $G(r, t)$ reveals that the dynamics of the NPs is strongly heterogeneous and non-Gaussian, with the degree of heterogeneity increasing strongly upon increase of C_r. While some NPs are trapped in the entanglement mesh and vibrate around their equilibrium with mean amplitude $\simeq \lambda_f$, other particles diffuse through a sequence of jumps from one local entanglement cage to another (hopping motion). It was also revealed by analysis of the distinct part of the van Hove function, $G_d(r, t)$, that, even in the cases in which the MSD reaches a diffusive regime, the NPs don't explore the entirety of the available space, but only a subset of it. Also the self intermediate scattering function $F_s(q, t)$ shows an interesting behavior when C_r is increased, going from a quasi-exponential single-step relaxation to a double-step relaxation reminiscent of the β and α relaxations is supercooled liquids. Overall, these results highlight the extremely rich behavior of network nanocomposites, and pave the way to further investigations through simulation studies, in which the effects of polymer-NP interaction, polymer rigidity and different entanglements-to-crosslinks ratios could be explored.

CHARACTERIZING THE MESH SIZE IN A POLYMER SOLUTION

In Chapter 8 we dealt with the problem of how to precisely evaluate the geometrical mesh size ξ in polymer solutions. What may seem like a technicality has actually deep consequences, since a precise knowledge of ξ is fundamental to predict the diffusivity of nanoparticles or proteins in polymeric materials. Usually, ξ is estimated either from scaling calculations or from the monomer-monomer structure factor $S(q)$ or radial distribution function $g(r)$, usually under the assumption that the small-q (for $S(q)$) and large-r (for $g(r)$) region can be described by the Ornstein-Zernike expression. However, scaling estimates only give ξ up to an unknown multiplicative factor, and the above mentioned correlation function gives the typical length scale ξ_c of the monomer density correlations (density fluctuation correlation length), which doesn't necessarily coincide with the intuitive concept of mesh size as the size of the "holes" in the system.

We proposed therefore a new method to measure ξ, which is based on the concept of pore size distribution (PSD). Loosely speaking, the PSD gives the distribution of the sizes of the holes in the system, an information which is precluded to the above mentioned methods. The geometrical mesh size is identified with the mean value $\langle r \rangle$ of the PSD. We considered solutions of monodisperse chains with lengths $N = 50, 200$ and 1000 in a wide range of monomer densities ρ, from the dilute to the concentrated regime. We tested two different definitions of the PSD, one due to Gubbins[335] and one due to Torquato[203], calculating the respective mean values $\langle r \rangle_G$ and $\langle r \rangle_T$. We observed that in the semidilute regime $\langle r \rangle_T$ coincides approximately with the correlation length ξ_c. Moreover, the ratio $\langle r \rangle_G / \langle r \rangle_T$ is approximately equal to 2, and depends very weakly on ρ. For both definitions of the PSD, we obtained the expected density scalings $\langle r \rangle \propto \rho^{-\nu/(3\nu-1)}$ in the semidilute regime and $\langle r \rangle \propto \rho^{-1/3}$ in the dilute regime, showing that it is sensible to identify $\langle r \rangle$ with the geometrical mesh size. We argued, however, that Gubbins's PSD gives a more immediate and easy to interpret information on the actual size of the pores, and therefore we suggest to use Gubbins's definition (although slightly more cumbersome to calculate) for most applications.

We then compared our results for Torquato's PSD with analytical predictions for systems of spheres, finding that it is possible to map a polymer solution on a system of hard or overlapping spheres with effective radius R_{eff} and effective density ρ_{eff}. Based on an extrapolation of the available data, we made the prediction that in the semidilute regime, for very large N we would obtain $R_{\text{eff}} \propto \xi \propto \rho^{-\nu/(3\nu-1)}$ and $\rho_{\text{eff}} \propto \xi^{-3} \propto \rho^{3\nu/(3\nu-1)}$. This *ansatz* is motivated by the fact that in the semidilute regime the only relevant length scale in the system is ξ, and since the PSD is a purely geometrical quantity it must scale as ξ. Finally, we have calculated $\langle r \rangle_T$ in the limit $\rho_{\text{eff}} R_{\text{eff}}^3 \to 0$, where the hard spheres and the overlapping spheres models give the same result, and showed that if one assumes that $R_{\text{eff}} = R_g$ (radius of gyration) and $\rho_{\text{eff}} = \rho / N$ a very good agreement with the measured $\langle r \rangle_T$ is obtained up to densities much higher than the overlap density. This result allows to estimate $\langle r \rangle_T$ with very good accuracy by only knowing R_g, ρ and N. Moreover, since $\langle r \rangle_G / \langle r \rangle_T \simeq 2$ as discussed above, this result can also be used to estimate $\langle r \rangle_G$.

The method we proposed allows to estimate the geometrical mesh size with great accuracy if the positions of the monomers are known. Moreover, it gives access to the distribution of mesh sizes (the PSD), whereas scaling estimates and measurements of the correlation length only give a single length scale. The range of applicability of the PSD method to evaluate the mesh size is very broad, and by no means limited to polymer solutions. Moreover, it can also

be extended to polymer networks and gels. We point out, however, that in gels there exist another relevant "mesh size", which is related to the average distance between neighboring crosslinks and is in general quite different from ξ[353]. If, for example, a polymer melt is crosslinked, one expects the structural properties, and therefore ξ, to remain basically unchanged with respect to the un-crosslinked system[76]. However, the diffusivity of a spherical probe particle will change significantly if the particle diameter is comparable to the average distance between the crosslinks. The same is of course true for entangled polymer melts, where $\xi \simeq 0$ and the relevant parameter controlling the diffusion of particles and the mechanical properties is nothing else than the diameter of the reptation tube[3], since on timescales shorter than the entanglement relaxation time the entanglements effectively act as crosslinks[185,191]. Another factor which should be taken into account is that the PSD does not depend on the flexibility of the polymers, although in reality this can have a very strong influence on the diffusion of nanoparticles in polymeric systems. For example, it has recently been shown in simulations that increasing the chain rigidity will decrease the diffusivity of nanoparticles in polymer solutions[236]. This, however, is also not accounted for in estimates based on scaling predictions and on measurements of the correlation length, which in addition only give access to an average mesh size, and not to the whole distribution. To summarize, the method which we have proposed to measure the mesh size should represent a substantial improvement over conventional methods such as scaling estimates and methods which identify the mesh size with the correlation length. It will be interesting, in further studies, to address the problem of characterizing the relevant mesh size in networks and gels and understanding the role played by polymer flexibility.

RÉSUMÉ ET CONCLUSIONS

Dans cette thèse, j'ai montré comment les simulations de dynamique moléculaire peuvent être utilisées pour acquérir une compréhension approfondie des nanocomposites à base de polymères (NCP), qui sont des systèmes à base de polymères contenant des nanoparticules (NP). En particulier, nous nous sommes concentrés sur le cas des NP sphériques, dispersées soit dans des solutions denses (Ch. 5) soit dans des réseaux réticulés (Ch. 7). En outre, une partie importante de ce travail a été consacrée à la caractérisation des propriétés statiques et dynamiques de ces systèmes, en particulier la taille de maille des solutions de polymères (Ch. 8) et les propriétés dynamiques des réseaux (Ch. 6). Nous présentons ici un bref résumé de la thèse, en soulignant les principaux résultats et en discutant des questions encore en suspens et des axes de recherche futurs possibles dans le domaine des NCP.

STRUCTURE ET DYNAMIQUE D'UN NCP

Dans le chapitre 5, nous avons étudié les propriétés statiques et dynamiques d'une solution de polymères dense non enchevêtrée contenant des NP. Alors que la plupart des études par simulation précédentes portaient sur le régime des faibles fractions volumiques de NP ϕ_N, nous avons considéré une très large gamme de valeurs ϕ_N, allant de $\phi_N \simeq 10^{-4}$ à $\phi_N \simeq 0,5$. Nous avons également considéré une large gamme de diamètres de NP σ_N, de $\sigma_N = \sigma$ (taille du monomère) à $\sigma_N \simeq R_g \simeq 6\sigma$ (rayon de giration du polymère). Le régime de taille $\sigma_N \lesssim 2R_g$, appelé régime "nanoparticule" ou "protéine", est le plus difficile à aborder sur le plan théorique, car l'action des polymères sur les NP ne peut être facilement décrite par un potentiel effectif comme dans la limite "colloïde" $\sigma_N \gg 2R_g$. Afin de nous assurer que les NP sont uniformément dispersées dans la matrice polymère et ne forment pas d'agrégats, nous avons introduit une interaction faiblement attractive entre les NP et les monomères.

En accord avec les observations expérimentales précédentes[140,159,161] et les prédictions théoriques[164], nous avons constaté que des NP uniformément dispersées de taille $\sigma_N > \sigma$ causent un gonflement des chaînes, agissant donc comme un bon solvant. Nous avons aussi constaté, cependant, que les NP de la taille des monomères ($\sigma_N = \sigma$) causent une *contraction* des chaînes. Nous avons interprété ces comportements comme résultant d'une concurrence entre le volume exclu (effet entropique) et l'interaction monomère-NP attractive (effet enthalpique). Lorsqu'une grosse NP entre dans le volume occupé par une chaîne, la NP induit un gonflement local de la chaîne en l'obligeant à prendre un chemin moins tortueux. Les petites NP, par contre, s'intègrent facilement dans le volume occupé par la chaîne, où elles se répartissent uniformément et provoquent une contraction de la chaîne, agissant comme un potentiel d'attraction effectif entre les monomères.. Il y a donc un "diamètre critique des NP" (dépendant du modèle) σ_N^* tel que la chaîne se dilate pour $\sigma_N > \sigma_N^*$, alors qu'elle se contracte pour $\sigma_N < \sigma_N^*$. A notre connaissance, c'est la première fois que cet effet est observé. Nous notons que la phénoménologie décrite ci-dessus est probablement fausse pour les NP plus grandes que les polymères ($\sigma_N > 2R_g$) : Dans ce cas, la chaîne pourrait être partiellement "aplatie" à la surface des NP et son R_g diminuerait en conséquence, puisque la taille d'une

chaîne réelle gonflée en deux dimensions serait de $N^{3/4}$.

À faible fraction volumique, le coefficient de diffusion D_N des NP ne suit pas la relation de Stokes-Einstein (SE), c.-à-d. $D_N \propto k_B T/\eta\sigma_N$, en accord qualitatif avec la théorie CPR[184]. (Sec. 4.2.2). Même si la relation de SE est valide pour $\sigma_N > 2R_g$ (comme le révèlent les simulations pour des NP de taille $\sigma_N = 10, 12$ et 14), on ne trouve pas, pour $\sigma_N < 2R_g$, la relation $D_N \propto \sigma_N^{-2}$ prédite par la théorie CPR. Il y a plusieurs raisons possibles à cet écart, comme les effets inertiels du mouvement des NP ou l'absence d'interactions hydrodynamiques dans nos simulations. Nous notons, cependant, que la relation $D_N \propto \sigma_N^{-2}$ devrait fonctionner en utilisant le *diamètre hydrodynamique* σ_h, qui est cependant difficile à définir puisque la relation de SE n'est pas valide. Nous avons testé différentes définitions de σ_h, ce qui a permis de montrer que l'accord entre les données et la théorie dépend assez significativement de la définition utilisée.

En ce qui concerne la dynamique des polymères, nous avons constaté que le coefficient de diffusion réduit des polymères, D_p/D_{p0}, suit une courbe maîtresse lorsqu'il est tracé en fonction de $h/2R_g$ (*paramètre de confinement*), où h est la distance entre les particules, c'est-à-dire, la distance moyenne entre les surfaces de NP voisines. Le même résultat avait déjà été observé dans plusieurs expériences[137,141,157,205]. Cependant, la plupart de ces travaux considéraient des NP de taille supérieure ou comparable à celle des polymères, qui pouvaient donc être considérées comme essentiellement immobiles sur l'échelle de temps de diffusion des polymères : il est donc surprenant de trouver le même résultat dans notre système, dans lequel les NP sont plus petites et diffusent plus rapidement que le polymère.

Nous avons également constaté que lorsqu'on abaisse la température, les données ne suivent plus la même courbe maîtresse. Puisqu'une baisse de température équivaut fondamentalement à une augmentation de l'interaction polymère-NP, ce résultat contraste avec une étude expérimentale précédente[141], qui a montré que des interactions attractives n'affectaient pas significativement la diffusion des polymères. Nous montrons que les données aux différentes températures peuvent suivre une courbe maîtresse à condition de remplacer, dans le paramètre de confinement, $2R_g$ par λ_d où λ_d est un paramètre d'ajustement. Ce paramètre augmente quand la température diminue, ce qui suggère qu'il pourrait être associé à une échelle de longueur de coopérativité. Cependant, à l'heure actuelle, nous n'avons pas été en mesure de trouver une interprétation satisfaisante de cette échelle de longueur, ni de trouver une quantité mesurable qui pourrait lui correspondre.

Le problème de la diffusion des nanoparticules dans les solutions denses est encore loin d'être complètement compris. En général, une caractérisation plus approfondie des propriétés structurales et dynamiques des NCP à forte fraction volumique de NP est nécessaire. De plus, la plupart des études par simulation n'ont jusqu'à présent pris en compte que les NCP dans le cas de fondus de polymères, et beaucoup moins d'attention a été accordée aux solutions de polymères. La raison principale vient du fait qu'en dessous d'une certaine densité de monomères, les interactions hydrodynamiques (IH) ne peuvent pas être négligées, or la simulation de systèmes avec IH est difficile. Toutefois il existe des prédictions théoriques pour les solutions de polymères, qui devraient être testées par simulation.

En complément de ces observations, nous pensons que les questions suivantes méritent une attention particulière : (1) Quel est le mécanisme général de contrôle de l'expansion/contraction de la chaîne dans un NCP, et comment dépend-il de $\sigma_N/2R_g$ et de la force de l'interaction polymère-NP ? (2) Dans quelle plage de T, ρ, N et ϵ_{mN} (force de l'interaction monomère-NP) le coefficient de diffusion des polymères suit-il une courbe maîtresse

lorsqu'il est représenté en fonction de h/λ_d, où λ_d est un paramètre choisi de façon adéquate ? Peut-on formuler un modèle microscopique qui explique l'origine de cette courbe maîtresse ? Quelle est l'interprétation de λ_d ? (3) Dans quelle plage de T, ρ, N et ϵ_{mN} le coefficient de diffusion des NP suit-il une courbe maîtresse lorsqu'il est représenté en fonction de h/R_h ? Peut-on formuler un modèle microscopique qui explique cette courbe maîtresse ? (4) Pourquoi n'observe-t-on pas, dans le régime où les NP sont diluées, la loi d'échelle $D_N \propto \sigma_N^{-2}$ prévue par la théorie CPR ? Enfin, même si ces questions n'ont pas été explorée dans ce travail : (5) Quel est l'effet d'une fraction volumique élevée de NP sur les enchevêtrements dans les solutions de polymères enchevêtrées et les fondus ? Comment cela dépend-il de $\sigma_N/2R_g$ et de l'interaction polymère-NP ? Des études par simulation antérieures existent, mais seule une gamme limitée de tailles et d'interactions a été explorée à ce jour[212,225].

STRUCTURE, DYNAMIQUE ET ÉLASTICITÉ DES RÉSEAUX POLYDISPERSES ET DÉSORDONNÉS

Dans le chapitre 6, nous avons étudié, par simulation de dynamique moléculaire, les propriétés structurales, dynamiques et élastiques de réseaux polydisperses, désordonnés et sans défaut. Les réseaux sont assemblés à partir d'un mélange de particules bifonctionnelles et f-fonctionnelles "patchy" (crosslinkers)[296,299]. Grâce à un potentiel qui permet des échanges de liaisons efficaces[304], un réseau presque entièrement lié se forme, avec $> 99.8\%$ de liaisons formées et $< 4\%$ de particules appartenant à des extrémités libres. Afin d'éviter les temps de relaxation exponentiels associés aux extrémités libres, celles-ci sont supprimées. Comme le réseau ainsi assemblé est à l'équilibre, la structure du réseau dépend uniquement de la valence des crosslinkers f, de la fraction de crosslinkers c et de la densité initiale. En particulier, la distribution des longueurs de brins dépend uniquement de f et de c : par conséquent, les réseaux ayant la même fraction de particules f-fonctionnelles et la même valence moyenne, mais assemblés à des densités différentes, auront la même longueur moyenne de brin N_s, mais, en général, une longueur moyenne d'enchevêtrement différente N_e.

Une fois le réseau assemblé et les extrémités libres enlevées, nous avons exécuté des simulations NPT à $T = 1$ et $P = 0$. Nous avons constaté que la dynamique du réseau est qualitativement bien décrite par le modèle de reptation d'Edwards et de Gennes[3]. En particulier, la longueur de localisation $\lambda_{(n+1)/2}$ des monomères centraux des brins est de $n^{1/4}$, où n est la longueur du brin, dans la limite de brins longs, comme prévu par le modèle. Nous avons aussi trouvé qu'à haute densité ρ le rapport entre le MSD, $\langle r_f^2(t)\rangle$, et celui des particules bifonctionnelles, $\langle r_2^2(t)\rangle$, est bien approximée par la relation $\langle r_f^2(t)\rangle / \langle r_2^2(t)\rangle \simeq 2/f$. Cette relation (qui a été vérifiée avec une très bonne précision pour $f = 3, 4$ et 5) peut être comprise en considérant chaque monomère comme un oscillateur harmonique attaché à $\mathcal{N}$ ressorts identiques, avec $\mathcal{N} = f$ pour les crosslinks et $\mathcal{N} = 2$ pour les monomères bifonctionels. En effet, l'équipartition de l'énergie donne pour ce système simple $\langle r_{\mathcal{N}}^2\rangle \propto \mathcal{N}^{-1}$, dont la relation mentionnée ci-dessus découle immédiatement. À faible densité, $\langle r_f^2(t)\rangle / \langle r_2^2(t)\rangle$ donne un résultat proche de celui du modèle de réseau fantôme (MRF): Cependant, il n'est pas clair si cela est dû au fait que les interactions de volume exclu deviennent moins importantes ou à d'autres facteurs, puisque la relation $\langle r_f^2(t)\rangle / \langle r_2^2(t)\rangle \simeq 2/f$ a également été trouvée dans la simulation des chaînes "fantômes" où toutes les interactions de volume exclu sont éteintes sauf celles entre voisins liés. Des investigations complémentaires sont donc nécessaires pour clarifier ce point. Un autre résultat intéressant des simulations de ces réseaux fantô-

mes désordonnés est que les données ne concordent pas avec la prédiction du MRF pour le module de cisaillement G, alors que l'accord est presque parfait pour les réseaux fantômes monodisperses à réseau diamant à haute densité. Ces observations suggèrent que le MRF ne donne pas une bonne description des réseaux polydispersés et désordonnés, même lorsque les interactions de volume exclu sont absentes.

En ce qui concerne les systèmes avec interactions de volume exclu, nous avons également constaté que la longueur de localisation λ_f des crosslinks varie comme ρ^{-2}. Puisque λ_f est proportionnel au diamètre du tube $d_e \propto N_e^{1/2}$, cette observation suggère que dans ces réseaux la longueur d'enchevêtrement varie comme $N_e \propto \rho^{-2}$. Ceci est également en accord avec le comportement du module de cisaillement G en fonction de la densité et avec les résultats préliminaires de la *primitive path analysis* (analyse de la trajectoire primitive).

En conclusion, nous avons proposé un modèle de réseau de polymères polydispersé, désordonné et sans extrémités libres, dont la structure globale est entièrement déterminée par la valence des crosslinkers f, la fraction de crosslinkers c et la densité initiale. En particulier, la longueur moyenne des brins est une fonction uniquement de f et c. De plus, nous avons montré que la longueur d'enchevêtrement N_e est contrôlée par la densité du système de façon assez simple, c'est-à-dire $N_e \propto \rho^{-2}$. Ces propriétés donnent accès à des réseaux de polymères polydispersés désordonnés où la longueur d'enchevêtrement peut être réglée en modifiant la densité initiale, alors que la longueur moyenne des brins N_s reste fixe, puisqu'elle ne dépend que de f et c. Ces réseaux sont donc pertinents pour étudier comment les propriétés du réseau passent d'un état dominé par la réticulation ($N_s < N_e$) à un état dominé par les enchevêtrements ($N_s > N_e$).

DIFFUSION DE NANOPARTICULES DANS DES RÉSEAUX DE POLYMÈRES

Dans le chapitre 7 nous avons utilisé des simulations de dynamique moléculaire pour étudier la diffusion de NP sphériques dans les mêmes réseaux qui ceux du chapitre 6. Nous avons considéré des réseaux trivalents contenant une fraction volumique $\phi_N < 2\%$ de NPs avec des diamètres allant de $\sigma_N = 2$ à $\sigma_N = 8$. Nous avons constaté que le paramètre contrôlant la diffusion des NP est le *ratio de confinement* $C_r = \sigma_N / \lambda_f$, où λ_f est la longueur de localisation des particules f-fonctionnelles, qui est de l'ordre du diamètre effectif du tube ($\lambda_f \approx d$). Alors que les petites particules ($C_r < 1$) peuvent diffuser librement à travers le réseau, les particules plus grosses ($C_r > 1$) sont piégées par le maillage du réseau. Il en résulte un régime sous-diffusif dans leurs déplacements au carré moyen (mean-squared displacement, MSD), $\langle r_N^2(t) \rangle \propto t^{\beta(t)}$ ($\beta < 1$), ces derniers présentant un plateau pour un confinement fort (C_r nettement supérieur à 1). La hauteur de ce plateau, c'est-à-dire la longueur de localisation des NP, est de l'ordre de λ_f, ce qui suggère que la localisation des NP est principalement contrôlée par les crosslinks. Ceci est également confirmé par le fait que le coefficient de diffusion des NP D_N est bien décrit par l'expression $D_N = A \exp(-C_r^2)/C_r$, avec $A > 0$, qui a été proposée dans Ref. 185 pour décrire le coefficient de diffusion des NP dans un réseau à forte densité de réticulation (comparée à la densité des enchevêtrements).

En complément de ces observations, une analyse des MSD des NP prises individuellement et de la fonction de van Hove $G(r,t)$ révèle que la dynamique des NP est fortement hétérogène et non Gaussienne, le degré d'hétérogénéité augmentant fortement avec l'augmentation de C_r. Alors que certaines NP sont piégées dans le maillage et vibrent autour de leur position d'équilibre avec une amplitude moyenne $\simeq \lambda_f$, d'autres particules diffusent via une séquence

de sauts d'une cage locale à une autre (mouvement par sauts). L'analyse de la partie distincte de la fonction de van Hove, $G_d(r,t)$ a également révélé que, même dans les cas où les MSD atteignent un régime diffusif, les NP n'explorent pas la totalité de l'espace disponible, mais seulement une partie de celui-ci. De plus, la fonction de diffusion intermédiaire "self" $F_s(q,t)$ montre un comportement intéressant lorsque C_r est augmenté, passant d'une relaxation quasi exponentielle en une seule étape à une relaxation en deux étapes rappelant les relaxations β et α des liquides surfondus. Dans l'ensemble, ces résultats mettent en évidence le comportement extrêmement riche des nanocomposites constitués d'un réseau de polymères et ouvrent la voie à d'autres études par simulation, dans lesquelles les effets de l'interaction polymère-NP, de la rigidité des polymères et des différents ratios entre crosslinks et enchevêtrements pourraient être étudiés.

CARACTÉRISATION DU MAILLAGE DANS UNE SOLUTION DE POLYMÈRES

Dans le chapitre 8 nous avons abordé le problème de l'évaluation précise de la taille caractéristique du maillage géométrique ξ dans les solutions de polymères. Ce qui peut paraître comme un point technique a en fait des conséquences profondes, puisqu'une connaissance précise de ξ est fondamentale pour prédire la diffusivité des nanoparticules ou protéines dans les matériaux polymères. Habituellement, ξ est estimé soit à partir des calculs de lois d'échelle, soit à partir du facteur de structure des monomères $S(q)$ ou de la fonction de distribution radiale $g(r)$, en supposant généralement que la région des faibles valeurs de q (pour $S(q)$) et des grandes valeurs de r (pour $g(r)$) peut être décrite par l'expression de Ornstein-Zernike. Cependant, les estimations à l'aide des lois d'échelle donnent des valeurs de ξ à un facteur multiplicatif près, et la fonction de corrélation mentionnée ci-dessus donne l'échelle de longueur typique ξ_c des corrélations de densité des monomères (longueur de corrélation des fluctuations de densité), qui ne correspond pas nécessairement à la notion intuitive de taille de maille comme taille des " trous " dans le système.

Nous avons donc proposé une nouvelle méthode pour mesurer ξ, qui est basée sur le concept de distribution de tailles de pores (pore-size distribution, PSD). En substance, la PSD donne accès à la distribution des tailles des trous dans le système, une information qui n'est pas accessible par les méthodes mentionnées ci-dessus. La taille caractéristique du maillage géométrique est identifié à la valeur moyenne $\langle r \rangle$ de la PSD. Nous avons considéré des solutions de chaînes monodisperses de longueurs $N = 50, 200$ et 1000 dans une large gamme de densités de monomères ρ, du régime dilué au régime concentré. Nous avons testé deux définitions différentes de la PSD, l'une due à Gubbins[335] et l'autre à Torquato[203], qui donnent accès aux valeurs moyennes respectives $\langle r \rangle_G$ et $\langle r \rangle_T$. Nous avons observé que dans le régime semi-dilué $\langle r \rangle_T$ coïncide approximativement avec la longueur de corrélation ξ_c. De plus, le ratio $\langle r \rangle_G / \langle r \rangle_T$ est approximativement égal à 2, et dépend très faiblement de ρ. Pour les deux définitions de la PSD, nous avons obtenu les lois d'échelle attendues en fonction de la densité, $\langle r \rangle \propto \rho^{-\nu/(3\nu-1)}$ dans le régime semi-dilué et $\langle r \rangle \propto \rho^{-1/3}$ dans le régime dilué, ce qui montre qu'il est raisonnable d'identifier $\langle r \rangle$ avec la taille géométrique caractéristique du maillage. Nous faisons toutefois remarquer que la PSD de Gubbins fournit une information plus immédiate et plus facile à interpréter sur la taille réelle des pores, et nous suggérons donc d'utiliser la définition de Gubbins (bien que légèrement plus lourde à calculer) pour la plupart des applications.

Nous avons ensuite comparé nos résultats obtenus avec la PSD de Torquato avec les pré-

dictions analytiques pour des systèmes constitués de sphères. Nous avons montré qu'il est possible de représenter une solution de polymères par un système de sphères dures ou de sphères qui se chevauchent avec un rayon effectif R_{eff} et une densité effective ρ_{eff}. En extrapolant les données disponibles, nous avons prédit que dans le régime semi-dilué, pour les valeurs de N élevées, nous obtiendrions $R_{\text{eff}} \propto \xi \propto \rho^{-\nu/(3\nu-1)}$ et $\rho_{\text{eff}} \propto \xi^{-3} \propto \rho^{3\nu/(3\nu-1)}$. Ceci est motivé par le fait que dans le régime semi-dilué, la seule échelle de longueur pertinente dans le système est ξ, et puisque la PSD est une grandeur purement géométrique, elle doit avoir le même comportement que ξ. Enfin, nous avons calculé $\langle r \rangle_T$ dans la limite $\rho_{\text{eff}} R_{\text{eff}}^3 \to 0$, où les sphères dures et les modèles de sphères chevauchantes donnent le même résultat. Cela nous a permis de montrer que si on suppose que $R_{\text{eff}} = R_g$ (rayon de giration) et $\rho_{\text{eff}} = \rho/N$, on obtient, pour les densités nettement supérieures à la densité de recouvrement, un très bon accord avec la valeur mesurée de $\langle r \rangle_T$. Ce résultat permet d'estimer $\langle r \rangle_T$ avec une très bonne précision en ne connaissant que R_g, ρ et N. De plus, puisque $\langle r \rangle_G / \langle r \rangle_T \simeq 2$ comme discuté ci-dessus, ce résultat peut aussi être utilisé pour estimer $\langle r \rangle_G$.

La méthode que nous avons proposée permet d'estimer la taille caractéristique du maillage géométrique dû aux polymères avec une grande précision si la position des monomères est connue. De plus, il donne accès à la distribution des tailles de mailles (PSD), alors que les valeurs déduites des lois d'échelle et les mesures de la longueur de corrélation ne donnent qu'une seule échelle de longueur. Le champ d'application de la méthode PSD pour évaluer le maillage est très large et ne se limite en aucun cas aux solutions de polymères. En effet, cette méthode peut également être étendue aux réseaux de polymères et aux gels. Nous soulignons, cependant, que dans les gels, il existe une autre "taille de maille" pertinente, qui est liée à la distance moyenne entre les points de réticulation voisins et qui est en général très différente de ξ[353]. Si, par exemple, un polymère fondu est réticulé, on s'attend à ce que les propriétés structurales, et donc ξ, restent pratiquement inchangées par rapport au système non réticulé[76]. Cependant, la diffusivité d'une particule sphérique changera de façon significative si le diamètre des particules est comparable à la distance moyenne entre les points de réticulation. Il en va de même pour les polymères fondus enchevêtrés, où $\xi \simeq 0$ et le paramètre pertinent contrôlant la diffusion des particules et les propriétés mécaniques n'est autre que le diamètre du tube de reptation[3], puisque sur des échelles de temps plus courtes que le temps de relaxation des enchevêtrements, ces derniers agissent effectivement comme des points de réticulation[185,191]. Un autre facteur à prendre en compte est le fait que la PSD ne dépend pas de la flexibilité des polymères, bien qu'en réalité cela puisse avoir une très forte influence sur la diffusion des nanoparticules dans les systèmes de polymères. Par exemple, il a récemment été démontré par des simulations que l'augmentation de la rigidité de la chaîne diminue la diffusivité des nanoparticules dans les solutions de polymères[236]. Cette rigidité n'est toutefois pas non plus prise en compte dans les estimations basées sur les lois d'échelle et dans les mesures de la longueur de corrélation, qui ne donnent en outre accès qu'à une valeur moyenne des tailles des mailles, et non à la distribution de ces tailles. En résumé, la méthode que nous avons proposée pour caractériser la géométrie du maillage devrait représenter une amélioration substantielle par rapport aux méthodes conventionnelles telles que les estimations basées sur les lois d'échelle et les méthodes qui identifient la taille caractéristique des mailles avec la longueur de corrélation. Il sera intéressant, dans des études futures, de trouver une façon pertinente de caractériser le maillage dans le cas de réseaux et de gels et de comprendre le rôle joué par la flexibilité des polymères.

A

THE ORNSTEIN-ZERNIKE CORRELATION FUNCTION

In this section, we will show how to derive the Ornstein-Zernike expression for the structure factor (Eq. (46)) and for the radial distribution function (Eq. (47)). Our presentation is based on the one of Ref. 40.

For a generic system of M particles with position vectors $\mathbf{r}_1, \ldots, \mathbf{r}_M$ and number density ρ, we can define the structure factor $S(\mathbf{q})$, Eq. (32), and the *pair correlation function*[1],

$$g(\mathbf{r}) \equiv \frac{1}{\rho M} \sum_{\substack{k=1 \\ j \neq k}}^{M} \langle \delta(\mathbf{r} + \mathbf{r}_k - \mathbf{r}_j) \rangle, \tag{A.1}$$

where δ is Dirac's delta distribution We note that the radial distribution function $g(r)$, Eq. (34), is nothing else than the spherical average of the pair correlation function.
It can be shown that $S(\mathbf{q})$ and $g(\mathbf{r})$ are connected by the following relation[1] (see also Eq. (35)):

$$S(\mathbf{q}) = 1 + \rho \tilde{h}(\mathbf{q}) + (2\pi)^3 \delta(\mathbf{q}), \tag{A.2}$$

where $\tilde{h}(\mathbf{q})$ is the Fourier transform of the function $h(\mathbf{r}) \equiv g(\mathbf{r}) - 1$ (*net correlation function*). The term containing the δ function only gives a contribution at $\mathbf{q} = 0$ (infinite wavelength), and we will therefore ignore it in the following. We have therefore

$$S(\mathbf{q}) = 1 + \rho \int h(\mathbf{r}) e^{-i\mathbf{q}\cdot\mathbf{r}} \mathrm{d}\mathbf{r}, \tag{A.3}$$

and the inverse relation

$$h(\mathbf{r}) = \frac{1}{(2\pi)^3 \rho} \int [S(\mathbf{q}) - 1] e^{i\mathbf{q}\cdot\mathbf{r}} \mathrm{d}\mathbf{q}. \tag{A.4}$$

The function $h(\mathbf{r})$ also satisfies the Ornstein-Zernike integral equation[1],

$$h(\mathbf{r}_1 - \mathbf{r}_2) = c(\mathbf{r}_1 - \mathbf{r}_2) + \rho \int c(\mathbf{r}_1 - \mathbf{r}_3) h(\mathbf{r}_3 - \mathbf{r}_2) \mathrm{d}\mathbf{r}_3, \tag{A.5}$$

where $c(\mathbf{r})$ is the so-called *direct correlation function*. Sometimes, Eq. (A.5) is taken as the very definition of c; however, other definitions of $c(\mathbf{r})$ are possible, which give to this function a direct physical meaning[1].

On taking the Fourier transform of both sides of Eq. (A.5), we get

$$1 + \rho\tilde{h}(\mathbf{q}) = \frac{1}{1 - \rho\tilde{c}(\mathbf{q})}. \tag{A.6}$$

From Eqs. (A.6) and (A.2) we get, neglecting the δ term,

$$S(\mathbf{q}) = \frac{1}{1 - \rho\tilde{c}(\mathbf{q})}. \tag{A.7}$$

Let us now assume that $\tilde{c}(\mathbf{q})$ has a Taylor expansion for $q \to 0$ (where $q = |\mathbf{q}|$). Since $c(\mathbf{r})$ is an even function, the expansion of $\tilde{c}(\mathbf{q})$ can only contain even powers of q:

$$\tilde{c}(\mathbf{q}) = \tilde{c}(0)[1 - aq^2 + \mathcal{O}(q^4)] \tag{A.8}$$

We thus readily obtain

$$S(q) \simeq \frac{S(0)}{1 + (q\xi)^2}, \tag{A.9}$$

where we have written $S(q)$ to highlight the fact that S only depends on the magnitude of $\mathbf{q}$. The parameters $S(0)$ and ξ are given by

$$S(0) = \frac{1}{1 - \rho\tilde{c}(0)}; \quad \xi^2 = \frac{\rho\tilde{c}(0)a}{1 - \rho\tilde{c}(0)}. \tag{A.10}$$

From Eq. (A.4), we readily obtain, using the fact that S is independent on the direction of $\mathbf{q}$,

$$\begin{aligned} h(\mathbf{r}) &\simeq \frac{4\pi}{(2\pi)^3\rho}\int_0^\infty \frac{\sin(qr)}{qr} S(q) q^2 \mathrm{d}q - \frac{\delta(\mathbf{r})}{\rho} \\ &= \frac{S(0)}{4\pi\xi^2\rho}\left(\frac{e^{-r/\xi}}{r}\right) - \frac{\delta(\mathbf{r})}{\rho}. \end{aligned} \tag{A.11}$$

The δ term appearing in Eq. (A.11) should be considered an artifact coming from the fact that we have performed a low-wavevector approximation of S, and should be disregarded. However, we note that it is necessary if one wants to use Eq. (A.3) to formally transform back the expression (A.11) and obtain (A.9). We thus finally obtain, for large r,

$$g(r) = 1 + h(r) \simeq 1 + \frac{S(0)}{4\pi\xi^2\rho}\left(\frac{e^{-r/\xi}}{r}\right). \tag{A.12}$$

B

CALCULATION OF THE MSD IN THE PHANTOM NETWORK MODEL

Assuming that the network has a Bethe lattice structure and that all the strands are ideal and have the same length n, the phantom network model (PNM) predicts that the MSD of the crosslinks is[74]

$$\langle r_f^2(t)\rangle = \langle R_e^2(n)\rangle_0 \frac{f-1}{f(f-2)}, \tag{B.13}$$

where $\langle R_e^2(n)\rangle_0$ is the mean-squared end-to-end distance of the strands in the unperturbed state, i.e., it is the value $\langle R_e^2(n)\rangle_0$ would have if the strand was not attached to the network. Since the strands are assumed to be ideal, $\langle R_e^2(n)\rangle_0 = C_n n\ell^2$, where ℓ is the bond length and $C_n > 0$.

To calculate the MSD of any given monomer in a strand, we enumerate the strand monomers from $i = 1$ to $i = n$, taking in addition $i = 0$ and $i = n+1$ to represent the crosslinks at the two extremities of the strand (i.e., $i \in [0, n+1]$). The MSD of the ith monomer in the strand is then given by the following expression[74]

$$\begin{aligned}\langle r_i^2(t)\rangle &= \langle R_e^2(n)\rangle_0 \left[\frac{f-1}{f(f-2)} + \frac{\zeta_i(1-\zeta_i)(f-2)}{f}\right] \\ &= \langle r_f^2(t)\rangle + \langle R_e^2(n)\rangle_0 \left[\frac{\zeta_i(1-\zeta_i)(f-2)}{f}\right],\end{aligned} \tag{B.14}$$

where ζ_i is defined as

$$\zeta_i \equiv \frac{i}{n+1} \quad (0 \le \zeta_i \le 1). \tag{B.15}$$

We note that for $i = 0, n+1$ we obtain $\langle r_i^2(t)\rangle = \langle r_f^2(t)\rangle$, as expected. To obtain the MSD of the bifunctional particles, we calculate the average of Eq. (B.14) over i, excluding the values $i = 0, n+1$, which correspond to the crosslinks. We have therefore to calculate

$$\sum_{i=0}^{n+1} p_i\, \zeta_i(1-\zeta_i), \tag{B.16}$$

where

$$p_i = \begin{cases} 0 & i = 0, n+1 \\ 1/n & \text{otherwise,} \end{cases} \tag{B.17}$$

since we are neglecting the crosslinks. We thus obtain

$$\begin{aligned} \sum_{i=0}^{n+1} p_i \, \zeta_i(1-\zeta_i) &= \frac{1}{n} \sum_{i=1}^{n} \zeta_i(1-\zeta_i) \\ &= \frac{1}{n} \sum_{i=1}^{n} \left(\frac{i}{n+1} \right) \left(1 - \frac{i}{n+1} \right) \\ &= \frac{1}{n(n+1)^2} \sum_{i=1}^{n} i(n+1-i) \\ &= \frac{n+2}{6(n+1)}, \end{aligned} \tag{B.18}$$

and therefore, from Eq. (B.14),

$$\langle r_2^2(t) \rangle = \langle r_f^2(t) \rangle + \langle R_e^2(n) \rangle_0 \left(\frac{f-2}{f} \right) \left(\frac{n+2}{6(n+1)} \right). \tag{B.19}$$

We note that since $\langle R_e^2(n) \rangle_0 \propto n$ for an ideal chain, the fluctuations are always larger for longer strands. We thus obtain

$$\frac{\langle r_f^2(t) \rangle}{\langle r_2^2(t) \rangle} = \left[1 + \frac{(f-2)^2}{f-1} \left(\frac{n+2}{6(n+1)} \right) \right]^{-1} \tag{B.20}$$

In the limit of large n, Eq. (B.20) becomes

$$\frac{\langle r_f^2(t) \rangle}{\langle r_2^2(t) \rangle} = \frac{6(f-1)}{f(f+2)-2} \quad (n \text{ large}). \tag{B.21}$$

From Eq. (B.21) we obtain $\frac{12}{13} \simeq 0.92$ for $f = 3$, $\frac{9}{11} \simeq 0.82$ for $f = 4$ and $\frac{8}{11} \simeq 0.73$ for $f = 5$. We also observe that for large f, one obtains

$$\frac{\langle r_f^2(t) \rangle}{\langle r_2^2(t) \rangle} \simeq \frac{6}{f} \quad (n, f \text{ large}). \tag{B.22}$$

C

MEASUREMENT OF THE SHEAR MODULUS

To measure the shear modulus G of the polymer networks, the method described in Ref. 300 is used. In this Section, we briefly describe this method, following the presentation of Ref. 300.

One starts by defining the deformation gradient tensor $\hat{F}$, which is defined with respect to a stress-free reference configuration. By taking as a reference configuration $L_\alpha = \langle L_\alpha \rangle$, where L_α ($\alpha = x, y, z$) are the box sides, one obtains

$$\hat{F} \equiv \begin{pmatrix} \frac{L_x}{\langle L_x \rangle} & 0 & 0 \\ 0 & \frac{L_y}{\langle L_y \rangle} & 0 \\ 0 & 0 & \frac{L_z}{\langle L_z \rangle} \end{pmatrix}. \tag{C.23}$$

The Green-Lagrange strain tensor $\hat{C} \equiv \hat{F}^T \hat{F}$ can then be calculated:

$$\hat{C} = \begin{pmatrix} \left(\frac{L_x}{\langle L_x \rangle}\right)^2 & 0 & 0 \\ 0 & \left(\frac{L_y}{\langle L_y \rangle}\right)^2 & 0 \\ 0 & 0 & \left(\frac{L_z}{\langle L_z \rangle}\right)^2 \end{pmatrix}. \tag{C.24}$$

One can then build the following strain invariants:

$$J = \sqrt{\det(\hat{C})} \tag{C.25a}$$

$$I_1 = \mathrm{tr}(\hat{C}) J^{-2/3} \tag{C.25b}$$

$$I_2 = \frac{1}{2}[tr^2(\hat{C}) - tr(\hat{C}^T \hat{C})] J^{-4/3}. \tag{C.25c}$$

$$\tag{C.25d}$$

The probability distributions $P(J)$, $P(I_1)$ and $P(I_2)$ are then calculated. Following the Mooney-Rivlin theory of rubber elasticity[5,354], the energy due to thermal fluctuations can be written as a function of the strain invariants:

$$\begin{aligned} E(J, I_1, I_2) &= E_0 + W(J) + W(I_1) + W(I_2) \\ &= E_0 + \mathcal{V}\left[\frac{K}{2}(J-1)^2 + c_{10}(I_1 - 3) + c_{01}(I_2)\right] \end{aligned} \tag{C.26}$$

where E_0 is the energy of the reference configuration, $\mathcal{V} \equiv \langle L_x \rangle \langle L_y \rangle \langle L_z \rangle$, K is the bulk modulus (see Sec 3.5.2) and $2(c_{01} + c_{10}) = G$ (here c_{ij} are the elements of the $\hat{C}$ tensor). Assuming that the deformations are statistically independent, one can approximate the W functions with the potentials of mean force extracted from the respective probability distributions:

$$W(X) = -k_B T \ln[P(X)] + \text{const.} \quad (X = J, I_1, I_2). \tag{C.27}$$

The approximated potentials of mean force are then fitted to the functional form

$$W(X) = M_X (X - X_0)^\gamma + A_X, \tag{C.28}$$

where A_X are constants, $\gamma = 2$ for $X = J$ and $\gamma = 1$ for $X = I_1, I_2$. The shear modulus is then estimated as

$$G = \frac{2(M_{I_1} + M_{I_2})}{V}. \tag{C.29}$$

It is also possible to estimate the bulk modulus K as

$$K = \frac{2M_J}{V}, \tag{C.30}$$

or equivalently from the density fluctuations, as the inverse of the isothermal compressibility κ_T [1]

$$K = \kappa_T^{-1} = \left(k_B T \frac{\langle V^2 \rangle - \langle V \rangle^2}{\langle V \rangle} \right)^{-1}. \tag{C.31}$$

where $V = L_x L_y L_z$. Finally, the Young modulus can then be obtained from Eq. (91).

BIBLIOGRAFIA

[1] J.-P. Hansen and I. R. McDonald, *Theory of simple liquids*. Elsevier, 1990.

[2] P.-G. de Gennes, *Scaling concepts in polymer physics*. Cornell University Press, 1979.

[3] M. Doi and S. F. Edwards, *The theory of polymer dynamics*. Oxford university press, 1986.

[4] P. Bolhuis, A. Louis, J. Hansen, and E. Meijer, "Accurate effective pair potentials for polymer solutions," *The Journal of Chemical Physics*, vol. 114, no. 9, pp. 4296–4311, 2001.

[5] M. Rubinstein and R. H. Colby, *Polymer physics*. Oxford University Press New York, 2003.

[6] K. Binder, *Monte Carlo and molecular dynamics simulations in polymer science*. Oxford University Press, 1995.

[7] S. F. Edwards, "The statistical mechanics of polymers with excluded volume," *Proceedings of the Physical Society*, vol. 85, no. 4, p. 613, 1965.

[8] S. K. Kumar, V. Ganesan, and R. A. Riggleman, "Perspective: Outstanding theoretical questions in polymer-nanoparticle hybrids," *The Journal of Chemical Physics*, vol. 147, no. 2, p. 20901, 2017.

[9] R. Mülhaupt, "Hermann Staudinger and the origin of macromolecular chemistry," *Angewandte Chemie International Edition*, vol. 43, no. 9, pp. 1054–1063, 2004.

[10] H. Staudinger and J. Fritschi, "Über isopren und kautschuk. 5. mitteilung. über die hydrierung des kautschuks und über seine konstitution," *Helvetica Chimica Acta*, vol. 5, no. 5, pp. 785–806, 1922.

[11] P. J. Flory, *Principles of polymer chemistry*. Cornell University Press, 1953.

[12] W. S. Johnson, W. H. Stockmayer, and H. Taube, "John Paul Flory," *Biographical Memoirs*, vol. 82, p. 115, 2002.

[13] M. Warner, "Sir Samuel Edwards," *Biographical Memoirs of Fellows of the Royal Society*, vol. 63, pp. 243–271, 2017.

[14] N. Goldenfeld, "Samuel Frederick Edwards: Founder of modern polymer and soft matter theory," *Proceedings of the National Academy of Sciences*, vol. 113, no. 1, pp. 10–11, 2016.

[15] S. F. Edwards and P. W. Anderson, "Theory of spin glasses," *Journal of Physics F: Metal Physics*, vol. 5, no. 5, p. 965, 1975.

[16] S. Edwards, "The statistical mechanics of polymerized material," *Proceedings of the Physical Society*, vol. 92, no. 1, p. 9, 1967.

[17] J.-F. Joanny and M. Cates, "Pierre-Gilles de Gennes. 24 October 1932—18 May 2007," 2019.

[18] P.-G. de Gennes, "Reptation of a polymer chain in the presence of fixed obstacles," *The Journal of Chemical Physics*, vol. 55, no. 2, pp. 572–579, 1971.

[19] S. F. Edwards, "The theory of rubber elasticity," *British Polymer Journal*, vol. 9, no. 2, pp. 140–143, 1977.

[20] P.-G. de Gennes, "Exponents for the excluded volume problem as derived by the Wilson method," *Physics Letters A*, vol. 38, no. 5, pp. 339–340, 1972.

[21] K. Kremer and G. S. Grest, "Dynamics of entangled linear polymer melts: A molecular-dynamics simulation," *The Journal of Chemical Physics*, vol. 92, no. 8, pp. 5057–5086, 1990.

[22] F. T. Wall, S. Windwer, and P. J. Gans, "Monte Carlo methods applied to configurations of flexible polymer molecules," *Methods of Computational Physics*, vol. 1, 1963.

[23] R. Eckhardt, "Stan Ulam, John von Neumann, and the Monte Carlo method," *Los Alamos Science*, vol. 15, no. 131-136, p. 30, 1987.

[24] N. Metropolis, "The beginning of the Monte Carlo method," *Los Alamos Science*, vol. 15, no. 584, pp. 125–130, 1987.

[25] F. T. Wall and J. J. Erpenbeck, "New method for the statistical computation of polymer dimensions," *The Journal of Chemical Physics*, vol. 30, no. 3, pp. 634–637, 1959.

[26] N. Clisby, "Accurate estimate of the critical exponent ν for self-avoiding walks via a fast implementation of the pivot algorithm," *Physical Review Letters*, vol. 104, no. 5, 2010.

[27] K. Kremer and K. Binder, "Monte Carlo simulation of lattice models for macromolecules," *Computer Physics Reports*, vol. 7, no. 6, pp. 259–310, 1988.

[28] M. Bishop, M. Kalos, and H. Frisch, "Molecular dynamics of polymeric systems," *The Journal of Chemical Physics*, vol. 70, no. 3, pp. 1299–1304, 1979.

[29] K. Kremer, G. S. Grest, and I. Carmesin, "Crossover from Rouse to reptation dynamics: A molecular-dynamics simulation," *Physical Review Letters*, vol. 61, no. 5, p. 566, 1988.

[30] I. Teraoka, *Polymer Solutions: An Introduction to Physical Properties*. John Wiley & Sons, Inc., 2002.

[31] S. G. Gregory, K. F. Barlow, K. E. McLay, R. Kaul, D. Swarbreck, A. Dunham, C. E. Scott, K. L. Howe, K. Woodfine, C. C. A. Spencer, and Others, "The DNA sequence and biological annotation of human chromosome 1," *Nature*, vol. 441, no. 7091, p. 315, 2006.

[32] K. Falconer, *Fractal geometry: mathematical foundations and applications*. John Wiley & Sons, 2004.

[33] G. F. Lawler and V. Limic, *Random walk: a modern introduction*. Cambridge University Press, 2010.

[34] J. Baschnagel, J. P. Wittmer, and H. Meyer, "Monte Carlo Simulation of Polymers: Coarse-Grained Models," in *Computational Soft Matter: From Synthetic Polymers to Proteins (Lecture Notes)*, pp. 83–140, NIC, 2004.

[35] J. S. Higgins and H. C. Benoit, *Polymers and neutron scattering*. Oxford university press, 1994.

[36] J. Wittmer, P. Beckrich, A. Johner, A. Semenov, S. Obukhov, H. Meyer, and J. Baschnagel, "Why polymer chains in a melt are not random walks," *EPL (Europhysics Letters)*, vol. 77, no. 5, p. 56003, 2007.

[37] W. Paul, K. Binder, D. W. Heermann, and K. Kremer, "Crossover scaling in semidilute polymer solutions: a Monte Carlo test," *Journal de Physique II*, vol. 1, no. 1, pp. 37–60, 1991.

[38] I. Gerroff, A. Milchev, K. Binder, and W. Paul, "A new off-lattice Monte Carlo model for polymers: A comparison of static and dynamic properties with the bond-fluctuation model and application to random media," *The Journal of Chemical Physics*, vol. 98, no. 8, pp. 6526–6539, 1993.

[39] L. Verlet, "Computer" experiments" on classical fluids II - equilibrium correlation functions," *Physical Review*, vol. 165, no. 1, p. 201, 1968.

[40] M. E. Fisher, "Correlation functions and the critical region of simple fluids," *Journal of Mathematical Physics*, vol. 5, no. 7, pp. 944–962, 1964.

[41] R. Koshy, T. Desai, P. Keblinski, J. Hooper, and K. S. Schweizer, "Density fluctuation correlation length in polymer fluids," *The Journal of Chemical Physics*, vol. 119, no. 14, pp. 7599–7603, 2003.

[42] R. Evans, J. R. Henderson, D. C. Hoyle, A. O. Parry, and Z. A. Sabeur, "Asymptotic decay of liquid structure: oscillatory liquid-vapour density profiles and the Fisher-Widom line," *Molecular Physics*, vol. 80, no. 4, pp. 755–775, 1993.

[43] R. Evans, R. J. F. Leote de Carvalho, and D. C. Hoyle, "Asymptotic decay of correlations in liquids and their mixtures," *The Journal of Chemical Physics*, vol. 100, no. January, pp. 591–603, 1994.

[44] A. Einstein, *Investigations on the Theory of the Brownian Movement*. Courier Corporation, 1956.

[45] W. Paul, G. Smith, D. Y. Yoon, B. Farago, S. Rathgeber, A. Zirkel, L. Willner, and D. Richter, "Chain motion in an unentangled polyethylene melt: A critical test of the rouse model by molecular dynamics simulations and neutron spin echo spectroscopy," *Physical Review Letters*, vol. 80, no. 11, p. 2346, 1998.

[46] J. T. Padding and W. J. Briels, "Zero-shear stress relaxation and long time dynamics of a linear polyethylene melt: A test of Rouse theory," *The Journal of Chemical Physics*, vol. 114, no. 19, pp. 8685–8693, 2001.

[47] G. D. Smith, W. Paul, M. Monkenbusch, and D. Richter, "On the non-gaussianity of chain motion in unentangled polymer melts," *The Journal of Chemical Physics*, vol. 114, no. 9, pp. 4285–4288, 2001.

[48] W. Paul, K. Binder, D. W. Heermann, and K. Kremer, "Dynamics of polymer solutions and melts. reptation predictions and scaling of relaxation times," *The Journal of Chemical Physics*, vol. 95, no. 10, pp. 7726–7740, 1991.

[49] A. Kopf, B. Dünweg, and W. Paul, "Dynamics of polymer "isotope" mixtures: Molecular dynamics simulation and Rouse model analysis," *The Journal of Chemical Physics*, vol. 107, no. 17, pp. 6945–6955, 1997.

[50] M. Doi, "Explanation for the 3.4 power law of viscosity of polymeric liquids on the basis of the tube model," *Journal of Polymer Science: Polymer Letters Edition*, vol. 19, no. 5, pp. 265–273, 1981.

[51] M. Doi, "Explanation for the 3.4-power law for viscosity of polymeric liquids on the basis of the tube model," *Journal of Polymer Science: Polymer Physics Edition*, vol. 21, no. 5, pp. 667–684, 1983.

[52] H.-P. Hsu and K. Kremer, "Static and dynamic properties of large polymer melts in equilibrium," *The Journal of Chemical Physics*, vol. 144, no. 15, p. 154907, 2016.

[53] B. J. Berne and R. Pecora, *Dynamic light scattering: with applications to chemistry, biology, and physics*. Courier Corporation, 2000.

[54] A. Falcao, J. S. Pedersen, and K. Mortensen, "Structure of randomly crosslinked poly (dimethylsiloxane) networks produced by electron irradiation," *Macromolecules*, vol. 26, no. 20, pp. 5350–5364, 1993.

[55] P. J. Flory, "Molecular size distribution in three dimensional polymers. i. gelation1," *Journal of the American Chemical Society*, vol. 63, no. 11, pp. 3083–3090, 1941.

[56] P. J. Flory, "Molecular size distribution in three dimensional polymers. ii. trifunctional branching units," *Journal of the American Chemical Society*, vol. 63, no. 11, pp. 3091–3096, 1941.

[57] P. J. Flory, "Constitution of three-dimensional polymers and the theory of gelation.," *The Journal of Physical Chemistry*, vol. 46, no. 1, pp. 132–140, 1942.

[58] W. H. Stockmayer, "Theory of molecular size distribution and gel formation in branched-chain polymers," *The Journal of Chemical Physics*, vol. 11, no. 2, pp. 45–55, 1943.

[59] W. H. Stockmayer, "Theory of molecular size distribution and gel formation in branched polymers ii. general cross linking," *The Journal of Chemical Physics*, vol. 12, no. 4, pp. 125–131, 1944.

[60] E. Zaccarelli, S. Buldyrev, E. La Nave, A. Moreno, I. Saika-Voivod, F. Sciortino, and P. Tartaglia, "Model for reversible colloidal gelation," *Physical Review Letters*, vol. 94, no. 21, p. 218301, 2005.

[61] J. Russo, P. Tartaglia, and F. Sciortino, "Reversible gels of patchy particles: role of the valence," *The Journal of Chemical Physics*, vol. 131, no. 1, p. 014504, 2009.

[62] R. Ziff and G. Stell, "Kinetics of polymer gelation," *The Journal of Chemical Physics*, vol. 73, no. 7, pp. 3492–3499, 1980.

[63] E. Bianchi, P. Tartaglia, E. La Nave, and F. Sciortino, "Fully solvable equilibrium self-assembly process: fine-tuning the clusters size and the connectivity in patchy particle systems," *The Journal of Physical Chemistry B*, vol. 111, no. 40, pp. 11765–11769, 2007.

[64] F. Sciortino and E. Zaccarelli, "Reversible gels of patchy particles," *Current Opinion in Solid State and Materials Science*, vol. 15, no. 6, pp. 246–253, 2011.

[65] L. D. Landau and E. M. Lifshitz, *Course of Theoretical Physics Vol. 7: Theory of Elasticity (2nd ed.)*. Pergamon press, 1970.

[66] L. Treloar, "The elasticity of a network of long-chain molecules i," *Transactions of the Faraday Society*, vol. 39, pp. 36–41, 1943.

[67] L. Treloar, "The elasticity of a network of long-chain molecules ii," *Transactions of the Faraday Society*, vol. 39, pp. 241–246, 1943.

[68] P. J. Flory, "Molecular theory of rubber elasticity," *Polymer journal*, vol. 17, no. 1, p. 1, 1985.

[69] J. E. Mark, *Physical properties of polymers handbook*, vol. 1076. Springer, 2007.

[70] H. M. James and E. Guth, "Theory of the increase in rigidity of rubber during cure," *The Journal of Chemical Physics*, vol. 15, no. 9, pp. 669–683, 1947.

[71] H. M. James, "Statistical properties of networks of flexible chains," *The Journal of Chemical Physics*, vol. 15, no. 9, pp. 651–668, 1947.

[72] P. Flory, "Statistical thermodynamics of random networks," *Proceedings of the Royal Society of London. A. Mathematical and Physical Sciences*, vol. 351, no. 1666, pp. 351–380, 1976.

[73] D. S. Pearson, "Scattered intensity from a chain in a rubber network," *Macromolecules*, vol. 10, no. 3, pp. 696–701, 1977.

[74] A. Kloczkowski, J. Mark, and B. Erman, "Chain dimensions and fluctuations in random elastomeric networks. 1. phantom gaussian networks in the undeformed state," *Macromolecules*, vol. 22, no. 3, pp. 1423–1432, 1989.

[75] R. Everaers, S. K. Sukumaran, G. S. Grest, C. Svaneborg, A. Sivasubramanian, and K. Kremer, "Rheology and microscopic topology of entangled polymeric liquids," *Science*, vol. 303, no. 5659, pp. 823–826, 2004.

[76] E. R. Duering, K. Kremer, and G. S. Grest, "Structure and relaxation of end-linked polymer networks," *The Journal of Chemical Physics*, vol. 101, no. 9, pp. 8169–8192, 1994.

[77] J. T. Kalathi, U. Yamamoto, K. S. Schweizer, G. S. Grest, and S. K. Kumar, "Nanoparticle Diffusion in Polymer Nanocomposites," *Physical Review Letters*, vol. 108301, no. March, pp. 1–5, 2014.

[78] K. Kremer, "Polymer dynamics: Long time simulations and topological constraints," in *Computer Simulations in Condensed Matter Systems: From Materials to Chemical Biology Volume 2*, pp. 341–378, Springer, 2006.

[79] M. P. Allen and D. J. Tildesley, *Computer simulation of liquids*. Oxford university press, 2017.

[80] D. Frenkel and B. Smit, *Understanding molecular simulation: from algorithms to applications*, vol. 1. Elsevier, 2001.

[81] M. Tuckerman, *Statistical mechanics: theory and molecular simulation*. Oxford university press, 2010.

[82] W. C. Swope, H. C. Andersen, P. H. Berens, and K. R. Wilson, "A computer simulation method for the calculation of equilibrium constants for the formation of physical clusters of molecules: Application to small water clusters," *The Journal of Chemical Physics*, vol. 76, no. 1, pp. 637–649, 1982.

[83] T. Schneider and E. Stoll, "Molecular-dynamics study of a three-dimensional one-component model for distortive phase transitions," *Physical Review B*, vol. 17, no. 3, p. 1302, 1978.

[84] B. Dünweg and W. Paul, "Brownian dynamics simulations without gaussian random numbers," *International Journal of Modern Physics C*, vol. 2, no. 03, pp. 817–827, 1991.

[85] R. Kubo, "The fluctuation-dissipation theorem," *Reports on Progress in Physics*, vol. 29, no. 1, p. 255, 1966.

[86] A. Malevanets and R. Kapral, "Mesoscopic model for solvent dynamics," *The Journal of Chemical Physics*, vol. 110, no. 17, pp. 8605–8613, 1999.

[87] B. Dünweg, "Mesoscopic simulations for problems with hydrodynamics, with emphasis on polymer dynamics," in *Computer Simulations in Condensed Matter Systems: From Materials to Chemical Biology Volume 2*, pp. 309–340, Springer, 2006.

[88] E. M. Purcell, "Life at low Reynolds number," *American Journal of Physics*, vol. 45, no. 1, pp. 3–11, 1977.

[89] J. G. Curro and P. Pincus, "A theoretical basis for viscoelastic relaxation of elastomers in the long-time limit," *Macromolecules*, vol. 16, no. 4, pp. 559–562, 1983.

[90] G. S. Grest, K. Kremer, S. T. Milner, and T. Witten, "Relaxation of self-entangled many-arm star polymers," *Macromolecules*, vol. 22, no. 4, pp. 1904–1910, 1989.

[91] K. Binder and W. Paul, "Monte Carlo simulations of polymer dynamics: Recent advances," *Journal of Polymer Science Part B: Polymer Physics*, vol. 35, no. 1, pp. 1–31, 1997.

[92] I. Carmesin and K. Kremer, "The bond fluctuation method: a new effective algorithm for the dynamics of polymers in all spatial dimensions," *Macromolecules*, vol. 21, no. 9, pp. 2819–2823, 1988.

[93] H. Deutsch and K. Binder, "Interdiffusion and self-diffusion in polymer mixtures: A Monte Carlo study," *The Journal of Chemical Physics*, vol. 94, no. 3, pp. 2294–2304, 1991.

[94] J. Baschnagel, K. Binder, and H.-P. Wittmann, "The influence of the cooling rate on the glass transition and the glassy state in three-dimensional dense polymer melts: a Monte Carlo study," *Journal of Physics: Condensed Matter*, vol. 5, no. 11, p. 1597, 1993.

[95] V. Tries, W. Paul, J. Baschnagel, and K. Binder, "Modeling polyethylene with the bond fluctuation model," *The Journal of Chemical Physics*, vol. 106, no. 2, pp. 738–748, 1997.

[96] D. Marx and J. Hutter, *Ab initio molecular dynamics: basic theory and advanced methods*. Cambridge University Press, 2009.

[97] F. Müller-Plathe, "Coarse-graining in polymer simulation: from the atomistic to the mesoscopic scale and back," *ChemPhysChem*, vol. 3, no. 9, pp. 754–769, 2002.

[98] J. E. Jones, "On the determination of molecular fields.—ii. from the equation of state of a gas," *Proceedings of the Royal Society of London. Series A, Containing Papers of a Mathematical and Physical Character*, vol. 106, no. 738, pp. 463–477, 1924.

[99] J. Liu, Y. Gao, D. Cao, L. Zhang, and Z. Guo, "Nanoparticle dispersion and aggregation in polymer nanocomposites: Insights from molecular dynamics simulation," *Langmuir*, vol. 27, no. 12, pp. 7926–7933, 2011.

[100] C. Bennemann, W. Paul, K. Binder, and B. Dünweg, "Molecular-dynamics simulations of the thermal glass transition in polymer melts: α-relaxation behavior," *Physical Review E*, vol. 57, no. 1, p. 843, 1998.

[101] J. D. Weeks, D. Chandler, and H. C. Andersen, "Role of repulsive forces in determining the equilibrium structure of simple liquids," *The Journal of Chemical Physics*, vol. 54, no. 12, pp. 5237–5247, 1971.

[102] J. Wittmer, P. Beckrich, H. Meyer, A. Cavallo, A. Johner, and J. Baschnagel, "Intramolecular long-range correlations in polymer melts: The segmental size distribution and its moments," *Physical Review E*, vol. 76, no. 1, p. 011803, 2007.

[103] R. C. Armstrong, "Kinetic theory and rheology of dilute solutions of flexible macromolecules. i. steady state behavior," *The Journal of Chemical Physics*, vol. 60, no. 3, pp. 724–728, 1974.

[104] M. Bishop, D. Ceperley, H. Frisch, and M. Kalos, "Investigations of static properties of model bulk polymer fluids," *The Journal of Chemical Physics*, vol. 72, no. 5, pp. 3228–3235, 1980.

[105] G. S. Grest and K. Kremer, "Molecular dynamics simulation for polymers in the presence of a heat bath," *Physical Review A*, vol. 33, no. 5, p. 3628, 1986.

[106] R. Faller, A. Kolb, and F. Müller-Plathe, "Local chain ordering in amorphous polymer melts: influence of chain stiffness," *Physical Chemistry Chemical Physics*, vol. 1, no. 9, pp. 2071–2076, 1999.

[107] R. Auhl, R. Everaers, G. S. Grest, K. Kremer, and S. J. Plimpton, "Equilibration of long chain polymer melts in computer simulations," *The Journal of Chemical Physics*, vol. 119, no. 24, pp. 12718–12728, 2003.

[108] M. Bulacu and E. van der Giessen, "Effect of bending and torsion rigidity on self-diffusion in polymer melts: A molecular-dynamics study," *The Journal of Chemical Physics*, vol. 123, no. 11, p. 114901, 2005.

[109] H.-P. Hsu and K. Kremer, "A coarse-grained polymer model for studying the glass transition," *The Journal of Chemical Physics*, vol. 150, no. 9, p. 091101, 2019.

[110] Y. Kojima, A. Usuki, M. Kawasumi, A. Okada, Y. Fukushima, T. Kurauchi, and O. Kamigaito, "Mechanical properties of nylon 6-clay hybrid," *Journal of Materials Research*, vol. 8, no. 5, pp. 1185–1189, 1993.

[111] A. Usuki, Y. Kojima, M. Kawasumi, A. Okada, Y. Fukushima, T. Kurauchi, and O. Kamigaito, "Synthesis of nylon 6-clay hybrid," *Journal of Materials Research*, vol. 8, no. 5, pp. 1179–1184, 1993.

[112] M. Vert, Y. Doi, K.-H. Hellwich, M. Hess, P. Hodge, P. Kubisa, M. Rinaudo, and F. Schué, "Terminology for biorelated polymers and applications (iupac recommendations 2012)," *Pure and Applied Chemistry*, vol. 84, no. 2, pp. 377–410, 2012.

[113] F. Croce, G. Appetecchi, L. Persi, and B. Scrosati, "Nanocomposite polymer electrolytes for lithium batteries," *Nature*, vol. 394, no. 6692, p. 456, 1998.

[114] H.-L. Tyan, Y.-C. Liu, and K.-H. Wei, "Thermally and mechanically enhanced clay/polyimide nanocomposite via reactive organoclay," *Chemistry of Materials*, vol. 11, no. 7, pp. 1942–1947, 1999.

[115] R. Gangopadhyay and A. De, "Conducting polymer nanocomposites: a brief overview," *Chemistry of Materials*, vol. 12, no. 3, pp. 608–622, 2000.

[116] T. Merkel, B. Freeman, R. Spontak, Z. He, I. Pinnau, P. Meakin, and A. Hill, "Ultrapermeable, reverse-selective nanocomposite membranes," *Science*, vol. 296, no. 5567, pp. 519–522, 2002.

[117] R. J. Nussbaumer, W. R. Caseri, P. Smith, and T. Tervoort, "Polymer-tio2 nanocomposites: a route towards visually transparent broadband uv filters and high refractive index materials," *Macromolecular Materials and Engineering*, vol. 288, no. 1, pp. 44–49, 2003.

[118] B. J. Ash, R. W. Siegel, and L. S. Schadler, "Mechanical behavior of alumina/poly (methyl methacrylate) nanocomposites," *Macromolecules*, vol. 37, no. 4, pp. 1358–1369, 2004.

[119] T. Ramanathan, H. Liu, and L. C. Brinson, "Functionalized swnt/polymer nanocomposites for dramatic property improvement," *Journal of Polymer Science Part B: Polymer Physics*, vol. 43, no. 17, pp. 2269–2279, 2005.

[120] A. C. Balazs, T. Emrick, and T. P. Russell, "Nanoparticle polymer composites: where two small worlds meet," *Science*, vol. 314, no. 5802, pp. 1107–1110, 2006.

[121] J. Oberdisse, "Aggregation of colloidal nanoparticles in polymer matrices," *Soft Matter*, vol. 2, no. 1, pp. 29–36, 2006.

[122] S. K. Kumar and R. Krishnamoorti, "Nanocomposites: structure, phase behavior, and properties," *Annual Review of Chemical and Biomolecular Engineering*, vol. 1, pp. 37–58, 2010.

[123] H.-X. Zhou, G. Rivas, and A. P. Minton, "Macromolecular crowding and confinement: biochemical, biophysical, and potential physiological consequences," *Annual Review of Biophysics*, vol. 37, pp. 375–397, 2008.

[124] H.-X. Zhou, "Influence of crowded cellular environments on protein folding, binding, and oligomerization: biological consequences and potentials of atomistic modeling," *FEBS Letters*, vol. 587, no. 8, pp. 1053–1061, 2013.

[125] K. S. K. Soppimath, T. M. T. M. Aminabhavi, A. R. A. R. Kulkarni, and W. E. Rudzinski, "Biodegradable polymeric nanoparticles as drug delivery devices," *Journal of Controlled Release*, vol. 70, no. 1-2, pp. 1–20, 2001.

[126] I. Brigger, C. Dubernet, and P. Couvreur, "Nanoparticles in cancer therapy and diagnosis," *Advanced Drug Delivery Reviews*, vol. 54, no. 5, pp. 631–651, 2002.

[127] S. K. Lai, D. E. O'Hanlon, S. Harrold, S. T. Man, Y.-Y. Wang, R. Cone, and J. Hanes, "Rapid transport of large polymeric nanoparticles in fresh undiluted human mucus," *Proceedings of the National Academy of Sciences*, vol. 104, no. 5, pp. 1482–1487, 2007.

[128] K. Cho, X. U. Wang, S. Nie, D. M. Shin, and Others, "Therapeutic nanoparticles for drug delivery in cancer," *Clinical Cancer Research*, vol. 14, no. 5, pp. 1310–1316, 2008.

[129] P. G. Bolhuis, E. J. Meijer, and A. A. Louis, "Colloid-polymer mixtures in the protein limit," *Physical Review Letters*, vol. 90, no. 6, p. 68304, 2003.

[130] S. Asakura and F. Oosawa, "On interaction between two bodies immersed in a solution of macromolecules," *The Journal of Chemical Physics*, vol. 22, no. 7, pp. 1255–1256, 1954.

[131] S. Asakura and F. Oosawa, "Interaction between particles suspended in solutions of macromolecules," *Journal of Polymer Science*, vol. 33, no. 126, pp. 183–192, 1958.

[132] H. N. W. Lekkerkerker, W.-K. Poon, P. N. Pusey, A. Stroobants, and P. B. . Warren, "Phase behaviour of colloid+ polymer mixtures," *EPL (Europhysics Letters*, vol. 20, no. 6, p. 559, 1992.

[133] W. C. K. Poon, "The physics of a model colloid–polymer mixture," *Journal of Physics: Condensed Matter*, vol. 14, 2002.

[134] E. J. Meijer and D. Frenkel, "Colloids dispersed in polymer solutions. A computer simulation study," *The Journal of Chemical Physics*, vol. 100, no. 9, pp. 6873–6887, 1994.

[135] M. Dijkstra, J. M. Brader, and R. Evans, "Phase behaviour and structure of model colloid-polymer mixtures," *Journal of Physics: Condensed Matter*, vol. 11, no. 50, p. 10079, 1999.

[136] M. Fuchs and K. S. Schweizer, "Structure of colloid – polymer suspensions," *Journal of Physics: Condensed Matter*, vol. 14, pp. 239–269, 2002.

[137] S. Gam, J. S. Meth, S. G. Zane, C. Chi, B. A. Wood, M. E. Seitz, K. I. Winey, N. Clarke, and R. J. Composto, "Macromolecular diffusion in a crowded polymer nanocomposite," *Macromolecules*, vol. 44, no. 9, pp. 3494–3501, 2011.

[138] M. Tatou, A.-C. Genix, A. Imaz, J. Forcada, A. Banc, R. Schweins, I. Grillo, and J. Oberdisse, "Reinforcement and polymer mobility in silica–latex nanocomposites with controlled aggregation," *Macromolecules*, vol. 44, no. 22, pp. 9029–9039, 2011.

[139] A. Dorigato, Y. Dzenis, and A. Pegoretti, "Filler aggregation as a reinforcement mechanism in polymer nanocomposites," *Mechanics of Materials*, vol. 61, pp. 79–90, 2013.

[140] M. E. Mackay, A. Tuteja, P. M. Duxbury, C. J. Hawker, B. Van Horn, Z. Guan, G. Chen, and R. S. Krishnan, "General strategies for nanoparticle dispersion," *Science*, vol. 311, no. 5768, pp. 1740–1743, 2006.

[141] C. C. Lin, S. Gam, J. S. Meth, N. Clarke, K. I. Winey, and R. J. Composto, "Do attractive polymer-nanoparticle interactions retard polymer diffusion in nanocomposites?," *Macromolecules*, vol. 46, no. 11, pp. 4502–4509, 2013.

[142] J. B. Hooper, K. S. Schweizer, T. G. Desai, R. Koshy, and P. Keblinski, "Structure, surface excess and effective interactions in polymer nanocomposite melts and concentrated solutions," *The Journal of Chemical Physics*, vol. 121, no. 14, pp. 6986–6997, 2004.

[143] J. B. Hooper and K. S. Schweizer, "Contact aggregation, bridging, and steric stabilization in dense polymer- particle mixtures," *Macromolecules*, vol. 38, no. 21, pp. 8858–8869, 2005.

[144] J. B. Hooper and K. S. Schweizer, "Theory of Phase Separation in Polymer Nanocomposites," *Macromolecules*, pp. 5133–5142, 2006.

[145] L. M. Hall and K. S. Schweizer, "Many body effects on the phase separation and structure of dense polymer-particle melts," *The Journal of Chemical Physics*, vol. 128, no. 23, p. 234901, 2008.

[146] R. Tuinier, J. Dhont, and C. De Kruif, "Depletion-induced phase separation of aggregated whey protein colloids by an exocellular polysaccharide," *Langmuir*, vol. 16, no. 4, pp. 1497–1507, 2000.

[147] J. S. Smith, D. Bedrov, and G. D. Smith, "A molecular dynamics simulation study of nanoparticle interactions in a model polymer-nanoparticle composite," *Composites science and technology*, vol. 63, no. 11, pp. 1599–1605, 2003.

[148] D. Bedrov, G. D. Smith, and J. S. Smith, "Matrix-induced nanoparticle interactions in a polymer melt: A molecular dynamics simulation study," *The Journal of Chemical Physics*, vol. 119, no. 19, pp. 10438–10447, 2003.

[149] N. A. Mahynski, T. Lafitte, and A. Z. Panagiotopoulos, "Pressure and density scaling for colloid-polymer systems in the protein limit," *Physical Review E*, vol. 85, no. 5, p. 051402, 2012.

[150] N. A. Mahynski, B. Irick, and A. Z. Panagiotopoulos, "Structure of phase-separated athermal colloid-polymer systems in the protein limit," *Physical Review E*, vol. 87, no. 2, p. 022309, 2013.

[151] D. Meng, S. K. Kumar, S. Cheng, and G. S. Grest, "Simulating the miscibility of nanoparticles and polymer melts," *Soft Matter*, vol. 9, no. 22, pp. 5417–5427, 2013.

[152] A. Karatrantos, N. Clarke, R. J. Composto, and K. I. Winey, "Polymer conformations in polymer nanocomposites containing spherical nanoparticles," *Soft Matter*, vol. 11, no. 2, pp. 382–388, 2015.

[153] C. N. Likos, "Effective interactions in soft condensed matter physics," *Physics Reports*, vol. 348, no. 4-5, pp. 267–439, 2001.

[154] L. Meli and P. F. Green, "Aggregation and coarsening of ligand-stabilized gold nanoparticles in poly (methyl methacrylate) thin films," *Acs Nano*, vol. 2, no. 6, pp. 1305–1312, 2008.

[155] S. E. Harton and S. K. Kumar, "Mean-field theoretical analysis of brush-coated nanoparticle dispersion in polymer matrices," *Journal of Polymer Science Part B: Polymer Physics*, vol. 46, no. 4, pp. 351–358, 2008.

[156] A. Jayaraman and K. S. Schweizer, "Effective interactions, structure, and phase behavior of lightly tethered nanoparticles in polymer melts," *Macromolecules*, vol. 41, no. 23, pp. 9430–9438, 2008.

[157] J. Choi, M. J. A. Hore, J. S. Meth, N. Clarke, K. I. Winey, and R. J. Composto, "Universal scaling of polymer diffusion in nanocomposites," *ACS Macro Letters*, vol. 2, no. 6, pp. 485–490, 2013.

[158] A. Karatrantos, N. Clarke, and M. Kröger, "Modeling of polymer structure and conformations in polymer nanocomposites from atomistic to mesoscale: A Review," *Polymer Reviews*, vol. 56, no. 3, pp. 385–428, 2016.

[159] A. I. Nakatani, W. Chen, R. G. Schmidt, G. V. Gordon, and C. C. Han, "Chain dimensions in polysilicate- filled poly (dimethyl siloxane)," *Polymer*, vol. 42, pp. 3713–3722, 2001.

[160] S. Sen, Y. Xie, S. K. Kumar, H. Yang, A. Bansal, D. L. Ho, L. Hall, J. B. Hooper, and K. S. Schweizer, "Chain conformations and bound-layer correlations in polymer nanocomposites," *Physical Review Letters*, vol. 98, no. 12, p. 128302, 2007.

[161] A. Tuteja, P. M. Duxbury, and M. E. MacKay, "Polymer chain swelling induced by dispersed nanoparticles," *Physical Review Letters*, vol. 100, no. 7, pp. 21–24, 2008.

[162] N. Jouault, F. Dalmas, S. Said, E. Di Cola, R. Schweins, J. Jestin, and F. Boué, "Direct measurement of polymer chain conformation in well-controlled model nanocomposites by combining SANS and SAXS," *Macromolecules*, vol. 43, no. 23, pp. 9881–9891, 2010.

[163] M. Crawford, R. Smalley, G. Cohen, B. Hogan, B. Wood, S. Kumar, Y. B. Melnichenko, L. He, W. Guise, and B. Hammouda, "Chain conformation in polymer nanocomposites with uniformly dispersed nanoparticles," *Physical Review Letters*, vol. 110, no. 19, p. 196001, 2013.

[164] A. L. Frischknecht, E. S. McGarrity, and M. E. MacKay, "Expanded chain dimensions in polymer melts with nanoparticle fillers," *The Journal of Chemical Physics*, vol. 132, no. 20, 2010.

[165] A. G. Ogston, B. N. Preston, and J. D. Wells, "On the transport of compact particles through solutions of chain-polymers," *Proceedings of the Royal Society of London. Series A*, vol. 333, no. 1594, pp. 297–316, 1973.

[166] A. R. Altenberger and M. Tirrell, "On the theory of self-diffusion in a polymer gel," *The Journal of Chemical Physics*, vol. 80, no. 5, pp. 2208–2213, 1984.

[167] L. Johansson, C. Elvingson, and J. E. Loefroth, "Diffusion and interaction in gels and solutions. 3. Theoretical results on the obstruction effect," *Macromolecules*, vol. 24, no. 22, pp. 6024–6029, 1991.

[168] G. D. J. Phillies, G. S. Ullmann, K. Ullmann, and T.-H. Lin, "Phenomenological scaling laws for "semidilute"macromolecule solutions from light scattering by optical probe particles," *The Journal of Chemical Physics*, vol. 82, no. 11, pp. 5242–5246, 1985.

[169] G. D. J. Phillies, "Universal scaling equation for self-diffusion by macromolecules in solution," *Macromolecules*, vol. 19, no. 9, pp. 2367–2376, 1986.

[170] R. I. Cukier, "Diffusion of Brownian spheres in semidilute polymer solutions," *Macromolecules*, vol. 17, no. 2, pp. 252–255, 1984.

[171] T. Odijk, "Depletion theory of protein transport in semi-dilute polymer solutions," *Biophysical Journal*, vol. 79, no. 5, pp. 2314–2321, 2000.

[172] T.-H. Fan, J. K. G. Dhont, and R. Tuinier, "Motion of a sphere through a polymer solution," *Physical Review E*, vol. 75, no. 1, p. 11803, 2007.

[173] R. Tuinier and T.-H. Fan, "Scaling of nanoparticle retardation in semi-dilute polymer solutions," *Soft Matter*, vol. 4, no. 2, pp. 254–257, 2008.

[174] L. Masaro and X. X. Zhu, "Physical models of diffusion for polymer solutions, gels and solids," *Progress in Polymer Science*, vol. 24, no. 5, pp. 731–775, 1999.

[175] F. Brochard-Wyart and P.-G. de Gennes, "Viscosity at small scales in polymer melts," *The European Physical Journal E*, vol. 1, no. 1, pp. 93–97, 2000.

[176] B. U. Felderhof, "Diffusion of interacting Brownian particles," *Journal of Physics A: Mathematical and General*, vol. 11, no. 5, pp. 929–937, 1978.

[177] F. Ould-Kaddour and D. Levesque, "Molecular-dynamics investigation of tracer diffusion in a simple liquid: Test of the Stokes-Einstein law," *Physical Review E*, vol. 63, no. 1, p. 11205, 2000.

[178] A. Tuteja, M. E. Mackay, S. Narayanan, S. Asokan, and M. S. Wong, "Breakdown of the continuum stokes- einstein relation for nanoparticle diffusion," *Nano letters*, vol. 7, no. 5, pp. 1276–1281, 2007.

[179] J. Liu, D. Cao, and L. Zhang, "Molecular dynamics study on nanoparticle diffusion in polymer melts: a test of the Stokes- Einstein law," *Journal of Physical Chemistry C*, vol. 112, no. 17, pp. 6653–6661, 2008.

[180] C. A. Grabowski, B. Adhikary, and A. Mukhopadhyay, "Dynamics of gold nanoparticles in a polymer melt," *Applied Physics Letters*, vol. 94, no. 2, p. 21903, 2009.

[181] I. Kohli and A. Mukhopadhyay, "Diffusion of nanoparticles in semidilute polymer solutions: effect of different length scales," *Macromolecules*, vol. 45, no. 15, pp. 6143–6149, 2012.

[182] F. Babaye Khorasani, R. Poling-Skutvik, R. Krishnamoorti, and J. C. Conrad, "Mobility of nanoparticles in semidilute polyelectrolyte solutions," *Macromolecules*, vol. 47, no. 15, pp. 5328–5333, 2014.

[183] R. Poling-Skutvik, R. Krishnamoorti, and J. C. Conrad, "Size-Dependent Dynamics of Nanoparticles in Unentangled Polyelectrolyte Solutions," *ACS Macro Letters*, vol. 4, no. 10, pp. 1169–1173, 2015.

[184] L.-H. Cai, S. Panyukov, and M. Rubinstein, "Mobility of nonsticky nanoparticles in polymer liquids," *Macromolecules*, vol. 44, no. 19, pp. 7853–7863, 2011.

[185] L.-H. Cai, S. Panyukov, and M. Rubinstein, "Hopping diffusion of nanoparticles in polymer matrices," *Macromolecules*, vol. 48, no. 3, pp. 847–862, 2015.

[186] S. A. Egorov, "Anomalous nanoparticle diffusion in polymer solutions and melts: A mode-coupling theory study," *The Journal of Chemical Physics*, vol. 134, no. 8, p. 84903, 2011.

[187] U. Yamamoto and K. S. Schweizer, "Theory of nanoparticle diffusion in unentangled and entangled polymer melts," *The Journal of Chemical Physics*, vol. 135, no. 22, p. 224902, 2011.

[188] K. S. Schweizer and J. G. Curro, "Integral equation theories of the structure, thermodynamics, and phase transitions of polymer fluids," *Advances in Chemical Physics*, vol. 98, pp. 1–142, 1997.

[189] U. Yamamoto and K. S. Schweizer, "Microscopic theory of the long-time diffusivity and intermediate-time anomalous transport of a nanoparticle in polymer melts," *Macromolecules*, vol. 48, no. 1, pp. 152–163, 2014.

[190] S. Bhattacharyya and B. Bagchi, "Anomalous diffusion of small particles in dense liquids," *The Journal of Chemical Physics*, vol. 106, no. 5, pp. 1757–1763, 1997.

[191] Z. E. Dell and K. S. Schweizer, "Theory of localization and activated hopping of nanoparticles in cross-linked networks and entangled polymer melts," *Macromolecules*, vol. 47, no. 1, pp. 405–414, 2013.

[192] K. S. Schweizer and E. J. Saltzman, "Entropic barriers, activated hopping, and the glass transition in colloidal suspensions," *The Journal of Chemical Physics*, vol. 119, no. 2, pp. 1181–1196, 2003.

[193] R. A. Omari, A. M. Aneese, C. A. Grabowski, and A. Mukhopadhyay, "Diffusion of nanoparticles in semidilute and entangled polymer solutions," *The Journal of Physical Chemistry B*, vol. 113, no. 25, pp. 8449–8452, 2009.

[194] G. D. Phillies, "Dynamics of polymers in concentrated solutions: the universal scaling equation derived," *Macromolecules*, vol. 20, no. 3, pp. 558–564, 1987.

[195] C. A. Grabowski and A. Mukhopadhyay, "Size effect of nanoparticle diffusion in a polymer melt," *Macromolecules*, vol. 47, no. 20, pp. 7238–7242, 2014.

[196] J. C. Maxwell, *A treatise on electricity and magnetism*, vol. 1. Oxford: Clarendon Press, 1873.

[197] H. Fricke, "A mathematical treatment of the electric conductivity and capacity of disperse systems," *Physical Review*, vol. 24, pp. 555–575, 1924.

[198] R. A. Waggoner, F. D. Blum, and J. MacElroy, "Dependence of the solvent diffusion coefficient on concentration in polymer solutions," *Macromolecules*, vol. 26, no. 25, pp. 6841–6848, 1993.

[199] A. Karatrantos, R. J. Composto, K. I. Winey, and N. Clarke, "Polymer and spherical nanoparticle diffusion in nanocomposites," *The Journal of Chemical Physics*, vol. 146, no. 20, p. 203331, 2017.

[200] M. Muthukumar and A. Baumgärtner, "Effects of entropic barriers on polymer dynamics," *Macromolecules*, vol. 22, no. 4, pp. 1937–1941, 1989.

[201] M. Muthukumar and A. Baumgärtner, "Diffusion of a polymer chain in random media," *Macromolecules*, vol. 22, no. 4, pp. 1941–1946, 1989.

[202] J. S. Meth, S. Gam, J. Choi, C. C. Lin, R. J. Composto, and K. I. Winey, "Excluded volume model for the reduction of polymer diffusion into nanocomposites," *Journal of Physical Chemistry B*, vol. 117, no. 49, pp. 15675–15683, 2013.

[203] S. Torquato, *Random heterogeneous materials: microstructure and macroscopic properties*. Springer Science & Business Media, 2013.

[204] C.-C. Lin, E. Parrish, and R. J. Composto, "Macromolecule and particle dynamics in confined media," *Macromolecules*, vol. 49, no. 16, pp. 5755–5772, 2016.

[205] S. Gam, J. S. Meth, S. G. Zane, C. Chi, B. A. Wood, K. I. Winey, N. Clarke, and R. J. Composto, "Polymer diffusion in a polymer nanocomposite: effect of nanoparticle size and polydispersity," *Soft Matter*, vol. 8, no. 24, pp. 6512–6520, 2012.

[206] C.-C. Lin, P. J. Griffin, H. Chao, M. J. Hore, K. Ohno, N. Clarke, R. A. Riggleman, K. I. Winey, and R. J. Composto, "Grafted polymer chains suppress nanoparticle diffusion in athermal polymer melts," *The Journal of Chemical Physics*, vol. 146, no. 20, p. 203332, 2017.

[207] M. Mu, N. Clarke, R. J. Composto, and K. I. Winey, "Polymer diffusion exhibits a minimum with increasing single-walled carbon nanotube concentration," *Macromolecules*, vol. 42, no. 18, pp. 7091–7097, 2009.

[208] M. Mu, R. J. Composto, N. Clarke, and K. I. Winey, "Minimum in diffusion coefficient with increasing mwcnt concentration requires tracer molecules to be larger than nanotubes," *Macromolecules*, vol. 42, no. 21, pp. 8365–8369, 2009.

[209] J. Choi, N. Clarke, K. I. Winey, and R. J. Composto, "Fast polymer diffusion through nanocomposites with anisotropic particles," *ACS Macro Letters*, vol. 3, no. 9, pp. 886–891, 2014.

[210] E. Senses, S. M. Ansar, C. L. Kitchens, Y. Mao, S. Narayanan, B. Natarajan, and A. Faraone, "Small particle driven chain disentanglements in polymer nanocomposites," *Physical Review Letters*, vol. 118, no. 14, p. 147801, 2017.

[211] G. Schneider, K. Nusser, L. Willner, P. Falus, and D. Richter, "Dynamics of entangled chains in polymer nanocomposites," *Macromolecules*, vol. 44, no. 15, pp. 5857–5860, 2011.

[212] Y. Li, M. Kröger, and W. K. Liu, "Nanoparticle effect on the dynamics of polymer chains and their entanglement network," *Physical Review Letters*, vol. 109, no. 11, p. 118001, 2012.

[213] J. T. Kalathi, S. K. Kumar, M. Rubinstein, and G. S. Grest, "Rouse mode analysis of chain relaxation in homopolymer melts," *Macromolecules*, vol. 47, no. 19, pp. 6925–6931, 2014.

[214] G. D. Smith, D. Bedrov, L. Li, and O. Byutner, "A molecular dynamics simulation study of the viscoelastic properties of polymer nanocomposites," *The Journal of Chemical Physics*, vol. 117, no. 20, pp. 9478–9489, 2002.

[215] Y. Li, M. Kröger, and W. K. Liu, "Dynamic structure of unentangled polymer chains in the vicinity of non-attractive nanoparticles," *Soft Matter*, vol. 10, no. 11, p. 1723, 2014.

[216] L.-J. Dai, C.-L. Fu, Y.-L. Zhu, and Z.-Y. Sun, "Heterogeneous dynamics of unentangled chains in polymer nanocomposites," *The Journal of Chemical Physics*, vol. 150, no. 18, p. 184903, 2019.

[217] T. Desai, P. Keblinski, and S. K. Kumar, "Molecular dynamics simulations of polymer transport in nanocomposites," *The Journal of Chemical Physics*, vol. 122, no. 13, p. 134910, 2005.

[218] M. Vacatello, "Monte Carlo simulations of polymer melts filled with solid nanoparticles," *Macromolecules*, vol. 34, no. 6, pp. 1946–1952, 2001.

[219] P. J. Dionne, R. Ozisik, and C. R. Picu, "Structure and dynamics of polyethylene nanocomposites," *Macromolecules*, vol. 38, no. 22, pp. 9351–9358, 2005.

[220] F. M. Erguney, H. Lin, and W. L. Mattice, "Dimensions of matrix chains in polymers filled with energetically neutral nanoparticles," *Polymer*, vol. 47, no. 10, pp. 3689–3695, 2006.

[221] G. Allegra, G. Raos, and M. Vacatello, "Theories and simulations of polymer-based nanocomposites: From chain statistics to reinforcement," *Progress in Polymer Science*, vol. 33, no. 7, pp. 683–731, 2008.

[222] Y. Termonia, "Chain confinement in polymer nanocomposites and its effect on polymer bulk properties," *Journal of Polymer Science Part B: Polymer Physics*, vol. 48, no. 6, pp. 687–692, 2010.

[223] F. W. Starr, T. B. Schrøder, and S. C. Glotzer, "Molecular dynamics simulation of a polymer melt with a nanoscopic particle," *Macromolecules*, vol. 35, no. 11, pp. 4481–4492, 2002.

[224] F. W. Starr, J. F. Douglas, and S. C. Glotzer, "Origin of particle clustering in a simulated polymer nanocomposite and its impact on rheology," *The Journal of Chemical Physics*, vol. 119, no. 3, pp. 1777–1788, 2003.

[225] J. T. Kalathi, G. S. Grest, and S. K. Kumar, "Universal viscosity behavior of polymer nanocomposites," *Physical Review Letters*, vol. 109, no. 19, p. 198301, 2012.

[226] A. Patti, "Molecular dynamics of spherical nanoparticles in dense polymer melts," *The Journal of Physical Chemistry B*, vol. 118, no. 13, pp. 3731–3742, 2014.

[227] J. T. Kalathi, S. K. Kumar, M. Rubinstein, and G. S. Grest, "Rouse mode analysis of chain relaxation in polymer nanocomposites," *Soft Matter*, vol. 11, no. 20, pp. 4123–4132, 2015.

[228] I. V. Volgin, S. V. Larin, E. Abad, and S. V. Lyulin, "Molecular Dynamics Simulations of Fullerene Diffusion in Polymer Melts," *Macromolecules*, vol. 50, no. 5, pp. 2207–2218, 2017.

[229] R. Chen, R. Poling-Skutvik, A. Nikoubashman, M. P. Howard, J. C. Conrad, and J. C. Palmer, "Coupling of nanoparticle dynamics to polymer center-of-mass motion in semidilute polymer solutions," *Macromolecules*, vol. 51, no. 5, pp. 1865–1872, 2018.

[230] A. Chen, N. Zhao, and Z. Hou, "The effect of hydrodynamic interactions on nanoparticle diffusion in polymer solutions: a multiparticle collision dynamics study," *Soft Matter*, vol. 13, pp. 8625–8635, 2017.

[231] U. Yamamoto, J.-M. Y. Carrillo, V. Bocharova, A. P. Sokolov, B. G. Sumpter, and K. S. Schweizer, "Theory and simulation of attractive nanoparticle transport in polymer melts," *Macromolecules*, vol. 51, no. 6, pp. 2258–2267, 2018.

[232] Y. Du, H. Jiang, and Z. Hou, "Study of active brownian particle diffusion in polymer solutions," *Soft Matter*, vol. 15, no. 9, pp. 2020–2031, 2019.

[233] A. Karatrantos, R. J. Composto, K. I. Winey, M. Kröger, and N. Clarke, "Modeling of entangled polymer diffusion in melts and nanocomposites: A review," *Polymers*, vol. 11, no. 5, p. 876, 2019.

[234] T. Ge, J. T. Kalathi, J. D. Halverson, G. S. Grest, and M. Rubinstein, "Nanoparticle Motion in Entangled Melts of Linear and Nonconcatenated Ring Polymers," *Macromolecules*, vol. 50, no. 4, pp. 1749–1754, 2017.

[235] R. Chen, R. Poling-Skutvik, A. Nikoubashman, M. P. Howard, J. C. Conrad, and J. C. Palmer, "Coupling of Nanoparticle Dynamics to Polymer Center-of-Mass Motion in Semidilute Polymer Solutions," *Macromolecules*, feb 2018.

[236] R. Chen, R. Poling-Skutvik, M. P. Howard, A. Nikoubashman, S. A. Egorov, J. C. Conrad, and J. C. Palmer, "Influence of polymer flexibility on nanoparticle dynamics in semidilute solutions," *Soft Matter*, vol. 15, no. 6, pp. 1260–1268, 2019.

[237] Y. Zhou and K. S. Schweizer, "Local structure, thermodynamics, and phase behavior of asymmetric particle mixtures: Comparison between integral equation theories and simulation," *The Journal of Chemical Physics*, vol. 150, no. 21, p. 214902, 2019.

[238] S. Gong, Q. Chen, J. F. Moll, S. K. Kumar, and R. H. Colby, "Segmental dynamics of polymer melts with spherical nanoparticles," *ACS Macro Letters*, vol. 3, no. 8, pp. 773–777, 2014.

[239] V. Sorichetti, V. Hugouvieux, and W. Kob, "Structure and dynamics of a polymer–nanoparticle composite: Effect of nanoparticle size and volume fraction," *Macromolecules*, vol. 51, no. 14, pp. 5375–5391, 2018.

[240] V. Sorichetti, V. Hugouvieux, and W. Kob, "Addition to structure and dynamics of a polymer–nanoparticle composite: Effect of nanoparticle size and volume fraction," *Macromolecules*, vol. 52, no. 16, pp. 6336–6337, 2019.

[241] "LAMMPS website." `https://lammps.sandia.gov`. [accessed 4 October 2019].

[242] S. Plimpton, "Fast parallel algorithms for short-range molecular dynamics," *Journal of Computational Physics*, vol. 117, no. 1, pp. 1–19, 1995.

[243] "fix nh – LAMMPS manual." `https://lammps.sandia.gov/doc/fix_nh`. [accessed 17 September 2019].

[244] K. Binder and W. Kob, *Glassy materials and disordered solids: An introduction to their statistical mechanics*. World scientific, 2011.

[245] T. C. Hales, "A proof of the Kepler conjecture," *Annals of Mathematics*, pp. 1065–1185, 2005.

[246] S. Wu, "Phase structure and adhesion in polymer blends: A criterion for rubber toughening," *Polymer*, vol. 26, no. 12, pp. 1855–1863, 1985.

[247] S. Torquato, T. M. Truskett, and P. G. Debenedetti, "Is random close packing of spheres well defined?," *Physical Review Letters*, vol. 84, no. 10, p. 2064, 2000.

[248] Y. Jiao and S. Torquato, "Maximally random jammed packings of Platonic solids: Hyperuniform long-range correlations and isostaticity," *Physical Review E - Statistical, Nonlinear, and Soft Matter Physics*, vol. 84, no. 4, pp. 1–7, 2011.

[249] M. D. Rintoul, S. Torquato, C. Yeong, D. T. Keane, S. Erramilli, Y. N. Jun, D. M. Dabbs, and I. A. Aksay, "Structure and transport properties of a porous magnetic gel via x-ray microtomography," *Physical Review E*, vol. 54, no. 3, p. 2663, 1996.

[250] V. Testard, L. Berthier, and W. Kob, "Intermittent dynamics and logarithmic domain growth during the spinodal decomposition of a glass-forming liquid," *The Journal of Chemical Physics*, vol. 140, no. 16, p. 164502, 2014.

[251] M. Abramowitz and I. A. Stegun, *Handbook of mathematical functions: with formulas, graphs, and mathematical tables*, vol. 55. Courier Corporation, 1965.

[252] C. Bennemann, J. Baschnagel, W. Paul, and K. Binder, "Molecular-dynamics simulation of a glassy polymer melt: Rouse model and cage effect," *Computational and Theoretical Polymer Science*, vol. 9, no. 3-4, pp. 217–226, 1999.

[253] W. Kob and H. C. Andersen, "Testing mode-coupling theory for a supercooled binary Lennard-Jones mixture. I: The van Hove correlation function," *Physical Review E*, vol. 51, no. 5, p. 4626, 1995.

[254] J. Horbach and W. Kob, "Static and dynamic properties of a viscous silica melt," *Physical Review B*, vol. 60, no. 5, p. 3169, 1999.

[255] B. Dünweg and K. Kremer, "Molecular dynamics simulation of a polymer chain in solution," *The Journal of Chemical Physics*, vol. 99, no. 9, pp. 6983–6997, 1993.

[256] I. C. Yeh and G. Hummer, "System-size dependence of diffusion coefficients and viscosities from molecular dynamics simulations with periodic boundary conditions," *Journal of Physical Chemistry B*, vol. 108, no. 40, pp. 15873–15879, 2004.

[257] A. Cavagna, "Supercooled liquids for pedestrians," *Physics Reports*, vol. 476, no. 4-6, pp. 51–124, 2009.

[258] L. Berthier and G. Biroli, "Theoretical perspective on the glass transition and amorphous materials," *Review of Modern Physics*, vol. 83, no. 2, p. 587, 2011.

[259] G. Adam and J. H. Gibbs, "On the temperature dependence of cooperative relaxation properties in glass-forming liquids," *J. Chem. Phys*, vol. 43, no. 1, pp. 139–146, 1965.

[260] L. Bocquet, J. P. Hansen, and J. Piasecki, "On the Brownian motion of a massive sphere suspended in a hard-sphere fluid. II. Molecular dynamics estimates of the friction coefficient," *Journal of Statistical Physics*, vol. 76, no. 1-2, pp. 527–548, 1994.

[261] J. R. Schmidt and J. L. Skinner, "Hydrodynamic boundary conditions, the Stokes-Einstein law, and long-time tails in the Brownian limit," *The Journal of Chemical Physics*, vol. 119, no. 15, pp. 8062–8068, 2003.

[262] J. T. Hynes, R. Kapral, and M. Weinberg, "Molecular theory of translational diffusion: Microscopic generalization of the normal velocity boundary condition," *The Journal of Chemical Physics*, vol. 70, no. 3, pp. 1456–1466, 1979.

[263] K. Huang, *Statistical Mechanics*. Taylor & Francis, Inc., 1963.

[264] B. Cichocki and B. U. Felderhof, "Long-time self-diffusion coefficient and zero-frequency viscosity of dilute suspensions of spherical Brownian particles," *The Journal of Chemical Physics*, vol. 89, no. 6, pp. 3705–3709, 1988.

[265] V. Sorichetti, A. Ninarello, V. Hugouvieux, W. Kob, L. Rovigatti, J. Ruiz-Franco, and E. Zaccarelli *In preparation*.

[266] F. Amblard, A. C. Maggs, B. Yurke, A. N. Pargellis, and S. Leibler, "Subdiffusion and anomalous local viscoelasticity in actin networks," *Physical Review Letters*, vol. 77, no. 21, p. 4470, 1996.

[267] I. Wong, M. Gardel, D. Reichman, E. R. Weeks, M. Valentine, A. Bausch, and D. A. Weitz, "Anomalous diffusion probes microstructure dynamics of entangled f-actin networks," *Physical Review Letters*, vol. 92, no. 17, p. 178101, 2004.

[268] C. C. Fritsch and J. Langowski, "Anomalous diffusion in the interphase cell nucleus: the effect of spatial correlations of chromatin," *The Journal of Chemical Physics*, vol. 133, no. 2, p. 07B602, 2010.

[269] T.-O. Peulen and K. J. Wilkinson, "Diffusion of nanoparticles in a biofilm," *Environmental science & technology*, vol. 45, no. 8, pp. 3367–3373, 2011.

[270] T. Stylianopoulos, M.-Z. Poh, N. Insin, M. G. Bawendi, D. Fukumura, L. L. Munn, and R. K. Jain, "Diffusion of particles in the extracellular matrix: the effect of repulsive electrostatic interactions," *Biophysical journal*, vol. 99, no. 5, pp. 1342–1349, 2010.

[271] K. Haraguchi and T. Takehisa, "Nanocomposite hydrogels: A unique organic–inorganic network structure with extraordinary mechanical, optical, and swelling/de-swelling properties," *Advanced materials*, vol. 14, no. 16, pp. 1120–1124, 2002.

[272] J. Nelson and Y. Hu, "Nanocomposite dielectrics—properties and implications," *Journal of Physics D: Applied Physics*, vol. 38, no. 2, p. 213, 2005.

[273] K. Haraguchi, "Nanocomposite hydrogels," *Current Opinion in Solid State and Materials Science*, vol. 11, no. 3-4, pp. 47–54, 2007.

[274] K. Haraguchi, "Synthesis and properties of soft nanocomposite materials with novel organic/inorganic network structures," *Polymer journal*, vol. 43, no. 3, p. 223, 2011.

[275] P. Thoniyot, M. J. Tan, A. A. Karim, D. J. Young, and X. J. Loh, "Nanoparticle–hydrogel composites: Concept, design, and applications of these promising, multi-functional materials," *Advanced Science*, vol. 2, no. 1-2, p. 1400010, 2015.

[276] P. A. Netz and T. Dorfmüller, "Computer simulation studies of diffusion in gels: Model structures," *The Journal of Chemical Physics*, vol. 107, no. 21, pp. 9221–9233, 1997.

[277] J. Sonnenburg, J. Gao, and J. Weiner, "Molecular dynamics simulations of gas diffusion through polymer networks," *Macromolecules*, vol. 23, no. 21, pp. 4653–4657, 1990.

[278] P. Licinio and A. Teixeira, "Anomalous diffusion of ideal polymer networks," *Physical Review E*, vol. 56, no. 1, p. 631, 1997.

[279] H. Zhou and S. B. Chen, "Brownian dynamics simulation of tracer diffusion in a cross-linked network," *Physical Review E*, vol. 79, no. 2, p. 021801, 2009.

[280] A. Godec, M. Bauer, and R. Metzler, "Collective dynamics effect transient subdiffusion of inert tracers in flexible gel networks," *New Journal of Physics*, vol. 16, no. 9, p. 092002, 2014.

[281] P. Kumar, L. Theeyancheri, S. Chaki, and R. Chakrabarti, "Transport of probe particles in polymer network: effects of probe size, network rigidity and probe-polymer interaction," *arXiv preprint arXiv:1909.04517*, 2019.

[282] N. Kamerlin and C. Elvingson, "Tracer diffusion in a polymer gel: simulations of static and dynamic 3d networks using spherical boundary conditions," *Journal of Physics: Condensed Matter*, vol. 28, no. 47, p. 475101, 2016.

[283] N. Kamerlin, T. Ekholm, T. Carlsson, and C. Elvingson, "Construction of a closed polymer network for computer simulations," *The Journal of Chemical Physics*, vol. 141, no. 15, p. 154113, 2014.

[284] K. Kratky, "New boundary conditions for computer experiments of thermodynamic systems," *Journal of Computational Physics*, vol. 37, no. 2, pp. 205–217, 1980.

[285] "ESPResSo website." `http://espressomd.org/wordpress`. [accessed 4 October 2019].

[286] E. R. Duering, K. Kremer, and G. S. Grest, "Relaxation of randomly cross-linked polymer melts," *Physical Review Letters*, vol. 67, no. 25, p. 3531, 1991.

[287] E. Duering, K. Kremer, and G. Grest, "Structural properties of randomly crosslinked polymer networks," in *Physics of Polymer Networks*, pp. 13–15, Springer, 1992.

[288] G. Grest, K. Kremer, and E. Duering, "Kinetics of end crosslinking in dense polymer melts," *EPL (Europhysics Letters)*, vol. 19, no. 3, p. 195, 1992.

[289] R. Everaers and K. Kremer, "Test of the foundations of classical rubber elasticity," *Macromolecules*, vol. 28, no. 21, pp. 7291–7294, 1995.

[290] R. Everaers and K. Kremer, "Topological interactions in model polymer networks," *Physical Review E*, vol. 53, no. 1, p. R37, 1996.

[291] R. Everaers, "Entanglement effects in defect-free model polymer networks," *New Journal of Physics*, vol. 1, no. 1, p. 12, 1999.

[292] M. Pütz, K. Kremer, and R. Everaers, "Self-similar chain conformations in polymer gels," *Physical Review Letters*, vol. 84, no. 2, p. 298, 2000.

[293] N. Gilra, C. Cohen, and A. Z. Panagiotopoulos, "A Monte Carlo study of the structural properties of end-linked polymer networks," *The Journal of Chemical Physics*, vol. 112, no. 15, pp. 6910–6916, 2000.

[294] N. Kenkare, S. Smith, C. Hall, and S. Khan, "Discontinuous molecular dynamics studies of end-linked polymer networks," *Macromolecules*, vol. 31, no. 17, pp. 5861–5879, 1998.

[295] D. R. Heine, G. S. Grest, C. D. Lorenz, M. Tsige, and M. J. Stevens, "Atomistic simulations of end-linked poly (dimethylsiloxane) networks: structure and relaxation," *Macromolecules*, vol. 37, no. 10, pp. 3857–3864, 2004.

[296] N. Gnan, L. Rovigatti, M. Bergman, and E. Zaccarelli, "In silico synthesis of microgel particles," *Macromolecules*, vol. 50, no. 21, pp. 8777–8786, 2017.

[297] L. Rovigatti, N. Gnan, and E. Zaccarelli, "Internal structure and swelling behaviour of in silico microgel particles," *Journal of Physics: Condensed Matter*, vol. 30, no. 4, p. 044001, 2017.

[298] F. Camerin, N. Gnan, L. Rovigatti, and E. Zaccarelli, "Modelling realistic microgels in an explicit solvent," *Scientific reports*, vol. 8, 2018.

[299] L. Rovigatti, N. Gnan, L. Tavagnacco, A. J. Moreno, and E. Zaccarelli, "Numerical modelling of non-ionic microgels: an overview," *Soft Matter*, vol. 15, no. 6, pp. 1108–1119, 2019.

[300] L. Rovigatti, N. Gnan, A. Ninarello, and E. Zaccarelli, "Connecting elasticity and effective interactions of neutral microgels: The validity of the hertzian model," *Macromolecules*, 2019.

[301] A. Ninarello, J. J. Crassous, D. Paloli, F. Camerin, N. Gnan, L. Rovigatti, P. Schurtenberger, and E. Zaccarelli, "Advanced modelling of microgel structure across the volume phase transition," *arXiv preprint arXiv:1901.11495*, 2019.

[302] F. A. Escobedo and J. J. de Pablo, "Monte Carlo simulation of branched and crosslinked polymers," *The Journal of Chemical Physics*, vol. 104, no. 12, pp. 4788–4801, 1996.

[303] F. A. Escobedo and J. J. de Pablo, "Simulation and theory of the swelling of athermal gels," *The Journal of Chemical Physics*, vol. 106, no. 2, pp. 793–810, 1997.

[304] F. Sciortino, "Three-body potential for simulating bond swaps in molecular dynamics," *The European Physical Journal E*, vol. 40, no. 1, p. 3, 2017.

[305] "oxDNA website." `https://dna.physics.ox.ac.uk/index.php/Main_Page`. [accessed 4 October 2019].

[306] L. Rovigatti, P. Šulc, I. Z. Reguly, and F. Romano, "A comparison between parallelization approaches in molecular dynamics simulations on gpus," *Journal of computational chemistry*, vol. 36, no. 1, pp. 1–8, 2015.

[307] W. Shinoda, M. Shiga, and M. Mikami, "Rapid estimation of elastic constants by molecular dynamics simulation under constant stress," *Physical Review B*, vol. 69, no. 13, p. 134103, 2004.

[308] G. J. Martyna, D. J. Tobias, and M. L. Klein, "Constant pressure molecular dynamics algorithms," *The Journal of Chemical Physics*, vol. 101, no. 5, pp. 4177–4189, 1994.

[309] M. Parrinello and A. Rahman, "Polymorphic transitions in single crystals: A new molecular dynamics method," *Journal of Applied physics*, vol. 52, no. 12, pp. 7182–7190, 1981.

[310] G. J. Martyna, M. L. Klein, and M. Tuckerman, "Nosé–hoover chains: The canonical ensemble via continuous dynamics," *The Journal of Chemical Physics*, vol. 97, no. 4, pp. 2635–2643, 1992.

[311] E. Bianchi, J. Largo, P. Tartaglia, E. Zaccarelli, and F. Sciortino, "Phase diagram of patchy colloids: Towards empty liquids," *Physical Review Letters*, vol. 97, no. 16, p. 168301, 2006.

[312] L. Rovigatti, D. de las Heras, J. M. Tavares, M. M. Telo da Gama, and F. Sciortino, "Computing the phase diagram of binary mixtures: A patchy particle case study," *The Journal of Chemical Physics*, vol. 138, no. 16, p. 164904, 2013.

[313] M. Wertheim, "Fluids with highly directional attractive forces. I. Statistical thermodynamics," *Journal of statistical physics*, vol. 35, no. 1-2, pp. 19–34, 1984.

[314] M. Wertheim, "Fluids with highly directional attractive forces. II. Thermodynamic perturbation theory and integral equations," *Journal of statistical physics*, vol. 35, no. 1-2, pp. 35–47, 1984.

[315] M. Wertheim, "Fluids with highly directional attractive forces. III. Multiple attraction sites," *Journal of statistical physics*, vol. 42, no. 3-4, pp. 459–476, 1986.

[316] M. Wertheim, "Fluids with highly directional attractive forces. IV. Equilibrium polymerization," *Journal of statistical physics*, vol. 42, no. 3-4, pp. 477–492, 1986.

[317] J. E. Martin and B. J. Ackerson, "Static and dynamic scattering from fractals," *Physical Review A*, vol. 31, no. 2, p. 1180, 1985.

[318] E. Del Gado and W. Kob, "Structure and relaxation dynamics of a colloidal gel," *EPL (Europhysics Letters)*, vol. 72, no. 6, p. 1032, 2005.

[319] T. Vilgis and F. Boué, "Deformation dependence of the form factor of a crosslinked chain in a rubber: Entanglement and orientational effect," *Polymer*, vol. 27, no. 8, pp. 1154–1162, 1986.

[320] S. K. Sukumaran, G. S. Grest, K. Kremer, and R. Everaers, "Identifying the primitive path mesh in entangled polymer liquids," *Journal of Polymer Science Part B: Polymer Physics*, vol. 43, no. 8, pp. 917–933, 2005.

[321] L. Fetters, D. Lohse, D. Richter, T. Witten, and A. Zirkel, "Connection between polymer molecular weight, density, chain dimensions, and melt viscoelastic properties," *Macromolecules*, vol. 27, no. 17, pp. 4639–4647, 1994.

[322] V. Sorichetti, V. Hugouvieux, and W. Kob *In preparation*.

[323] E. Parrish, M. A. Caporizzo, and R. J. Composto, "Network confinement and heterogeneity slows nanoparticle diffusion in polymer gels," *The Journal of Chemical Physics*, vol. 146, no. 20, p. 203318, 2017.

[324] S. Roldán-Vargas, L. Rovigatti, and F. Sciortino, "Connectivity, dynamics, and structure in a tetrahedral network liquid," *Soft Matter*, vol. 13, no. 2, pp. 514–530, 2017.

[325] W. Kob and H. C. Andersen, "Testing mode-coupling theory for a supercooled binary lennard-jones mixture. ii. intermediate scattering function and dynamic susceptibility," *Physical Review E*, vol. 52, no. 4, p. 4134, 1995.

[326] V. Sorichetti, V. Hugouvieux, and W. Kob, "Characterizing the mesh size of polymer solutions via the pore size distribution," *arXiv preprint arXiv:1908.01484*, 2019.

[327] S. R. Lustig and N. A. Peppas, "Solute Diffusion in Swollen Membranes .9. Scaling Laws for Solute Diffusion in Gels," *Journal of Applied Polymer Science*, vol. 36, no. 4, pp. 735–747, 1988.

[328] S. Rose, A. Marcellan, D. Hourdet, C. Creton, and T. Narita, "Dynamics of hybrid polyacrylamide hydrogels containing silica nanoparticles studied by dynamic light scattering," *Macromolecules*, vol. 46, no. 11, pp. 4567–4574, 2013.

[329] E. Parrish, S. C. Seeger, and R. J. Composto, "Temperature-Dependent Nanoparticle Dynamics in Poly (N-isopropylacrylamide) Gels," *Macromolecules*, vol. 51, no. 10, pp. 3597–3607, 2018.

[330] A. E. Scheidegger, *The physics of flow through porous media*. Macmillan, 1957.

[331] S. Prager, "Interphase transfer in stationary two-phase media," *Chemical Engineering Science*, vol. 18, no. 4, pp. 227–231, 1963.

[332] S. Torquato, B. Lu, and J. Rubinstein, "Nearest-neighbor distribution functions in many-body systems," *Physical Review A*, vol. 41, no. 4, p. 2059, 1990.

[333] S. Torquato and M. Avellaneda, "Diffusion and reaction in heterogeneous media: Pore size distribution, relaxation times, and mean survival time," *The Journal of Chemical Physics*, vol. 95, no. 9, pp. 6477–6489, 1991.

[334] S. Torquato, "Nearest-neighbor statistics for packings of hard spheres and disks," *Physical Review E*, vol. 51, no. 4, p. 3170, 1995.

[335] L. D. Gelb and K. E. Gubbins, "Pore size distributions in porous glasses: a computer simulation study," *Langmuir*, vol. 15, no. 2, pp. 305–308, 1999.

[336] K. T. Thomson and K. E. Gubbins, "Modeling structural morphology of microporous carbons by reverse Monte Carlo," *Langmuir*, vol. 16, no. 13, pp. 5761–5773, 2000.

[337] J. Pikunic, C. Clinard, N. Cohaut, K. E. Gubbins, J.-M. Guet, R. J.-M. Pellenq, I. Rannou, and J.-N. Rouzaud, "Structural modeling of porous carbons: constrained reverse Monte Carlo method," *Langmuir*, vol. 19, no. 20, pp. 8565–8582, 2003.

[338] S. Bhattacharya and K. E. Gubbins, "Fast method for computing pore size distributions of model materials," *Langmuir*, vol. 22, no. 18, pp. 7726–7731, 2006.

[339] R. S. Hoy, K. Foteinopoulou, and M. Kröger, "Topological analysis of polymeric melts: Chain-length effects and fast-converging estimators for entanglement length," *Physical Review E*, vol. 80, no. 3, p. 31803, 2009.

[340] L. J. Fetters, D. J. Lohse, S. T. Milner, and W. W. Graessley, "Packing length influence in linear polymer melts on the entanglement, critical, and reptation molecular weights," *Macromolecules*, vol. 32, no. 20, pp. 6847–6851, 1999.

[341] M. Kröger and S. Hess, "Rheological evidence for a dynamical crossover in polymer melts via nonequilibrium molecular dynamics," *Physical Review Letters*, vol. 85, no. 5, p. 1128, 2000.

[342] J. Wittmer, H. Meyer, J. Baschnagel, A. Johner, S. Obukhov, L. Mattioni, M. Müller, and A. N. Semenov, "Long range bond-bond correlations in dense polymer solutions," *Physical Review Letters*, vol. 93, no. 14, p. 147801, 2004.

[343] L. Schäfer and K. Elsner, "Calculation of the persistence length of a flexible polymer chain with short-range self-repulsion," *The European Physical Journal E*, vol. 13, no. 3, pp. 225–237, 2004.

[344] H.-P. Hsu, W. Paul, and K. Binder, "Standard definitions of persistence length do not describe the local "intrinsic" stiffness of real polymer chains," *Macromolecules*, vol. 43, no. 6, pp. 3094–3102, 2010.

[345] M. L. Connolly, "Analytical molecular surface calculation," *Journal of Applied Crystallography*, vol. 16, no. 5, pp. 548–558, 1983.

[346] D. D. Do, L. F. Herrera, and H. D. Do, "A new method to determine pore size and its volume distribution of porous solids having known atomistic configuration," *Journal of Colloid and Interface Science*, vol. 328, no. 1, pp. 110–119, 2008.

[347] B. Lee and F. M. Richards, "The interpretation of protein structures: estimation of static accessibility," *Journal of Molecular Biology*, vol. 55, no. 3, pp. 379–400, 1971.

[348] F. M. Richards, "Areas, volumes, packing, and protein structure," *Annual Review of Biophysics and Bioengineering*, vol. 6, no. 1, pp. 151–176, 1977.

[349] W. H. Press, S. A. Teukolsky, W. T. Vetterling, and B. P. Flannery, *Numerical recipes 3rd edition: The art of scientific computing*. Cambridge university press, 2007.

[350] S. G. Johnson, "The nlopt nonlinear-optimization package." `http://github.com/stevengj/nlopt`.

[351] T. H. Rowan, *Functional Stability Analysis of Numerical Algorithms*. PhD thesis, Department of Computer Sciences, University of Texas at Austin, 1990.

[352] J. H. Davenport, Y. Siret, , and E. Tournier, *Computer Algebra: Systems and Algorithms for Algebraic Computation (2nd ed.)*. Academic press, 1993.

[353] Y. Tsuji, X. Li, and M. Shibayama, "Evaluation of mesh size in model polymer networks consisting of tetra-arm and linear poly (ethylene glycol) s," *Gels*, vol. 4, no. 2, p. 50, 2018.

[354] L. R. Treloar, "The mechanics of rubber elasticity," *Proceedings of the Royal Society of London. A. Mathematical and Physical Sciences*, vol. 351, no. 1666, pp. 301–330, 1976.